

The Optical Properties of Biological Tissue

by

Jeffrey Alan Bews

A thesis
presented to the University of Manitoba
in partial fulfillment of the
requirements for the degree of
PhD
in
Physics

Winnipeg, Manitoba

(c) Jeffrey Alan Bews, 1988

Permission has been granted to the National Library of Canada to microfilm this thesis and to lend or sell copies of the film.

The author (copyright owner) has reserved other publication rights, and neither the thesis nor extensive extracts from it may be printed or otherwise reproduced without his/her written permission.

L'autorisation a été accordée à la Bibliothèque nationale du Canada de microfilmer cette thèse et de prêter ou de vendre des exemplaires du film.

L'auteur (titulaire du droit d'auteur) se réserve les autres droits de publication; ni la thèse ni de longs extraits de celle-ci ne doivent être imprimés ou autrement reproduits sans son autorisation écrite.

ISBN 0-315-48123-4

THE OPTICAL PROPERTIES OF BIOLOGICAL TISSUE

BY

JEFFREY ALAN BEWS

A thesis submitted to the Faculty of Graduate Studies of
the University of Manitoba in partial fulfillment of the requirements
of the degree of

DOCTOR OF PHILOSOPHY

© 1988

Permission has been granted to the LIBRARY OF THE UNIVERSITY OF MANITOBA to lend or sell copies of this thesis, to the NATIONAL LIBRARY OF CANADA to microfilm this thesis and to lend or sell copies of the film, and UNIVERSITY MICROFILMS to publish an abstract of this thesis.

The author reserves other publication rights, and neither the thesis nor extensive extracts from it may be printed or otherwise reproduced without the author's written permission.

I hereby declare that I am the sole author of this thesis.

I authorize the University of Manitoba to lend this thesis to other institutions or individuals for the purpose of scholarly research.

Jeffrey Alan Bews

I further authorize the University of Manitoba to reproduce this thesis by photocopying or by other means, in total or in part, at the request of other institutions or individuals for the purpose of scholarly research.

Jeffrey Alan Bews

The University of Manitoba requires the signatures of all persons using or photocopying this thesis. Please sign below, and give address and date.

ABSTRACT

The ability of visible and infrared light to propagate through biological tissue has found much application in medicine, both in the treatment and diagnosis of disease (ie. Photodynamic therapy and Diaphanography). However, a poor understanding of this transport phenomenon has served to limit the effectiveness of those modalities which employ it in their operation. This thesis examines light propagation through biological tissue at a very fundamental level, its goal being to improve on the lack of knowledge that presently exists in this area.

A spectrophotometer type instrument, referred to as the DICOM-8 was developed to measure the diffuse spectral extinction of biological tissue over the range 550 to 900 nm. Sample irradiation was with a 100 w quartz tungsten halogen lamp while an RCA vidicon camera functioned as a detector. Results were presented for four classifications of breast tissue, normal, glandular, adipose and carcinoma. All curves were characterized by a common shape (extinction monotonically decreasing with increasing wavelength) but differed in magnitude below 700 nm with carcinoma possessing a higher extinction than glandular which in turn removed light more efficiently than adipose. Dissimilarities were shown to be the result of variations in blood concentration. Data obtained from these tissue measurements served as the basis for developing a homogeneous liquid, referred to as TEM, which simulated the optical properties of tissue over the range 550 to 900 nm. This synthetic model was composed of two components, an aqueous solution of coffee creamer and Methocel which served to scatter light in a manner similar to tissue and hemoglobin which simulated its absorption properties. TEM was used in the construction of a breast phantom for bench top diaphanography studies. Images of the transilluminated model acquired at 600, 700 and 850 nm demonstrated the improved visualization of carcinoma (simulated using blood filled, polyethylene tubes) that is attainable with short wavelength light. The technical problems resulting from the high tissue attenuation below 700 nm were overcome by employing a CCD camera with light amplifier. Digital image processing was shown to be a powerful aid in transillumination studies.

TEM was also used to examine the ability of Linear Transport and Diffusion models to theoretically describe the propagation of light through biological tissue. In this

application, TEM functioned as a test medium in which light distributions resulting from highly controlled irradiation geometries could be experimentally measured and compared with those obtained theoretically. The two input parameters required for generating theoretical distributions, the mean free path and scatter/absorption coefficient of TEM, were obtained experimentally. An application of Beer's law to thin sample (47 μm) extinction measurements yielded a MFP which ranged from 0.206 mm at 550 nm to 0.495 mm at 900 nm. Mean free path was found to be directly proportional to the square of the wavelength. The scatter/absorption coefficient, obtained by maximizing the agreement between theoretical and experimental distributions, assumed values of 0.9986459 at 550 nm and 0.9997315 at 850 nm. These results suggest that one of the conditions responsible for the breakdown of Diffusion theory, that of a scatter/absorption coefficient much smaller than unity, will not be encountered when dealing with the propagation of light through biological tissue. Agreement between experimental and theoretical distributions was found to be extremely good for both isotropic planar and isotropic point source irradiation.

Once the ability to describe light transport through TEM had been demonstrated, Linear Transport and Diffusion theory were utilized to gain a better understanding of this complex phenomenon. Theoretical data generated with the former model revealed the fact that small changes in MFP will have little effect on spatial light distributions. Similar changes in scatter/absorption coefficient, meanwhile, will drastically alter the efficiency of transport. The Linear Transport model also functioned as a tool for studying the effect of spectral changes in the relative importance of scatter and the frequency of interactions. Both absorption by hemoglobin and water were found to play a significant role in determining the spatial distribution of light in TEM, the former at wavelengths below 700 nm, the latter at wavelengths above. Of the four wavelengths studied (550, 600, 700 and 850 nm), light propagation was found to be optimal at 700 nm. At longer wavelengths, transport was found to be less efficient due to the increased absorption by water. Below 700 nm, the ability of light to propagate through TEM was also reduced, although now as a result of absorption by hemoglobin and increased scatter. Effects of source collimation on spatial light density in an irradiated TEM sample were examined by comparing distributions generated using Linear Transport theory for isotropic and collimated planar source geometries. Dissimilarities were found to exist only in the vicinity of the source, up to distances of 0.5 MFP in the presence of weak absorption and 1.7 MFP when absorption is strong. Perturbations in the spatial light density in the vicinity of an air interface were quantified by comparing the theoretical distributions

generated using Linear Transport theory for planar source irradiation of infinite and semi-infinite media (in the latter geometry, the source was assumed to reside at the location of the interface). Whereas light density within the former decreased monotonically with increasing distance from the source, the distribution within the semi-infinite medium assumed a maximum at a finite depth. At the interface, the density of light was approximately 75% of that predicted in its absence. Dissimilarities were found to decrease with distance from the interface, the two distributions being indistinguishable at depths greater than 3.0 MFP. In the final section of the thesis, errors incurred when using Diffusion theory to describe the propagation of light through tissue were quantified by comparing distributions obtained using this model with those of the exact Linear Transport theory. Proximal to an isotropic point source, Diffusion theory underestimated light density (it predicting a density 44.2% of its true value at 0.2 MFP). The magnitude of the errors were found to decrease with distance from the source and were virtually negligible at distances greater than 2.2 MFP. Errors incurred using Diffusion theory to describe planar source irradiation were negligible at distances greater than 0.2 MFP. Diffusion theory was also shown to break down in the vicinity of an air-tissue interface. In these regions, the first order approximation model overestimated light density, it predicting a value 141.1% of its true magnitude at the interface for media characterized by strong absorption. At distances greater than 3.3 MFP, errors associated with the Diffusion model were negligible. In media exhibiting weak absorption, both the magnitude of errors as well as the extent of the region over which they exist were found to be slightly reduced.

ACKNOWLEDGEMENTS

It is at this point that I would like to express my gratitude to the many individuals who have made contributions to this project. Without their support, the work presented here would not have been possible.

Firstly, (or should I say first off), I would like to thank my supervisor, Dr. S. Shalev, for the support and direction he has given to my research over the years. In spite of his heavy workload, he always found time to devote to my project and impromptu questions such as "Do you have a moment ?" were invariably answered with "Pull up a chair"! His suggestions were more than once responsible for steering me back on track when all that I could see ahead were "dead ends". Since entering the field of Medical Physics five years ago, I feel I have grown considerably as a physicist and much of this has to be credited to the guidance, knowledge and patience of Shlomo Shalev. I look forward to his continued friendship in the years to come.

Secondly, I would like to acknowledge Dr. J. Linford for his many contributions in the biological tissue measurements and development of TEM. These ranged from dissection of tissue samples to the suggestion that coffee creamer be used as the scatter component in the breast tissue model. Also deserved of mention are the members of my advisory committee, Drs. T. Lee, G. Tabisz, W. Lehn, H. Schipper and external examiner Dr. E. Profio for their guidance and helpful advice.

Others to be thanked are J. Legal (for his technical support in the development of the DICOM-8 spectrophotometer), J. Arenson and V. Goertzen (for their development of the DICOM-8 imaging computer), Drs. L. Lucman and H. Yazdi (for providing the biological tissue samples) and K. Leszczynski (for his development of the adaptive histogram equalization software).

Finally, I would like to express my love and appreciation to three people not involved in the academic side of this project but whose support played a major role in its completion: my wife, my mother and my father. My successes truly are their successes.

CONTENTS

ABSTRACT	iv
ACKNOWLEDGEMENTS	vii

<u>Chapter</u>		<u>page</u>
I.	INTRODUCTION	1
II.	PHOTODYNAMIC THERAPY	5
III.	DIAPHANOGRAPHY	10
IV.	BIOLOGICAL TISSUE - HISTOLOGY	14
	Connective Tissue	14
	Muscle Tissue	16
	Nervous Tissue	16
V.	LIGHT TRANSPORT THROUGH BIOLOGICAL TISSUE	18
VI.	GENERAL SCATTERING THEORY FOR A SINGLE PARTICLE	22
	Amplitude Function	24
	Extinction of Light by Scatter	26
	Mie Scattering Theory	28
	Rayleigh Scattering Theory	30
	Rayleigh-Gans Scattering Theory	33
	Anomalous Diffraction Theory	35
	Relationship Between Less- Rigorous Theories	38
VII.	SCATTER BY A MULTI-PARTICLE SYSTEM	42
VIII.	LINEAR TRANSPORT THEORY	46
	The Transport Equation	49
	Solutions in One Dimension	54
	Discrete Eigenvalues	57
	Continuous Eigenvalues	58
	Eigenfunction Orthogonality	58
	Discrete Eigenfunction Normalization	59
	Continuum Eigenfunction Normalization	60

IX.	DIFFUSION THEORY	61
	Derivation of the Diffusion Equation	62
	Validity of the Diffusion Equation	65
X.	SOLUTIONS OF THE LINEAR TRANSPORT EQUATION	68
	Collimated Planar Source/Infinite Medium	68
	Isotropic Planar Source/Infinite Medium	71
	Isotropic Point Source	71
	The Albedo Problem	76
	The Diffusion Approximation	84
XI.	SUMMARY OF THE LITERATURE	85
	Diffuse Transmittance	86
	Penetration Depth	88
	Half Value Layer	90
	Application of Transport Models	90
XII.	QUANTIFYING THE OPTICAL PROPERTIES OF TISSUE	95
	DICOM-8 Imaging System	97
	Calibration	102
	Verification of the Calibration Procedure	107
	Angle of Collection of the DICOM-8	112
XIII.	SPECTRAL EXTINCTION OF HUMAN BREAST TISSUE	113
XIV.	A BIOLOGICAL TISSUE PHANTOM	126
	History of Tissue Phantoms	128
	Development of TEM	130
	Concentration of Creamer Particles	139
XV.	MULTI-SPECTRAL DIGITAL IMAGING STUDIES	142
XVI.	APPLICATION OF THEORETICAL MODELS	152
	Mean Free Path	153
	Scatter/Absorption Coefficient	164
	Validity of the Transport Models	170
	Isotropic Point Source Irradiation	170
	Isotropic Planar Source Irradiation	181
	Limitations of Results	187
XVII.	THEORETICAL RESULTS USING LINEAR TRANSPORT THEORY	194
	Effect of Medium Composition and Wavelength	194
	Effect of Planar Source Collimation	204
	Effects of a Tissue-Air Interface	208
	The Errors of Diffusion Theory	213

XVIII.	SUMMARY	222
XIX.	REFERENCES	233

Chapter I

INTRODUCTION

Techniques which base their operation on the ability of visible and infrared light to propagate through biological tissue have found much application in medicine, both in the diagnosis and treatment of disease. Examples are: Diaphanography, a cancer detection modality which images lesions of the female breast with visible and infrared light; and Photodynamic Therapy (PDT), a cancer treatment technique which employs 630 nm radiation to destroy chemically photosensitized malignant tissue. Unfortunately, the light transport phenomenon which forms the very foundation of these techniques is poorly understood and as a result, all remain at levels of development far below the optimal. In some instances, as with PDT, this has resulted in the modality being unable to achieve its full clinical potential. In other cases, diaphanography being an example, the poor understanding of light propagation through tissue has retarded development to such an extent that clinical application has been extremely limited. Nonetheless, visible and infrared light techniques have demonstrated that they have much to offer modern medicine and with the optimization of their operation will come even greater benefits. Further development and improvement will, however, require a better understanding of light propagation through tissue. Ultimately, one would like to achieve the level of sophistication where this complex phenomenon could be accurately described mathematically, perhaps using a transport model such as Linear Transport or Diffusion theory. The work presented here is aimed at this very purpose. Light transport through tissue will be examined in detail with emphasis being placed on obtaining results which can be used to improve the current status of the two visible light modalities described above (diaphanography and Photodynamic therapy).

As specific results are to be obtained for diaphanography and Photodynamic therapy, this thesis will begin with a very general review of these two visible/infrared light techniques (chapter 2 and 3). Included are descriptions of their operation, a summary of their histories and a discussion of some of the major problems or limitations with which they are presently associated. Light propagation in tissue is a complex phenomenon which depends both on the nature of the electromagnetic radiation as well as the

composition and physical structure of the tissue itself. Because of this, a brief review of introductory histology is also presented (chapter 4).

The phenomenon of light propagation in tissue is formally introduced in chapter 5, with a general overview of the two mechanisms by which visible and infrared light interact with tissue, scatter and absorption. Scatter, the more complex of the two, is discussed in greater detail in chapters 6, 7, 8, 9 and 10. Chapter 6 examines the process at a very fundamental level (ie. scatter by a single particle). The concept of amplitude function as a quantitative method of describing scatter is introduced and four vastly different theoretical models which may be used to generate a mathematical expression for it, presented. This chapter also provides some insight into the underlying physical principles involved in the interaction process. Results are extended to light scatter by multi-particle systems in the four chapters following. Such an application is extremely simple provided the scatter phenomenon can be considered both independent and single. Under such conditions, Beer's law is applicable. This extension is made in chapter 7. Light scatter in biological tissue can be considered independent but not single and this simple theory does not apply. An application of the results of chapter 6 to light scatter in multi-scattering media such as tissue requires the use of transport models. Two of these, the Linear Transport and Diffusion theories, are discussed in chapters 8 and 9, respectively. Linear Transport theory will provide an exact description of a beam of light as it propagates through a multi-scattering/absorbing medium while Diffusion theory, a much simpler model, will provide only a first order approximation. In particular, Diffusion theory is expected to be inaccurate near a source of light, in the vicinity of an interface between two media of different optical properties and in materials where absorption is significant. Under the most general conditions, both transport models will be associated with three input parameters, referred to as the mean free path, scatter/absorption coefficient and phase function. These three parameters will be fundamental properties of the tissue medium in which light propagation is to be described and must be known before either transport model can be applied. The phase function parameter describes the angular distribution of light scattered by the individual particles in a medium. If the scattering process is assumed isotropic, the phase function becomes uniquely defined and is no longer treated as an explicit input parameter. Application of either transport model then requires that only mean free path and scatter/absorption coefficient be determined. All scattering media examined in this thesis are assumed to scatter isotropically.

Chapter 11 is a summary of published research pertaining to the propagation of light through biological tissue. Work carried out by others to quantify the optical properties of tissue through measurement of diffuse spectral transmittance, penetration depth and half value layer is presented. Also included is a summary of the research conducted to date on the application of transport models as a means of mathematically describing the propagation of light through tissue.

The remaining chapters in this thesis form the experimental portion of the light transport study. Chapter 12 examines in detail the development and operation of an instrument for measuring the spectral extinction of biological tissue (DICOM-8 spectrophotometer). In chapter 13 this instrument is used to generate diffuse spectral extinction curves for both normal and diseased breast tissue. The implications of these results for Diaphanography and Photodynamic therapy are discussed. Chapter 14 describes the development of a synthetic liquid material (TEM) which simulates the optical properties of tissue over the range 550 to 900 nm. Measurements performed in the previous chapter form the foundation for its construction, the materials used being chosen so as to result in TEM exhibiting the same diffuse spectral extinction as glandular breast tissue. A brief summary of published research pertaining to the development of synthetic tissue-like materials and a discussion of the possible applications of TEM are also included in this chapter. Chapter 15 sees TEM used in the construction of a breast phantom (complete with simulated lesions positioned at varying depths from its surface) for bench top Diaphanography studies. Images of the transilluminated phantom are collected with two types of video camera in order to demonstrate the advantages and feasibility of using short wavelength light (<700 nm) in clinical Diaphanography.

In chapter 16 the Linear Transport and Diffusion theories are applied to light propagation in biological tissue. The ability of the two models to describe this complex phenomenon are examined by comparing theoretical light distributions with those obtained experimentally in tissue samples irradiated under strictly controlled geometries. TEM is used to simulate tissue in the experimental measurements. The procedures used to determine the MFP and scatter/absorption coefficient of TEM, the two input parameters required by the transport models to generate theoretical distributions within this medium, are also outlined. Once the ability of the two models in describing light propagation through tissue has been established, they may be used to gain a better understanding of this complex transport phenomenon. This is the focus of chapter 17. In section 17.1, the effects of mean free path and

scatter/absorption coefficient on the efficiency of light transport is examined in detail. Subsequent sections probe the consequences of source collimation and tissue/air interfaces on the spatial light distributions. Finally, estimates of the magnitude of errors in using the first order approximation Diffusion theory to describe light propagation in tissue are presented.

Chapter II

PHOTODYNAMIC THERAPY

The treatment of disease through irradiation with visible light in the presence of a photosensitizing drug was initiated at the beginning of the century with the observation of the cytotoxic effect of visible light on *Paramecia* treated with acridine orange [3]. Since then, numerous studies dealing with the effects of light on photosensitized biological systems have been conducted but it was not until the development of a non-toxic photosensitizing drug with substantial tumor localizing properties that this phenomenon could gain widespread clinical application.

Photodynamic therapy is a relatively new cancer treatment modality in which localized malignant tumors are destroyed through the action of visible light on chemically photosensitized diseased tissue. The most commonly used sensitizing drug is haematoporphyrin derivative (HPD) which upon intravenous injection is quickly taken up by both normal and malignant tissue. Retention by the latter is, however, much greater and a three to ten fold difference in HPD concentration will be observed within approximately three days of administration of the drug. In this way, selective accumulation of the photosensitizer in diseased tissue is achieved. The tumor is then irradiated with light of 630 nm, the combined action of the photosensitizer and the light serving to generate a singlet oxygen in the cellular membrane, the first step in a chain of events which eventually leads to tissue death [1]. The HPD functions as a kind of reaction catalyst and is responsible for transferring the incident photon energy to the tissue thereby initiating the biochemical reaction. The treatment is usually rapid with necrosis being evident within twenty four hours of the exposure [2].

HPD is a complex mixture of porphyrins developed by Lipson and Baldes [4]. Figure 2.1 illustrates the absorption spectrum for HPD. In the years immediately following its development, HPD was used to localize and detect tumors. The drug was injected into the patient, selectively accumulated in the diseased tissue and upon exposure to visible or ultraviolet light, emitted a red fluorescence. By the mid 70's, however, its clinical use had spread to include the actual treatment of disease. At present, it is estimated

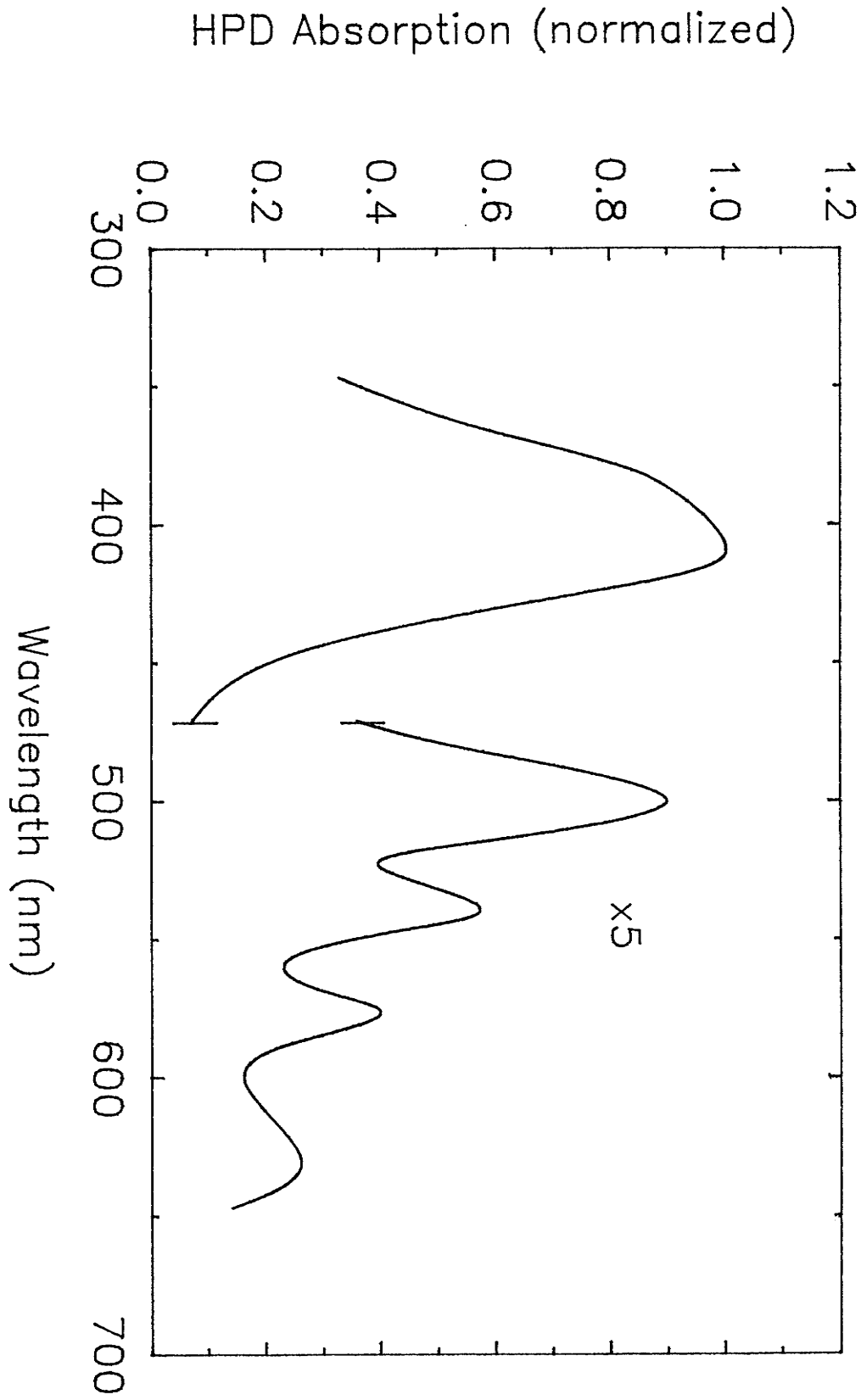


Figure 2.1: HPD absorption spectrum

that some 2000 patients have been treated worldwide [2]. Clinical studies have been numerous with many disease sites being treated in this manner [5].

The effectiveness of Photodynamic therapy depends on three factors: the selective accumulation of a photosensitizing drug in the diseased tissue; the delivery of an appropriate photon flux (characterized by a wavelength with the capabilities of exciting the drug) to all regions of the tumor mass; and the availability of a specific cellular component whose oxidation will result in disruption and destruction (for example, cell membranes). Of concern to the physicist are problems related to ensuring that a sufficient photon flux reaches all areas of the tumor. Regardless of the techniques used to administer light in a PDT treatment, certain regions of the target volume will lie at depth from the source. These sites receive their exposure from a light beam which may have travelled considerable distances through diseased or normal tissue. As a result of attenuation by the intervening tissue, the intensity of light reaching these locations may be significantly reduced from that emitted by the source. Steps must be taken to ensure that, in spite of this attenuation, the exposure received by distal regions is still sufficient for local control.

The effective treatment of disease with Photodynamic therapy requires that a suitable number of light photons be delivered to and absorbed at all locations in the tumor. Thus, the ideal wavelength of light for PDT is one which exhibits low tissue attenuation and strong absorption by the photosensitizing drug HPD. Unfortunately, such an ideal wavelength does not exist. For example, although HPD exhibits a strong absorption at 402 nm, light of this wavelength is strongly attenuated by tissue, making it impossible to deliver the required photon flux to distal target regions. Although long wavelength light will exhibit superior tissue transport properties, its absorption by HPD will be substantially reduced. A compromise, therefore, must be made when choosing a wavelength for Photodynamic therapy and 630 nm light is used clinically at present.

The first clinical Photodynamic treatments utilized noninvasive incandescent or gas discharge lamps to provide external irradiation. The output of these sources was heavily filtered to isolate the useful wavelength band around 630 nm. The limited ability of 630 nm light to penetrate tissue restricts the depth at which tumors can be treated using external irradiation, and early use of the modality was restricted to the treatment of superficial disorders such as skin lesions.

With the advent of the laser and optic fiber, it became possible to treat deep seated lesions through interstitial irradiation. In this approach, a single fiber optic is placed within a steel biopsy needle and inserted into the patient to a position at the center of the treatment volume. By coupling this fiber to a laser, the light source can effectively be placed within the target volume. In doing so, attenuation by overlying normal tissue is eliminated and a greater light flux can be delivered to the site of the disease. Interstitial irradiation also reduces the possibility of damaging surrounding normal tissue. Similarly, a single optic fiber can be placed inside the channel of a flexible endoscope to gain access to sites such as the lung, oesophagus and urogenital tract.

To date, CW argon lasers are the most frequently used light sources for interstitial applications. Their 514.5 nm output serves to pump a dye laser which fluoresces in the 630 nm region. Although power levels are suitable for Photodynamic purposes, these sources tend to be expensive and require frequent tuning. Alternatives are the gold vapour and helium-neon lasers. Both emit radiation of approximately 630 nm (627.8 and 632.8 nm, respectively) and hence eliminate the need of a dye laser. The HeNe laser, however, is characterized by a low output power making it less than ideal for Photodynamic therapy applications. Incandescent and gas discharge lamps are not used in conjunction with optic fibers due to their poor coupling efficiency.

In an attempt to ensure that all regions of a tumor receive adequate exposure, various techniques have been developed to control the spatial distribution of light in interstitial Photodynamic treatments. One such technique modifies the tip of the optic fiber. Fibers with flat, cleaved ends will exhibit an output which is forward directed and conical in shape. An isotropic output can be achieved by attaching a small, spherical volume of some highly scattering material to its tip, an isotropic output can be achieved. Likewise, a cylindrically symmetric line source can be produced by coating a fiber along its length with light scattering material [6]. Light distribution may also be controlled through the use of multiple fibers [7]. The simultaneous positioning of a number of source fibers in the target enables the treatment of much larger volumes and irregularly shaped tumors. Scanning sources provide a third means of regulating light dose pattern [8]. However, both the time and complexity of treatments are increased. Finally, light diffusing media have been used to control the geometrical distribution of light dose. Jocham [9] achieved uniform irradiation of the inner surface of the bladder by filling it with a dilute lipid colloid solution and placing an optic fiber source at the center; scatter by the lipid

colloid served to produce a uniform distribution throughout the cavity.

At present, clinical PDT treatments are prescribed, administered and described solely in terms of the output power of the source and the time of exposure [10]. Light density at depth, and therefore dose, remain unknown quantities. As a result, one can never be certain that all regions of a target volume receive a light flux sufficient to induce necrosis or that excessive damage is not being incurred by surrounding normal tissue. Thus, in its present form, the effectiveness of treatment will be far from optimum. Quite clearly a need exists to develop, test and subsequently apply mathematical models to describe the propagation of light through biological tissue. Once this level of sophistication has been attained, a procedure analogous to radiotherapy treatment planning would be possible. Irradiation geometry and treatment times could then be selected scientifically from theoretical light dose distributions rather than in the less rigorous manner characteristic of current procedures. Application of transport models will, however, require that the optical properties of biological tissue be quantified through experiment (ie. these models will require input parameters). Such measurements may also offer some insight, although limited, into the distribution of light at depth in irradiated tissue. Similarly, they may serve to answer questions such as "How do the optical properties of tissue vary with the wavelength of light" or "Are these optical properties dependant on tissue classification", both being of extreme importance to the further development of the modality. In summary, there is much room for improvement in current PDT practices. However, advancements will come only after a better understanding of light propagation in biological tissue is gained.

Chapter III

DIAPHANOGRAPHY

Diaphanography is the name coined by Gros [11] for transillumination of the female breast. It is an imaging modality which utilizes visible and infrared light to diagnose a wide range of breast diseases, including carcinoma, cysts and bleeding nipple. Its operation is based on the passage of a beam of light through the breast using a hand-held source pressed against the skin surface. Attenuation of the beam depends on the spatial arrangement of internal lesions and this information is then displayed as spatial variations in light intensity on the exit skin surface. For example, carcinoma lying in the path of the beam will produce dark shadows in the skin surface intensity pattern while cysts will be imaged as regions of increased light intensity. High concentrations of blood uncharacteristic of normal breast tissue will also appear as areas of reduced brightness although these images may be distinguished from those of carcinoma due to their much sharper boundaries. By moving the light source over the surface of the breast, all regions may be inspected.

The use of transillumination as an aid in the diagnosis of breast disease was first proposed by Cutler [12] in 1929. Examinations were carried out using an electric lamp while viewing the breast with the naked eye. In these very early studies Cutler demonstrated the ability of diaphanography to diagnose non-palpable tumors, to differentiate between cysts and carcinoma in cases where this was not possible during physical examination and to accurately locate bleeding nipple. He was unable, however, to distinguish benign from malignant tumors.

Transillumination as proposed by Cutler suffered from a number of technical limitations which made its application as a clinical tool impractical. The most serious of these shortcomings arose as a result of it being based on a visual examination of the transmitted light. Because of high tissue attenuation, the intensity of the light exiting the breast during a diaphanography examination is extremely low and direct viewing required a completely darkened room and dark adaptation by the examiner. Even when these steps were taken, viewing was difficult and a strain on the eyes. In addition, the absence of a hardcopy of the image required that the diagnosis be performed during the examination and

prevented future reference. As a result, diaphanography aroused little interest for many years.

In 1951, Gros [13] attempted to overcome the drawbacks associated with direct viewing by recording hardcopy images of diaphanography examinations on photographic film. Although successful in this respect (as well as for the first time enabling transillumination to be carried out in the infrared), new problems were introduced. Specifically, image display was not in real time. One could never be certain that the information stored on film was suitable until after processing, by which time the exam would have been long over.

It was not until the application of the video camera that diaphanography could be considered a practical clinical tool. It now became possible to collect and display images in real time without any of the problems associated with direct viewing. Jones [14] appears to be the first to employ video imaging techniques, using a commercial grade RCA vidicon tube. Morton [15], meanwhile, utilized an Ikegami camera with Nevicon tube, although permanent records were generated using 35 mm photography.

With these technical innovations, diaphanography has undergone a rebirth of sorts in the last few years. Due to the rising concern over the deleterious effects of ionizing radiation on the very radiosensitive female breast, new procedures are being sought to replace mammography, the conventional breast imaging modality. Diaphanography offers the advantage that its images are generated using nonionizing radiation, so that transillumination exams can be carried out on patients of any age, at regular intervals, without any risk of carcinogenesis. However, a number of clinical diaphanography studies carried out with commercial light scanning systems have demonstrated that although specificity is comparable to mammography, sensitivity is inferior [16-19]. It therefore appears that diaphanography cannot be considered a suitable replacement for mammography, especially for screening. Nonetheless, it has much to offer: it is risk-free, inexpensive and easy to perform and certainly has a role in breast imaging.

The underlying physical mechanisms upon which diaphanography is based (ie. light propagation in tissue) are poorly understood and neither the conditions of examination which yield optimum lesion visibility nor the limits of the modality are known. Because of this, diaphanography has been unable to attain its full clinical potential. The most important question to be answered in any study designed to optimize the procedure is "What wavelength(s) of light should be used for transillumination?" Gros et al. [11] report that light at

the two ends of the visible spectrum are undesirable, violet and blue light serving to decrease contrast because of its high scattering properties while long wavelength red produces large quantities of heat (making the exam uncomfortable for the patient). Arguments used to reject these two regions of the spectrum are, however, erroneous. As illustrated in chapter 13 of this thesis, normal/carcinoma tissue contrast is greatest at short wavelengths due to the differential absorption of light. The effect of scatter on tissue contrast is secondary. That long wavelength visible light will be associated with excessive patient heating is clearly untrue and Gros may have been thinking of infrared contamination. Ohlsson [20] suggested that the diagnostic capabilities of diaphanography could be greatly enhanced by employing infrared light and subsequently carried out an extensive study with photographic viewing (using infrared film). Breast images were found to exhibit a wide range of colors, malignancies being associated with brown-black regions, benign conditions red and cysts yellow. These results were attributed to variations in nitrogen concentration, and as a result absorption of infrared light, between the three pathological conditions. However, no experimental evidence was given to support this claim and it was quickly dismissed by others in the field. Watmough [21] later demonstrated that the variations in color in a diaphanography image recorded on infrared film were due to differences in tissue blood concentrations. Carlsen [22] developed a sophisticated light scanning system consisting of a flexible fiber optic light guide, silicon target vidicon camera and digital imaging hardware. Marketed by Spectrascan Inc., the unit uses a rotating filter wheel to alternately transilluminate the breast with visible and infrared light. Images were formed from the average of these two spectral components with a pseudo-color overlay indicating their ratio. It is claimed that cysts produce yellow images and carcinoma blue. Despite these endeavors, experimental data demonstrating the superiority of one particular wavelength does not exist. Studies of the limitations of diaphanography, both in terms of the minimum lesion size and maximum lesion depth of detection, are equally scarce. Drexler et al. [23] used a synthetic breast model, consisting of opaque objects positioned at various depths in a milk filled balloon, to study tumor visibility. These authors found that transillumination techniques were unable to detect opaque objects at depths more than twice their size. However, it is not known whether these results are applicable to diaphanography.

Many important questions must be answered before diaphanography can realize its full clinical potential. As in the case of Photodynamic therapy, this requires a better understanding of light propagation in tissue. Ultimately,

one would like to model the diaphanography process mathematically although less grandiose endeavors that propose to quantify the optical properties of tissue may also provide answers to many of the existing questions. Much important work in the study of light transport through tissue remains to be carried out before the optimization of diaphanography is possible.

Chapter IV

BIOLOGICAL TISSUE - HISTOLOGY

Biological tissue is a complex arrangement of cells and nonliving intercellular material. The human body contains only four types of tissues, epithelial, muscle, connective and nervous. Differentiation is made on the basis of constituent cell size, shape and arrangement as well as by the characteristics and amount of intercellular material. For example, in some tissues intercellular material is almost non-existent while in others it is the most abundant component. Each of the four tissue types will specialize in different functions vital to the existence of the body as a living entity. Epithelial tissue is responsible for moving substances in and out of the blood and for providing an outer protective barrier (the blood vessels, lymphatic vessels and epidermis are all composed of this type of tissue). Connective tissue holds together and supports the various organs of the body. Muscle tissue moves body parts while nervous tissue serves as a channel for communications. In light transport modalities such as PDT and diaphanography, it is the propagation of photons through connective, muscle and nervous (brain) tissues that is of importance. These three classifications will now be examined in more detail.

4.1 CONNECTIVE TISSUE

Connective tissue is by far the most abundant tissue in the human body. It takes on a wide variety of forms ranging from delicate webs to rigid bones and may be subclassified by the following 8 groups:

- a) loose ordinary
- b) adipose
- c) dense fibrous
- d) blood
- e) reticular
- f) bone
- g) cartilage
- h) hematopoietic

Connective tissue will be characterized by relatively few cells, consisting mostly of intercellular material referred

to as the matrix. Embedded in this matrix will be varying numbers and kinds of fibers. It is this matrix and the fibers it contains that will determine the physical characteristics of connective tissue.

Tissue fibers will fall into three categories, collagenous, reticular and elastic. Collagenous fibers are the most abundant protein compound in the body (constituting approx. 1/4 of all protein present) and serve to give tissue its great tensile strength. These colorless strands possess diameters ranging from 0.5 to 20 μm and are of indefinite length. The second type of fiber, reticular, is very delicate (dia. 0.5 to 2.0 μm); it functions as a support structure for nerves and capillaries. Elastic fibers, meanwhile, are responsible for the extensible nature of tissue. These slender fibers are slightly thinner than reticular, their diameters typically ranging between 0.2 and 1.0 μm . Elastic fibers are characterized by frequent branching.

Of the eight subclassifications of connective tissue, propagation of light through the first four are of importance to the modalities of PDT and Diaphanography. Loose ordinary is the most abundant; it connects adjacent structures of the body. The matrix of areolar tissue, as it is sometimes referred to, contains all three fiber types with collagen being present in the greatest numbers. Fibers tend to be loosely interwoven and run in all directions. The matrix itself exhibits no structural organization when viewed with a light microscope. Of the numerous cell types found in loose ordinary tissue, fibroblasts are the most common and tend to collect along bundles of collagen fibers. Fibroblast cells are fusiform in shape with long, tapering processes. Macrophages, leukocytes and plasma cells are also found in loose ordinary tissue. Adipose tissue differs from areolar in that it consists primarily of fat cells. These spherical cells reach diameters of 120 μm and accumulate in such large numbers that other cells are crowded out. As such, the number of fibroblasts found in adipose tissue is greatly reduced from that characteristic of loose ordinary tissue. Dense fibrous tissue forms the tendons and ligaments of the human body. It is characterized by bundles of collagenous or elastic fibers arranged in parallel rows in a fluid matrix. These fibers are closely interwoven and possess diameters ranging from 60 to 175 μm . As with adipose tissue, dense fibrous tissue contains few fibroblasts. Those that do exist assume rectangular shapes and align in long parallel rows between the collagen fibers. The final sub group of importance in PDT and diaphanography is that of blood. The structure of this tissue is quite different from that of the others, it consisting of billions of cells embedded in a fluid matrix referred to as plasma. Red cells (approx. 7 μm in diameter) are the most abundant with

concentrations of 5.5 million cells/mm³ of blood being typical. Their shape, best described as a biconcave disc, is highly consistent. Blood is void of any fibers.

4.2 MUSCLE TISSUE

Three subgroups of muscle tissue may be identified:

- a) skeletal
- b) visceral
- c) cardiac

The first comprises all muscle tissues which are attached to bone. Visceral tissue are those muscles found in the walls of hollow internal organs while cardiac is the subgroup designation given to the tissues which form the heart. All three subgroups are characterized by long, narrow, thread-like shaped cells. Muscle cells tend to align offset with respect to one another so that the middle section of one is juxtaposed to the ends of adjacent cells. Thickness at the cell center is larger than at the ends so that a cross sectional slice of muscle tissue reveals a complex mosaic of rounded or polygonal shapes varying from 1 to 100 μm across. Muscle cells can be exceptionally long (often exceeding 3.0 cm) and are tightly packed with intercellular spacings being typically 40 to 80 μm . Small bundles of collagen fibers are often lodged in the clefts between cells.

4.3 NERVOUS TISSUE

Both the brain and spinal cord are composed of nervous tissue, a complex assembly of two main cell types referred to as neurons and neuroglia. The human brain contains hundreds of billions of each.

Neurons are best described as consisting of a cell body, similar to that of other cells in the human body, with two or more threadlike extensions called nerve fibers. Clusters of neurons cell bodies (which appear gray in color when present in large concentrations) form the grey matter of the brain and spinal cord. Shape is varied, ranging from spherical to fusiform or polyhedral, as is size (4 to 150 μm in dia). The extensions fall into one of two classifications, dendrites and axons. The former, although limited in range, branch extensively. Axons, meanwhile, are single processes with lengths ranging from a few millimeters to over a meter (diameters also show considerable range, from 1 to 20 μm). Axons are often covered in a segmented

fashion by a fatty substance known as myelin. Bundles of myelinated fibers will appear white in color and form the white matter of the nervous system.

Neuroglia, the second major cell type found in nervous tissue, play the role of connective tissue in the nervous system and are responsible for holding nerve fibers together; they also form the blood-brain barrier.

Chapter V

LIGHT TRANSPORT THROUGH BIOLOGICAL TISSUE

The propagation of light through biological tissue is a complex phenomenon which depends not only on the nature of the electromagnetic radiation but also the composition and physical structure of the tissue itself.

As a collimated beam of light travels through a medium, it will interact with that material via two basic processes, absorption and scatter. With absorption, individual photons are destroyed, their energy being converted into some other form. Scatter, changes the direction of travel of the photons (some types of scatter are inelastic and result in a change in wavelength - however, because their probability is very small, these events can be ignored), the actual extent to which their course is altered being dependent on wavelength as well as the size, shape and index of refraction of the centers responsible for the interaction. This change in direction, regardless of its magnitude, may be considered to be a subtle form of removal of light from the transmitted beam. Thus, both interaction processes will reduce the intensity of light in the incident beam direction, this decrease being referred to as attenuation.

When a molecule is exposed to light characterized by an energy equal to the difference in energy between two of its electronic levels, the possibility exists for an electron in the lower state to be raised to the higher. The energy required for this change will be supplied by the incident radiation with one light quantum or photon being annihilated per transferred electron. This event is referred to as absorption, the result of which is the production of a molecule with a higher electron energy state (excited) and a reduction in the intensity of the incident beam.

The excess energy acquired by the molecule will quickly dissipate (within 10^{-8} sec) through one of three paths and the molecule will return to its lower energy state. By far the most probable means by which de-excitation will take place is through an increase in molecular motion - the excess energy is transferred into heat. A less common path of energy dissipation is referred to as luminescence, the emission of secondary radiation; this process can occur when ultra-violet or visible energies are absorbed. Finally, the newly acquired energy may be used to induce a chemical

reaction and thereby reorganize the structure of the molecule. This process is important in the photodynamic treatment of tissue where incident radiation absorbed by the photosensitizing drug is used to generate free radicals. These highly reactive species may then combine with oxygen to form oxidized cell constituents and eventually invoke tissue death.

Nuclear motion will perturb the energies associated with the electron orbitals in a molecule and in doing so will alter the wavelength of light which that molecule will absorb. Because a molecule may exist in any number of nuclear vibrational states, a collection of like particles will absorb radiation over a range of wavelengths rather than at one specific value [24]. This distribution of absorbed photon energies is referred to as an absorption peak.

As most organic molecules will absorb light in the ultraviolet (UV), tissue will show a very high attenuation towards radiation in this wavelength region. DNA and RNA, and in particular the organic bases associated with each (absorption peak at 260 nm), are partly responsible for this behaviour. Proteins (these molecules make up 15 to 20% of a cell) also show a strong absorption of UV light with a peak at 280 nm [25].

In the visible range, unpigmented cells will absorb light only slightly, this removal being directly attributable to the presence of cytochromes and flavoproteins in catalytic amounts [25]. Consequently, cells appear transparent when viewed under a microscope. However, absorption may be significant if pigment is present. Hemoglobin is one of the most important pigments in biological tissue. In an oxygenated state, this blood component will exhibit a very strong absorption peak at 412 nm and a much weaker double peak at 540 and 575 nm. In its deoxygenated form, the UV maximum will shift to higher wavelengths (430 nm) and the double peak in the visible will be replaced by a single peak about 550 nm. Absorption bands may also be detected at 760 and 930 nm (in both states of oxygenation) although their magnitudes will be extremely weak [26]. Beta-carotene is a second important absorber of visible light in tissues. This highly lipophilic substance will be found in larger concentrations in adipose tissue; it gives human fat a yellow appearance, absorbing light in the visible blue [26]. A third important chromophore in the study of the optical properties of human tissue is Bilirubin (CHCl_3). This compound may occur in both albumin-bound and free forms and as such, will be found both intravascular and extravascular. Bilirubin will exhibit a very strong, broad absorption peak at 450 nm [26]. The final absorbing component of importance, although existing only in the epidermal layer of the skin,

is melanin. This chromophore lacks discrete absorption bands but will attenuate more strongly at lower wavelengths [26].

Near infrared light (700 to 1400 nm) will be absorbed by water [25]. As all cells are composed mainly of water (80%), tissue will exhibit a substantial attenuation towards light of this energy. Absorption will be particularly strong between 1300 and 1400 nm while less pronounced absorption peaks occur at 810, 892, 928 and 967 nm [25b]. Absorption of infrared light by water is due to the excitation of molecules to higher vibrational and rotational energy states, rather than to higher electronic levels. However, the tendency will still be for this excess energy to be dissipated as heat.

Because of the very strong absorption of light below 600 nm by chromophores and at wavelengths greater than 1300 nm by water, only light within a very narrow spectral range will propagate through significant thicknesses of tissue. Within this 600 to 1300 nm optical window, photons will be characterized by energies between 2.0 and .95 eV and will only be able to exert chemical change through the destruction of very weak bonds. The production of singlet oxygen in PDT requires approximately 1 eV of energy [26]. The absorption of light at 630 nm by HPD is therefore sufficient to induce this chemical change.

The transport of light in a purely absorbing medium is relatively simple to model. Because there exists no mechanism by which constituent photons may change their direction of travel (all interactions with the medium will serve to destroy light quanta), the geometric cross section of a collimated beam (as well as its course) will remain fixed. Intensity will fall off exponentially with distance travelled.

The propagation of light through a scattering medium (tissue may be considered a strong scatterer of light) is much more difficult to model. Interactions with the material will serve to change the direction of travel of the individual photons. A collimated beam entering a scattering medium will spread out, moving into areas external to its geometrical projection and illuminating a greater volume. Thus, the removal of light from the incident direction is more complex than in the case of pure absorption. As the distance travelled by the beam increases, more and more photons will have undergone multiple scatters and their spatial distribution will become isotropic (regardless of the angular scatter pattern associated with the individual interaction centers). The actual depth at which isotropy is attained will depend on both the concentration of scatterers as well as the angular scatter pattern associated with each;

the lower the concentration or the more forward directed the individual particle scatter patterns, the greater the depth at which this occurs. Once it has taken on an isotropic appearance, the spatial distribution of photons cannot be reorganized by scatter of any type, even that which is highly forward directed. Because of its very complex nature, it will be useful to examine the phenomenon of light scatter in more detail. Chapters 6 to 10 are dedicated to this purpose.

Chapter VI

GENERAL SCATTERING THEORY FOR A SINGLE PARTICLE

In this chapter light scatter is examined on a very fundamental level (ie. by a single particle) with the hope that a better understanding of the physical principles involved may be obtained. The mathematical arguments presented in this section are based on the work of H. van de Hulst [27].

Consider the consequences of irradiating a small particle of arbitrary shape with monochromatic light from a distant source (see figure 6.1). Because of the large separation between source and particle, the incident disturbance may be assumed to be a plane wave. As the incident wave flows over its geometric volume, the particle will be induced to emit light of its own (of the same frequency). This secondary radiation, referred to as scattered light, will be spherical in nature, with energy travelling off in all directions. At any point in space the total disturbance will be given by the vector sum of the incident and scattered waves.

Because of its spherical nature, the intensity of the secondary wave at any point in space $P(r, \theta, \phi)$ will not only be proportional to the intensity of the incident beam, I_0 , but will fall off as $1/r^2$. In other words,

$$I_p(r, \theta, \phi) = (F(\theta, \phi)/k^2) (I_0/r^2) \quad (6.1)$$

where $F(\theta, \phi)/k^2$ is the constant of proportionality (k is the wave number of the incident disturbance and has been introduced explicitly only to simplify the mathematics). The function $F(\theta, \phi)$ is a characteristic property of the scattering particle. It is a dimensionless quantity, dependent on direction but not position, which describes the amount of light scattered by the particle in any particular direction (θ, ϕ) . F will depend on the state of polarization of the incident wave as well as the orientation of the scattering particle.

The total energy scattered by the particle may be calculated by integrating equation (1) over 4π steradians.

$$I = I_0 (1/k^2) \iint F(\theta, \phi) \sin\theta \, d\theta \, d\phi \quad (6.2)$$

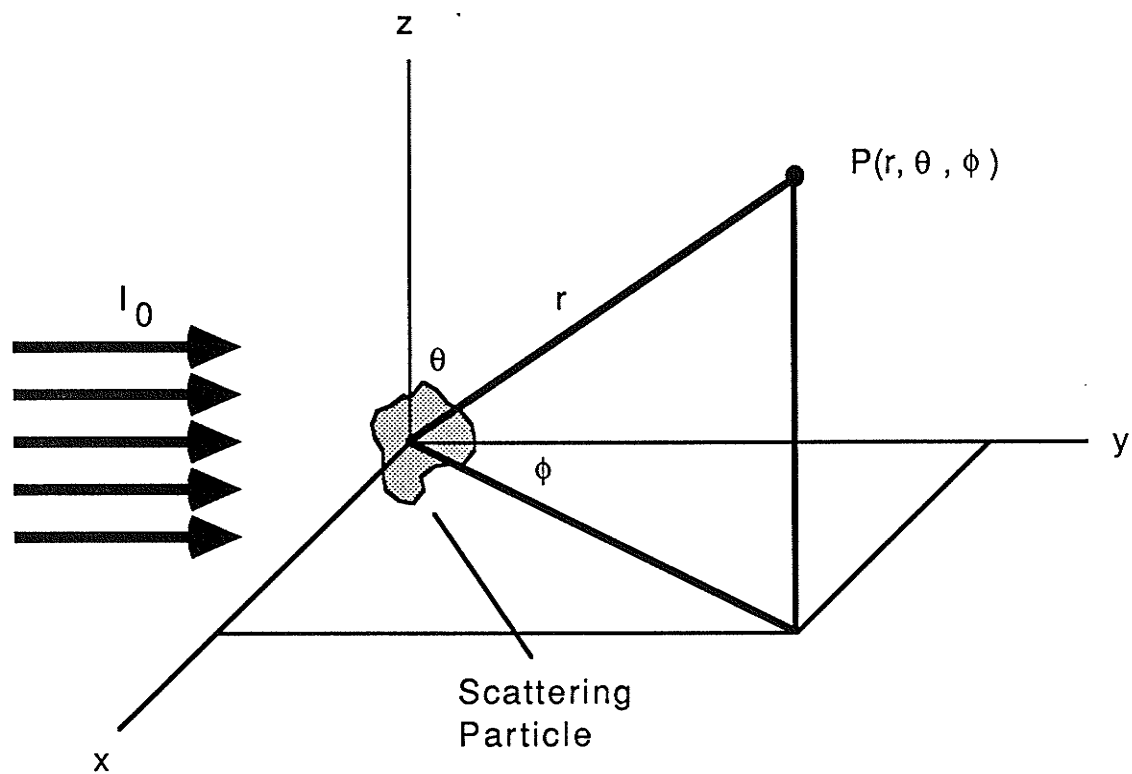


Figure 6.1: Irradiation of a small particle with light from a distant source.

This is equal to the amount of energy that would be intercepted by a flat disk of area $\chi(\text{sca})$, placed in the path of the incident beam, provided

$$\chi(\text{sca}) = (1/k^2) \iint F(\theta, \phi) \sin\theta \, d\theta \, d\phi \quad (6.3)$$

$\chi(\text{sca})$ is referred to as a scatter cross section. The interaction center will scatter an amount of light equal to that falling on its scatter cross section. In other words, in so far as its ability to scatter light is concerned, the particle behaves as if it possessed a cross sectional area of $\chi(\text{sca})$. Similarly, the particle may be associated with a cross section for absorption $\chi(\text{abs})$ and a cross section for attenuation $\chi(\text{att})$. These quantities denote the fact that when irradiated with a plane wave of light, the object will absorb and attenuate an amount of energy equal to that falling on an area $\chi(\text{abs})$ and $\chi(\text{att})$, respectively. Energy conservation requires that:

$$\chi(\text{att}) = \chi(\text{sca}) + \chi(\text{abs}) \quad (6.4)$$

A final quantity of importance in the study of light scattering by a particle is the efficiency factor Q , defined as

$$Q(\text{sca}) = \chi(\text{sca})/G \quad (6.5)$$

where G is the geometrical cross section of the particle. Efficiency factors for absorption and attenuation may also be defined.

In general, cross sections and efficiency factors will depend on particle orientation and the state of polarization of the incident wave disturbance. However, χ and Q for spherical particles will be independent of both.

6.1 AMPLITUDE FUNCTION

Besides intensity, polarization and phase must also be specified in order to completely describe a scattered wave. The F function, however, deals with neither. If one is interested in a more complete representation of the secondary disturbance, it is necessary to use an alternative concept, that of amplitude function, $S(\theta, \phi)$. Unlike F , $S(\theta, \phi)$ is a complex function which describes the amplitude, phase and polarization of the scattered wave in any particular direction (θ, ϕ) .

$$S(\theta, \phi) = s(\theta, \phi) \text{EXP}[i\sigma(\theta, \phi)] \quad (6.6)$$

Consider the case of a small particle irradiated with light from a distant source. Assume (to start with) that this light is plane polarized and travelling in the z direction. The incident disturbance may then be expressed mathematically as follows:

$$u_0 = \text{EXP}[-ikz + i\omega t] \quad (6.7)$$

Here u_0 represents either the electric or magnetic field of the wave, k its wave number, z the position of the wave, ω its frequency and t time. The particle is assumed to be located at the origin of the coordinate system. Due to its spherical nature, the scattered wave will be characterized by an amplitude which varies inversely with distance r from the particle.

$$u(\text{sca}) = S(\theta, \phi) \text{EXP}[-ikr + i\omega t] / ikr \quad (6.8)$$

$S(\theta, \phi)/ik$, the constant of proportionality, is referred to as the amplitude function of the particle (i and k being introduced explicitly only for convenience). By combining equations (6.7) and (6.8)

$$u(\text{sca}) = u_0 S(\theta, \phi) \text{EXP}[-ikr + ikz] / ikr \quad (6.9)$$

The intensity of the scattered wave is given by the square of the modulus of the above relation.

$$I(\text{sca}) = (s^2(\theta, \phi)/k^2) (I_0/r^2) \quad (6.10)$$

A comparison of equations (6.1) and (6.10) yields a very simple relationship between F function and amplitude function.

For the general case of non-polarized incident light, the amplitude function will be of the form of a 2x2 matrix defined as follows:

$$\begin{bmatrix} E_{\parallel} \\ E_{\perp} \end{bmatrix} = \begin{bmatrix} S_2(\theta, \phi) & S_3(\theta, \phi) \\ S_4(\theta, \phi) & S_1(\theta, \phi) \end{bmatrix} \frac{\text{EXP}[-ikr+ikz]}{ikr} \begin{bmatrix} E_{\parallel 0} \\ E_{\perp 0} \end{bmatrix} \quad (6.11)$$

where E_{\parallel} and E_{\perp} are the parallel and perpendicular components of the electric field vector of the scattered wave. $E_{\parallel 0}$ and $E_{\perp 0}$ are the corresponding components of the incident radiation. For spherical particles, $S_3=S_4=0$ while S_1 and S_2 are independent of ϕ .

6.2 EXTINCTION OF LIGHT BY SCATTER

The total disturbance at any point in space will be the vector sum of two components, the incident wave and the scattered wave. In order to gain an understanding of the mechanisms by which light scattering removes energy from the incident beam direction, one can calculate the intensity of the forward wave as measured by a large objective instrument positioned a considerable distance behind a pure scattering particle (figure 6.2). It will be assumed that the objective of the instrument lies in the plane $z=z_0$. Because z_0 is very large, the distance between the scattering particle and any point (x,y,z_0) on the objective may be approximated by

$$r = z + (x^2+y^2)/2z \quad (6.12)$$

Using equation (6.9), the total disturbance (moving in the forward direction) at the point (x,y,z) may be written as

$$u_0 + u(\text{sca}) = u_0 \{ 1 + S(0) \text{EXP}[-ik(x^2+y^2)/2z] / ikz \} \quad (6.13)$$

Intensity will be proportional to the square of the modulus of eq. (6.13)

$$\begin{aligned} I(x,y,z) &\propto |u_0 + u(\text{sca})|^2 \\ &= I_0 \{ 1 + (2/kz) \text{Re} \{ S(0) \text{EXP}[-ik(x^2+y^2)/2z] / i \} \} \end{aligned} \quad (6.14)$$

The total energy collected by the instrument is then obtained by integrating expression (6.14) over the surface area of the objective. The result can be expressed as the sum of two terms, T_1 and T_2

$$\text{Total Energy} = T_1 - T_2 \quad (6.15)$$

where T_1 is the integral of the first term in eq. (6.14) and T_2 the second. T_1 is simply the intensity of the incident beam times the area of the objective. It represents the energy which would be collected by the instrument in the absence of the particle. Term T_2 takes into account the effect of the particle. The most important point to note is that this term yields a negative contribution, indicating that the total energy collected by the instrument will be reduced by the particle's presence. If the objective of the collecting instrument is now made infinitely large (ie. if the limits of integration over the x and y variables are extended to infinity) term T_2 takes on a very simple form

$$T_2 = I_0 (4\pi/k^2) \text{Re} \{ S(0) \} \quad (6.16)$$

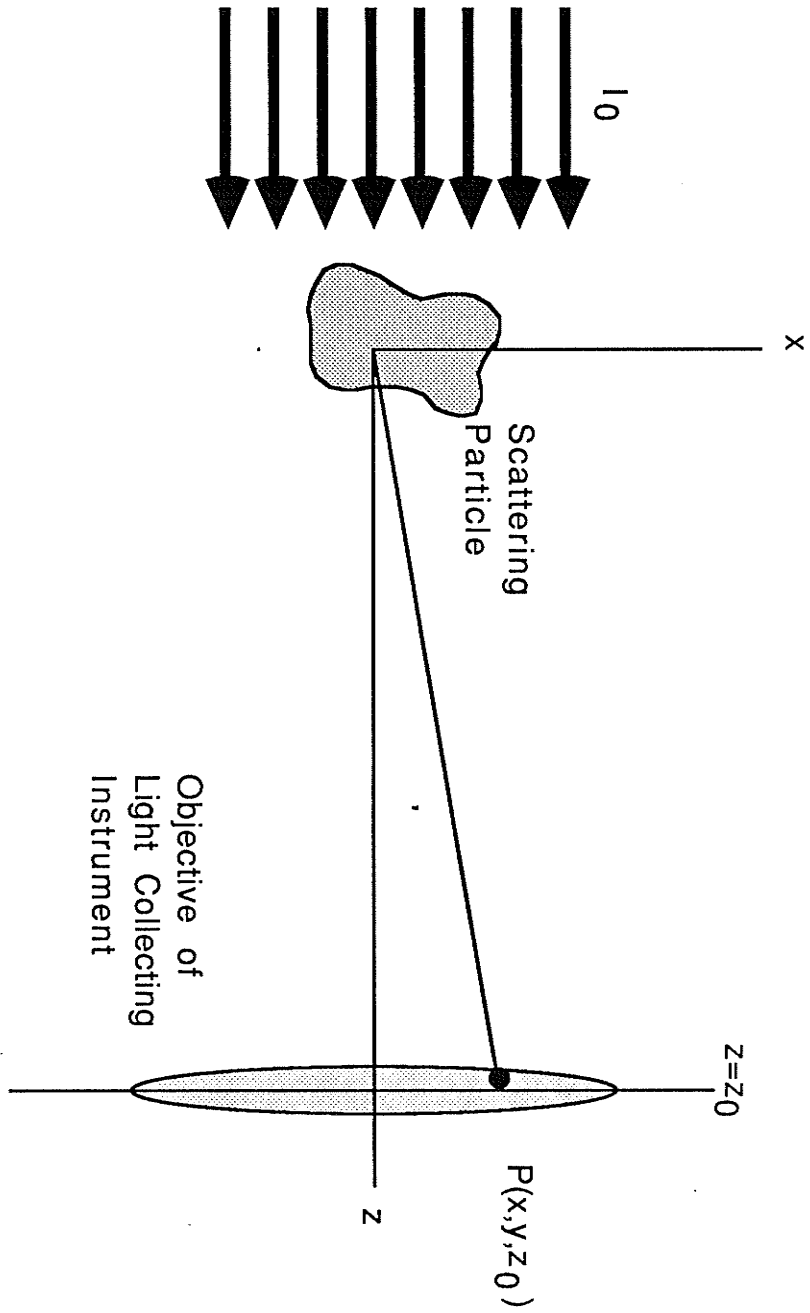


Figure 6.2: Using a large objective instrument to measure the total amount of light removed by a particle from the forward direction.

This represents the total energy removed from the forward direction by the scattering particle. By definition, the attenuation cross section of the particle must therefore be given by

$$\chi(\text{att}) = (4\pi/k^2) \text{Re}\{ S(0) \} \quad (6.17)$$

This expression is referred to as the Fundamental Extinction Formula. The discussion clearly illustrates that in the case of a pure scattering particle, the removal of light from the forward direction (attenuation) is due to a subtle interference phenomenon rather than a physical blocking of the energy as in the case of absorption. Energy which has been removed will re-appear in other directions (scatter). As the active area of the above double integral over x and y is of the order of $z\lambda$, any instrument to be used to measure the full attenuation of a particle must possess an objective with diameter larger than $(z\lambda)^{1/2}$.

6.3 MIE SCATTERING THEORY

Scatter by a particle irradiated with a plane wave of light can be completely described using the concept of amplitude function. This function may be calculated rigorously, for any arbitrary interaction center, using Maxwell's equations.

$$\nabla \times H = (4\pi\sigma/c)E + (1/c) (d/dt)\epsilon E \quad (6.18)$$

$$\nabla \times E = -(1/c) (d/dt)E \quad (6.19)$$

where H and E are the magnetic and electric fields of a disturbance (either incident or secondary), c the speed of light in vacuum, σ the conductivity of the medium through which it moves and ϵ the dielectric constant. Assuming light scattering to be a periodic phenomenon of frequency ω , equations (6.18) and (6.19) can be simplified

$$\nabla \times H = ikm^2E \quad (6.20)$$

$$\nabla \times E = -ikH \quad (6.21)$$

where $m^2 = \epsilon - i(4\pi\sigma/\omega)$; m is defined as the complex refractive index of the medium.

Outside the particle, space is traversed by two distinct waves, the incident (assumed to be planar) and the scattered (assumed spherical). The total disturbance at any point is given by the vector sum of the two. Inside the particle, this distinction is not made and the disturbance is treated as a single entity. A brief overview of the procedure used

to determine the amplitude function associated with a particle is as follows: Given the exact mathematical form of the incident disturbance, that of the scattered wave and the interior wave are selected from an infinite number of possibilities by requiring that a series of conditions be met. Firstly, both waves must satisfy Maxwell's equations. Secondly, each must adhere to certain boundary conditions. Explicitly stated, these include the restriction that the amplitude of the scattered wave reduce to zero at large distances from the particle, that the interior wave be finite at the origin (assumed to be located at the center of the particle) and that the following conditions hold at the interface between interaction center and surrounding medium:

$$\hat{n} \times (H_2 - H_1) = 0 \quad (6.22)$$

$$\hat{n} \times (E_2 - E_1) = 0 \quad (6.23)$$

$$\hat{n} \cdot (m_2^2 E_2 - m_1^2 E_1) = 0 \quad (6.24)$$

$$\hat{n} \cdot (H_2 - H_1) = 0 \quad (6.25)$$

where \hat{n} is the unit normal vector to the interface and H and E represent the net magnetic and electric fields, respectively; 2 denotes the fields inside the particle, 1 those outside. The above mentioned requirements enable one to formulate an exact mathematical description of both the external scattered wave and the net internal disturbance. By referring to the defining relation eq. (6.8), the amplitude function can be read directly from the expression describing the electric field strength of the scattered wave.

The use of Maxwell's equations to describe light scattering by a particle is referred to as Mie Scattering Theory. It is an exact procedure which can be applied to interaction centers of any size and refractive index. In other words, Mie Scattering Theory is completely general. However, this rigorous treatment suffers from a number of important shortcomings. Firstly, it is extremely complex, even when the scattering particles assume such simple shapes as spheres and cylinders. Amplitude function calculations are tedious and time consuming and as a result, have to date been carried out for only a small number of particle sizes, shapes and refractive indices. The second major drawback associated with Mie Scattering is that it provides very little insight into the physical mechanisms responsible for the light scattering phenomenon.

Because of these shortcomings, simpler, less rigid theories are often employed to generate amplitude function expressions. Those most important to the study of light propagation in tissue are Rayleigh theory, Rayleigh-Gans theory and the theory of Anomalous Diffraction. These models

not only reduce the complexity of calculations but supply a physical picture of the underlying processes involved in light scattering. Unfortunately, all are very specific and apply only to particles within very limited ranges of size and index of refraction. In the brief discussion of the less rigorous theories that follows, the interaction centers will be assumed spherical in shape and surrounded by vacuum so as to simplify the mathematics.

6.4 RAYLEIGH SCATTERING THEORY

Rayleigh theory is a non-rigorous treatment of scattering which is valid for particles satisfying the following conditions:

$$ka \ll 1 \quad (6.26)$$

$$2ka(m-1) \ll 1 \quad (6.27)$$

where a is the radius of the particle and m its refractive index relative to the surrounding medium. Although the electric field of the incident radiation will vary sinusoidally in both the spatial and temporal domain, the irradiated particle, as a result of its diminutive size (condition (6.26)) may be considered to exist in a homogeneous electric field. This applied field will polarize the particle. As a result of its oscillating nature (the induced dipole P will exhibit the same temporal dependence as the incident disturbance), the dipole will radiate energy of its own in all directions. The secondary dipole radiation will in turn serve to modify the incident wave, both inside and outside of the particle, with the net disturbance at any point in space being given by the vector sum of the two. This modification to the incident radiation is referred to as Rayleigh Scattering.

For a particle to be adequately described by Rayleigh Scattering Theory, it is not sufficient that its size be small compared to the wavelength of light. It is also necessary that the electric field incident upon the particle penetrate quickly so that polarization be induced in a very short time compared to the period of the wave. Condition (6.27) will ensure that this is the case. It is only in the event of both (6.26) and (6.27) being satisfied that the scattering particle may be treated as residing in a truly uniform electric field.

For a particle described by an electric polarizability tensor α which is linear, isotropic and homogeneous (in this case, the induced particle dipole and the incident electric field will lie in the same direction) Rayleigh theory predicts the following amplitude function:

$$\begin{bmatrix} S_2 & S_3 \\ S_4 & S_1 \end{bmatrix} = ik^3 a \begin{bmatrix} \cos\theta & 0 \\ 0 & 1 \end{bmatrix} \quad (6.28)$$

where

$$a = (m^2 - 1)a^3 / (m^2 + 2) \quad (6.29)$$

and θ is the scattering angle measured with respect to the incident beam direction. Once the amplitude function is known, it is a simple matter to calculate the electric field strength, and therefore the intensity, of the scattered wave. In the case of irradiation with non-polarized light, the intensity of this secondary radiation is given by:

$$I = (1 + \cos^2\theta)k^4 a^2 I_0 / 2r^2 \quad (6.30)$$

Equation (6.30) is plotted in figure 6.3. Scatter is seen to be almost isotropic. Integrating this expression over 4π steradians to obtain the total energy scattered by the particle and employing the definition of scatter cross section eq. (6.3), one finds

$$\chi(\text{sca}) = (8/3)\pi k^4 a^2 \quad (6.31)$$

This relation illustrates the fact that for a Rayleigh particle, scatter will be inversely proportional to the fourth power of wavelength. In other words, blue light will suffer a significantly higher degree of scatter than red. Also, scatter can be seen to increase with the square of the particle volume.

By applying the Fundamental Extinction Formula to the amplitude function given in eq. (6.28), an expression for particle attenuation cross section may be generated.

$$\chi(\text{att}) = (8/3)\pi k^4 a^2 + 4\pi k \operatorname{Re}\{ia\} \quad (6.32)$$

Finally, as a result of the conservation of energy principle,

$$\chi(\text{abs}) = \chi(\text{att}) - \chi(\text{sca}) = 4\pi k \operatorname{Re}\{ia\} \quad (6.33)$$

Two important points are to be noted. Firstly, particle absorption will vary inversely with wavelength. Thus, in the case of small particles, absorption, if present, will tend to be the dominant mode of interaction (scatter will be inversely proportional to the fourth power of wavelength). Secondly, the absorption cross section exhibits a linear dependence on particle volume.

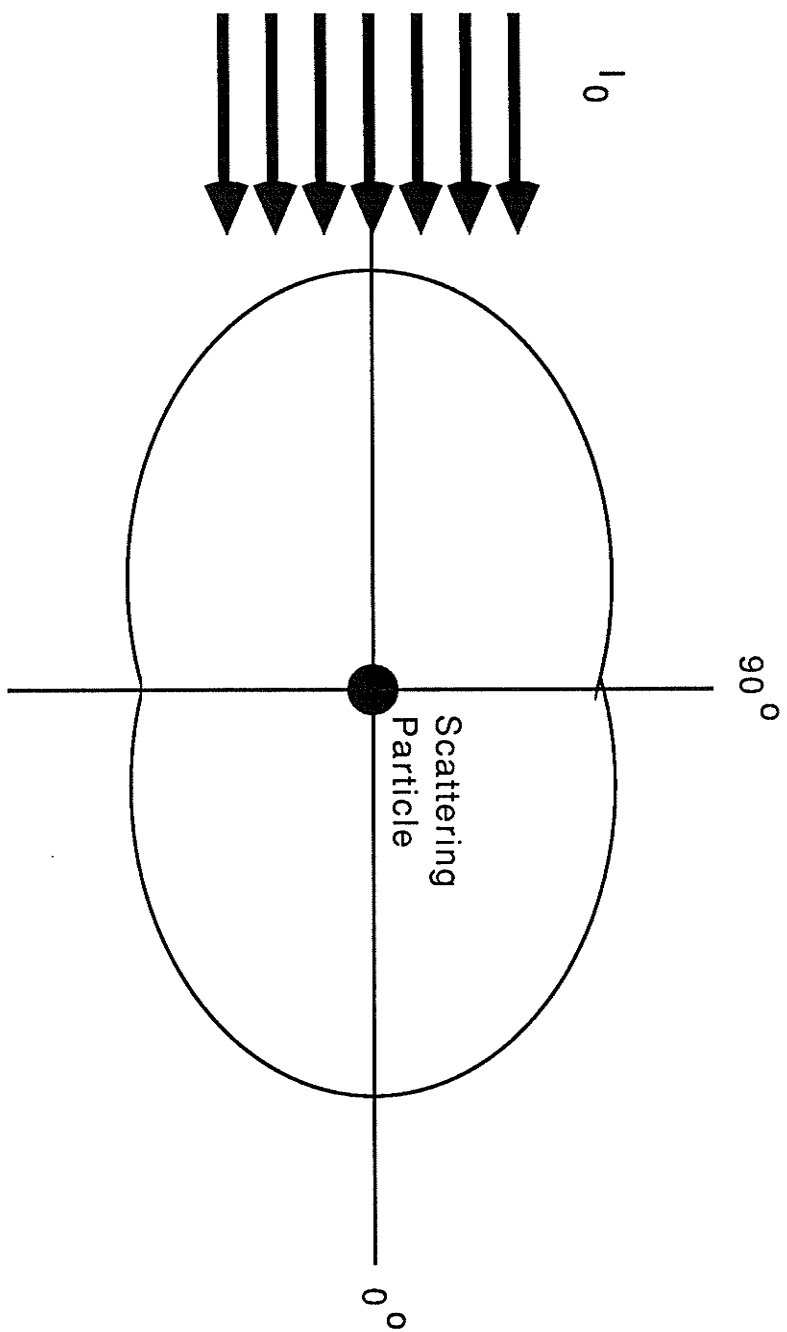


Figure 6.3: The angular dependence of scatter for a Rayleigh particle.

6.5 RAYLEIGH-GANS SCATTERING THEORY

Rayleigh-Gans scattering theory is an extension of the Rayleigh model. It is applicable to particles which satisfy the following conditions:

$$(m-1) \ll 1 \quad (6.34)$$

$$2ka(m-1) \ll 1 \quad (6.35)$$

Criterion (6.34) requires that the index of refraction of the particle be close to that of the medium in which it is embedded. Condition (6.35) demands that the phase shift experienced by an electromagnetic wave upon travelling through the interaction center be small. It is apparent that the restriction on particle size has been somewhat relaxed from that of Rayleigh scattering theory. Provided they satisfy (6.34) and (6.35), particles may now be large compared to the wavelength of light.

In Rayleigh-Gans theory, the scattering particle is divided into a large number of small volume elements and Rayleigh scattering theory applied to each. Condition (6.34) ensures that the electric field to which the individual elements are exposed is nearly equal to that of the original wave. Phrased differently, the incident wave moves through the particle as if it were not actually present. Similarly, the wave scattered by any one element will not be distorted by the presence of the others. As a result of this behavior, it is possible to treat the differential volumes as isolated entities, at least when dealing with the light scatter from each.

However, because the constituent volume elements reside at different locations in space, the phase angle of the emitted dipole radiation will vary from one particle to the next. This will lead to destructive interference. As the arrangement of differential elements is non-stochastic in nature, a definite, well defined phase relationship will exist between the component scattered waves and any summation to determine the net disturbance at a point in space must take this into account. In other words, each wave must be referenced to a common axis and the complex amplitudes added. The most important consequence of this inter element interference is the reduction of light scatter by the particle as a whole from that which would otherwise be predicted by Rayleigh theory. As particle size decreases, destructive interference becomes less significant in all directions and scatter increases.

For a spherical particle, Rayleigh-Gans theory predicts the following amplitude function:

$$\begin{bmatrix} S_2 & S_3 \\ S_4 & S_1 \end{bmatrix} = ik^3 a R(\theta, \phi) \begin{bmatrix} \cos\theta & 0 \\ 0 & 1 \end{bmatrix} \quad (6.36)$$

where V is the particle volume and $R(\theta, \phi)$ is a geometric integral which takes into account the variation in phase between the scatter from different volume elements.

$$R(\theta, \phi) = (9\pi/2u^3)^{1/2} J_{3/2}(u) \quad (6.37)$$

where

$$u = 2ka \sin(\theta/2) \quad (6.38)$$

It is interesting to note that the amplitude function associated with the particle is simply that predicted by Rayleigh theory multiplied by the function $R(\theta, \phi)$ (see eq.(6.28)).

The intensity of the scattered wave can be readily obtained by computing the square of the modulus of the electric field associated with the disturbance. For nonpolarized incident radiation

$$I = (1 + \cos^2\theta) (k^4 V^2 / 2r^2) (m-1/2\pi)^2 R^2(\theta, \phi) I_0 \quad (6.39)$$

For the special case $\theta=0$ (ie. in the forward direction) the function $R(\theta, \phi)$ takes on a value of 1 (see page 99 of "Light Scattering by Small Particles"). In other words, scatter in the incident beam direction will be identical to that of a Rayleigh particle. However, at all other angles, R will take on a value less than 1 and secondary radiation will be reduced. Scatter by a Rayleigh-Gans particle therefore tends to be slightly forward directed. Although the form of equation (6.37) is quite complex, it does offer some insight into the angular dependence of scatter by a Rayleigh-Gans particle. As the product ka is increased (corresponding to a decrease in wavelength or an increase in particle size or both), forward scattering becomes more pronounced. For example, for $ka=2.25$, $R(\theta, \phi)$ will take on a value of 0 at $\theta=180$ degrees. In other words, the intensity of the wave scattered directly back will be zero. As ka increases, this minimum will shift to smaller angles. Most of the secondary energy will appear, however, at angles between the forward direction and this first zero. Thus, scatter will become more concentrated around small angles as ka is increased.

By integrating equation (6.39) over 4π steradians and invoking defining relation (6.3), one arrives at the following expression for scatter cross section.

$$\chi(\text{sca}) = (m-1)^2 (k^4 V^2 / 8\pi) \int R^2(\theta, \phi) (1 + \cos^2(\theta)) \sin\theta \, d\theta \quad (6.40)$$

As in the case of a Rayleigh particle, light scatter will be inversely proportional to the fourth power of wavelength. Short wavelength light will be much more heavily scattered than long.

The absorption cross section of a Rayleigh-Gans particle can be shown to be identical to that of a Rayleigh interaction center. Once again, absorption will be inversely proportional to wavelength and show a linear dependence with particle volume. Thus, as a particle grows in size and enters the realm of Rayleigh-Gans, the relative increase in scatter will be significantly less than that for absorption. At larger particle sizes, therefore, the tendency is for absorption (if present) to be the dominant mode of interaction.

6.6 ANOMALOUS DIFFRACTION THEORY

Anomalous Diffraction theory is applicable to interaction centers which satisfy the following conditions:

$$ka \gg 1 \quad (6.41)$$

$$(m-1) \ll 1 \quad (6.42)$$

This model of light scatter draws heavily on the particle theory of light which states that a plane wave of infinite size behaves as if composed of a large number of "particles" or rays (called photons) which pursue their own path and act independently of one another. Any small section of a wave front may be considered to define a ray provided its width is greater than the wavelength of light. The actual distance of travel over which such a ray may be considered a distinct entity will depend on this width, a length l requiring a width of the order of $(l\lambda)^{1/2}$. When an irradiated interaction center possesses a size greater than 20 times the wavelength of light, it becomes possible to deal with the energy-mass interaction in terms of individual rays (ie. localization of photons becomes possible). Clearly, these "particles" can be separated into two groups, those incident on the interaction center and those passing around it. Each will give rise to a different scattering phenomenon.

In the absence of absorption, photons incident upon the interaction center/surrounding medium interface will fall into one of two subsets, those which undergo reflection and those which pass into the particle. The first subgroup suffer a very radical change in the direction of travel and quite clearly contribute scattered rays. That the second subgroup of photons contribute to scatter is not as

apparent. Upon entering the particle volume, light rays will be refracted as a result of the changing index of refraction. Before re-emerging into the surrounding medium, these photons may also undergo a second refraction and possibly several internal reflections. In other words, it is likely that rays exiting the particle will do so with directions of travel which differ from their original. Thus, both subgroups may contribute to the scattering process. In the most general case where the interaction center also exhibits some degree of absorption, a third subset must be identified since a portion of the incident photons will be destroyed before undergoing a reflection or passing completely through the particle.

The light rays passing around the scattering particle may be thought of as a single entity, an incomplete wave front (the missing portion being equal in size and shape to the interaction center). As a result of Huygen's wave principle, this partial wave front will bend around the particle to form a Fraunhofer diffraction pattern (this bending of light constitutes scatter). The intensity distribution of the particular pattern formed will depend on the size and shape of the scatterer but will be independent of composition and surface quality.

Thus, the scattering of light by a large particle may be attributed to two very different phenomena, diffraction and reflection/refraction. These two processes will not only depend on different physical properties of the particle but will lead to scatter with different angular distributions. To gain insight into the consequences of this two part system, it is useful to examine the attenuation of light by a large, opaque particle irradiated with a distant source. All photons incident upon the particle are assumed to be removed from the incident beam. To simplify the discussion, the particle is viewed as a flat disk of cross sectional area $G=\pi a^2$.

Attenuation may be attributed to two processes, the absorption of light striking the particle and the subtle removal of radiation by diffraction (in this special case, reflection and refraction make no contribution). Compare this to the attenuation by a large opaque screen containing a central hole of the same size, shape and location as the aforementioned disk. In this system, all light photons incident upon the screen will be absorbed. Diffraction will still be present but its appearance will now be due to that portion of the incident wave passing through the screen hole. It is important to note that the two incomplete wave fronts responsible for diffraction in the disk and screen experiments can be combined to yield the original incident planar wave. This implies that the diffraction patterns generated in the two experiments must add to zero; in other

words, they must be equal in magnitude but opposite in sign. Their squares, determining the intensity of the diffracted light, will therefore be equal. This is Babinet's principle.

The disturbance behind an opaque particle is due solely to the incomplete wave front passing around that obstruction (ie. incident wave minus that portion striking the particle). Thus, it may be thought of as the resultant obtained by subtracting the diffraction pattern of the screen experiment from the planar disturbance generated by a complete wave in the absence of the interaction center. Quite clearly then, the intensity of light in the forward direction will be reduced by the presence of the particle (attenuation). This lost energy will appear in other directions as scatter.

From Babinet's principle, the diffraction by a large, opaque particle of geometric cross section πa^2 will be identical to that generated by an opaque screen containing a hole of identical cross section. Thus, the effective particle cross section for scatter will be equal to πa^2 . However, as the particle will remove all photons incident upon its surface area, it will also possess a cross section for absorption, in this instance equal to πa^2 . The total cross section for attenuation will therefore be $2\pi a^2$. In other words, the particle will remove twice as much light as that falling on its geometric area. This is known as the extinction paradox. It is important to keep in mind that this result is based on two assumptions, the first being that light scattered at even the smallest of angles is considered removed from the incident beam and secondly, that the disturbance is viewed at very large distances behind the particle.

Consider a second, very specific case, in which the interaction center exhibits no absorption. In this instance, light photons striking the particle will not be removed from the system. Instead, each will pass completely through the object. As a consequence of requirement (6.42), this subset of rays will suffer only slight deviations when passing through the particle/surrounding medium interfaces. Condition (6.42) also implies that any reflections may be neglected. Thus, the amplitude of that portion of the wave passing through the particle will be unaltered. Only its phase will have changed. All points to the rear of the particle will now be traversed by two distinct disturbances, that due to the wave front passing around the obstruction and that due to the wave front propagating through it. The precise nature of the scatter from such a particle will depend on the manner in which these two components interfere. Depending upon its actual size and index of refraction, the removal of light from the incident beam direction may be much smaller or much larger than that of a

completely absorbing but otherwise identical object. In fact, a plot of $Q(\text{sca})$ as a function of the product $ka(m-1)$ will exhibit a series of maxima and minima, the former being the result of constructive interference between transmitted and diffracted light, the latter due to destructive interference (see figure 6.4). As the product $ka(m-1)$ increases (this corresponds to a decrease in the wavelength of the incident disturbance or alternately, an increase in either particle size or index of refraction), so too will the phase lag experienced by that portion of the wave front passing through the interaction center. This will in turn lead to less complete interference (constructive and destructive) and the minima and maxima of the $Q(\text{sca})$ curve become much reduced. At high $ka(m-1)$ values, the curve will be characterized by a damped oscillation about $Q(\text{sca})=2$, the efficiency of attenuation of a totally absorbing sphere. Light scattering in the realm of Anomalous Diffraction theory will be much more efficient (particles will possess larger $Q(\text{sca})$) than in Rayleigh-Gans. Also, it will be much more forward directed and essentially independent of wavelength.

In the most general case, an interaction center will absorb a percentage of the light incident upon it. The effect of this absorption will be to reduce the amplitude of the light transmitted through the particle. As with increasing $ka(m-1)$, this serves to make both the destructive and constructive interference less complete and contrast between the minima and maxima of the particle's $Q(\text{sca})$ curve will appear reduced (ie. the system becomes more heavily damped). If the particle completely absorbs all light striking its surface, there will be no transmitted component with which the diffracted light can interfere. In this case, the particle will behave as an opaque sphere with $Q(\text{att})=2$, half being due to scatter, half to absorption.

6.7 RELATIONSHIP BETWEEN LESS-RIGOROUS THEORIES

The Rayleigh, Rayleigh-Gans and Anomalous Diffraction theories described above provide relatively simple models of the light scattering process. The advantages offered by each are two-fold. Firstly, the complexity of calculations are greatly reduced from that of Mie scattering theory. Secondly, all three convey a physical picture of the underlying mechanisms involved in light scatter. This is not the case with the application of Maxwell's equations. However, they are very specific and provide exact descriptions of scatter only over limited ranges of particle size and index of refraction.

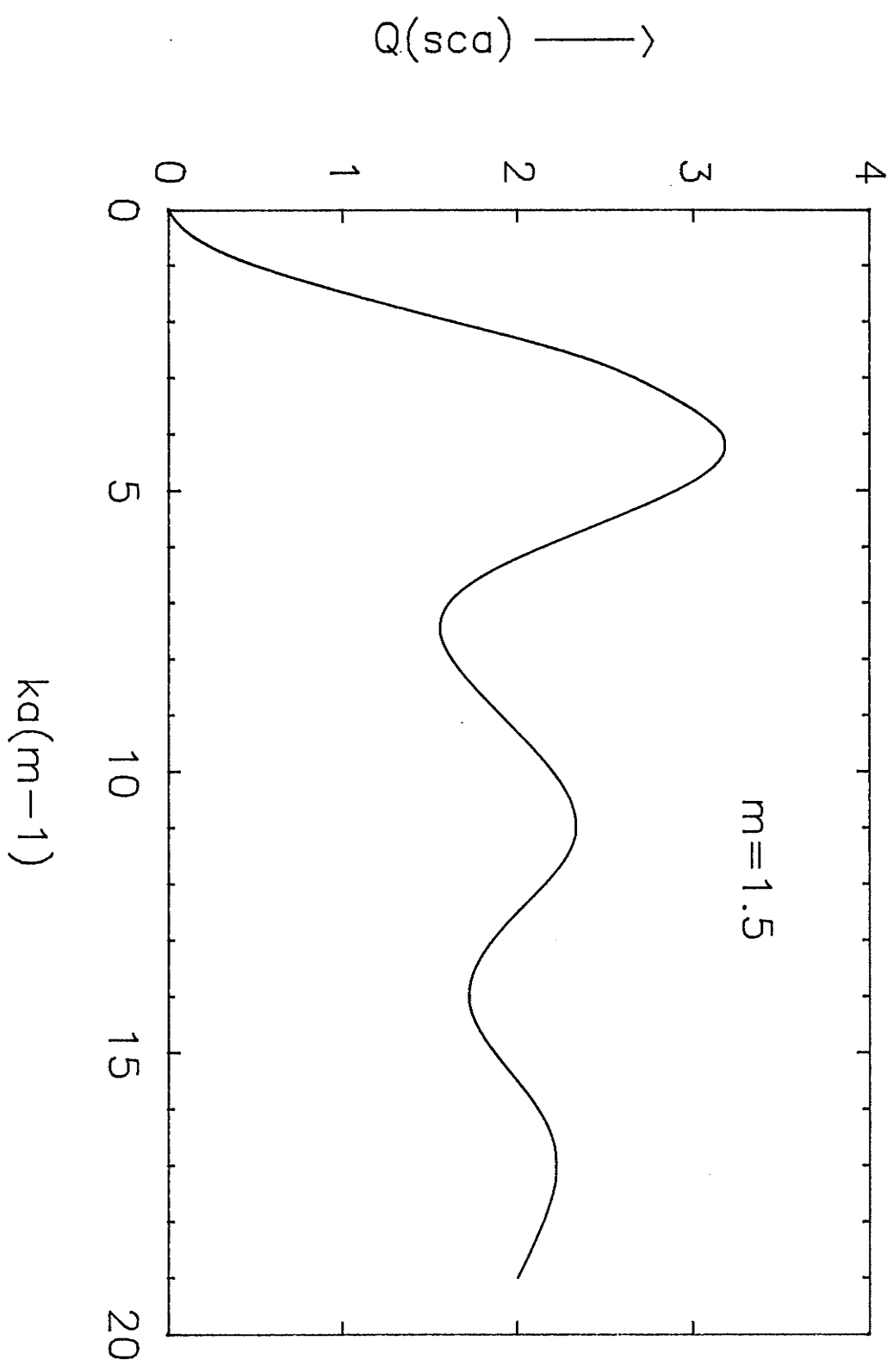


Figure 6.4: Scatter efficiency factor for an Anomalous Diffraction particle

It is important to realize that the boundaries between the three models are not well defined and there exist regions of overlap so that transitions from a Rayleigh scatterer to a Rayleigh-Gans scatterer (or alternatively, from a Rayleigh-Gans to an Anomalous Diffraction particle) are gradual. Although their treatment of scatter will be fundamentally different, the predicted results of two models in an overlap region will be identical. This behaviour lends credibility to the Rayleigh, Rayleigh-Gans and Anomalous Diffraction theories. Table 6.1 illustrates this point. It shows the efficiency of attenuation applicable to a spherical particle at the boundaries (ie. extreme limits) of each of the three models. When overlap exists, results are identical.

Region		Theory	Efficiency for Attenuation Q
ka	$(m-1)$		
small	large	overlap	$(8/3) (ka)^4$
small	arbitrary	Rayleigh	---
small	small	overlap	$(32/27) (m-1)^2 (ka)^4$
arbitrary	small	Rayleigh-Gans	---
large	small	overlap	$2 (m-1)^2 (ka)^2$
large	small	Anomalous Dif.	---
large	small	overlap	2

Table 6.1: Attenuation efficiency

Chapter VII

SCATTER BY A MULTI-PARTICLE SYSTEM

An extension of the theory presented in chapter 6 to include scatter by multi-particle systems is quite simple provided two conditions are satisfied: scatter must be independent and single.

The first condition, that of independent scatter, puts an upper limit on the concentration of interaction centers. To more fully understand this concept, it is useful to take a closer look at scattering media. Light scatter is a consequence of inhomogeneities. A beam of light travelling through a perfectly homogeneous material will suffer no scatter. It is only when the beam encounters fluctuations in medium composition that this type of interaction will take place. However, as all media (with the exception of vacuum) may be regarded as collections of minute concentrations of matter (nuclei) separated by empty space, all will be inhomogeneous. As a result, all materials will scatter light with the individual nuclear particles serving as centers for the interaction. The particular characteristics of this scatter will depend very heavily on the arrangement of these microscopic building blocks. For example, a perfect crystal at absolute zero will exhibit no detectable scatter. Individual nuclei will still function as interaction centers but (as a result of their very regular arrangement) the total energy scattered from each will interfere in such a way that the intensity of light in all but the incident beam direction will be zero. The final result is that the crystal appears to produce no scatter. The only consequence of the molecular interactions is a reduction in the speed of propagation through the medium. However, at higher temperatures, the thermal motion of the molecules will destroy this regular arrangement and destructive interference in off-axis directions will not be as complete. Scatter will now be detectable. Similarly, scatter will also be observed in liquids, gases and generally any solids not demonstrating highly periodic molecular structures.

In the previous discussion, light scatter was treated as a cooperative effect between the constituent molecular building blocks of the medium. In other words, the characteristics of the scattered light are dependent on the phase relationship between neighboring interaction centers. This type of interaction is referred to as dependent

scatter. The major difficulty associated with the treatment of this type of scatter is one of being able to arrive at an accurate description of the phase relationships. Scatter must be considered dependent when the mutual distances between particles is small compared to the wavelength of light (this in turn restricts particle size; the interaction centers must necessarily be small).

Often, scattering media will exhibit inhomogeneities at levels above the molecular. Such materials may be viewed as two component systems consisting of alien bodies embedded in media which are homogeneous at all levels above the molecular. These variations in composition will also lead to the scatter of light. However, if the distance of separation between neighboring interaction centers is sufficient (ie. large compared to the wavelength of light), the scatter of each may be dealt with independently. Although the secondary radiation emitted from neighboring centers may still interfere, there will be no systematic relationships between phases. Because of this, phase may be ignored when adding the intensities of the component scattered waves. This is referred to as independent scatter. Scatter at this level is much more significant than at the molecular.

The second condition which must be satisfied by a multi-particle system puts restrictions on the nature of the light incident on the individual inhomogeneities. For a system to be classified as a single scatterer, the disturbance to which each interaction center is exposed must be that of the original beam. In other words, light reaching a particle as a result of scattering by its neighbors must be negligible. Also, each must "see" the full intensity of the original beam. Stated differently, that portion of the disturbance incident on a scatter center must not have suffered partial attenuation as a result of previous interactions.

When scatter is both independent and single, a very simple relation exists between the total light removed from an incident beam and the number of interactions centers contained in the system. For a collection of N identical scattering bodies, the total attenuation of light by the system will be equal to N times that which would be removed by a single inhomogeneity irradiated in complete isolation of the others.

Consider a planar system of N identical particles per unit volume irradiated with a very broad beam of light as illustrated in figure 7.1. In particular, let the intensity of the radiation incident on the infinitesimal slice dx be I . If scatter is assumed independent and single then the total amount of light removed from the forward direction dI , by the slice dx , will be equal to the amount removed by a single particle times the number of particles in that slice.

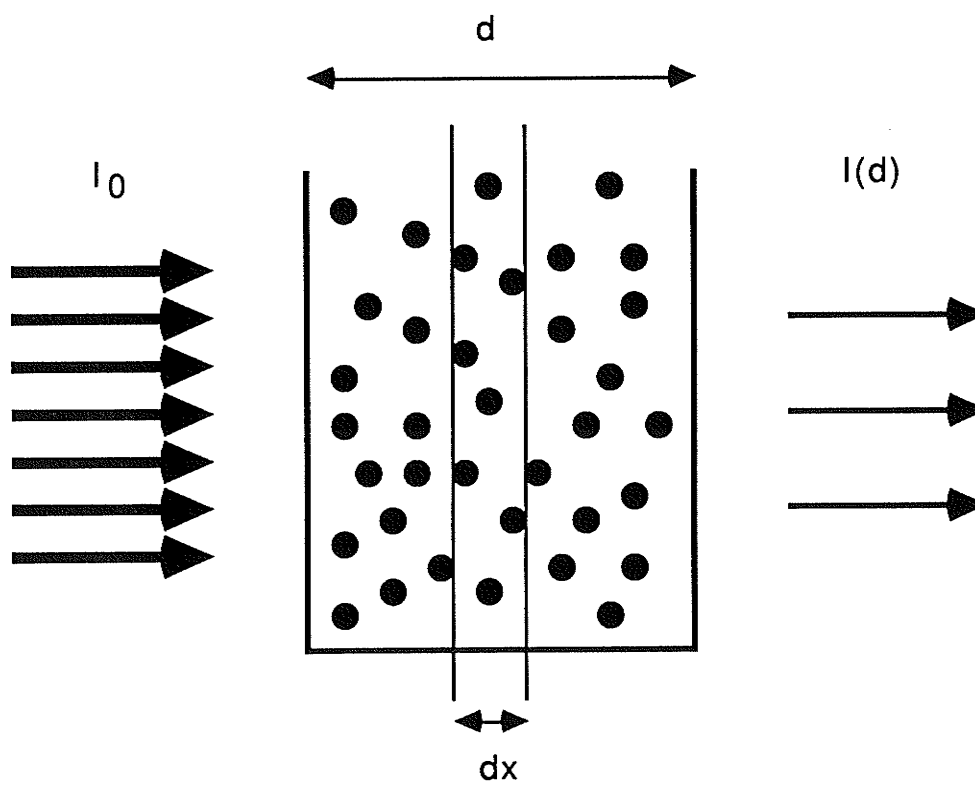


Figure 7.1: Attenuation of a multi-particle system characterized by single and independent scatter.

$$dI = N \chi(\text{att}) dx I$$

or

$$I = I_0 \text{EXP}[-N \chi(\text{att}) x] \quad (7.1)$$

This simple exponential relationship is known as Beer's law and will describe the intensity of the disturbance in the forward direction as a function of depth in the medium. It assumes that scatter is both single and independent.

By employing Beer's law, mathematical expressions may be generated for two quantities of importance in the study of light propagation through a multi-particle system, that of transmittance and extinction. Transmittance T is defined as the intensity of light exiting a sample of thickness d in the forward direction divided by the intensity of light incident upon it. From Beer's law,

$$T = I(d)/I_0 = \text{EXP}[-N \chi(\text{att}) d] \quad (7.2)$$

A closely related quantity is extinction, defined as

$$E = \text{LOG}[1/T] = N \chi(\text{att}) d \quad (7.3)$$

Extinction is a measure of the sample's ability to remove light from an incident beam.

It is important to keep in mind that both equations (7.2) and (7.3) describe the transmission or removal of light in the incident beam direction. In other words, the measurement of either requires one to collect only photons exiting the sample in the forward direction - that is, only photons which pass completely through the system without interacting. It also should be noted that the mathematical expressions (7.2) and (7.3) assume independent and single scatter.

Chapter VIII

LINEAR TRANSPORT THEORY

The histologic description of tissue given in chapter 4 emphasizes the existence of inhomogeneities at levels above the molecular. Cells, their larger organelles and fibers, the positioning of which will be highly irregular, constitute centers of scatter which possess sizes of the order of the wavelength of light (visible and infrared) and larger. At still higher levels, tissue will possess irregular interfaces (ie. abrupt changes in the type and arrangement of interaction centers) designating boundaries between two tissue types. In the study of light propagation through tissue it is scattering at these levels that is important, molecular scattering being weak and therefore of very little significance. Figure 8.1 illustrates this point. It shows the relative importance of scatter as a function of incident light wavelength for a spherical interaction center of fixed radius and index of refraction 1.33 (relative to the surrounding medium). When the wavelength is much greater than the size of the particle (Rayleigh), scattering is weak. This region is characterized by scatter which is isotropic and which falls off inversely with the fourth power of wavelength. Maximum scatter occurs when the incident light possesses a wavelength of the order of the particle size. Here, scatter will be less isotropic and the wavelength dependence much weaker. In the other limiting case, when the wavelength of light is much smaller than the interaction center (Anomalous Diffraction), scatter will once again be reduced. Light scatter will also be highly forward directed and independent of wavelength. Because of their size and abundance, collagen fibers will serve as the main source of scatter in connective tissue (blood being void of fibers is the exception - in this case, red cells will be responsible for most of the scatter). In muscle, meanwhile, this role will be played by the muscle cells themselves.

It is not practical to extend Mie Theory (or for that matter, Rayleigh, Rayleigh-Gans and Anomalous Diffraction theories) to include the scatter of light in tissue. Although scatter is primarily by inhomogeneities at levels above the molecular and as such, may be considered independent, it cannot be classified as single. Because of the high concentration of interaction centers, a significant portion of the light incident upon any one such

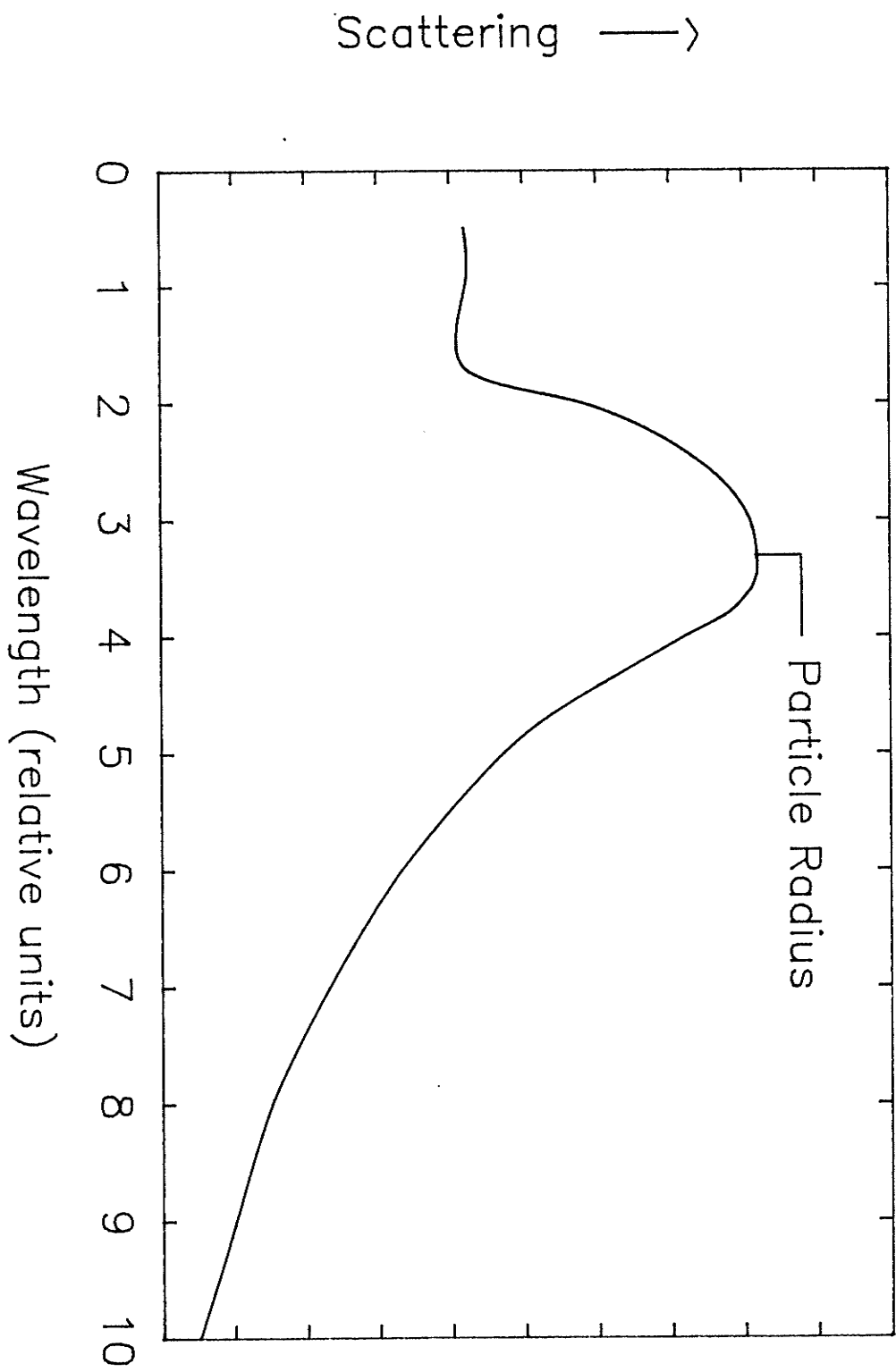


Figure 8.1: Relative importance of scatter

inhomogeneity will be as a result of scatter from its neighbors. In fact, at very small depths (of the order of a mm), the energy incident upon particles will be due solely to that scattered by others. The possibility now exists for light photons which have been scattered out of the incident beam direction to be directed back in and experimental transmittance measurements on tissue samples of reasonable thickness will yield erroneous results. Under these conditions the detector will not only collect those light photons passing through the sample without interacting but also a fraction of those undergoing multiple scattering. Thus, readings will not be representative of true transmittance and Beer's Law will certainly not be applicable. Nonetheless, such measurements are useful in quantifying the optical properties of biological tissue and are referred to as diffuse transmittance measurements.

Light scatter in tissue does not involve any new physical principles. Because it is independent, each interaction center may still be treated as an isolated entity exposed to light from a distant source (in this case the source may simply be another inhomogeneity rather than the original light source). Mie, Rayleigh-Gans and Anomalous Diffraction theories still apply to the individual centers but determining the intensity of light incident upon each will now be an extremely difficult task. As such, the application of these models to scattering in tissue becomes impractical. Instead, transport models such as Linear Transport and Diffusion theory are used.

The linear transport equation has found application in many areas of physics including the theory of plasmas, sound propagation and neutron diffusion. Its earliest application was that of radiative transfer, the description of light as it passes through a star's atmosphere.

The linear transport equation is a balance equation, a linearized form of the Boltzman equation whose derivation is based on the conservation of particles within a small volume element of phase space. The equation will provide an exact description of a beam of light as it passes through a multi-scattering and absorbing medium provided the beam may be considered to consist of a large number of neutral "particles" or rays which pursue their own path and act independently of one another. Thus, the wave nature so heavily drawn upon in the treatment of single scatter systems must now be replaced by the particle theory of light. The mathematical arguments presented in this chapter are based on the work of Case and Zweifel [28].

8.1 THE TRANSPORT EQUATION

In linear transport theory, the distribution of particles within a scattering/absorbing medium is completely described by the angular distribution function $\Psi(r,v,t)$ where

$$\Psi(r,v,t) d^3r d^3v \quad (8.1)$$

represents the number of particles in a volume element d^3r about a point r in a medium whose velocities lie in the element of velocity space d^3v about v at a time t .

Consider the change, dN , in the number of particles within the velocity element d^3v about v which are located in a small volume of space V , with surface S , about the point r , in a time dt .

$$dN = d^3v dt \int_V (d/dt)\Psi(r,v,t) d^3r \quad (8.2)$$

However, because of conservation principles, a balance must exist; the change in the number of particles within V must also be given by

$$dN = -A - B + C + D \quad (8.3)$$

where

- A = the net number of particles flowing out of S in dt (accounts for particles which enter and leave the volume with no change in direction)
- B = the number of particles with velocity v suffering collisions in V within the time dt (accounts for particles leaving the velocity element with no change in position)
- C = the number of particles acquiring velocity v in dt due to collisions within V (accounts for particles entering the velocity element with no change in position)
- D = the number of particles of velocity v produced in V in dt by sources

(see figure 8.2)

Term A:

To determine the explicit form of the first term in the above equation, a small cylinder of base area dS , length $|v|dt$ and axis parallel to v is constructed. The number of particles which leave the cylinder by crossing dS in a time dt will be equal to the number of particles within the cylinder which possess velocities in d^3v about v . Since

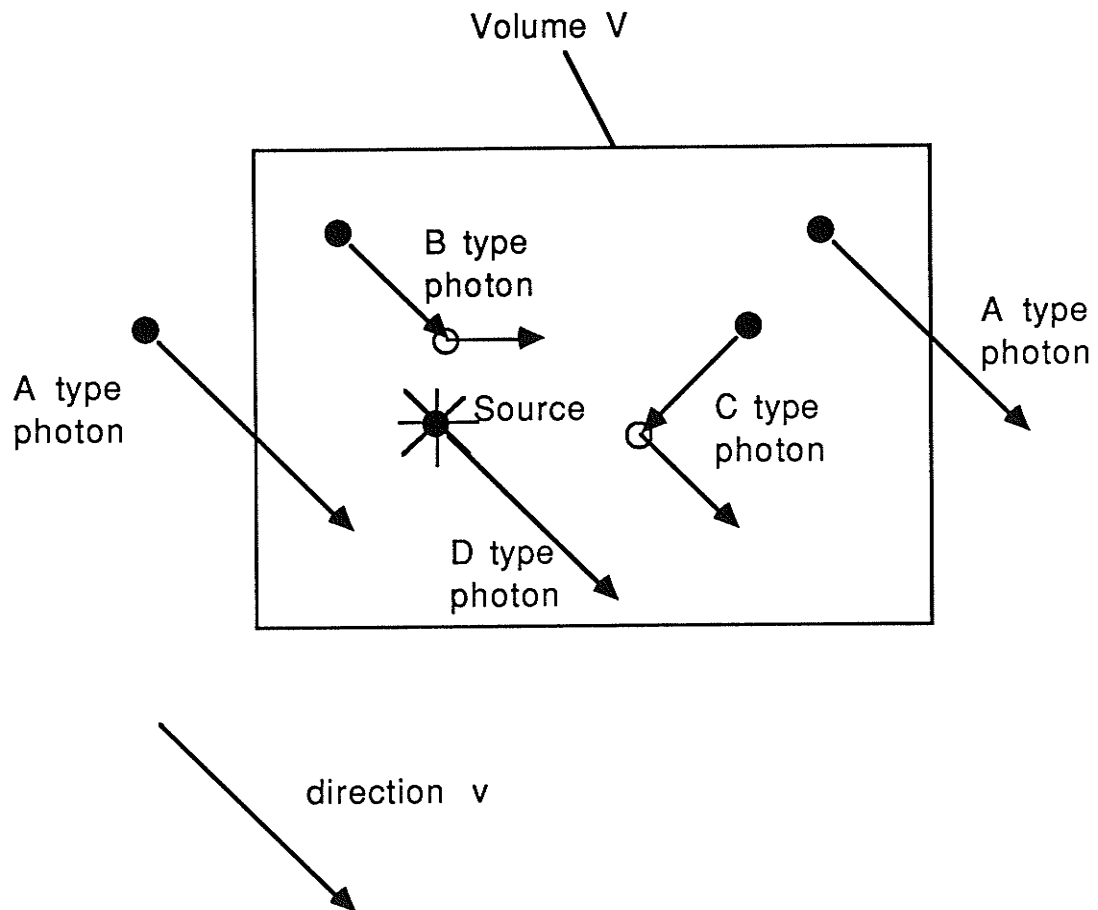


Figure 8.2: The four processes responsible for changes in the number of photons with velocity v contained in the volume element V .

$\int_V \mathbf{v} \cdot d\hat{\mathbf{n}} dS$ ($\hat{\mathbf{n}}$ being the unit normal to dS) is the total volume of the cylinder, this quantity can be represented by

$$\int_V \mathbf{v} \cdot \hat{\mathbf{n}} \Psi(r, \mathbf{v}, t) d^3v dt dS \quad (8.4)$$

Thus, the net number of particles of velocity within d^3v about \mathbf{v} flowing out of the volume V in a time dt is given by

$$\begin{aligned} A &= d^3v dt \int_S \mathbf{v} \Psi(r, \mathbf{v}, t) \cdot \hat{\mathbf{n}} ds \\ &= d^3v dt \int_V \nabla \cdot \mathbf{v} \Psi(r, \mathbf{v}, t) d^3r \end{aligned} \quad (8.5)$$

Term B:

As a neutral particle travels through a medium, it will undergo a series of collisions with interaction centers lying along its path. The average distance a particle of velocity \mathbf{v} and position \mathbf{r} will travel between each interaction is referred to as the mean free path $l(r, \mathbf{v})$. In one second, such a particle will experience an average of $|\mathbf{v}|/l(r, \mathbf{v})$ collisions. Assuming a particle density of $\Psi(r, \mathbf{v}, t)$, the rate of collisions for particles of velocity \mathbf{v} at a point \mathbf{r} in the medium will be

$$(|\mathbf{v}| \Psi(r, \mathbf{v}, t) / l(r, \mathbf{v})) d^3r d^3v \quad (8.6)$$

The total number suffering collisions in volume V in a time dt , and therefore experiencing a change in velocity, is

$$B = d^3v dt \int_V |\mathbf{v}| \Psi(r, \mathbf{v}, t) / l(r, \mathbf{v}) d^3r \quad (8.7)$$

Term C:

The inverse of the mean free path is called the cross section per unit volume for attenuation

$$\sigma(\text{att}, r, \mathbf{v}) = 1/l(r, \mathbf{v}) \quad (8.8)$$

It represents the sum of the cross sections of all interaction centers in the unit volume of medium centered about \mathbf{r} .

$$\sigma(\text{att}, r, \mathbf{v}) = \sum_i N_i(r) \chi_i(\text{att}, \mathbf{v}) \quad (8.9)$$

where $N_i(r)$ is the density of interaction centers of type i at \mathbf{r} and $\chi_i(\text{att}, \mathbf{v})$ is the cross section for attenuation of a single interaction center of type i . $\chi_i(\text{att})$ is the sum of a two components, a cross section for elastic scatter $\chi_i(\text{sca})$ and absorption $\chi_i(\text{abs})$.

$$\chi_i(\text{att}) = \chi_i(\text{sca}) + \chi_i(\text{abs}) \quad (8.10)$$

Partial cross sections per unit volume may then be defined. For example, the cross section per unit volume for elastic scatter at a point r is

$$\sigma(\text{sca}) = \sum_i N_i \chi_i(\text{sca}) \quad (8.11)$$

This quantity represents the probability that a particle of velocity v and position r will undergo an elastic scatter interaction.

To simplify notation, it is often useful to introduce the concept of scatter/absorption coefficient, defined as

$$c = \sigma(\text{sca}) / [\sigma(\text{sca}) + \sigma(\text{abs})] \quad (8.12)$$

This coefficient describes the relative importance of absorption interactions in the medium. If absorption is negligible, $c=1.0$. If, on the other hand, it is the only reaction resulting from collisions, $c=0$. The scatter/absorption coefficient is, therefore, a measure of the complete removal of particles of velocity v from the system as a result of interactions with the medium at r . Throughout the remainder of the thesis, all cross sections per unit volume are to be assumed cross sections for attenuation unless otherwise explicitly stated.

Using a notation similar to that above, let

$$v' \sigma(v', t' \rightarrow v, t; r) \Psi(r, v', t') d^3v' d^3v d^3r dt \quad (8.13)$$

represent the probability that a particle of velocity v' and position r will, at a time t' , undergo a collision and as a result acquire a new velocity v at a time t . To a very good approximation, one can assume that any new particles produced as a result of an interaction will appear at the point and time of the collision. Notation may then be simplified

$$\sigma(v', t' \rightarrow v, t; r) = \sigma(v' \rightarrow v; r) \quad (8.14)$$

Clearly,

$$\int \sigma(v' \rightarrow v, r) d^3v = c(r, v') \sigma(r, v') \quad (8.15)$$

the right hand side denoting the probability that a particle of velocity v' and position r will undergo a scatter interaction. Using this simplified notation eq. (8.13) may be rewritten as

$$v' \sigma(v' \rightarrow v, r) \Psi(r, v', t) d^3v' d^3v d^3r dt \quad (8.16)$$

The third term of dN , C , can therefore be expressed as

$$C = d^3v dt \int_V \int_{v'} v' \Psi(r, v', t) \sigma(v' \rightarrow v, r) d^3r d^3v' \quad (8.17)$$

Term D:

The final term in the expression is given by

$$D = d^3v dt \int_V q(r, v, t) d^3r \quad (8.18)$$

where $q(r, v, t) d^3r d^3v dt$ represents the number of particles inserted into d^3r at r and d^3v at v between time t and $t+dt$ due to sources.

Explicitly stated, the particle balance equation becomes (noting that V is an arbitrary volume)

$$\begin{aligned} (d/dt)\Psi(r, v, t) + v \cdot \nabla \Psi(r, v, t) + |v| \sigma(r, v) \Psi(r, v, t) \\ = q(r, v, t) + \int v' \sigma(v' \rightarrow v, r) \Psi(r, v', t) d^3v' \end{aligned} \quad (8.19)$$

since v is an independent variable and $\nabla \cdot v \Psi = v \cdot \nabla \Psi$. This expression is referred to as the linear transport equation. The solution of this equation gives $\Psi(r, v, t)$, the angular distribution function of particles in a medium.

When the transport equation is used to describe a light beam traversing a scattering and absorbing medium, the constituent particles of the beam (photons) all possess the same speed, $|v|$. Secondly, elastic scatter collisions do not change a photon's speed, they merely serve to change its direction of travel. Thus, the linear transport equation applicable to a beam of light propagating through a scatter/absorbing medium will be of the form

$$\begin{aligned} |v| \Omega \cdot \nabla \Psi(r, \Omega) + |v| \sigma(r) \Psi(r, \Omega) \\ = q(r, \Omega) + |v| \sigma(r) c(r) \int \Psi(r, \Omega') f(\Omega' \cdot \Omega, r) d\Omega' \end{aligned} \quad (8.20)$$

where Ω now represents a direction relative to some reference vector and $f(\Omega' \cdot \Omega, r)$ is defined as

$$f(\Omega' \cdot \Omega, r) = \sigma(\Omega' \cdot \Omega, r) / c(r) \sigma(r) \quad (8.21)$$

It should be pointed out that a further simplification was employed in obtaining equation (21). Because only time invariant angular distributions are of importance, any time dependance in the transport equation may be removed. Solving this form of the transport equation gives the particle

angular distribution function $\Psi(r, \Omega)$ where Ψ is now dependant only on position and direction of travel in the medium.

8.2 SOLUTIONS IN ONE DIMENSION

From an examination of the transport equation, it appears that to obtain a solution, it is necessary to specify both the particle distribution at some initial time $t=t_0$ and the particle sources throughout all space. However, it turns out that solutions obtained in this manner are too complete. For example, one is often only interested in the particle distribution within a small well defined region of space. In general, many different source arrangements will produce the same particle distribution in the region of interest (although distributions in areas outside this region may differ). The Uniqueness Theorem permits the reduction of all these problems (ie. those problems involving different source distributions which yield identical particle densities within a particular region of interest) to a single problem. The theorem states

"The particle angular distribution within a volume V of space bounded by a surface S is uniquely determined by

- 1) the initial angular distribution in V
- 2) sources within V
- 3) the angular distribution incident on S "

In other words, in so far as the distribution of particles within V is concerned, exterior sources may be replaced by the incident angular distribution of particles on S .

The simplest problems of interest in the study of light propagation through a medium are those which possess plane symmetry. An example is the distribution that results from an infinite planar source irradiating in a scattering/absorbing medium which occupies all of space. Plane symmetry is said to exist if $\sigma(r, \Omega)$, $\sigma(\Omega' \rightarrow \Omega, r)$ and $q(r, \Omega)$, as well as any boundary conditions, depend only on one spatial coordinate, say z , and any angular dependence they may exhibit can be accurately represented by $\Omega \cdot \hat{z} = \mu$. For one dimensional problems of this nature, the transport equation reduces to

$$\mu(d/dz)\Psi(z, \mu) + \Psi(z, \mu) = (c/2) \int_{-1}^1 \Psi(z, \mu') d\mu' + q(z, \mu) \quad (8.22)$$

This reduction has also assumed isotropic scattering in which case $f(\Omega' \cdot \Omega) = 1/4\pi$. Integration has been carried out over the azimuthal angle yielding a factor of 2π . By

defining the Boltzman operator B, the transport equation may be expressed as

$$B \Psi(z, \mu) = q(z, \mu) \quad (8.23)$$

where

$$B = \mu(d/dz) + 1 - (c/2) \int_{-1}^1 d\mu' \quad (8.24)$$

The most widely used method for solving the one dimensional transport equation was first introduced by Case. It is very similar to the conventional method for solving ordinary differential equations in which the solution is expanded as a series of solutions of the homogeneous equation (or normal modes).

Consider the classical theory boundary problems in which an operator O and its associated eigenfunctions Ψ_κ and eigenvalues λ_κ are defined such that

$$O \Psi_\kappa(r) = \lambda_\kappa \Psi_\kappa(r) \quad (8.25)$$

If the eigenfunctions form a complete and orthogonal set, a problem of the form

$$O f(r) = g(r) \quad (8.26)$$

(g(r) being a known function) may be solved by expanding f(r) and g(r) as

$$f(r) = \sum f_\kappa \Psi_\kappa(r) \quad (8.27)$$

$$g(r) = \sum g_\kappa \Psi_\kappa(r) \quad (8.28)$$

The coefficients g_κ are known while the f_κ are to be determined. Substituting these forms of f(r) and g(r) into the defining relation and applying the operator to each term gives

$$\sum f_\kappa \lambda_\kappa \Psi_\kappa(r) = \sum g_\kappa \Psi_\kappa(r) \quad (8.29)$$

Because the Ψ_κ are orthogonal

$$f_\kappa = g_\kappa / \lambda_\kappa \quad (8.30)$$

To solve the linear transport equation, a similar approach is used. Many problems of interest can be expressed as solutions to a homogeneous equation subject to certain boundary conditions (Uniqueness theorem). In other words, it is equations of the form

$$B f(z, \mu) = 0 \quad (8.31)$$

which must be solved. An example of a typical boundary condition is: at $z=0$, $f(0, \mu)$ is equal to $f_0(\mu)$. To solve this type of equation, $f(z, \mu)$ is expanded in terms of the solutions of the homogeneous equation

$$f(z, \mu) = \sum f_\nu \Psi_\nu(z, \mu) \quad (8.32)$$

Using the boundary conditions

$$\sum f_\nu \Psi_\nu(0, \mu) = f_0(\mu) \quad (8.33)$$

The expansion coefficients, f_ν , are then found by applying the orthogonality relations.

The translational invariance of the homogeneous transport equation suggests solutions of the form

$$\Psi_\nu(z, \mu) = \phi_\nu(\mu) \exp(-z/\nu) \quad (8.34)$$

where ϕ_ν is referred to as an eigenfunction of the operator B with corresponding eigenvalue ν . Inserting this solution into the homogeneous form of the transport equation

$$(\nu - \mu) \phi_\nu(\mu) / \nu = (c/2) \int_{-1}^1 \phi_\nu(\mu') d\mu' \quad (8.35)$$

This represents a linear homogeneous equation of the variable ϕ_ν ; as such, normalization is arbitrary and may conveniently be chosen as

$$\int_{-1}^1 \phi_\nu(\mu') d\mu' = 1 \quad (8.36)$$

Thus, the eigenfunctions are given by

$$(\nu - \mu) \phi_\nu(\mu) = c\nu/2 \quad (8.37)$$

or

$$\phi_\nu(\mu) = (c\nu/2) (1/(\nu - \mu)) \quad (8.38)$$

However, eq.(8.38) must be altered so as to allow for the possibility of $\mu = \nu_0$. This is accomplished by adding to the right hand side a term $\lambda(\nu) \delta(\nu - \mu)$ where $\lambda(\nu)$ is an arbitrary function. In addition, no loss of generality follows from attaching the symbol P to the factor $1/(\nu - \mu)$ so as to denote the Cauchy Principle Value. The final form of the eigenfunctions become

$$\phi_\nu(\mu) = (c\nu/2) P(1/(\nu - \mu)) + \lambda(\nu) \delta(\nu - \mu) \quad (8.39)$$

That this form still represents a solution to eq.(8.37) can be verified by direct substitution (noting that by

definition $x\delta(x)=0$). It should be noted that the eigenfunctions are actually distributions and as such are not functions in the usual sense. They have no real physical meaning and the only reason for using them is their usefulness in arriving at a solution to the transport equation (ie. their use leads to no serious difficulties).

To use the eigenfunctions in solving the linear transport equation, it is necessary to prove both their orthogonality and completeness. Only then can the solution be expanded as a series of eigenfunctions (solutions to the homogeneous transport equation) and the coefficients determined from the boundary conditions.

8.3 DISCRETE EIGENVALUES

As is typical of homogeneous equations, eq.(8.35) does not possess solutions for every value of ν . To find the allowed eigenvalues of the operator B, first consider ν to lie outside the region -1 to 1 on the real axis. As the possibility of $\mu=\nu$ does not exist, the eigenfunctions may be expressed as

$$\phi_{\nu}(\mu) = (c\nu/2) (1/(\nu-\mu)) \quad (8.40)$$

Using the normalization condition

$$n(\nu) = 1 - (c\nu/2) \int_{-1}^1 (1/(\nu-\mu)) d\mu = 0 \quad (8.41)$$

The eigenvalues of B are solutions of this equation, referred to as the dispersion function. Stated explicitly,

$$n(\nu) = 1 - (c\nu/2) \ln[(1+\nu^{-1})/(1-\nu^{-1})] = 0 \quad (8.42)$$

Examination of (8.41) and (8.42) reveals two very important properties of the dispersion function. Firstly, $n(\nu)=n(-\nu)$ so that if ν is a root of the equation, so is $-\nu$. Secondly, if ν is a solution then so too is ν^* , the complex conjugate of ν . It can be shown that the dispersion relation (8.41) has only two solutions. In other words, outside the interval -1 to 1, the Boltzman operator possesses only two eigenvalues, referred to as discrete eigenvalues. Keeping in mind the aforementioned properties of the dispersion relation, this necessarily means that the roots of $n(\nu)$ must either lie on the real axis or the imaginary axis. To determine which is actually the case, consider the behaviour of the dispersion function along the positive real axis.

$$n(\nu) \rightarrow -\text{infinity} \quad \text{as} \quad \nu \rightarrow 1^+ \quad (8.43)$$

$$n(\nu) \rightarrow 1-c \quad \text{as} \quad \nu \rightarrow \text{infinity} \quad (8.44)$$

As c is less than 1, $n(\nu)$ will change sign as one moves along the positive real axis from 1 to infinity. In other words, a zero exists on the positive real axis. Since $n(\nu)$ possesses only two roots and these must occur in pairs, the dispersion relation must also possess a zero at the same distance from the origin along the negative real axis. The two roots, or discrete eigenvalues, are represented $+\nu_0$ and $-\nu_0$. As $c \rightarrow 0$, the positive root ν_0 of $n(\nu)$ will approach unity. Furthermore, as $c \rightarrow 1$, $+\nu_0$ will move towards infinity.

8.4 CONTINUOUS EIGENVALUES

Consider now the interval between -1 and 1 on the real axis. Over this region, the eigenfunction equation is given by

$$\phi_\nu(\mu) = (c\nu/2) P(1/\nu - \mu) + \lambda(\nu)\delta(\nu - \mu) \quad (8.45)$$

Applying the normalization condition, one obtains

$$\lambda(\nu) = 1 - (c\nu/2) P \int_{-1}^1 (1/\nu - \mu) d\mu \quad (8.46)$$

As $\lambda(\nu)$ is arbitrary, a suitable function can always be chosen to satisfy this equation. Thus, any value of ν in the interval $[-1, 1]$ will be an acceptable solution of the equation. These ν 's are referred to as the continuous eigenvalues of the operator B . That the union of the above mentioned continuous and discrete eigenfunctions form a complete set has been proven by Case and Zweifel.

8.5 EIGENFUNCTION ORTHOGONALITY

The second property that must be demonstrated for the eigenfunctions to be of use in solving the linear transport equation is that of orthogonality.

$$\int_{-1}^1 \mu \phi_\nu(\mu) \phi_{\nu'}(\mu) d\mu = 0 \quad \nu \neq \nu' \quad (8.47)$$

where ν and ν' may be either elements of the discrete or continuous set of eigenvalues.

This relation can be proven by substituting the expression for a particular eigenfunction into the transport equation.

$$(1 - (\mu/\nu)) \phi_\nu(\mu) = (c/2) \int_{-1}^1 \phi_{\nu'}(\mu') d\mu' \quad (8.48)$$

A similar expression may be obtained for $\phi_{\nu'}(\mu)$

$$(1 - (\mu/\nu')) \phi_{\nu'}(\mu) = (c/2) \int_{-1}^1 \phi_{\nu'}(\mu') d\mu' \quad (8.49)$$

Multiplying the first by $\phi_{\nu'}(\mu)$, the second by $\phi_{\nu}(\mu)$, subtracting the two equations and then integrating the result over μ gives

$$[(1/\nu') - (1/\nu)] \int_{-1}^1 \mu \phi_{\nu}(\mu) \phi_{\nu'}(\mu) d\mu = 0 \quad (8.50)$$

If $\nu' \neq \nu$ then

$$\int_{-1}^1 \mu \phi_{\nu}(\mu) \phi_{\nu'}(\mu) d\mu = 0 \quad (8.51)$$

Thus, the eigenfunctions of the Boltzman operator are orthogonal.

8.6 DISCRETE EIGENFUNCTION NORMALIZATION

The normalization integral for the discrete modes can be determined quite simply.

$$\begin{aligned} N_{0\pm} &= \int_{-1}^1 \mu \phi_{0\pm}^2(\mu) d\mu \\ &= [c\nu_0/2]^2 \int_{-1}^1 \mu / (\pm\nu_0 - \mu)^2 d\mu \end{aligned} \quad (8.52)$$

Consider first N_{0+} . Using the dispersion relation

$$n(\nu) = 1 - (c\nu/2) \int_{-1}^1 1/(\nu - \mu) d\mu \quad (8.53)$$

one finds

$$\begin{aligned} (d/d\nu)n(\nu) &= (-c/2) \int_{-1}^1 1/(\nu - \mu) d\mu + (c\nu/2) \int_{-1}^1 1/(\nu - \mu)^2 d\mu \\ &= (c/2) \int_{-1}^1 \mu / (\nu - \mu)^2 d\mu \end{aligned} \quad (8.54)$$

Thus,

$$\begin{aligned} N_{0+} &= (c\nu_0^2/2) (d/d\nu)n(\nu) |_{\nu=\nu_0} \\ &= (c\nu_0^2/2) (d/d\nu)[1 - c\nu \tanh^{-1}(1/\nu)] |_{\nu=\nu_0} \\ &= (c\nu_0^3/2) [c(\nu_0^2 - 1)^{-1} - (\nu_0)^{-2}] \end{aligned} \quad (8.55)$$

By setting $\nu_0 = -\nu_0$, one finds

$$-N_{0-} = N_{0+} \quad (8.56)$$

8.7 CONTINUUM EIGENFUNCTION NORMALIZATION

Normalization constants for the continuum modes may be obtained using similar, although more complex, arguments. It can be shown that

$$\int_{-1}^1 \mu \phi_{\nu}(\mu) \phi_{\nu'}(\mu) d\mu = N(\nu) \delta(\nu - \nu') \quad (8.57)$$

where

$$N(\nu) = \nu [\lambda^2(\nu) + c^2 \pi^2 \nu^2 / 4] \quad (8.58)$$

Chapter IX

DIFFUSION THEORY

In many situations the distribution of particles within a scattering/absorbing medium is described by a transport equation which is too complicated to solve analytically. Numerical schemes of integrating the transport equation must then be used. The two most common are the Spherical Harmonics and Discrete Ordinates methods.

The Discrete Ordinates scheme is mentioned only in passing. With this technique, the domain of the parameter describing angular dependence, μ , is divided into N intervals $[\mu_j, \mu_{j+1}]$, $j=1,2,\dots,N$. By assuming the angular distribution function $\Psi(\mu)$ to vary linearly with μ over each interval, the angular integration contained in the transport equation may be carried out. The transport equation itself is then integrated over each interval to yield a set of N equations in the N unknowns $\Psi(\mu_j)$. Profio et al [42,48] have made use of the Discrete Ordinates method to model light transport in tissue.

With the Spherical Harmonics technique, the angular distribution function $\Psi(\mu)$ is expanded in a series of spherical harmonics. Approximate solutions to the transport equation are then obtained by truncation of this series. The lowest order approximation generated using the Spherical Harmonics method is referred to as Diffusion theory and is the focus of this chapter. The mathematical arguments presented are based on the work of Case and Zweifel [26].

Consider the one speed, time independent transport equation

$$\begin{aligned} \Omega \cdot \nabla \Psi(r, \Omega) + \sigma(r) \Psi(r, \Omega) \\ = (1/|\mathbf{v}|) q(r, \Omega) + c(r) \sigma(r) \int_{-1}^1 \Psi(r, \Omega') f(\Omega' \cdot \Omega) d\Omega' \end{aligned} \quad (9.1)$$

In the Spherical Harmonics Method, $\Psi(r, \Omega)$ and $q(r, \Omega)$ are expanded in terms of the spherical harmonics. For example,

$$\Psi(r, \Omega) = \sum_{l=0}^{\infty} \sum_{m=-l}^l ((2l+1)/4\pi)^{1/2} \Psi_{l,m}(r) Y_{l,m}(\Omega) \quad (9.2)$$

where $\Psi_{l,m}(r)$ represents the radial component of $\Psi(r, \Omega)$ and $Y_{l,m}(\Omega)$ the spherical harmonics. $f(\Omega' \cdot \Omega)$, in turn, is expanded as a series of Legendre Polynomials.

$$\begin{aligned}
 f(\Omega' \bullet \Omega) &= \sum_{l=0}^{\infty} ((2l+1)/4\pi) f_{l, P_l}(\Omega' \bullet \Omega) \\
 &= \sum_{l=0}^{\infty} \sum_{m=-l}^l f_{l, Y_{l,m}^*}(\Omega') Y_{l,m}(\Omega)
 \end{aligned} \tag{9.3}$$

where the last equality is a result of the addition theorem. The expressions for $\Psi(r, \Omega)$, $q(r, \Omega)$ and $f(\Omega' \bullet \Omega)$ are substituted into the transport equation, the result multiplied by $Y_{l,m}(\Omega)$ and an integration over Ω performed. This process yields an infinite number of coupled differential equations in the unknown $\Psi_{l,m}$. An approximate solution to the transport equation, called the P_L approximation, is obtained by truncating this set on the assumption that all $\Psi_{l,m}$ vanish for $l > L$. The lowest order spherical harmonics approximation, the P_1 approximation, is referred to as diffusion theory. It assumes that the angular distribution function expansion contains only those terms with $l=0$ and 1 .

$$\Psi(r, \Omega) = (1/4\pi)^{1/2} \Psi_{00}(r) Y_{00}(\Omega) + (3/4\pi)^{1/2} \sum_{m=-1}^1 \Psi_{1m}(r) Y_{1m}(\Omega) \tag{9.4}$$

Substituting this into the transport equation, expanding $q(r, \Omega)$ and $f(\Omega' \bullet \Omega)$ in a similar fashion and carrying out the above mentioned integration, one obtains four equations in four unknowns. This is the diffusion approximation to the transport equation.

9.1 DERIVATION OF THE DIFFUSION EQUATION

Because the procedure outlined in the previous section is both tedious and complex, an alternative method of deriving the diffusion approximation is often employed. Since $\Psi_{00} = (1/4\pi)^{1/2}$ is a scalar and since $\Psi_{1,-1}$, Ψ_{10} and Ψ_{11} may be treated as the three components of a vector, the angular distribution function of diffusion theory may be written as

$$\Psi(r, \Omega) = A + \Omega \bullet B \tag{9.5}$$

where A is a scalar and B a vector quantity. Integrating $\Psi(r, \Omega)$ over Ω gives the density of light $P(r)$ at a point r in space

$$P(r) = \int \Psi(r, \Omega) d\Omega = \int (A + \Omega \bullet B) d\Omega = 4\pi A \tag{9.6}$$

since $\int \Omega \bullet B d\Omega = 0$. Therefore, $A = P(r)/4\pi$. If the expression for $\Psi(r, \Omega)$ is first multiplied by Ω and then integrated over Ω

$$\begin{aligned}
 \int \Omega \Psi(r, \Omega) d\Omega &= \int A \Omega d\Omega + \int \Omega (\Omega \bullet B) d\Omega \\
 (1/|v|) \int v \Psi(r, \Omega) d\Omega &= \int \Omega A d\Omega + \int \Omega (\Omega \bullet B) d\Omega \\
 (1/|v|) \int J(r, \Omega) d\Omega &= \int \Omega A d\Omega + \int \Omega (\Omega \bullet B) d\Omega
 \end{aligned}$$

$$J(r)/|v| = 0 + 4\pi B/3 = 4\pi B/3 \quad (9.7)$$

where $J(r, \Omega)$ is referred to as the angular current or net drift velocity of the distribution at a point r and $J(r) = \int J(r, \Omega) d\Omega$. Thus, in the diffusion approximation, the angular distribution function is given by

$$\Psi(r, \Omega) = (1/4\pi) [P(r) + 3J(r) \cdot \Omega / |v|] \quad (9.8)$$

A similar expression exists for $q(r, \Omega)$

$$q(r, \Omega) = (1/4\pi) [q_0(r) + 3\Omega \cdot q_1(r)] \quad (9.9)$$

Inserting these equations into the transport equation

$$\begin{aligned} \Omega \cdot \nabla [P(r) + 3\Omega \cdot J(r) / |v|] + \sigma(r) [P(r) + 3\Omega \cdot J(r) / |v|] \\ = (1/|v|) [q_0(r) + 3\Omega \cdot q_1(r)] + \\ c(r) \sigma(r) \int [P(r) + 3\Omega' \cdot J(r) / |v|] f(\Omega' \cdot \Omega) d\Omega' \end{aligned} \quad (9.10)$$

This expression can be simplified by noting that

$$\int f(\Omega' \cdot \Omega) d\Omega' = 1 \quad (9.11)$$

and

$$\begin{aligned} \int \Omega' f(\Omega' \cdot \Omega) d\Omega' \text{ is proportional to } \Omega \\ = a\Omega \end{aligned} \quad (9.12)$$

where a is the constant of proportionality. This last result can be deduced from the following argument: The left hand side of the expression is a vector. Therefore, the right hand side must also be a vector. Since the vector Ω' is a variable of integration, the only possible vector remaining is Ω ; the integral must, therefore, be proportional to it. Taking the scalar product of the last equation with Ω yields

$$a = \int (\Omega \cdot \Omega') f(\Omega' \cdot \Omega) d\Omega' = \mu_0 \quad (9.13)$$

The transport equation then reduces to

$$\begin{aligned} [\Omega \cdot \nabla + \{1 - c(r)\}\sigma(r)]P(r) + [\Omega \cdot \nabla + \{1 - c(r)\mu_0\}\sigma(r)] 3\Omega \cdot J(r) / |v| \\ = (1/|v|) [q_0(r) + \Omega \cdot q_1(r)] \end{aligned} \quad (9.14)$$

Further simplification requires that this expression be put in the form of two coupled equations in two unknowns, $P(r)$ and $J(r)$. This mathematical splitting can be achieved through a two step process. By integrating over Ω ,

$$[1 - c(r)]\sigma(r)P(r) + (1/|v|)\nabla \cdot J(r) = (1/|v|)q_0(r) \quad (9.15)$$

where use has been made of the fact that for any two arbitrary vectors A and B

$$\int \Omega \cdot A \, d\Omega = 0 \quad (9.16)$$

and

$$\int (\Omega \cdot A)(\Omega \cdot B) \, d\Omega = 4\pi(A \cdot B)/3 \quad (9.17)$$

If the transport equation is first multiplied by Ω and then integrated over Ω

$$(1/3) P(r) + (1/|v|)\sigma(r)[1-c(r)\mu_0]J(r) = (1/|v|)q_1(r) \quad (9.18)$$

where use has been made of the fact that

$$\int \Omega(A \cdot \Omega) \, d\Omega = 4\pi A/3 \quad (9.19)$$

and

$$\int \Omega(A \cdot \Omega)(B \cdot \Omega) \, d\Omega = 0 \quad (9.20)$$

Eq.(9.15) and (9.18) are the basic equations of diffusion theory. By eliminating $J(r)$, the pair of equations may be re-combined to once again yield a single diffusion expression. Assuming an isotropic source (ie $q_1=0$), eq.(9.18) may be expressed as

$$J(r) = -|v|D(r) P(r) \quad (9.21)$$

where $D(r)$ is the diffusion coefficient, defined as

$$D(r) = (1/3)[\sigma(r)\{1-c(r)\mu_0\}]^{-1} \quad (9.22)$$

Eq.(9.21) relates the net current of the distribution to the gradient of the particle density. It states that the net current of particles across a surface within a medium is proportional to the rate at which the density of particles decreases across that surface. Also, the direction of the net current corresponds to the direction in which the density is decreasing at its maximum rate. In other words, the particle population tends to drift from regions of high concentration to those of low concentration, like a gas diffusing through a porous plug. This drift gives rise to a net current. Eq.(9.21) is often referred to as Fick's Law. Substitution into eq.(9.15) yields a single diffusion equation.

$$-\nabla \cdot D(r)\nabla P(r) + \sigma(\text{abs},r)P(r) = (1/|v|)q_0(r) \quad (9.23)$$

where $\sigma(\text{abs},r)$ is the absorption cross section per unit volume, defined as

$$\sigma(\text{abs}, r) = [1 - c(r)] \sigma(r) \quad (9.24)$$

9.2 VALIDITY OF THE DIFFUSION EQUATION

Fick's Law is based on the assumption that the angular distribution function $\Psi(r, \Omega)$ is of the form

$$\Psi(r, \Omega) = A + \Omega \cdot B \quad (9.25)$$

where A and B are scalar and vector functions of position but not direction, respectively. As shown previously, the components of the vector B will be functions of the corresponding components of the net drift velocity of the particle population ie.

$$B_x = (3/4\pi |v|) J_x = (3\hat{x}/4\pi |v|) \int v_x \Psi(r, \Omega) d\Omega \quad (9.26)$$

where J_x is the x component of the net drift velocity vector and v_x is the x component of a particular particle's velocity vector.

In order to gain a better understanding of the underlying assumptions of the diffusion approximation, it is useful to examine the special case in which all three components of the net drift velocity J are zero. Then,

$$\Psi(r, \Omega) = A \quad (9.27)$$

The number of particles at r, moving in a direction Ω , will be independent of Ω and a polar plot of $\Psi(r, \Omega)$ will yield a sphere.

Now consider the case where A and J_x take on positive, finite values while J_y and J_z remain equal to zero (ie. a net drift in the positive x direction). In this instance, the angular distribution function will be large in one preferred direction and spherical symmetry will no longer exist. Similarly, finite values of J_y and J_z (ie. net drift velocities in the y and z directions) will also result in a non-spherically symmetric distribution function. For a nonzero net drift velocity, the particle distribution is said to be linearly anisotropic.

The magnitude of the vector function B must at all times be less than or equal to the scalar function A. Otherwise $\Psi(r, \Omega)$ will take on negative values for certain directions Ω , a meaningless concept for a density function. Thus, the magnitude of the components of the net drift velocity can never become too large. Because of this, the expression for $\Psi(r, \Omega)$ will not be able to represent particle distributions

which assume beam-like characteristics. Stated differently, Fick's Law is expected to be a poor approximation whenever the angular distribution function is large in one preferred direction. Such a distribution can exist in a medium where absorption is significant, near an interface between two media exhibiting differences in either absorption or scattering cross sections, or in the vicinity of a source.

Although the existence of a highly directed distribution in the vicinity of a source is quite obvious, such is not the case for the other two conditions mentioned. To illustrate why non-isotropic distributions exist near an interface and in a heavily absorbing medium, consider the situation shown in figure 9.1. In particular, consider the angular distribution of particles travelling through a medium containing an interface between two regions of different scatter and absorption cross sections per unit volume. Region I is characterized by an absorption cross section per unit volume which is much smaller than that of scatter. In region II, absorption is the dominant mode of interaction. Finally, let the absorption cross section per unit volume of region II be much greater than that of I. The net movement of particles is from I to II.

Because the scatter cross section per unit volume of region II is small, few particles in this region will be scattered back into I. Thus, near the interface, $\Psi(r, \Omega)$ will be large for directions pointing from I to II but small for directions opposite. Fick's Law will therefore be a poor approximation in the vicinity of the interface. Moreover, it will continue to be a poor approximation for all points within II. Because of the heavy absorption in this region, $\Psi(r, \Omega)$ will fall off rapidly in all directions as one moves away from the interface. However, in the absence of scatter, no mechanism will exist to re-distribute the arrangement of particles and the highly directed distribution established at the interface will persist. To the left of the interface, any dependence of $\Psi(r, \Omega)$ on Ω would be quickly lost. In this region, the high probability scatter interactions serve to rearrange the particles until an isotropic distribution is established; beam-like distributions cannot persist. Under such conditions, the particles will behave like a gas diffusing through a porous plug and although there may be a net drift of particles, their distribution will be accurately described by diffusion theory.

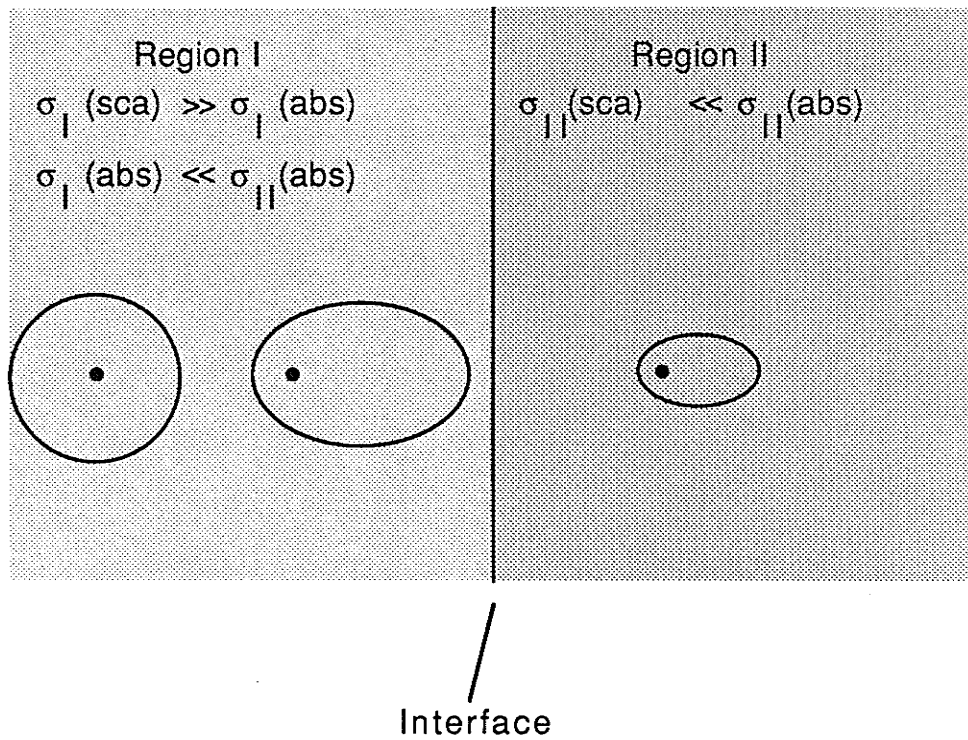


Figure 9.1: Angular distribution of particles within the vicinity of an interface between two media of different optical properties.

Chapter X

SOLUTIONS OF THE LINEAR TRANSPORT EQUATION

In this chapter, four solutions of the Linear Transport equation are presented (solutions are based on the work of Case and Zweifel [28]). All are complex expressions which describe the spatial distribution of light density within a scattering/absorbing medium for a different irradiation geometry. Computer programs have been written which permit the evaluation of these functions at select locations in the medium. However, the mean free path and scatter/absorption coefficient of the medium must be known for numerical results to be generated (MFP and c are the input parameters of these computer models - although MFP does not appear explicitly in the formal transport solutions, all distances are expressed relative to it). The numerical light distributions generated with these solutions are presented in chapter 16.

10.1 COLLIMATED PLANAR SOURCE/INFINITE MEDIUM

A particularly important problem in photon transport, one which can be used as a very simple model of light propagation in biological tissue, is that of the large planar source irradiating within an infinite scatter/absorbing medium (see figure 10.1).

Of interest is the spatial distribution of light from such a source, assumed to be of unit strength located at $z=z_0$ and emitting in the direction $\mu=\mu_0$. Other constraints on the system include the extension of the source to infinity in both the x and y directions and that the medium which fills the rest of space be uniform and homogeneous. Because of the plane symmetry, the transport equation describing this situation will take on the form

$$\begin{aligned} &\mu(d/dz)\Psi(z_0, \mu_0 \rightarrow z, \mu) + \Psi(z_0, \mu_0 \rightarrow z, \mu) \\ &= (c/2) \int_{-1}^1 \Psi(z_0, \mu_0 \rightarrow z, \mu') d\mu' + \delta(z) \delta(\mu - \mu_0) / 2\pi \end{aligned} \quad (10.1)$$

However, the same problem can be represented by a homogeneous equation (Uniqueness Theorem)

$$\mu(d/dz)\Psi(z, \mu) + \Psi(z, \mu) = (c/2) \int_{-1}^1 \Psi(z, \mu') d\mu' \quad (10.2)$$

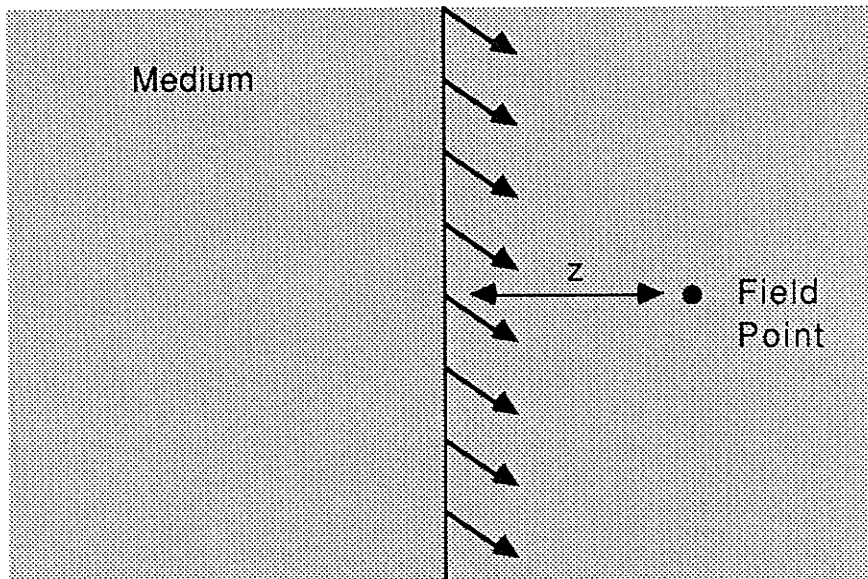


Figure 10.1: Collimated planar source irradiating within an infinitely large homogeneous medium

subject to the boundary conditions

$$\Psi(0^+, \mu) - \Psi(0^-, \mu) = \delta(\mu - \mu_0) / 2\pi\mu \quad (10.3)$$

$$\lim_{|z| \rightarrow \infty} \Psi(z, \mu) = 0 \quad (10.4)$$

To satisfy the last condition, the solution to the transport equation must be of the form

$$\Psi(z, \mu) = a_{0+} \Psi_{0+}(z, \mu) + \int_0^1 A(\nu) \Psi_\nu(z, \mu) d\nu \quad z > 0 \quad (10.5)$$

$$\Psi(z, \mu) = -a_{0-} \Psi_{0-}(z, \mu) - \int_{-1}^0 A(\nu) \Psi_\nu(z, \mu) d\nu \quad z < 0 \quad (10.6)$$

where a_{0+} and a_{0-} are unknown constants and $A(\nu)$ is an unknown function. For the case $z > 0$, the modes which diverge at infinity have been omitted. Thus, Ψ_{0-} is not included and the integral in the second term is from 0 to 1. Similar arguments hold for the $z < 0$ solution, those modes which diverge at minus infinity being excluded. Keep in mind that

$$\Psi_\nu(z, \mu) = \exp[-z/\nu] \phi_\nu(\mu) \quad (10.7)$$

Letting $z \rightarrow 0$ in the assumed solutions (10.5) and (10.6)

$$\Psi(0^+, \mu) = a_{0+} \phi_{0+}(\mu) + \int_0^1 A(\nu) \phi_\nu(\mu) d\nu \quad (10.8)$$

$$\Psi(0^-, \mu) = -a_{0-} \phi_{0-}(\mu) - \int_{-1}^0 A(\nu) \phi_\nu(\mu) d\nu \quad (10.9)$$

Applying the boundary conditions for $z \rightarrow 0$

$$\delta(\mu - \mu_0) / 2\pi\mu = a_{0+} \phi_{0+}(\mu) + a_{0-} \phi_{0-}(\mu) + \int_{-1}^1 A(\nu) \phi_\nu(\mu) d\nu \quad (10.10)$$

The expansion coefficients are then obtained by multiplying this equation by $\mu \phi_\nu(\mu)$, integrating over μ and using the orthogonality relations. This yields

$$\begin{aligned} a_{0\pm} &= (1/N_{0\pm}) \int_{-1}^1 \mu \phi_{0\pm}(\mu) \delta(\mu - \mu_0) (2\pi\mu)^{-1} d\mu \\ &= \phi_{0\pm}(\mu_0) / 2\pi N_{0\pm} \end{aligned} \quad (10.11)$$

and

$$A(\nu) = \phi_\nu(\mu_0) / 2\pi N(\nu) \quad (10.12)$$

Thus,

$$\begin{aligned} \Psi(z_0, \mu_0 \rightarrow z, \mu) &= \pm \phi_{0\pm}(\mu_0) \phi_{0\pm}(\mu) \exp[-|z - z_0| / \nu_0] / 2\pi N_{0\pm} \\ &+ \int_{\pm 1}^1 \phi_{\pm\nu}(\mu) \phi_{\pm\nu}(\mu_0) \exp[-|z - z_0| / \nu] / N(\pm\nu) d\nu \end{aligned} \quad (10.13)$$

with the upper sign applying to the region $z > 0$ and the lower sign for $z < 0$.

The light density at a point in the medium can be found by multiplying the angular distribution function by 2π and integrating over all angles μ .

$$\begin{aligned} P(z_0, \mu_0 \rightarrow z) &= 2\pi \int_{-1}^1 \Psi(z_0, \mu_0 \rightarrow z, \mu) d\mu \\ &= \phi_0(\mu_0) \exp(-|z-z_0|/\nu_0) / T(\nu_0) \\ &\quad + \int_0^1 \phi_\nu(\mu_0) \exp(-|z-z_0|/\nu) / N(\nu) d\nu \end{aligned} \quad (10.14)$$

where

$$T(\nu_0) = (1/2)c\nu_0^3 [c(\nu_0^2-1)^{-1} - \nu_0^{-2}] \quad (10.15)$$

Here the normalization condition $\int_{-1}^1 \phi_\nu(\mu) d\mu = 1$ has been used.

The computer program CPLSIM was used to evaluate this expression at a particular value of z and μ_0 . Its flow chart is illustrated in figure 10.2.

10.2 ISOTROPIC PLANAR SOURCE/INFINITE MEDIUM

The geometry of this problem differs from that of the previous only in so far as the planar source is now an isotropic emitter of radiation. A theoretical expression describing the distribution of light under these conditions can be obtained by integrating eq.(10.14) with respect to μ_0 and multiplying the result by $1/2$.

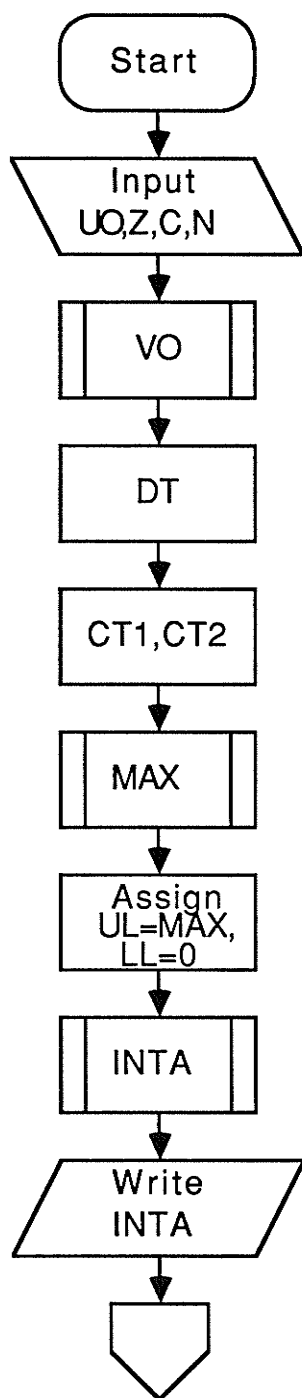
$$\begin{aligned} P(z_0 \rightarrow z) &= (1/2) \int_{-1}^1 P(z_0, \mu_0 \rightarrow z) d\mu_0 \\ &= (1/2) [\exp(-|z-z_0|/\nu_0) / T(\nu_0) + \int_0^1 \exp(-|z-z_0|/\nu) / N(\nu) d\nu] \end{aligned} \quad (10.16)$$

Numerical evaluation of this expression was carried out using the computer program IPLSIM, the flow chart of which is illustrated in figure 10.3.

10.3 ISOTROPIC POINT SOURCE

The density of light at a field point in a homogeneous infinite scattering/absorbing medium due to an isotropic point source of unit strength (see figure 10.4) can be generated from results obtained in section 10.2 using the relation

$$P_{pT}(r) = -(1/2\pi r)(d/dr)P_{pL}(r) \quad (10.17)$$



U_0 represents the direction of the incident beam, Z the perpend. distance from the source, C the scatter/absorption coefficient and N 1/2 the # of subintervals used in the composite integration performed in evaluating cont. term

The discrete eigenvalue of the Boltzman operator is calculated; subroutine CALCDE is used

The discrete term of the transport equation is calculated

Continuous term is separated into 3 sub-terms, one (CT3) being an integral; At this stage the two non-integral terms are evaluated

In evaluating CT3, interval of integration is split in two and numerical quadrature applied to each separately; **MAX**, the point at which the split is made is determined using sub. MAXI
Upper and lower limits of 1st interval of CT3 integration are set

Integral over the 1st interval of CT3 integration is calculated; subroutine COMPGQ is used.

Figure 10.2: Flow chart of the program CPLSIM.

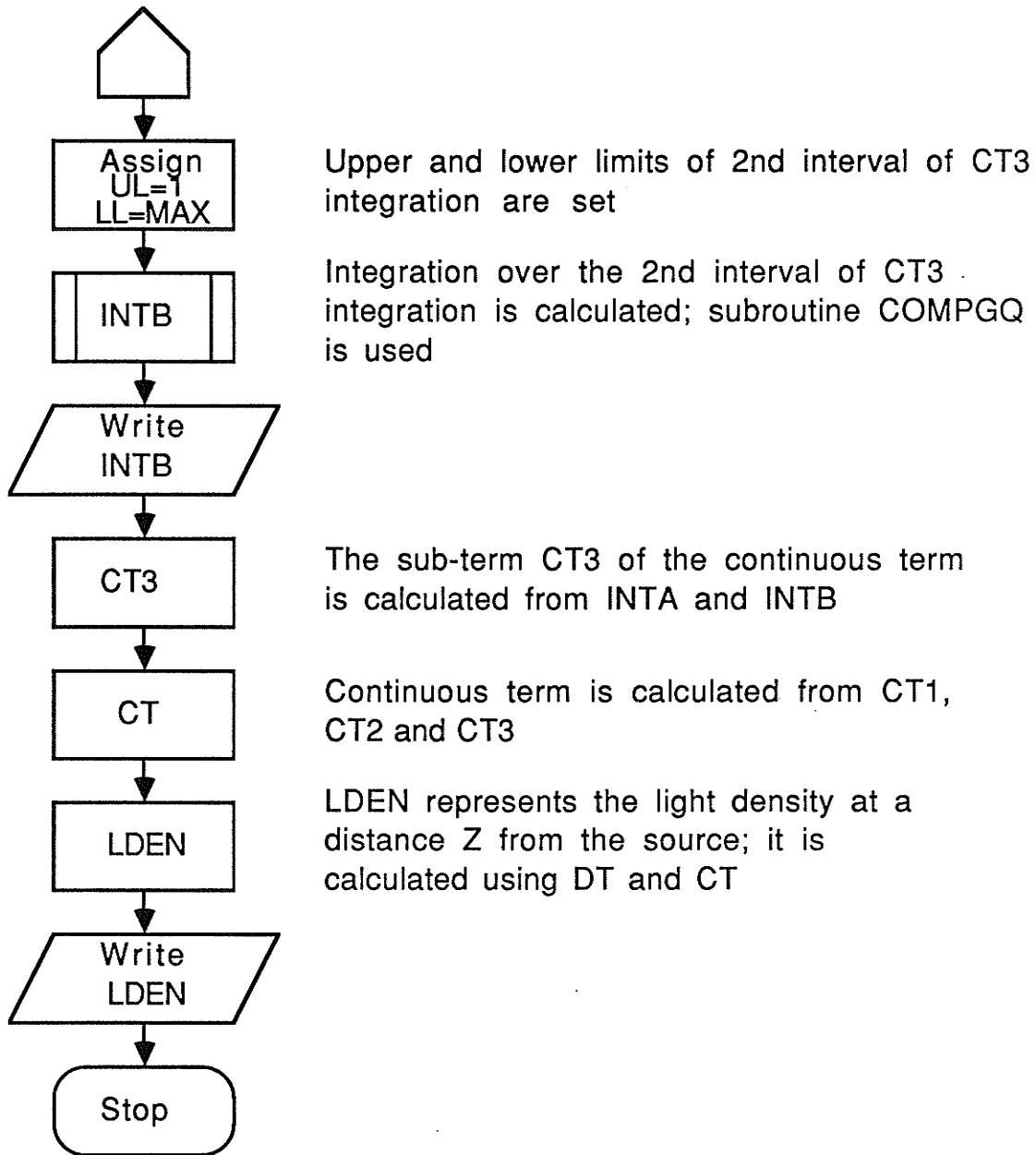


Figure 10.2: continued

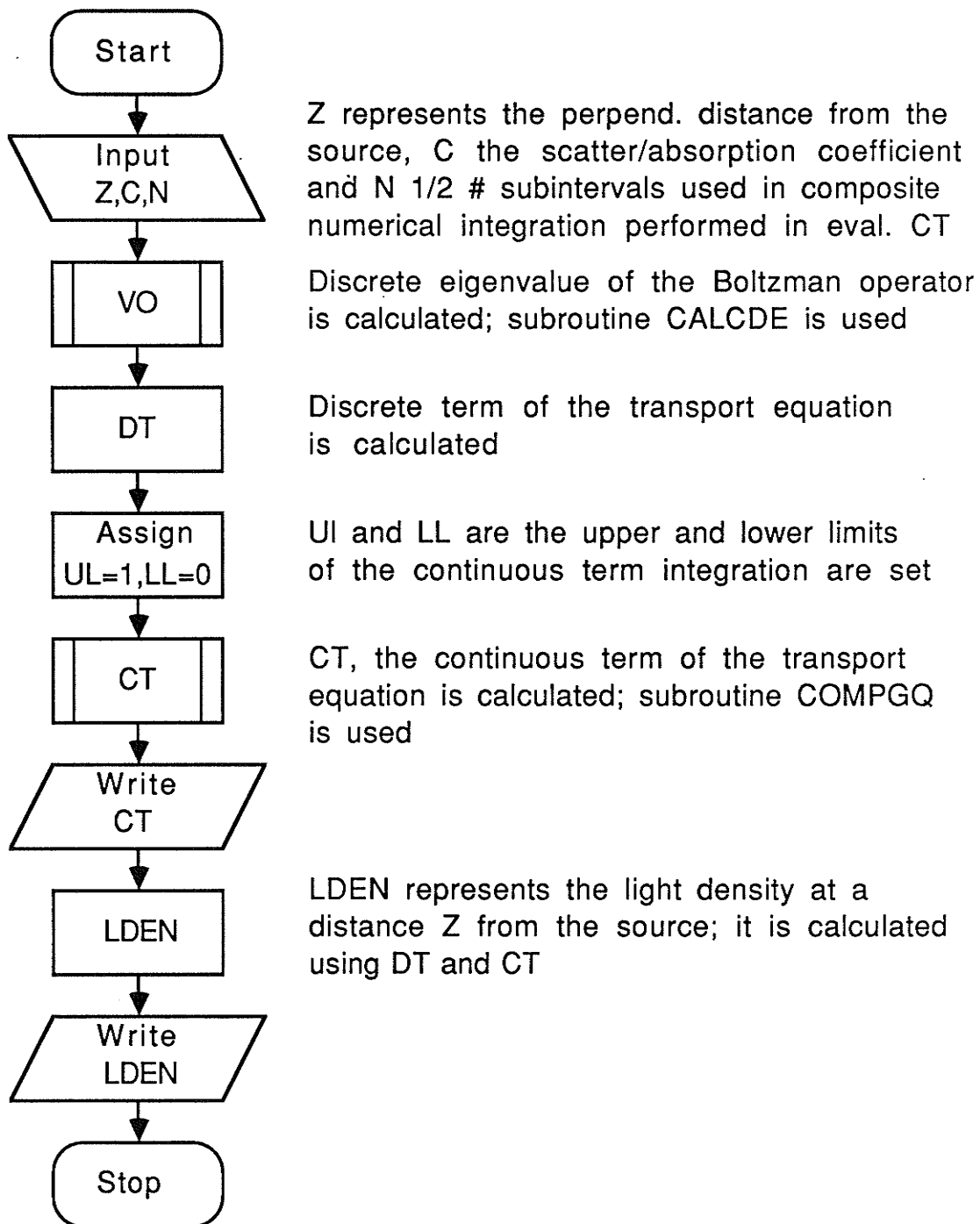


Figure 10.3: Flow chart for the program IPLSIM.

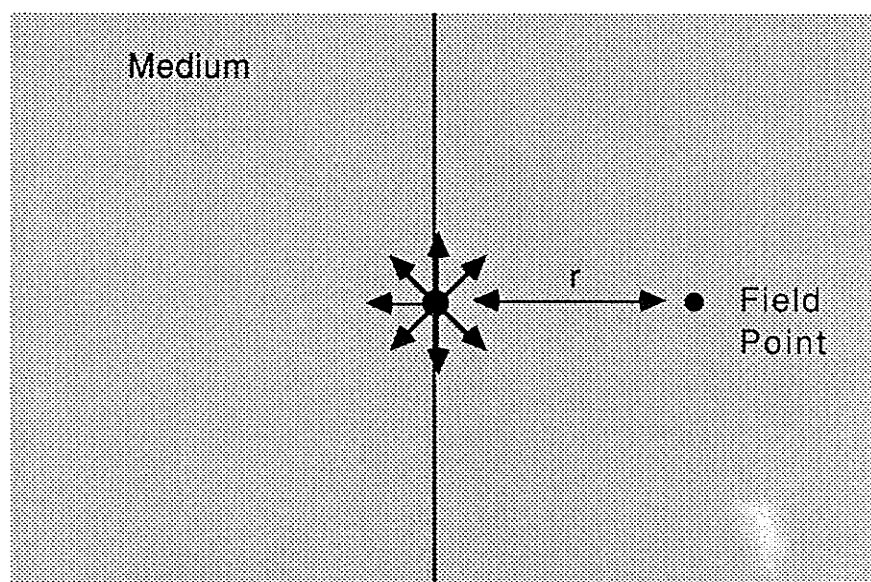


Figure 10.4: Isotropic point source irradiating within an infinitely large homogeneous medium.

where P_{ρ_L} is the density of light due to an infinite planar source. This gives

$$P_{\rho_T}(r_0 \rightarrow r) = (1/4\pi|r-r_0|) [\exp(-|r-r_0|/\nu_0)/\nu_0 T(\nu_0) + \int \exp(-|r-r_0|/\nu)/\nu N(\nu) d\nu] \quad (10.18)$$

where r_0 is the position vector of the point source.

Numerical evaluation of this expression at a particular value of r was carried out using the program IPSIM. Its flow diagram is shown in figure 10.5.

10.4 THE ALBEDO PROBLEM

A fourth irradiation geometry which can be used to gain insight into photon transport through tissue is referred to as the Albedo problem. In this geometry the scattering/absorbing medium occupies half of all space ($-\infty < x, y < +\infty$ and $0 < z < +\infty$) forming an interface with vacuum in the plane $z=0$ (see figure 10.6). Of interest is the spatial distribution of light for parallel beam irradiation of the medium from the vacuum half space. The intensity of the incident light is assumed uniform over the interface and the scattering/absorbing material homogeneous. Using the boundary conditions

$$\Psi(0, \mu) = \delta(\mu - \mu_0) \quad \mu, \mu_0 > 0 \quad (10.19)$$

$$\lim_{|z| \rightarrow \infty} \Psi(z, \mu) = 0 \quad (10.20)$$

the Linear Transport equation can be solved to yield an expression for the density of light as a function of perpendicular distance from the interface

$$P(z, \mu_0) = 2\pi [-2\gamma(\mu_0)\exp(-z/\nu_0)/c\nu_0 X(\nu_0) + (\nu_0 - \mu_0)\gamma(\mu_0) \int_0^1 \nu \phi_{\nu}(\mu_0)\exp(-z/\nu)/N(\nu)\gamma(\nu)(\nu_0 - \nu) d\nu] \quad (10.21)$$

μ_0 is the direction of the incident beam, $X(\mu)$ the well-known X-functions of Linear Transport theory and

$$\gamma(\mu) = (c\mu/2) (1/X(-\mu)(\nu_0^2 - \mu^2)(1-c)) \quad (10.22)$$

The computer program ALBEDO was used to evaluate this expression at particular values of z and μ_0 . Its flow chart is illustrated in figure 10.7.

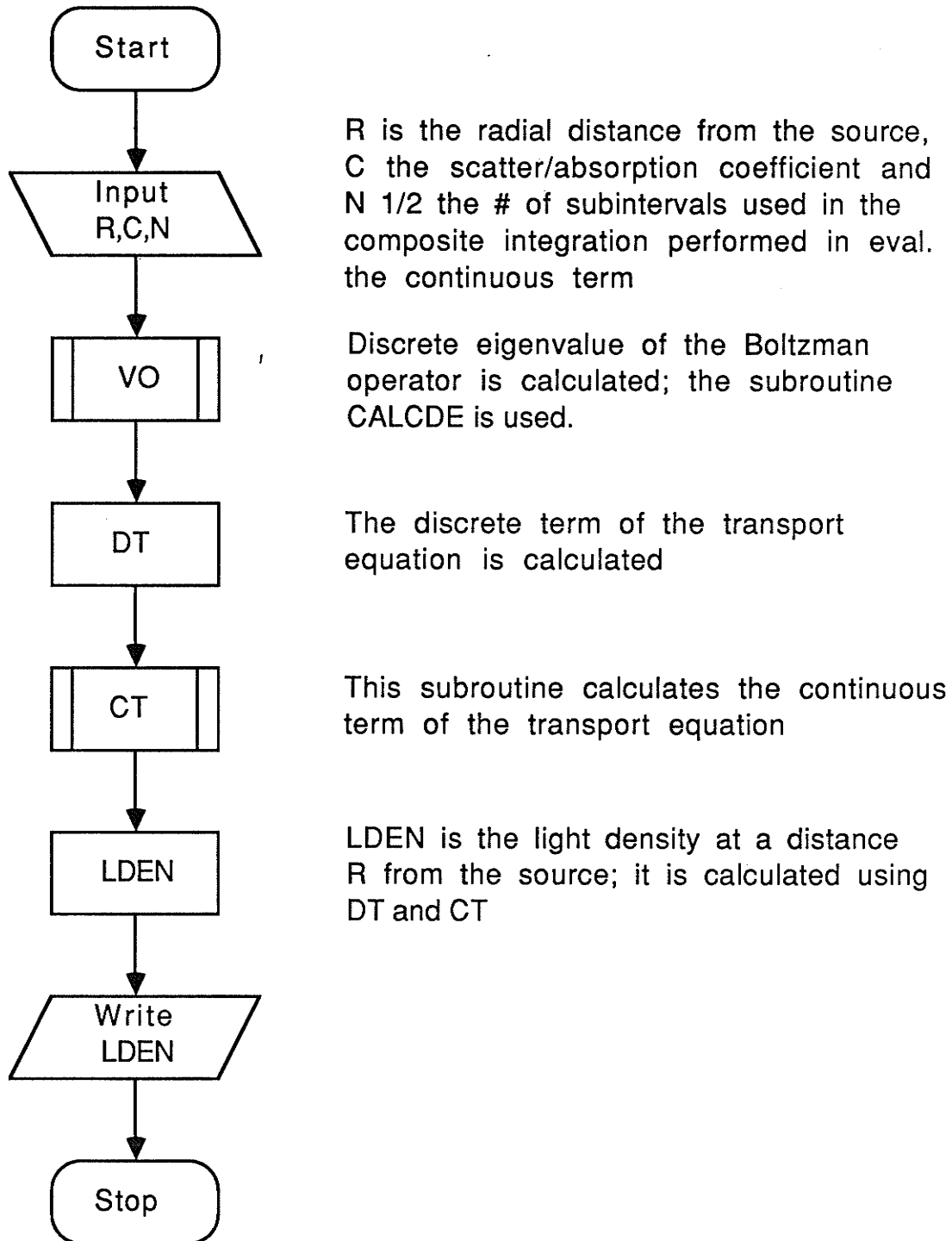


Figure 10.5: Flow chart for the program IPSIM.

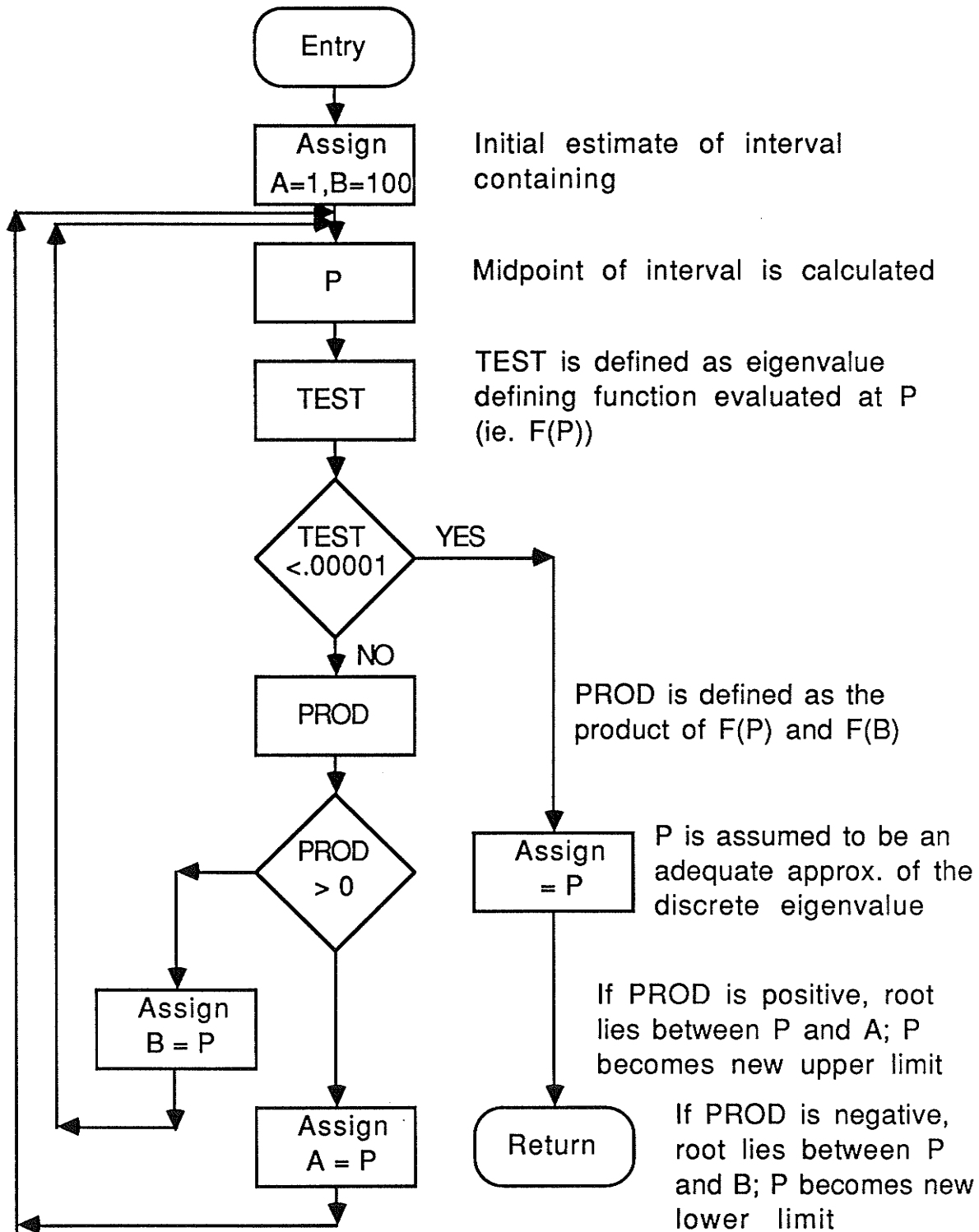


Figure 10.5B: Flow chart for subroutine CALCDE. This sub. calculates the discrete eigenfunction of the Boltzman operator by applying a bisection algorithm to the eigenvalue defining function.

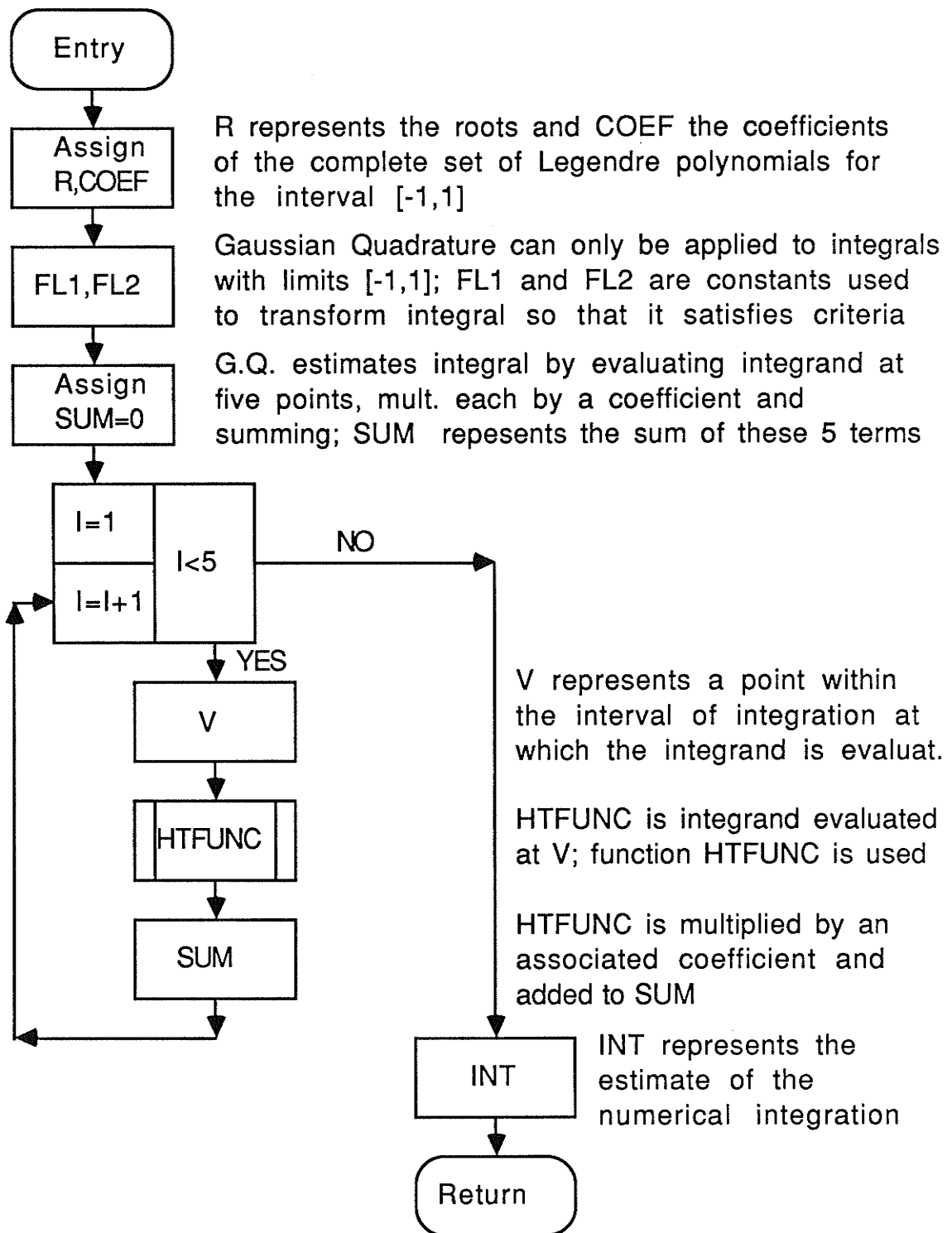


Figure 10.5C: Flow chart for the subroutine HTGAUS. This subroutine performs a numerical integration using a five point Gaussian Quadrature algorithm.

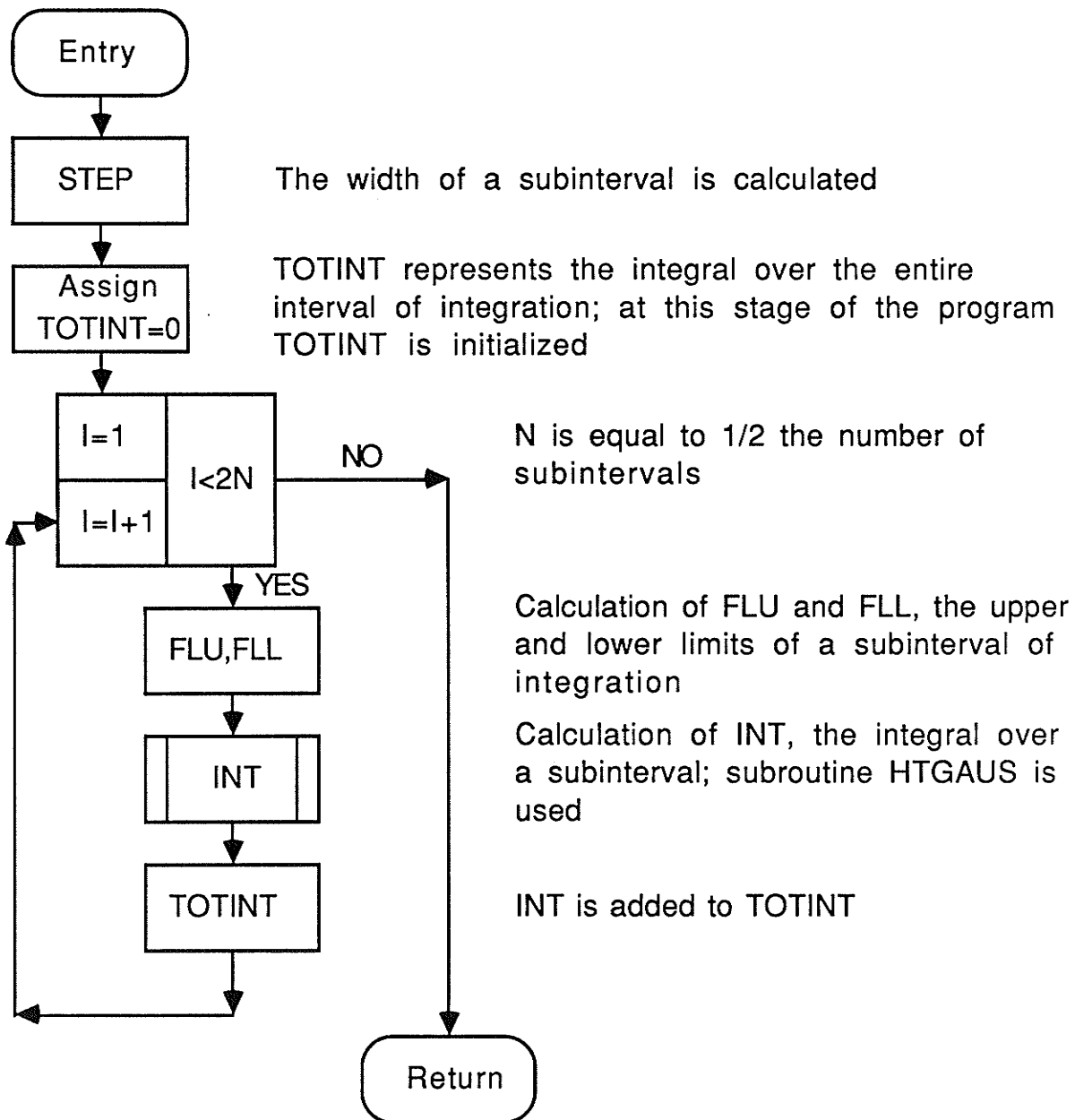


Figure 10.5D: Flow chart for subroutine COMPGQ. This sub. performs a numerical integration by applying a composite rule (ie. the interval of integration is split into a number of subintervals and a numerical integration performed over each separately - the results are then summed to give the total integral).

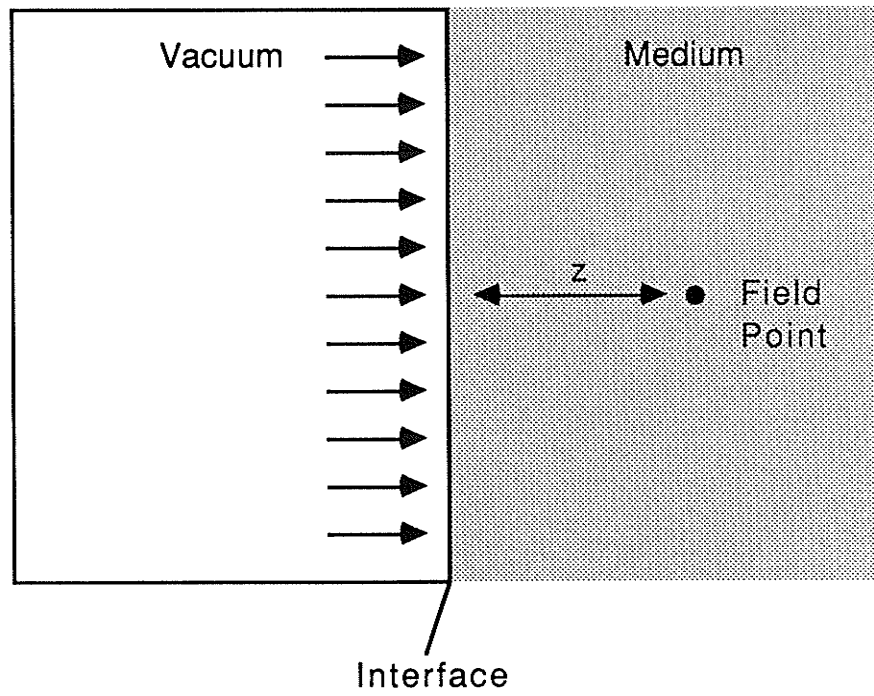
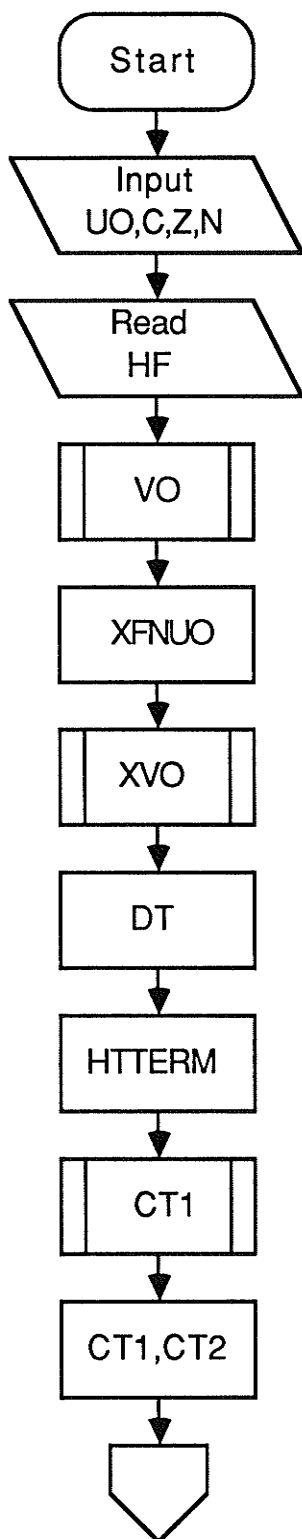


Figure 10.6: Albedo irradiation geometry.



UO represents the direction of the incident beam, C the scatter/absorption coefficient, Z the perpendicular distance from the source and $N/2$ the number of evaluation points used in the numerical integration performed in evaluating continuous term

Array containing Chandrasekhar's H-functions (evaluated at discrete points) is read from disk.

The discrete eigenvalue of the Boltzmann operator is calculated; sub. CALCDE is used

The X-function is evaluated at $-UO$

The X-function is evaluated at VO

The discrete term of the transport equation is calculated

HTERM, the term arising as a result of performing a Hilbert transformation on the continuous term integral is calculated

The continuous term of the solution is split into 3 sub terms, one of which (CT1) is an integral; subroutine CALCTA is used to evaluate it

The 2nd and 3rd terms of the split continuous term are calculated; both are non-integral terms

Figure 10.7: Flow chart for the program ALBEDO.

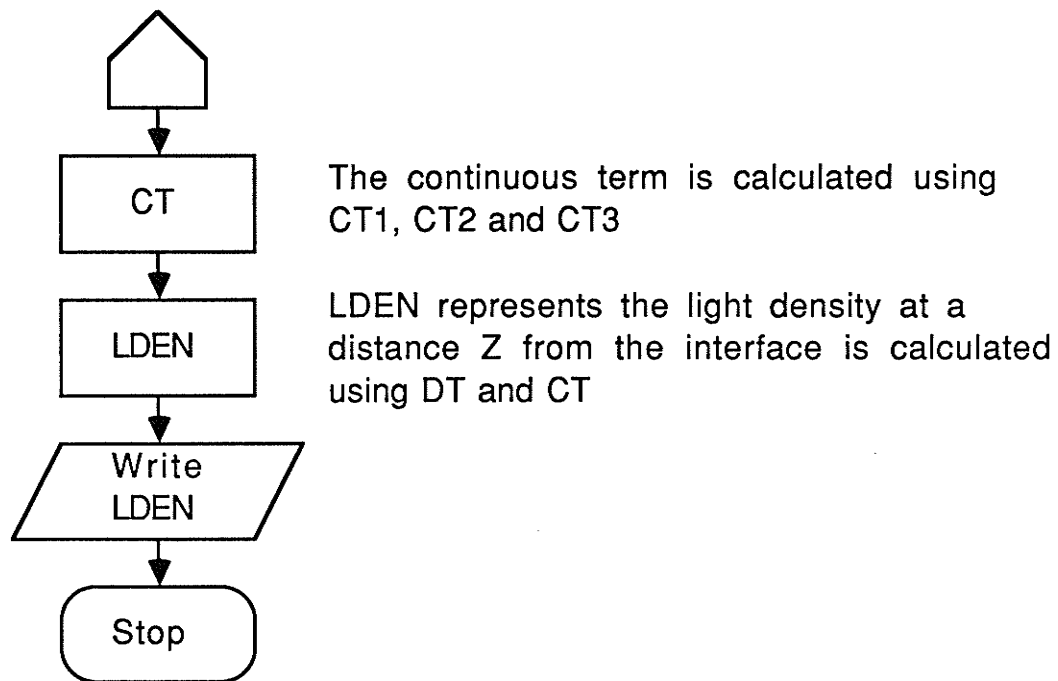


Figure 10.7: continued

10.5 THE DIFFUSION APPROXIMATION

Regardless of the irradiation geometry employed, all solutions of the Linear Transport equation will have the following form

$$P(z) = a_{0+} \exp(-z/\nu_0) + a_{0-} \exp(z/\nu_0) + \int_{-1}^1 A(\nu) \exp(-z/\nu) d\nu \quad (10.23)$$

Because $\nu_0 > 1$, the continuous term of this expression will fall to zero with increasing z much faster than the discrete terms. As a result, in regions distal to source of photons or an interface between two media of different optical properties, light density may be expressed as

$$P(z) = a_{0+} \exp(-z/\nu_0) + a_{0-} \exp(z/\nu_0) \quad (10.24)$$

Eq.(10.11) is referred to as the asymptotic form of the distribution. Substitution of this relation into eq.(9.23) shows that the asymptotic form of the Linear Transport distribution will be a solution of the Diffusion equation provided

$$\nu_0 = (D/(1-c))^{1/2} = (1/3(1-c))^{1/2} \quad (10.25)$$

Thus, Diffusion theory distributions may be generated from the exact Linear Transport solutions by setting the continuous term to zero and approximating ν_0 by eq.(10.12). For example, the spatial distribution of light within an infinitely large medium due to isotropic planar source irradiation will be given by

$$P(z_0 \rightarrow z) = (3/2) (3(1-c))^{-1/2} \exp(-(3(1-c))^{1/2} |z-z_0|) \quad (10.26)$$

For planar source irradiation geometry, Diffusion theory predicts that the density of light will fall off exponentially with distance from the source. The distance over which the Diffusion model predicts light density to drop by a factor of $1/e$ is often referred to as the diffusion length of the medium z_{DIF} . From eq.(10.13), this distance will be given by

$$z_{DIF} = (3(1-c))^{-1/2} \quad (10.27)$$

All of the Diffusion distributions presented in this thesis were generated from the exact Linear Transport solutions.

Chapter XI

SUMMARY OF THE LITERATURE

Ideally, one would like to describe the propagation of light through tissue using transport models such as Linear Transport or Diffusion theories. Once this level of sophistication has been achieved, many of the problems associated with visible and infrared light techniques may be resolved. However, application of either of the transport models discussed in chapters 8 and 9 requires that the scatter and absorption cross sections per unit volume be known for all tissue types in the human body. Any spectral dependence or variation of these parameters from one patient to the next must also be determined.

It is extremely difficult to determine experimentally the absorption and scatter cross sections of tissue. Direct measurement of these parameters require that very thin samples of tissue (less than a few tenths of a mm) be transilluminated and Beer's Law applied (see section 16.1). Besides the technical difficulties associated with producing such thin samples, these measurements often yield results which are representative of local inhomogeneities rather than the tissue type in general. Indirect measurement of the fundamental properties of tissue involves the fitting of suitable mathematical models to experimentally determined light distributions resulting from the irradiation of tissues under fixed conditions. With this technique, accurate results require that the theoretical and experimental irradiation geometries employed be identical. Often such a match is impossible to produce.

In an effort to quantify the optical properties of tissue, some authors have turned to the measurement of parameters less fundamental than absorption and scatter cross section. The most commonly used alternatives are diffuse transmittance, penetration depth and half value layer. These quantities are easier to measure and although they do not supply the information required to apply theoretical transport models, they do yield a great deal of insight into the underlying principles upon which light propagation in tissue is based. For example, measurements of any one of the three may be used to answer such questions as "What wavelengths of light are associated with the highest transmittance through tissue?", "How does propagation vary from one patient to the next?" and "Is light transport

through some tissues more efficient than in others?", all of which are important in the optimization of Photodynamic Therapy and Diaphanography. However, it is important to note that diffuse transmittance, penetration depth and half value layer are not true fundamental properties and will be dependant on the geometrical set-up used in their measurement (ie. on tissue sample thickness and collection angle of the detector).

Attempts to experimentally quantify the optical properties of biological tissue have been limited, both in terms of the measurement of interaction cross sections and less fundamental parameters. Most studies which have been carried out have been done so on animal tissues. A brief summary of the work carried out to date is presented in the following paragraphs.

11.1 DIFFUSE TRANSMITTANCE

The parameter used most often to quantify the optical properties of tissue is diffuse transmittance (see chapter 12 for a discussion of the subtle difference between diffuse transmittance and true transmittance). Ertefai et al. [29] measured the diffuse transmittance of three types of female breast tissue, glandular, adipose and carcinoma, over the spectral range 600 to 1060 nm. The three resulting spectral curves were found to be quite similar in shape. All were characterized by a sharp increase in transmittance from 600 to 700 nm. Between 700 and 900 nm, diffuse transmittance exhibited almost no dependance on wavelength. Minima were observed at 970 and 760 nm (the latter being much weaker), both being attributed to absorption by water. In spite of these similarities, slight variations in shape were found to exist. For example, adipose tissue exhibited neither of the water-related minima. In contrast, the magnitude of the diffuse transmittance curves of the three tissue types differed significantly. Carcinoma exhibited a much lower transmittance at all wavelengths than glandular tissue which in turn transmitted light less efficiently than adipose. Similar results were obtained by Bolin et al. [30] for measurements on bovine adipose, striated skeletal muscle, lung, heart, kidney, liver and pancreas.

Of particular importance to Photodynamic Therapy is the variation in optical properties between similar tissue types removed from different patients. If differences are negligible, mathematical models used to predict the spatial distribution of light during a treatment may employ absorption and scatter cross sections (the two input parameters required by most mathematical models) which are universal (in that they depend on tissue classification and

not patient). Then cross sections need only be determined once for each tissue type and considered appropriate for all patients. If however, the optical properties of tissue are found to differ markedly from one patient to another, any application of theoretical models in Photodynamic Therapy would require that absorption and scatter cross sections be determined for each patient treated. Thus, results of patient variation studies will have a great effect on clinical Photodynamic Therapy in the future. Wan et al. [31] have published diffuse spectral transmittance measurements which suggest that universal absorption and scatter coefficients are not appropriate. Using a flood lamp source and a radiometer detector, these authors carried out transmittance measurements on six different human cadavers immediately post mortem, specifically concentrating on skull, brain, chest wall, abdominal wall and scrotum. Substantial differences in attenuation were found to exist between similar tissue types of different cadavers. Most, but not all, of these variations were attributed to differences in tissue thickness. Quite surprisingly, skull transmittance was found to be similar to that of soft tissue. Wilson et al. [32] also noted variations in the optical properties of similar tissue types removed from the brain of different rats (although the concept of penetration depth rather than diffuse spectral transmittance was used to quantify these changes). However, it was not obvious whether these differences were genuine characteristics of the tissue or as a result of damage during measurement.

Preuss et al. [33] concluded from measurements of diffuse spectral transmittance on bovine skeletal muscle (over the range of 400 to 1100 nm) that a very large portion of tissue attenuation is due to remittance, the back scatter of light photons through the entrance face of the sample. Its contribution to attenuation was much higher for adipose tissue than for muscle. However, the fraction of non-remitted light transmitted through tissue is much greater in the case of the former. As remittance will also be observed at tissue-tissue interfaces, a beam of light will experience significant attenuation in passing across a boundary characterized by an abrupt change in optical properties. Preuss et al. also found that small changes in the thickness of a tissue sample would greatly alter both the magnitude and shape of the measured diffuse spectral transmittance curve. For example, the curve for an 11.4 mm thick sample of bovine skeletal muscle was characterized by two minima (at 775 and 950 nm) which were attributed to absorption by water. However, besides being reduced in magnitude, the spectral extinction curves obtained for 1.5 and 3.3 mm thicknesses of muscle (removed from the same specimen) exhibited no such minima. Adipose content was also found to affect both the shape and magnitude of the muscle sample spectra.

In an attempt to explain the formation of Diaphanography images, specifically the range of colors Ohlsson obtained through infrared photography, Watmough [21] measured the diffuse spectral transmittance of normal, benign and neoplastic samples removed from the female breast. In all, seven samples were examined over the range 400 to 900 nm. No characteristic differences were observed between the spectra of the three tissue classifications and Watmough concluded that it is not the optical properties of the tissues themselves that is responsible for the formation of Diaphanography images. However, the presence of hemoglobin absorption bands (575, 540 and 412 nm) in the spectra of all samples studied suggested that it may be variations in blood content between tissue types that is the primary underlying mechanism of diaphanography. To prove this hypothesis, Watmough measured the diffuse spectral transmittance of red blood cell suspensions over a wide range of concentrations (from 1:2000 to whole blood). Each dilution was shown to possess its own characteristic lower wavelength limit below which it transmitted no light. For low concentrations, no cut-off existed while for a medium dilution, this lower wavelength resided in the blue. As concentration was increased further, the cut-off moved into the red. These results imply that blood samples of different concentrations will yield images of different colors when transilluminated and subsequently photographed with color infrared film. Watmough concluded that it was indeed variations in blood concentration between different pathological conditions that was responsible for each possessing its own characteristic color in a Diaphanography image.

11.2 PENETRATION DEPTH

A second parameter often used to quantify the optical properties of biological tissue is that of penetration depth. A number of authors [34,35] have found that the intensity of a collimated beam of light propagating through a thick slab of tissue will fall off in an almost exponential fashion with distance travelled. Hence, the ability of light to propagate through a particular type of tissue can be defined as the thickness required to reduce a collimated beam to $1/e$ of its initial intensity. This thickness is referred to as the penetration depth of that tissue.

Powers et al. [35] studied the effect of the photosensitizing drug HPD on penetration depth in tissue. The results of this study are quite important to the clinical application of Photodynamic therapy. The presence of HPD will serve to shield distant tissues by increasing the effectiveness with which light is removed from the

incident beam. Thus, although increasing the concentration of a photosensitive drug increases the probability that light reaching any point in the tissue can be used to induce necrosis, the resulting poor penetration may inhibit an adequate amount of radiation from reaching distal regions of a large tumor and thereby actually reduce the effectiveness of treatment. Measurements of penetration depth were performed in vivo on the unsensitized brain tissue of anesthetized rats, at both 488 and 633 nm (the latter being the wavelength at which clinical Photodynamic treatments are carried out). Estimates of this parameter were also obtained for brain tissue treated with HPD at 633 nm. Results from these experiments indicate that the penetration depth of normal rat brain is 3.4 and 4.9 mm for blue green and red light, respectively. HPD was shown to reduce the penetration depth of 633 nm light to 3.8 mm, a value very similar to that for blue-green light in normal tissue. It is quite clear that when dealing with light transport in tissue, one must take into account not only attenuation by tissue but also any photosensitizer present.

To date, most experimental measurements of the optical properties of tissue have been carried out in vitro, on samples excised from specimens post mortem. The question then arises "Do these post mortem values accurately reflect the optical properties of tissue in vivo?" Wilson et al. [32] utilized the concept of penetration depth to examine this question. Three types of tissue were studied, brain (pig), muscle (rabbit) and liver (rabbit), chosen so as to provide a wide range of absorption and scatter properties. Results obtained by Wilson et al. suggest that significant changes in the optical properties of tissue may take place at all wavelengths immediately post mortem. In muscle and brain, the low penetration depth observed at 425 nm in vivo was considerably increased post mortem. In addition, the double minima around 540 and 575 nm were replaced by a single band at 550 nm. Penetration depth in the vicinity of this 550 nm minimum was also increased. These changes were attributed to the deoxygenation of blood upon death. HbO_2 will exhibit characteristic absorption bands about 540 and 575 nm. Hb, meanwhile, possesses a single absorption band about 550 nm. Above 600 nm, the penetration depth of muscle was found to increase immediately post mortem, although similar changes were not observed in brain tissue. At these wavelengths, hemoglobin shows very little absorption so that changes in the optical properties of tissue cannot be attributed to the deoxygenation of blood. In this instance, changes in blood concentration (and therefore, scatter by red cells) may be responsible. In contrast, no changes were noticed in the optical properties of liver. This was attributed to the fact that attenuation of light in liver is primarily by pigments. As such, changes due to variations in blood content or oxygenation are masked.

Svaasand et al. [36] carried out measurements of the optical penetration depth of five human brain tissue samples, two neonatal and three adult, one to two days post mortem. Penetration depth was found to increase rapidly with wavelength between 488 and 710 nm. Above 710 nm, this parameter showed almost no dependence on the wavelength of light. Typical penetration depths for the adult brain are .4 to .7 mm for blue and green light, 1.2 to 1.6 mm for red and 2.9 to 4.3 mm for infrared. The attenuation of light in adult brain was attributed to scattering by myelin and absorption by hemoglobin. It is also interesting to note that the penetration depth of adult brain was found to be three to five times smaller than that for neonatal tissue at all wavelengths. This phenomenon was thought to be as a result of incomplete myelination in the neonatal brain.

11.3 HALF VALUE LAYER

Half value layer is defined as the thickness of tissue required to reduce the intensity of a collimated beam of light to 1/2 its original value. Preuss et al. [37] have made measurements of HVL for skeletal muscle, adipose tissue, liver and kidney using laser light of 632 nm. Results were as follows: 1.0 mm for muscle, 2.0 mm for adipose tissue, .65 mm for liver and .75 mm for kidney.

11.4 APPLICATION OF TRANSPORT MODELS

The use of mathematical transport models to describe the propagation of light through biological tissue has been quite limited. The following is a brief summary of the progress made to date.

Svaasand et al. [38] used diffusion theory to model the propagation of light in a number of diseased brain tissues, including four gliomas, one meningioma and one metastasis. Tumors with volumes typically 0.1 to 0.2 cm³ were embedded in normal white matter brain tissue to yield specimens ranging from 5 to 10 cm³ in size. Each sample was then irradiated interstitially using a single optic fiber (coupled to one of three lasers) placed at the center of the tumor tissue. A second single optic fiber was coupled to a detector and used to measure the light intensity as a function of distance from the source along the optical axis. Central axis distributions were obtained at three wavelengths, 514, 635 and 1060 nm for all four tissue types. Svaasand et al. then made the assumption that the distribution of light in these tumor samples would become isotropic within a few mm of the optic fiber source. This

enabled the authors to employ the diffusion approximation, specifically to fit the diffusion equation applicable to a point source in an infinite medium to each set of data (data points proximal to the source were neglected). In all cases, diffusion theory was found to provide a very good fit to the experimental data and permitted the determination of experimental diffusion lengths. For meningioma, diffusion lengths of 5.4, 1.8 and 0.8 mm were observed at wavelengths of 1060, 635 and 514 nm, respectively. The gliomas were found to possess substantially smaller diffusion lengths, typically 3.0, 1.7 and 0.5 mm for the same series of wavelengths.

The ability of diffusion theory to describe the propagation of light in biological tissue was also examined by McKenzie [39]. In this study, a single optic fiber/detector assembly was used to measure the density of light as a function of position within a slab of bovine muscle irradiated with a 1 mm diameter external beam from a 633 nm He-Ne laser. Slits cut in the tissue with a scalpel allowed for movement of the detector probe through the solid tissue mass. The data collected were used to construct a series of light density isodose curves. These curves were found to be concentric semi-circles centered about the point at which the light entered the tissue. This result suggests that scatter in tissue is strong and that the distribution of light will become diffuse within a very short distance of the entrance surface. In other words, light transport in bovine muscle tissue appears to be a diffusion process. McKenzie fit the diffusion equation applicable to a point source in an infinite medium to the data collected along the central beam axis using linear regression analysis. A diffusion length of 1.7 mm was obtained.

To effectively treat a resection cavity using Photodynamic principles, the entire cavity must be uniformly exposed to light. To facilitate such treatments, Wilson et al. [40] developed a specialized light source, its clinical application providing the authors with an opportunity to measure the diffusion length of human brain tissue in vivo. The light source applicator consisted of a balloon fastened to the end of a single optic fiber. The opposite end of the fiber was coupled to a 7.5 watt argon laser. To treat with this applicator, the balloon was placed in the resection cavity and inflated with a homogeneous, pure scattering liquid (Nutralipid) to occupy the same volume as the removed tissue. The Nutralipid served two purposes. Firstly, it controlled cavity shape; if a cavity were to collapse during treatment, a portion of the target tissue would be shadowed from the light source and as a result, receive an inadequate exposure. Secondly, the Nutralipid was responsible for smoothing the highly forward directed output of the fiber optic/laser assembly. Scatter was sufficient to ensure that

the intensity of light exiting the applicator was constant over the surface of the balloon. It was during the clinical application of this specialized light source that Wilson et al. performed in vivo diffusion length measurements. A single optic fiber, placed in a biopsy needle and coupled to a photometer, was inserted into brain tissue undergoing Photodynamic therapy with the cavity applicator. Light flux readings were then made as the detector was moved radially inward towards the balloon. Because scattering within both the applicator and brain tissue is very high, Wilson et al. assumed that diffusion theory would adequately describe the propagation of light in this situation. The diffusion equation applicable to an isotropic point source within an infinite scattering/absorbing medium was fitted to the light density versus tissue depth data to yield diffusion lengths of 4.1 and 4.9 mm for the two patients studied.

Diffusion theory will break down when absorption is significant, near an interface or in the vicinity of a source. It is also difficult to incorporate real geometries (both source and sample) when using this model. In an effort to deal with light transport under conditions more representative of those encountered in clinical PDT, Wilson et al. [41] has suggested a Monte Carlo approach be used. In this technique, a computer is used to simulate a light beam as it travels through a medium, the history of each individual photon being traced. Distributions due to two source geometries were simulated, an external parallel beam of light of diameter B and an implanted optic fiber of numerical aperture N . Light density distributions were constructed with 10,000 photons. Wilson found that for external irradiation of a medium exhibiting strong absorption, the isodose distributions were almost cylindrical in shape. As scatter within the medium increased, the distributions became more isotropic with regions outside the geometric edge of the incident beam receiving significant exposures. For internal irradiation (implanted fibers) of media exhibiting significant absorption, the shape of the isodose curves were found to depend strongly on numerical aperture. This was not the case for scatter dominant materials.

Profio et al. [42] have used Linear Transport theory to determine the density of light as a function of depth in an infinite slab, 10 mean free paths thick, irradiated with a collimated beam of light of unit power density and normal incidence. Distributions were obtained for slabs characterized by various scatter/absorption ratios. Isotropic scatter and non-reflective boundary conditions were assumed. For a medium in which absorption is the dominant mode of interaction, light density was found to decrease exponentially with depth. In this case, penetration depth was equal to the mean free path length in the slab.

For a slab in which scatter is dominant, light density was found to be increased at all depths. This was due to the fact that photons undergoing interactions with the medium are not destroyed, only re-directed. As a result, photons will continue to move through the slab, undergoing successive scatters, until they reach the exit face or experience a very low probability absorption. Perturbations in the photon density were also found to exist at the boundaries when scatter was the dominant mode of interaction. This is a result of the slab being bounded on either side by a non-scattering medium. Once a photon leaves the slab, there is no chance of it being scattered back in. Thus, points near the boundaries will receive back scattered photons from a much smaller volume than those far removed from the slab interfaces. As a result, light density was found to assume a maximum at some distance from the entrance surface rather than at the entrance surface itself (as in the case of high absorption). Profio et al. demonstrated that this maximum will move towards the entrance surface as the scatter/absorption coefficient associated with the slab decreases. In regions removed from either boundary and in the presence of strong scatter, light density was once again found to decrease exponentially with depth. However, penetration depth was several times larger than the mean free path length, the difference between the two becoming more marked with increasing absorption/scatter coefficient.

Wilson et al. [2] obtained theoretical light density distributions for an infinite planar slab (10 mean free paths thick), irradiated with a collimated beam of infinite area and normal incidence, using four different mathematical models: linear transport theory, Kubelka-Munk methods, diffusion theory and Monte Carlo techniques. Results were obtained for slabs possessing scatter/absorption coefficients of .99 and .90. The linear transport distribution was assumed to be exact. Distributions obtained using diffusion theory, Monte Carlo techniques and the Kubelka-Munk methods were all found to differ from that of linear transport theory near the interfaces with the Kubelka-Munk model proving to be the least accurate.

Very few measurements of attenuation cross section per unit volume have been carried out. Profio et al. [42] determined the attenuation cross section per unit volume for lung tissue over the visible spectrum. Values were obtained from transmittance measurements on thin slabs of lung tissue (100 μ thick). The attenuation cross section per unit volume was found to vary from 9000 m^{-1} (.11 mm mean free path) in the violet to 5000 m^{-1} (.20 mm mean free path) in the red. Although not measured, estimates of the absorption cross section per unit volume were made by assuming blood to be the principal absorber in lung tissue and that its concentration was normal. A value of 4600 m^{-1} was obtained

for violet light. These cross sections were then used to calculate the scatter/absorption coefficient of lung tissue for short wavelength visible light; a coefficient of 0.5 was obtained. In the red region of the visible spectrum, Profio et al. assumed absorption by hemoglobin to be negligible (implying a scatter/absorption coefficient approximately equal to 1.0 at these wavelengths). Marynissen and Star [43] arrived at values of 4300 and 8300 m^{-1} for the attenuation cross section per unit volume of chicken and bovine muscle, respectively (red light).

Chapter XII

QUANTIFYING THE OPTICAL PROPERTIES OF TISSUE

One quantity often used to characterize the optical properties of biological tissue is that of diffuse spectral transmittance. This quantity can be determined using the set-up of figure 12.1. A large collimated beam of light of intensity I_0 is incident upon a slab of tissue of known, uniform thickness, d . The detector serves to measure the intensity of the light exiting the sample $I(d)$. Diffuse transmittance is then defined as the ratio

$$T = I(d)/I_0 \quad (12.1)$$

One must keep in mind the distinction between diffuse transmittance and true transmittance. A measurement of the latter requires that only light photons exiting the sample in the direction of the incident beam be detected; in other words, only those passing through the tissue without having interacted are to be collected. This, however, cannot be achieved in practical experiments.

All physical detectors will pick up a certain fraction of those photons which have undergone interactions. The reason for this is two-fold. Firstly, a physical detector, regardless of its construction, will possess a finite collection angle as illustrated in figure 12.1. This will result in the collection not only of photons exiting the sample along the optical axis, but also those which are scattered at small angles to this direction. In figure 12.1, all photons scattered at angles less than or equal to γ will be detected; γ is referred to as the collection half angle. The direct result of a finite γ is the collection of a greater number of photons and transmittance measurements will, in general, be larger than true sample transmittance.

When measurements are carried out on tissue samples of "reasonable" thickness (ie. on specimens of thickness greater than a few tenths of a millimeter) a second factor becomes important in limiting one's ability to determine true transmittance. Due to the very high density of interaction centers in tissue, all specimens greater than a few tenths of a mm in thickness must be classified as multi-scattering media. In other words, when transmittance measurements are carried out on such samples, there will be

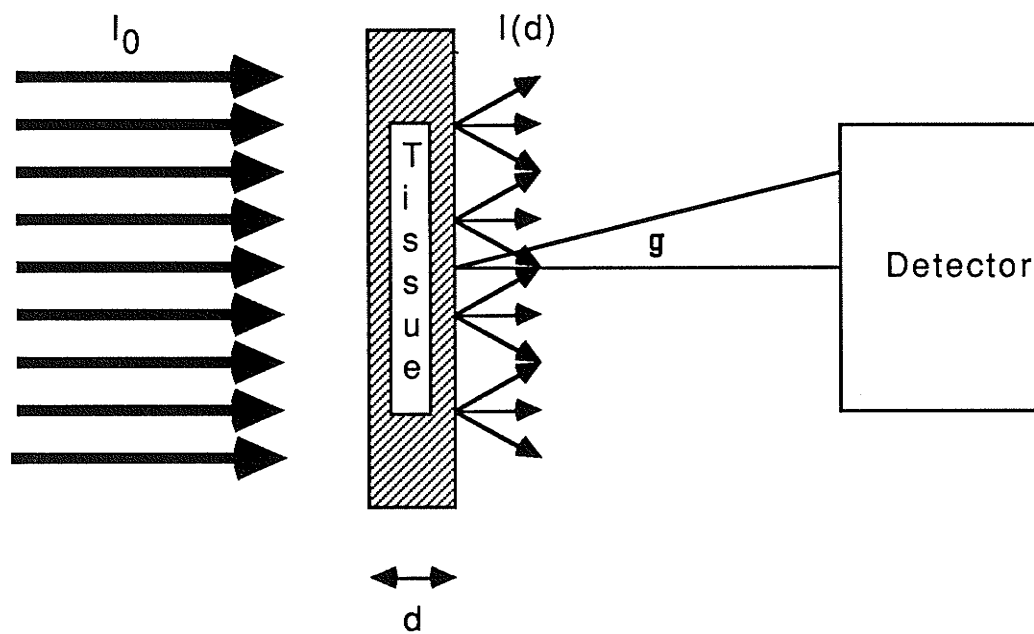


Figure 12.1: Experimental setup for measuring diffuse spectral transmittance.

a very high probability that photons exiting the medium will do so only after having undergone more than one interaction. The possibility then exists for photons which have been scattered out of the solid angle of collection of the detector to be scattered back in (as a result of a subsequent interaction). Once again, the detector reading is augmented by a fraction of the photons having taken part in interactions. Transmittance measurements carried out on multiple scattering samples with a finite angle of collection detector will therefore differ from the true transmittance; these measured values, so as to distinguish them from true transmittance, are referred to as diffuse transmittance.

Because biological tissue is inhomogeneous, great care must be taken to ensure that diffuse transmittance measurements are representative of a tissue type in general, and not of some local fluctuation in composition. To ensure representative values, two steps may be taken. Firstly, measurements should be carried out on thick specimens. Although the beam of light passing through the sample will still encounter inhomogeneities, the probability is much higher that the average composition along its path will be more representative of the general characteristics of the tissue type. Secondly, an average should be obtained from a large number of repeat diffuse transmittance measurements.

From the above discussion one concludes that there are a number of important characteristics which any instrument used to measure the diffuse transmittance of a biological tissue sample should possess. Because measurements should be carried out on thick samples which tend to greatly reduce the intensity of the beam used for transillumination, the detection system must be able to measure very low transmittances. Also, the instrument should enable a large number of repeat measurements to be carried out quickly and with relative ease.

12.1 DICOM-8 IMAGING SYSTEM

A system exhibiting the above characteristics has been developed at the Manitoba Cancer Treatment and Research Foundation for measurement of the diffuse transmittance of biological tissues. It is known as the Digital Imaging Computer 8 (DICOM-8) and its main components are illustrated in figure 12.2. The tissue sample is placed in a holder, positioned between a light source and detector, and transilluminated.

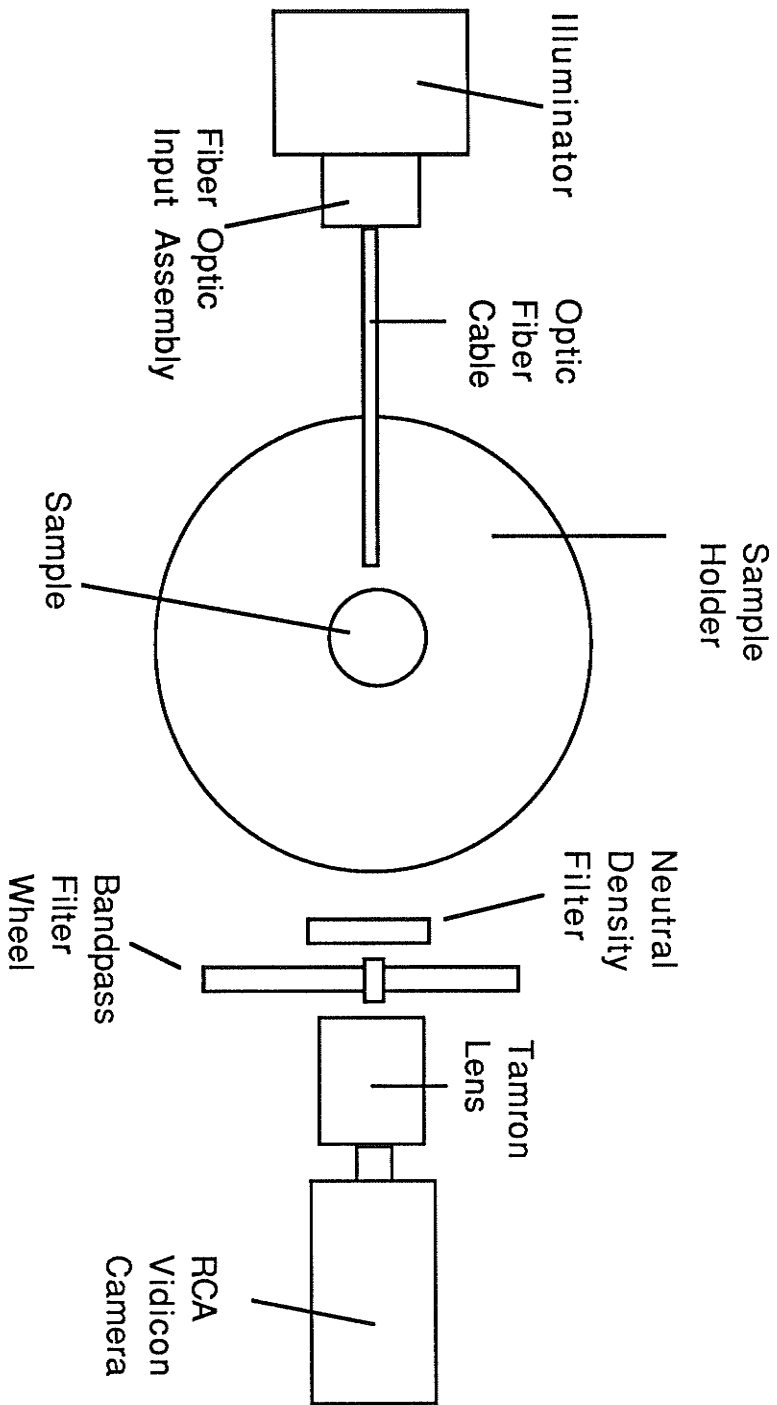


Figure 12.2: The DICOM-8 spectrophotometer.

The light source assembly is manufactured by Oriel, the main component of which is a 100 watt quartz tungsten halogen lamp mounted in a rugged blower cooled housing (referred to as the illuminator). This lamp generates an intense, continuous spectra of high stability in the visible and near infrared. An f/1 fused silica condensing lens inside the housing focusses the lamp output to produce a 35 mm diameter collimated beam. This broad beam of light then enters the second component of the lamp system, the fiber optic input assembly. It functions as a coupling between the illuminator and an optic fiber cable, focussing the broad beam output of the former onto the entrance face of the latter by means of a f/1.5 fused silica lens. The final component, the fiber optic cable, transports the visible and infrared radiation to the tissue sample. The cable consists of an incoherent (energy transfer) bundle of glass fibers protected by a stainless steel sheathing. The glass fiber bundle has a diameter of 3.2 mm and a numerical aperture of 0.55 (acceptance angle of 68 degrees). Transmittance is over the range 380 to 1300 nm. The light assembly was used to irradiate samples contained in 0.8 cm dia. glass tubes. To restrict the output beam to the central area of these samples, an opaque plastic cap with a narrow slit opening (2.9 x 20.0 mm) was placed over the exit face of the fiber optic cable. It should be pointed out that the light source used in the DICOM-8 system was not, in the strictest sense, collimated. The effect of using a non-collimated beam was, however, negligible due to the fact that measurements were carried out on very thick samples (0.8 cm). All light photons exiting such samples would have done so only after undergoing a very large number of scatter interactions, making it impossible for the vidicon camera to receive any information regarding source collimation.

The detector is an RCA 4532/H, 1' Low Bloom Silicon Target Vidicon with separate mesh and magnetic focus. Sensitivity, in terms of faceplate illumination, is .002 fc. while the signal to noise is better than 43 dB. The camera lens is a Tamron TV Zoom of f=12.5/80 mm. The detector was positioned 18 cm from the holder (measured from the front of the lens) and focussed on the rear face of the sample. The automatic gain control of the camera was switched off.

The sample is transilluminated with light from the optic fiber - lamp assembly and the output signal from the vidicon detector digitized and displayed on the DICOM-8 computer. This computer is based on a 4 MHz Z80-A microprocessor (Matrox ZBC-80 CPU board). Imaging hardware consists of an 8-bit video acquisition and display board (Matrox VAF-512), two 512x512x8 bit video refresh planes (multiple Matrox RGB-graph/64 boards) and a control card (MCTRF VAU-512) for multiplane manipulations and real time arithmetic and logic operations. The 8-bit capabilities of the video display

planes implies that digital image brightness will be displayed in terms of grey levels ranging from 0 to 255. The actual grey level associated with an image or portion of an image will depend on the brightness of the object being examined by the camera. Because this object is, in fact, the exit surface of the transilluminated specimen, image grey level will contain information pertaining to sample transmittance. A computer algorithm has been developed which extracts this information and converts image grey level to sample extinction (defined as the logarithm of the inverse of transmittance). A more detailed discussion of the calibration system is given in section 12.2.

Transmittance is studied at select wavelengths over the visible and near infrared by employing bandpass interference filters (obtained from Melles-Griot). These filters are multi-layer thin film devices which transmit over a narrow wavelength interval while at the same time rejecting the passage of light at both larger and shorter wavelengths. Filter operation is similar to that of a Fabry-Perot interferometer, their actual transmittance characteristics being determined by the nature of the interference among reflections at the many thin film boundaries. Filters were employed which isolate bands about the wavelengths 550, 600, 650, 700, 750, 800, 850 and 900 nm. The visible filters (550 to 700 nm) possessed bandwidths of 40 nm, the infrared (750 to 900 nm) 10 nm. A wheel capable of holding seven filters at any one time was mounted on the front of the camera to allow for ease of wavelength selection. Because both the bandwidth and central wavelength spacing of the Melles-Griot filters were rather large, resolution of the DICOM-8 system was poor. As such, detail in measured tissue spectra was coarse. Nonetheless, much insight was gained into the spectral dependence of light transport through tissue using this system (see chapter 13). In addition, these tissue measurements were more than adequate as a basis for the construction of a tissue equivalent material (chapter 14). As synthetic materials cannot be expected to simulate the fine spectral details of biological tissue, high resolution measurements are not required.

The useful range of the camera is increased by employing neutral density filters (positioned in front of the camera) and f-stop adjustments. Both serve to reduce the light level incident upon the entrance face of the vidicon to the extent that it falls within the range of camera sensitivity. This, in turn, enables a meaningful video output signal to be generated (and subsequently digitized and mapped to an extinction value) from an input light level which would otherwise result in saturation. The calibration procedure then adjusts the resulting extinction value to account for the f-stop adjustments and/or the presence of neutral filters. These two light reduction procedures enabled the

measurement of sample extinctions over the range 0.0 to 5.6 at 700 nm. This extinction range will vary with wavelength due to spectral variations in lamp output and vidicon sensitivity.

The Tamron lens used in the DICOM-8 system possessed f-stops from 1.8 to 22. However, only full stops between 2.8 and 11 were utilized, theoretically enabling camera entrance light intensity to be reduced by factors of 2, 4, 8 and 16.

The neutral density filters employed were manufactured by Melles-Griot for use over the spectral range 200 to 2500 nm. Like the camera f-stop adjustments, these filters provided a means for attenuating the light entering the camera, without significant change in chromaticity, but to a much greater degree. The four filters used possessed nominal extinction values of 1.0, 2.0, 3.0 and 4.0, enabling one to reduce the incident light by factors of 10, 100, 1,000 and 10,000, respectively. Each consists of a thin metallic alloy film deposited on a grade A fine annealed glass substrate. Their attenuation is a result of both absorption and reflection from the thin metallic film; the substrates are pitch polished so as to reduce light scattering by this component to a minimum.

The DICOM-8 system also lends itself well to multiple repeat measurements on the same sample. The specimen to be transilluminated is inserted into a transparent, cylindrical glass tube which is in turn placed in the instrument sample holder. This holder is coupled to a small electric motor which serves to rotate the holder - sample tube assembly through 360 degrees at a rate of .30 revolutions per sec. After one complete revolution, the direction of rotation is automatically reversed. Images of the exit face of the rotating, transilluminated sample are then collected at video rates (30 per second) by the video camera; because of the rotation, each will correspond to the transmission of light through different paths (although of equal length) in the specimen. These images are then averaged to yield a grey level, and corresponding extinction value, which represents the average of a series of repeat transmittance measurements. This automated procedure enables the average of 100 measurements through different paths in a single tissue sample to be carried out within 13 sec (image processing rather than image acquisition taking up the majority of the time).

12.2 CALIBRATION

The calibration procedure used to map digital image grey level to sample extinction is based on a calibrated densitometer step film manufactured by Sargent-Welch. This step film consists of 21 segments, each possessing a known, uniform extinction over its area. Consecutive steps differ in extinction by approximately 0.2, the entire strip covering the range 0.3 to 4.02 extinction units. By placing each of the strip film segments in turn in the path of the DICOM-8 light beam, at the position of the specimen holder and in the absence of any sample, and acquiring a digitized image of those which are associated with a "meaningful" video signal (ie. one which is below saturation but above the dark current level), one can obtain a mapping between image grey level and extinction at a discrete number of points (typically six). All grey levels must be corrected for zero offset. A cubic spline is then used to interpolate between these points to yield a continuous mapping over the extinction range covered by the subset of steps which possess "meaningful" images.

A tissue sample can then be placed in the holder, transilluminated, an image of its exit face produced and the digitized grey level (corrected for zero offset) determined. As long as the intensity of the light leaving the sample falls between that which exited the two extreme "meaningful" steps, its extinction may be read from the spline calibration curve. If not, an f-stop adjustment or neutral filter can be used to reduce the light entering the camera until it does fall within this range. Corrections can then be applied to take into account these adjustments. A more detailed discussion of these corrections follows. The calibration system is therefore one of comparison between the digitized images of a transilluminated sample and the calibrated step film (of known extinction), positioned at the same location.

Because the formulation of the calibration procedure is a comparison, all extinction values generated by it will possess the same characteristics as the extinction of the step film. In particular, if the step film extinction values were determined using an instrument with a half angle of collection γ , the values assigned to the tissue samples will be as if measured on an instrument of half angle γ . In other words, the collection angle of the Dicom-8 spectrophotometer will always be equal to that of the instrument used in calibrating the step film.

Since the extinction values supplied by Sargent-Welch for each step of the strip film refer to a continuous spectrum, we were obliged to obtain new values under conditions of band-limited spectrum. Step film extinction values were

determined using the system illustrated in figure 12.3. Each step was transilluminated with light from the 100 watt quartz lamp - fiber optic assembly with the transmitted radiation being detected as shown. The detection system consisted of an International Light (IL730A) radiometer with a broad band silicon detector probe (SEE100) calibrated over the range 330 to 1000 nm. Attached to the probe was an F flat response filter and a 7 mm limiting aperture. The radiometer probe was placed 18 cm from the exit face of the transilluminated film to yield a half angle of collection of 1.1 degrees. By measuring the intensity of the light incident upon the radiometer detector in the presence and absence of the step film, one can calculate the extinction of each step under this small angle collection geometry. The placement of the Melles-Griot bandpass interference filters directly in front of the probe detector enabled the measurement of step film extinction at all wavelengths utilized in the Dicom-8 spectrophotometer system.

One can construct a calibration curve similar to that labelled as $f=2.8$ in figure 12.4 by positioning the Sargent-Welch film at the location of the Dicom-8 spectrophotometer sample holder, transilluminating each step with light of 700 nm, digitizing the images of those associated with a "meaningful" video out signal using a camera stop of 2.8 and subsequently determining the associated computer grey level (corrected for zero offset) of each. If the camera f -stop is increased by 1 and the above procedure repeated, the curve designated as $f=4.0$ will be obtained. It should be noted that the shape of this curve is identical to that generated at $f=2.8$, the only difference being a horizontal shift along the extinction axis. Similar curves can be generated for all other camera stops.

This procedure for generating grey level mappings can also be carried out with each of the four neutral filters in place in front of the camera to produce the set of curves shown in figure 12.5. It should once again be noted that each is identical in shape to that obtained for $f=2.8$ with no neutral filter. As before, the only difference is a horizontal shift along the extinction axis.

The final result of these measurements is a family of curves, each member representing a map of grey level to extinction for a specific set of image acquisition conditions characterized by f -stop and neutral filter. At this point, sample extinction can be determined. One merely places the sample to be measured in the holder and determines the grey level of its digitized image. The corresponding extinction can then be read directly off the appropriate calibration curve characteristic of the conditions under which the sample image was collected (ie. same f -stop and neutral filter). However, in practice, a

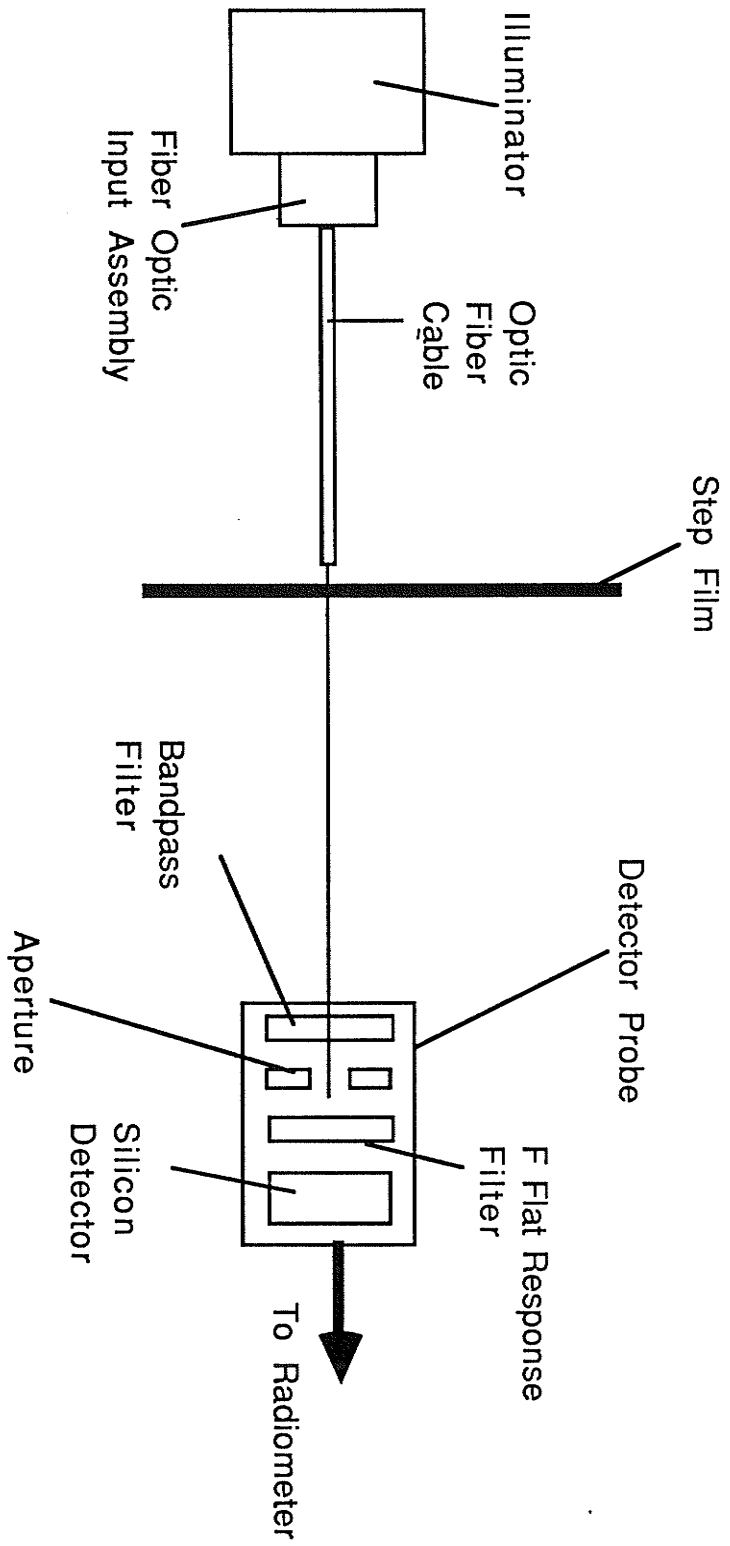


Figure 12.3: Experimental setup for measuring step film extinction.

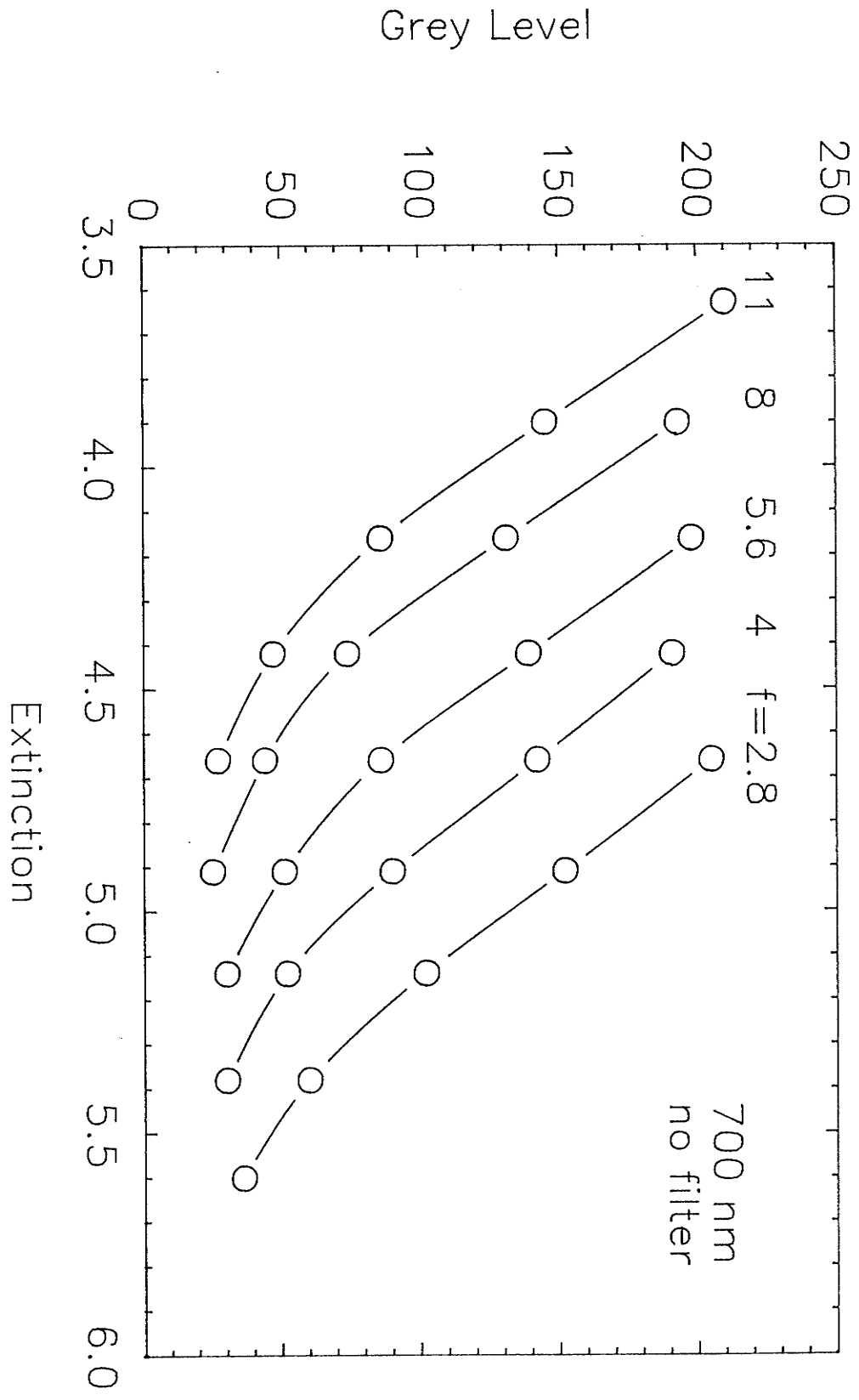


Figure 12.4: F-stop calibration curves

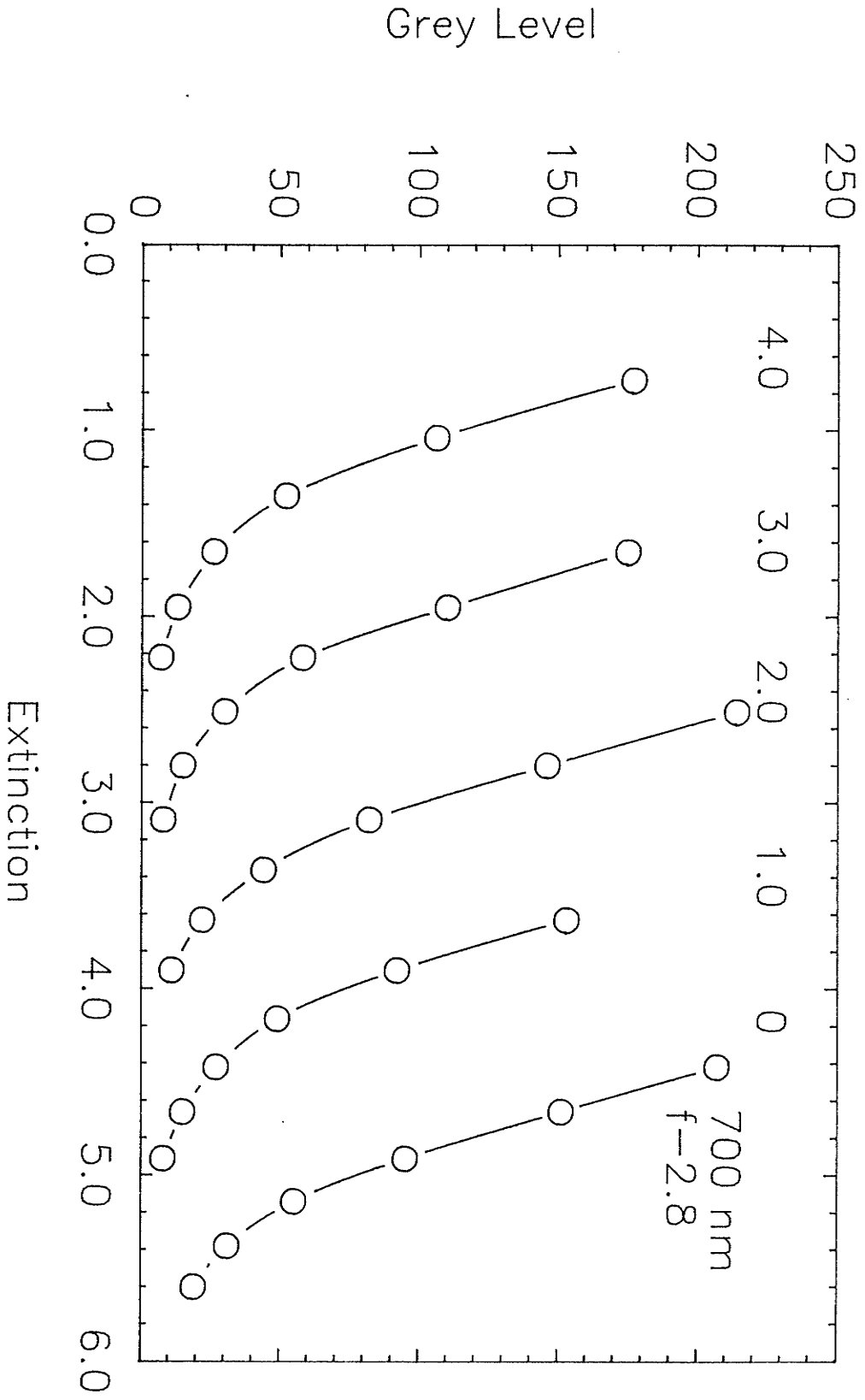


Figure 12.5: Neutral density filter calibration curves

much less cumbersome approach is taken. Only one calibration curve is generated before each experimental run, that for a wavelength of 700 nm, f-stop=2.8 and no neutral filter. This single mapping is then used for all samples, regardless of the particular conditions under which their images were obtained. Correction factors are then added to take into account the fact that the conditions under which transillumination was carried out are not necessarily those used to generate the calibration curve. These correction factors are equal to the shifts between the appropriate curves of the above mentioned family (which must be generated only once and the shifts stored for future reference).

The extension to measurements at other wavelengths is simple. As above, calibration curves can be generated for f=2.8 and no neutral filter, for all wavelengths of interest, by replacing the 700 nm filter with one of a different bandpass. The resulting family of curves is illustrated in figure 12.6. All are identical in shape and differ only by a horizontal shift along the extinction axis. Thus, the grey level of the samples transilluminated at any wavelength may be converted to extinction using the single calibration curve generated at 700 nm and adding the appropriate correction shift. With such a calibration procedure, the effects of spectral variations in detector sensitivity and lamp output on measured extinction are accounted for implicitly. As the Melles-Griot neutral density filters used to increase the dynamic range of the vidicon detector were not truly gray, filter calibration curves (and filter correction factors) were generated at each wavelength studied.

12.3 VERIFICATION OF THE CALIBRATION PROCEDURE

To check the validity of the calibration procedure, two tests have been carried out. The first is a comparison with a commercially available spectrophotometer, a Spectronic 710 (Bausch and Lomb). For this purpose, a red blood cell sample was obtained from the hematology department of the Manitoba Cancer Foundation. This sample contained 5400×10^6 cells/ml and had been removed from a patient free of any known blood disorders. The specimen was diluted with phosphate buffered saline (PBS) to a concentration of 7.8×10^6 cells/ml and spectral extinction measurements carried out with both the Dicom-8 and Spectronic 710 systems. Figure 12.7 shows the results. Two points should be noted. Firstly, the two curves differ in magnitude, the line representing measurements obtained with the Spectronic falling below that of the Dicom-8. This is to be expected due to the difference in collection angle of the two instruments. The Spectronic

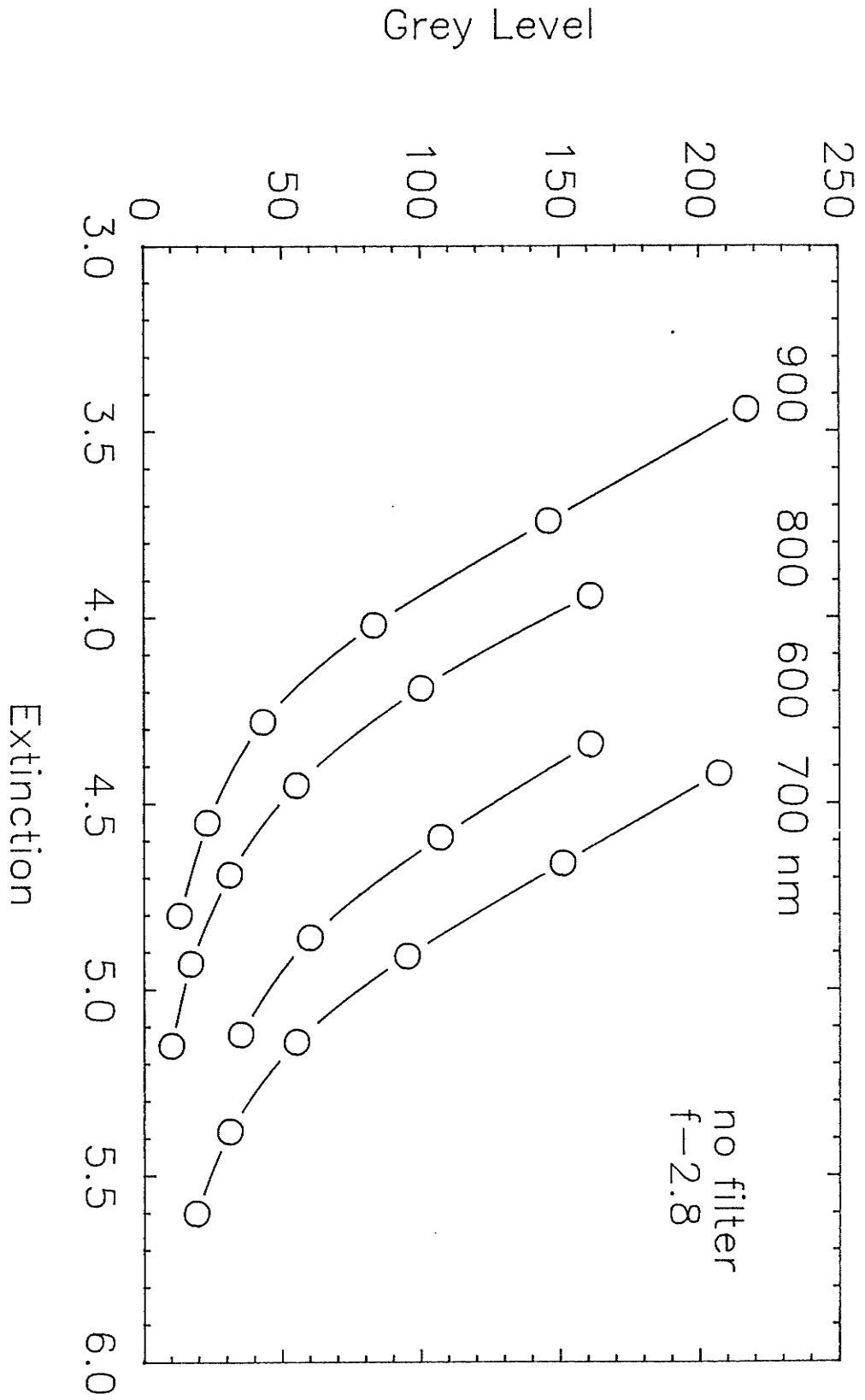


Figure 12.6: Wavelength calibration curves

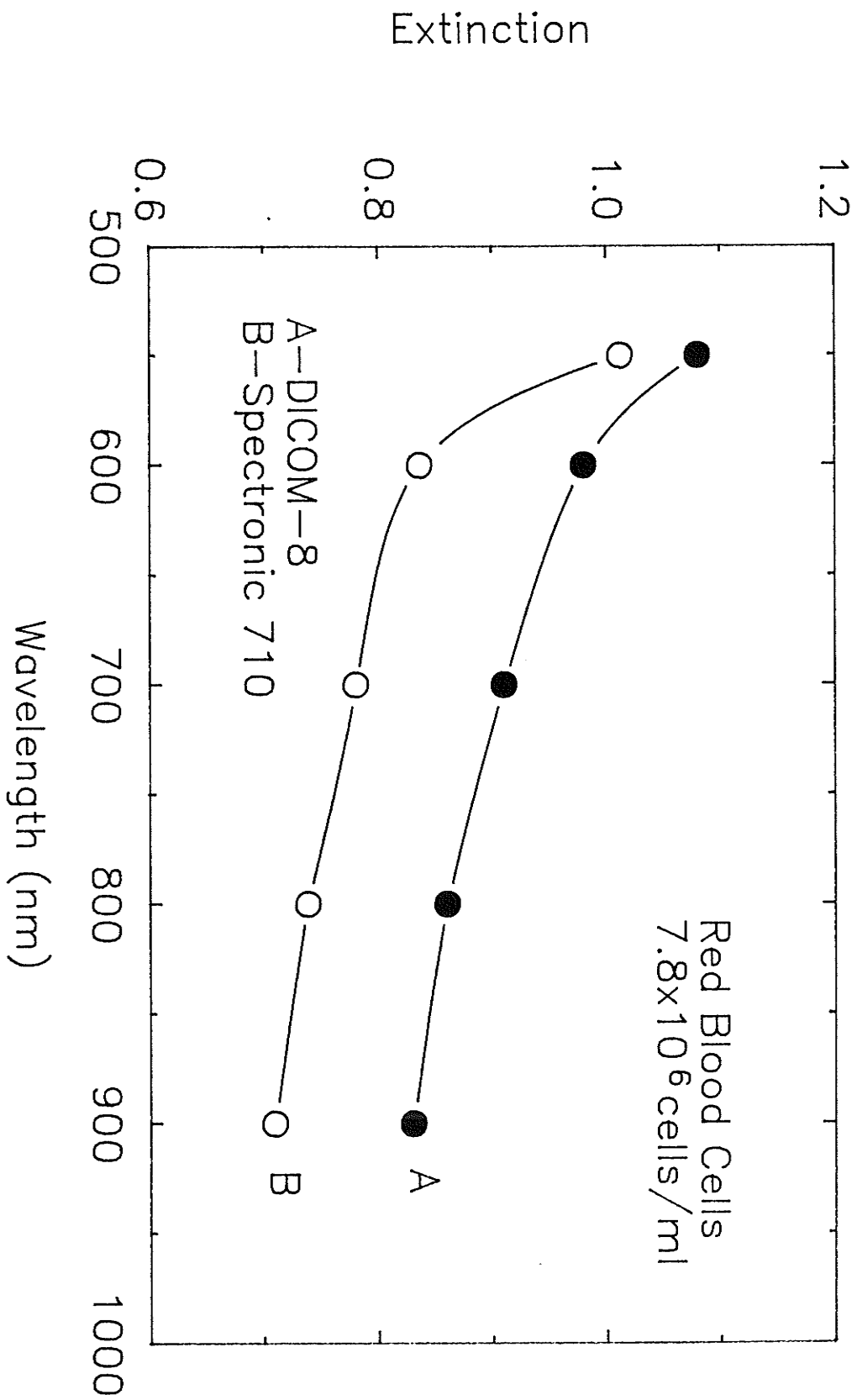


Figure 12.7: Diffuse spectral extinction of an aqueous suspension of red blood cells

710 has a much larger acceptance half angle than the Dicom-8 (6 degrees as compared to 1.1) and as a result will collect a greater percentage of the light scattered by the sample. This will result in a larger detected light intensity and therefore a smaller measured extinction. The second point of interest is that the two curves possess the same shape, thus providing some indication of the validity of the Dicom-8 results.

This comparison was carried one step further. In the above paragraph, the assumption was made that any differences in measured extinction between the two instruments is due to differences in angle of collection rather than errors in the Dicom-8 system itself. The validity of this assumption was tested using a solution of trypan blue and PBS. Trypan blue is a liquid dye which possesses a 50 nm wide absorption band at 650 nm; this substance is homogeneous at all levels above the molecular. Thus, the trypan blue - PBS solution may be considered a pure absorber at 650 nm. Stated differently, light scatter at this wavelength will be insignificant when compared to absorption. The light exiting the trypan blue solution will, therefore, consist entirely of photons which have passed through the sample without interaction. In the absence of scatter, differences in collection angle will be without consequence and the detected intensity of light leaving the sample should be the same for measurements made with both the Dicom-8 and Spectronic 710. When the measurements were actually performed, this was indeed found to be true, the Dicom-8 yielding an extinction at 650 nm of 0.77, the Spectronic 710, 0.764. This result lends proof to the assumption that the lack of agreement in extinction values obtained using the two instruments is due only to differences in half angle of collection.

The second test to check the validity of the Dicom-8 system was carried out using Melles-Griot neutral density filters of nominal extinction .1, 0.3, 0.5, 1.0, 2.0 and 3.0. These filters were treated as specimens, placed in the Dicom-8 sample holder, transilluminated and measured for extinction. The results are shown in table 12.1. Included are the extinctions obtained through measurements with the same radiometer set-up employed in the Sargent-Welch strip film experiments. It should be noted that the samples chosen for this test ensure that a wide range of measurement conditions are used so as to verify all aspects of the calibration procedure, wavelength corrections, stop corrections and neutral filter corrections. Agreement between the two sets of measured values is seen to be quite good, thereby lending credibility to the Dicom-8 system.

Nominal Extinction of Sample Filter	Stop	Neutral Filter	DICOM-8 Extinction	Radiometer Extinction
0.5	4.0	4.0	0.49	0.46
0.5	5.6	4.0	0.45	0.46
0.3	4.0	4.0	0.29	0.28
0.3	5.6	4.0	0.30	0.28
0.1	5.6	4.0	0.12	0.09
0.1	8.0	4.0	0.09	0.09
1.0	5.6	3.0	1.07	1.02
2.0	2.8	3.0	1.84	1.84
3.0	5.6	1.0	3.00	2.91

Table 12.1: Measured extinction of Melles Griot neutral filters.

12.4 ANGLE OF COLLECTION OF THE DICOM-8

Because the DICOM-8 calibration procedure is based on a comparison between sample image and the images of a series of film segments of known extinction, angle of collection is determined not by f-stop setting or sample/detector distance, but rather the geometry of the independent instrument used in the measurement of the step film extinctions (ie. the radiometer geometry illustrated in figure 12.3). The DICOM-8 merely assigns extinctions relative to the radiometer measured film values. The half angle of collection of the radiometer set-up, and therefore the half angle of collection of the DICOM-8, was 1.1 degree.

Calibration using the step film method is valid only as long as the sample and film images being compared are acquired under identical imaging conditions. It was for this reason that strip film curves were generated for all combinations of neutral filter, bandpass filter and camera f-stop. However, in systems such as the DICOM-8 where imaging conditions are not fixed, this condition is not sufficient to ensure that measured results are meaningful. In addition, the calibration procedure must be able to retain the correct relative relationship between sample extinctions measured under different conditions. For this criterion to be satisfied by the DICOM-8 system, the effect of neutral filter, bandpass filter and f-stop adjustment on transillumination image brightness must be the same for both step film and tissue samples. That changes in neutral filter and bandpass filter setting satisfy this criterion is obvious. However, for the same to be true of f-stop adjustments, the angular distribution of light exiting the two types of sample must be similar, at least through an angle of approx. 10 degrees centered about the optical axis (this being the portion of the distribution that is sampled with an f-stop of 2.8). Although the angular distribution of light emerging from a transilluminated sample of film may not be identical to that emerging from a sample of tissue, differences are not expected to be large, especially over the small angle required to be similar by the calibration procedure. As such, results obtained using the DICOM-8 are expected to be meaningful.

Chapter XIII

SPECTRAL EXTINCTION OF HUMAN BREAST TISSUE

Twenty one human tissue samples, removed from the breasts of 10 female patients, were obtained from the pathology department of the St. Boniface Hospital. Another 8 breast tissue samples (taken from 4 patients) were obtained from the department of pathology at the Health Sciences Center. Specimens were classified by pathologists as either normal or carcinoma as shown in table 13.1. Eight of the normal tissues were further subdivided into adipose and glandular groupings. The samples were stored at -18°C . Two hours before extinction measurements were to be conducted, the tissues were thawed, cut into specimens of appropriate size and firmly inserted into an 8.5 mm diameter glass tube to yield small, cylindrical samples. The glass tubes were then positioned in the specimen holder of the DICOM-8 system and transilluminated. Sample images were collected at wavelengths over the range 550 to 900 nm (in 50 nm steps) and the corresponding extinctions calculated. The resulting spectral extinction curves were then referenced to measurements made on an identical glass tube filled with water so as to correct for the contribution to extinction made by the specimen container itself. It must once again be emphasized that diffuse extinction measurements are not absolute and depend heavily on experimental geometry (in particular, angle of collection and sample thickness). As such, results presented in this chapter are only important in a relative sense. Reproduction of these results by other labs will require that the DICOM-8 geometry be accurately simulated.

Figure 13.1 demonstrates the need for determining the average extinction of a tissue sample from a large number of repeat measurements (as discussed in the previous section). Curve A represents the spectral extinction curve of sample 10491-G (glandular tissue) as obtained from a single video image (ie. no sample rotation). Curve B shows the spectral extinction curve of the same sample after a 45 degree rotation of the glass cylinder (once again, obtained with a single video image) and curve C after a 90 degree rotation. All three curves represent the spectral extinction of specimen 10491-G but for different light paths through that sample. All subsequent extinction curves were obtained using automatic sample rotation during transillumination.

Sample Number	Tissue Classification	Pathology Dept.
10491-A	adipose	St. B.
10491-G	glandular	St. B.
10491-C	carcinoma	St. B.
11256-A	adipose	St. B.
11256-G	glandular	St. B.
41613-A	adipose	St. B.
41613-G	glandular	St. B.
56173-A	adipose	St. B.
56173-G	glandular	St. B.
302823-C	carcinoma	St. B.
367658-N	normal	St. B.
7808-N	normal	St. B.
7808-C	carcinoma	St. B.
7484-N	normal	St. B.
7484-C	carcinoma	St. B.
428334-N	normal	St. B.
428334-C	carcinoma	St. B.
8604-N	normal	St. B.
8604-C	carcinoma	St. B.
8736-N	normal	St. B.
8736-C	carcinoma	St. B.
16952-N	normal	H.S.C.
16952-C	carcinoma	H.S.C.
16932-N	normal	H.S.C.
16932 -C	carcinoma	H.S.C.
18175-N	normal	H.S.C.
18175-C	carcinoma	H.S.C.
19177-N	normal	H.S.C.
19177-C	carcinoma	H.S.C.

Table 13.1: Tissue classification.

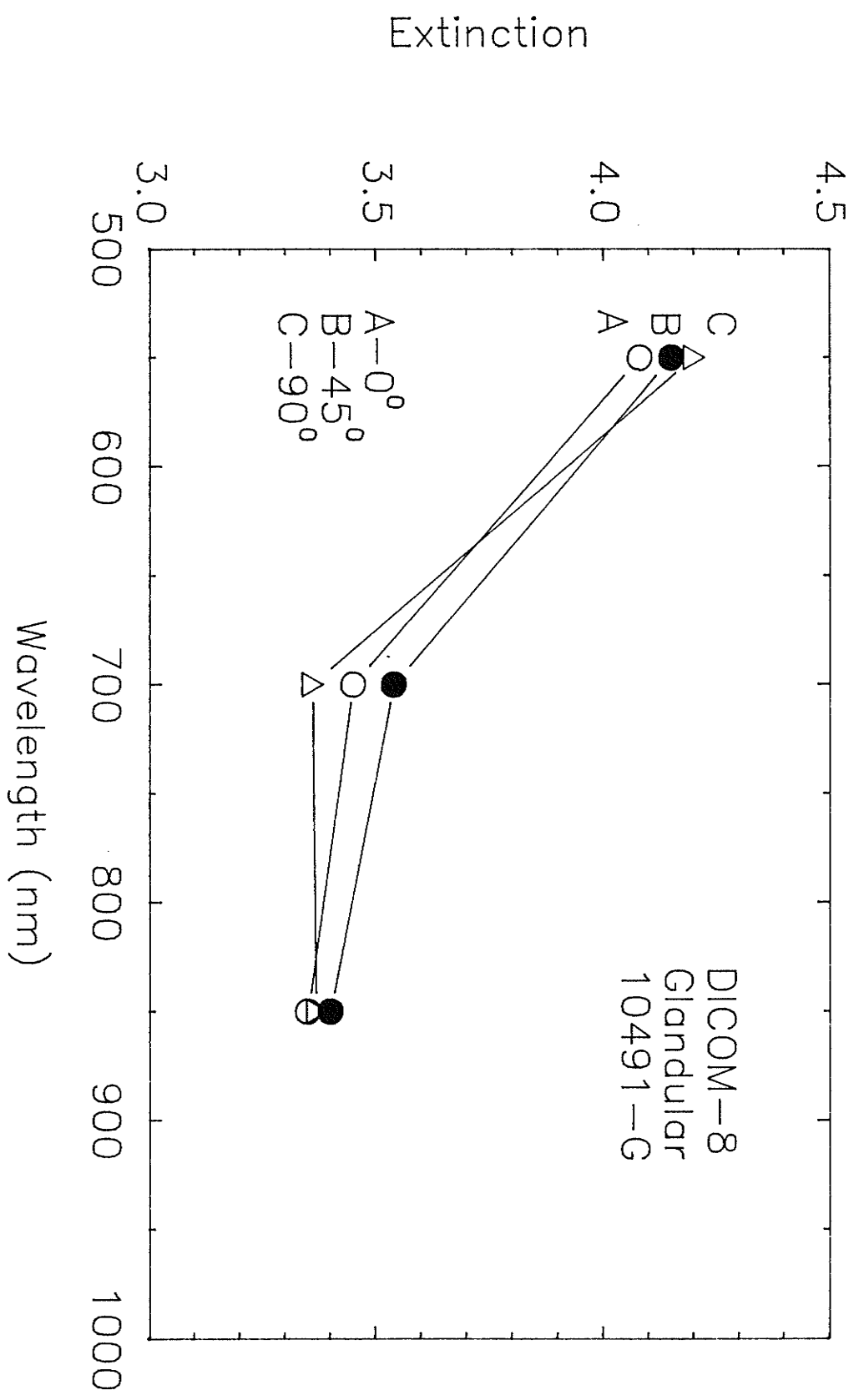


Figure 13.1: Diffuse spectral extinction of sample 10491-G for three different light paths

Figure 13.2 gives some indication of the reproducibility achievable in the tissue measurements. Curve A is the spectral extinction of sample 41613-G (glandular tissue). Curve B represents a repeat of these measurements after removing and re-inserting the same tissue sample into the glass container. Variations are due solely to differences in sample packing.

One very important question in the study of light transport through tissue is whether or not the optical properties of a particular tissue type vary between patients. Figure 13.3 displays the spectral extinction curves of each tissue sample designated as adipose by the pathologist. Figures 13.4, 13.5 and 13.6 represent the same data for glandular, "normal" and carcinoma, respectively. The variations between curves of similar tissue type suggest that the optical characteristics of tissue will differ significantly from one patient to another, especially at short wavelengths. It therefore seems inappropriate to assign one set of optical parameters, which are universally applicable, to a particular tissue type. Instead, these parameters must be measured and assigned on an individual basis.

The four curves of figure 13.7 represent the average diffuse spectral extinction of adipose, glandular, normal and cancerous tissue. The adipose tissue extinction curve was obtained by averaging the data of all adipose tissue samples included in table 13.1 (4 samples). Similarly, the curves for glandular, normal and carcinoma were constructed from averages over 4, 18 and 11 specimens, respectively. Two important points should be noted. Firstly, all four curves possess roughly the same shape, characterized by a continuous reduction in extinction with increasing wavelength. Below 700 nm, the principal factor in determining the shape of the spectral extinction curves is absorption by hemoglobin. Light scatter by the tissue matrix will serve to broaden the characteristic 550 nm absorption peak of this blood component, pushing it out to higher wavelengths [44]. Stated differently, when present in a scatter medium, hemoglobin will make a measureable contribution to the extinction of that mixture (as a result of the increased probability of absorption that accompanies the larger mean free path of a scattering material) at wavelengths much longer than otherwise would be expected from an examination of its characteristic transmittance spectrum. This absorption phenomenon is responsible for the very steep slope observed below 700 nm. In the near infrared, hemoglobin will exhibit no appreciable absorption and the shape of the four spectral extinction curves will be determined by the scatter properties of tissue (absorption by water is not evident due to the manner in which measurements were referenced). As the scatter cross section

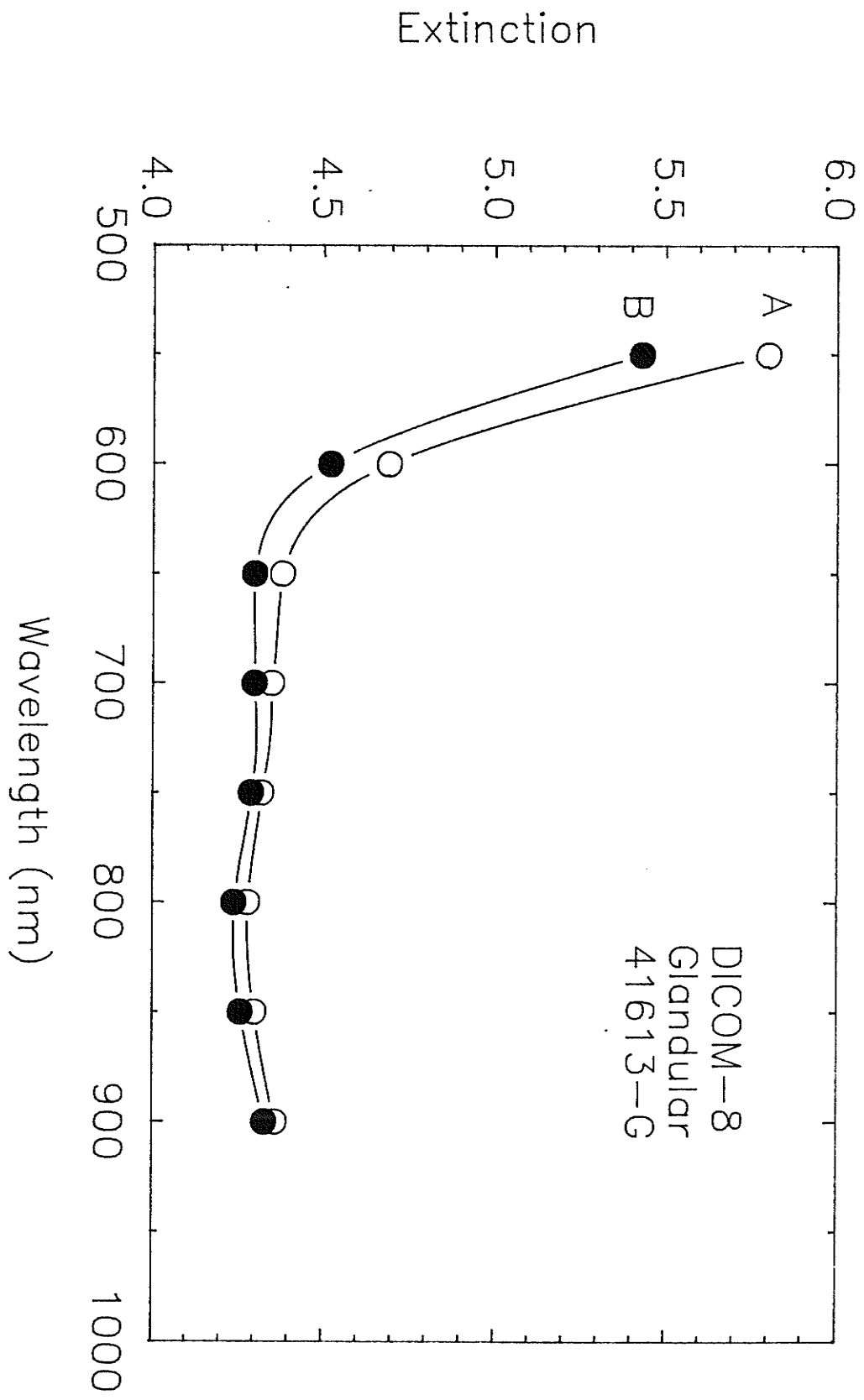


Figure 13.2: Reproducibility of DICOM-8 tissue measurements

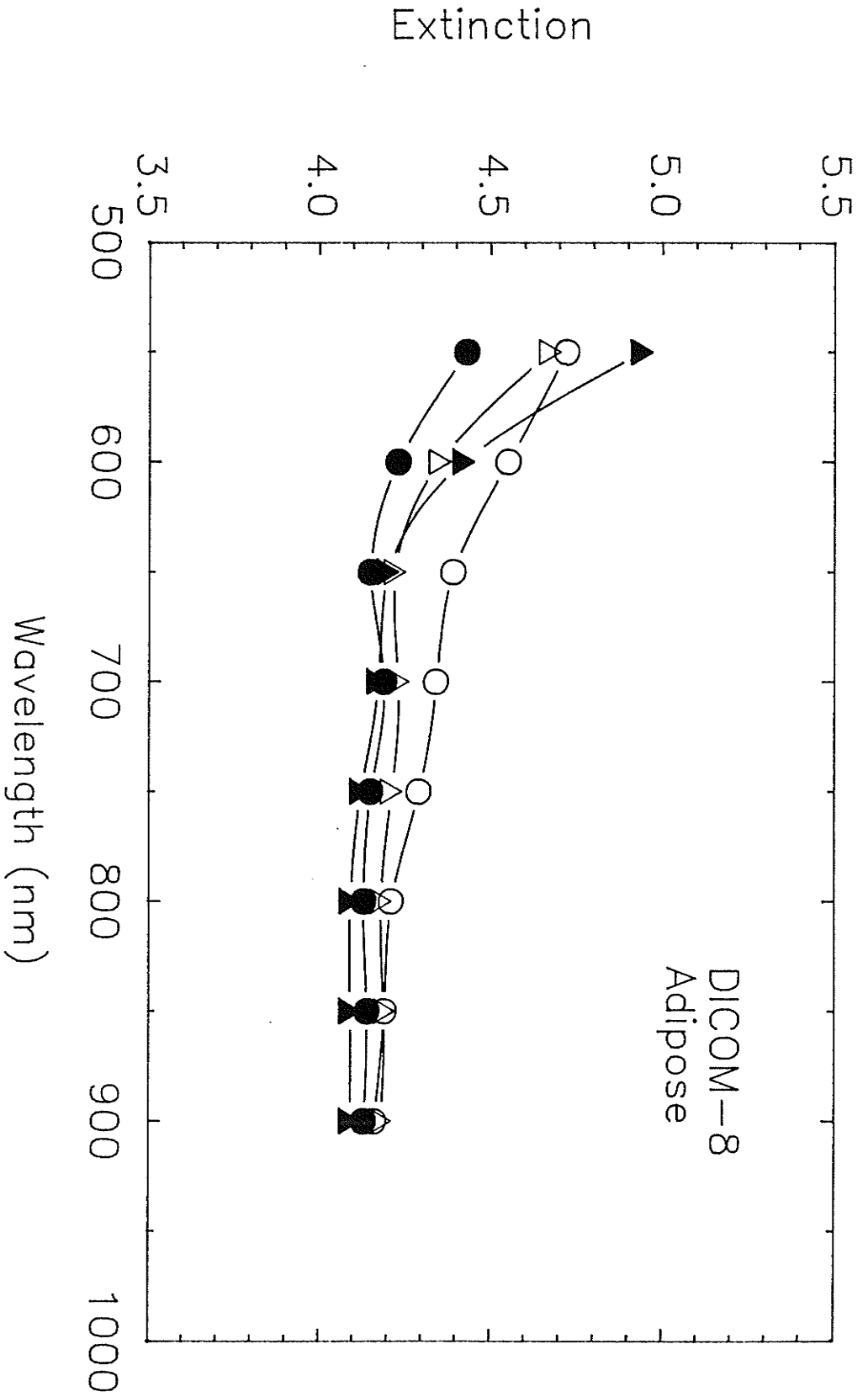


Figure 13.3: Diffuse spectral extinction of adipose tissue samples

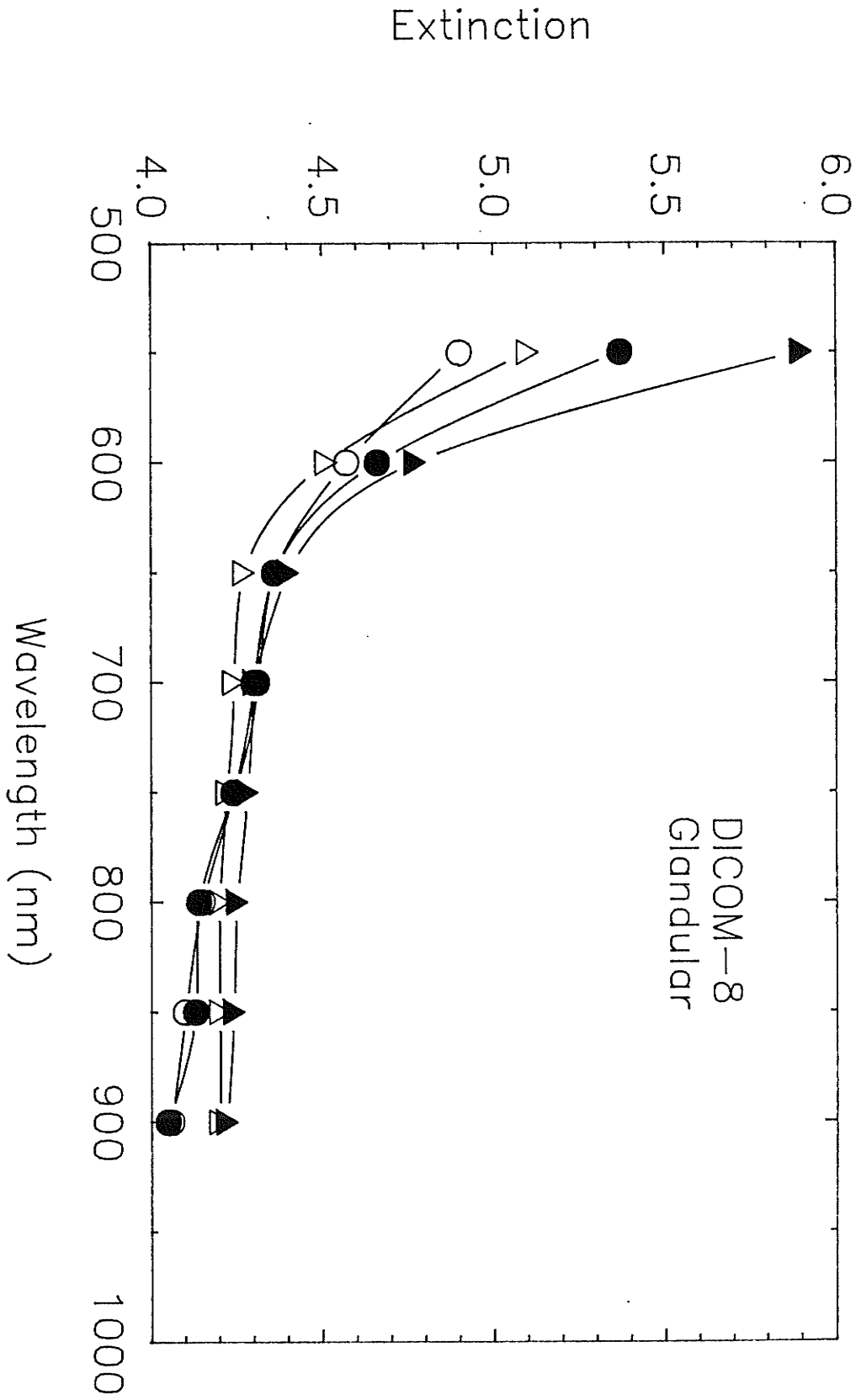


Figure 13.4: Diffuse spectral extinction of glandular tissue samples

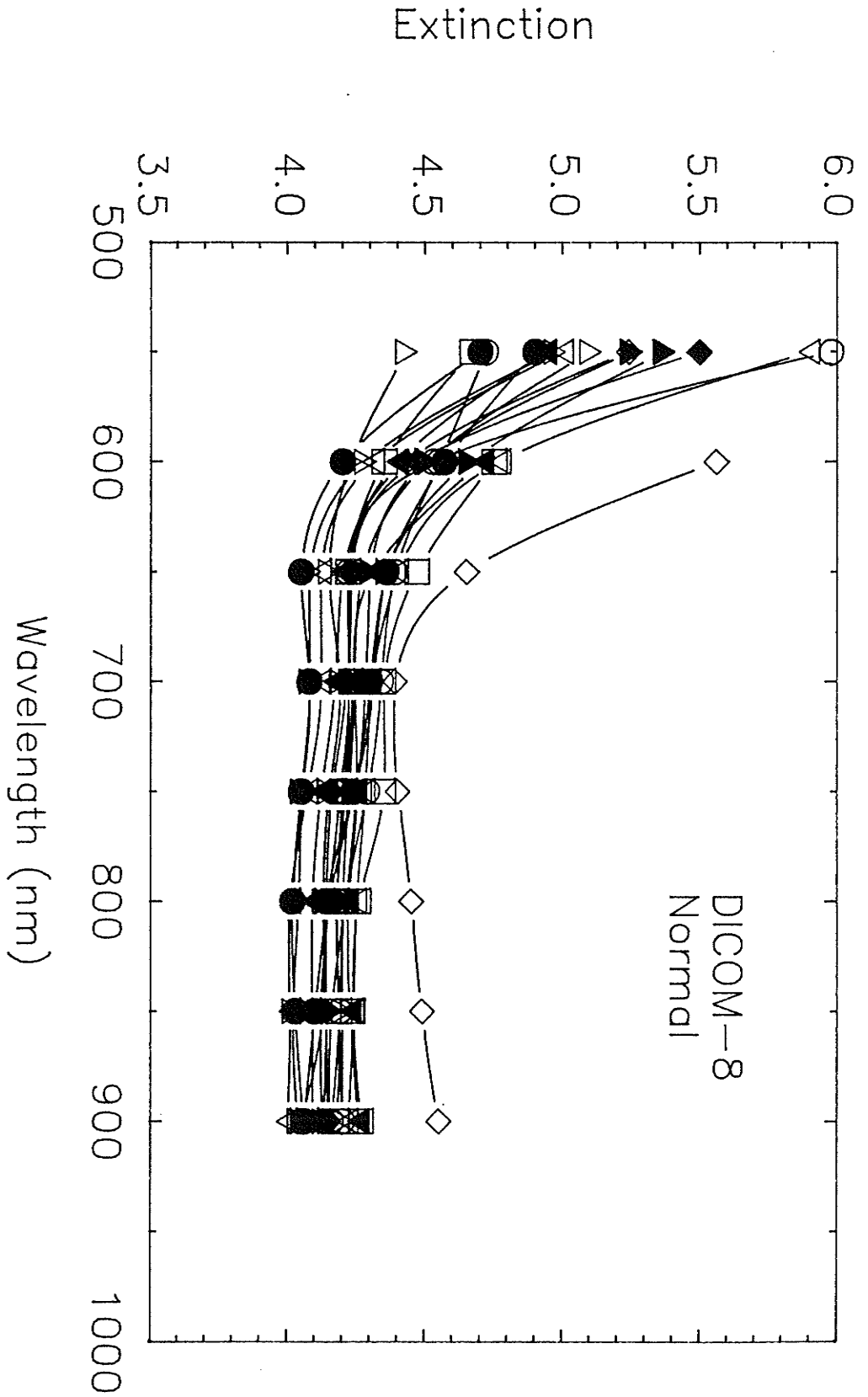


Figure 13.5: Diffuse spectral extinction of normal tissue samples

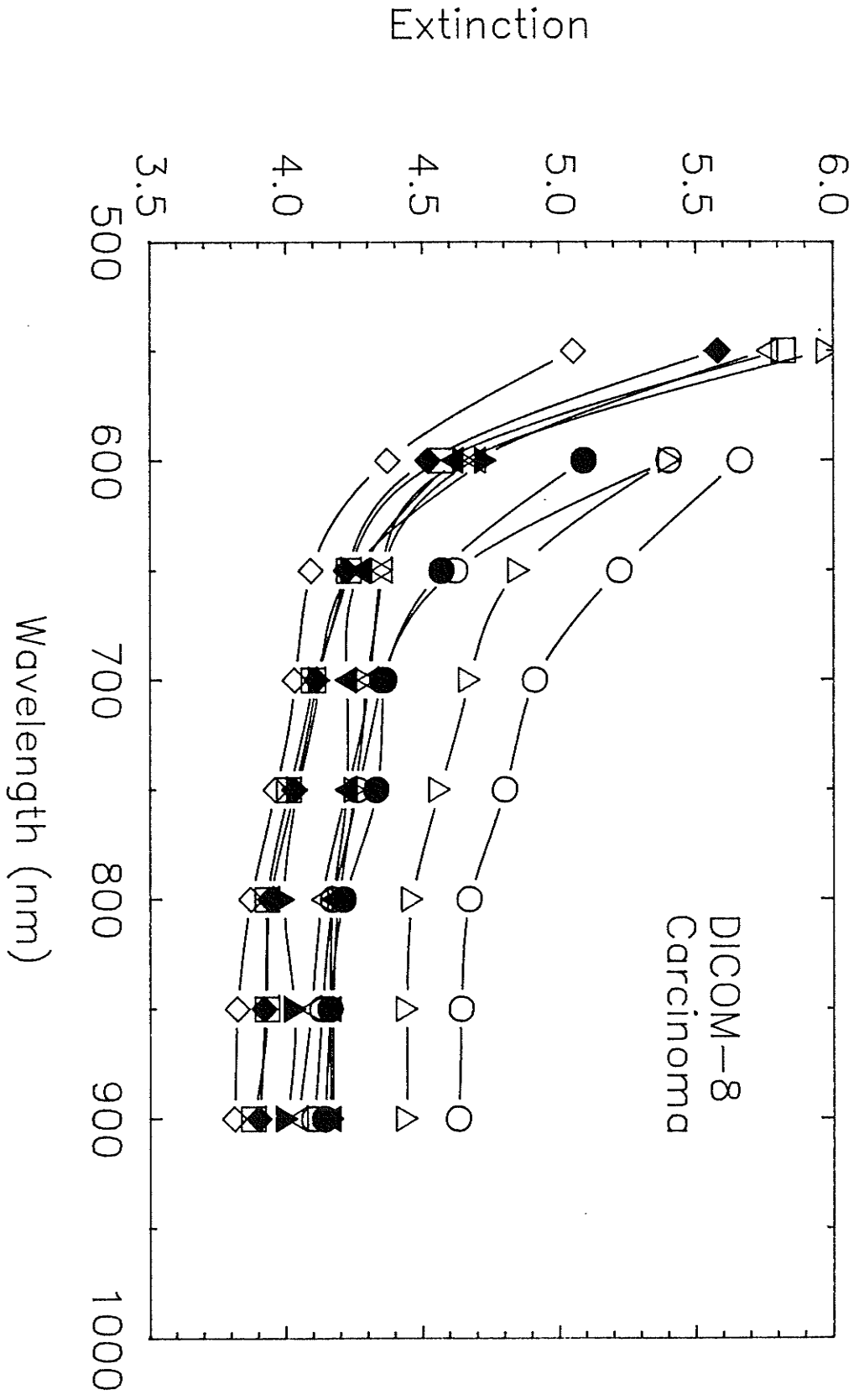


Figure 13.6: Diffuse spectral extinction of carcinoma tissue samples

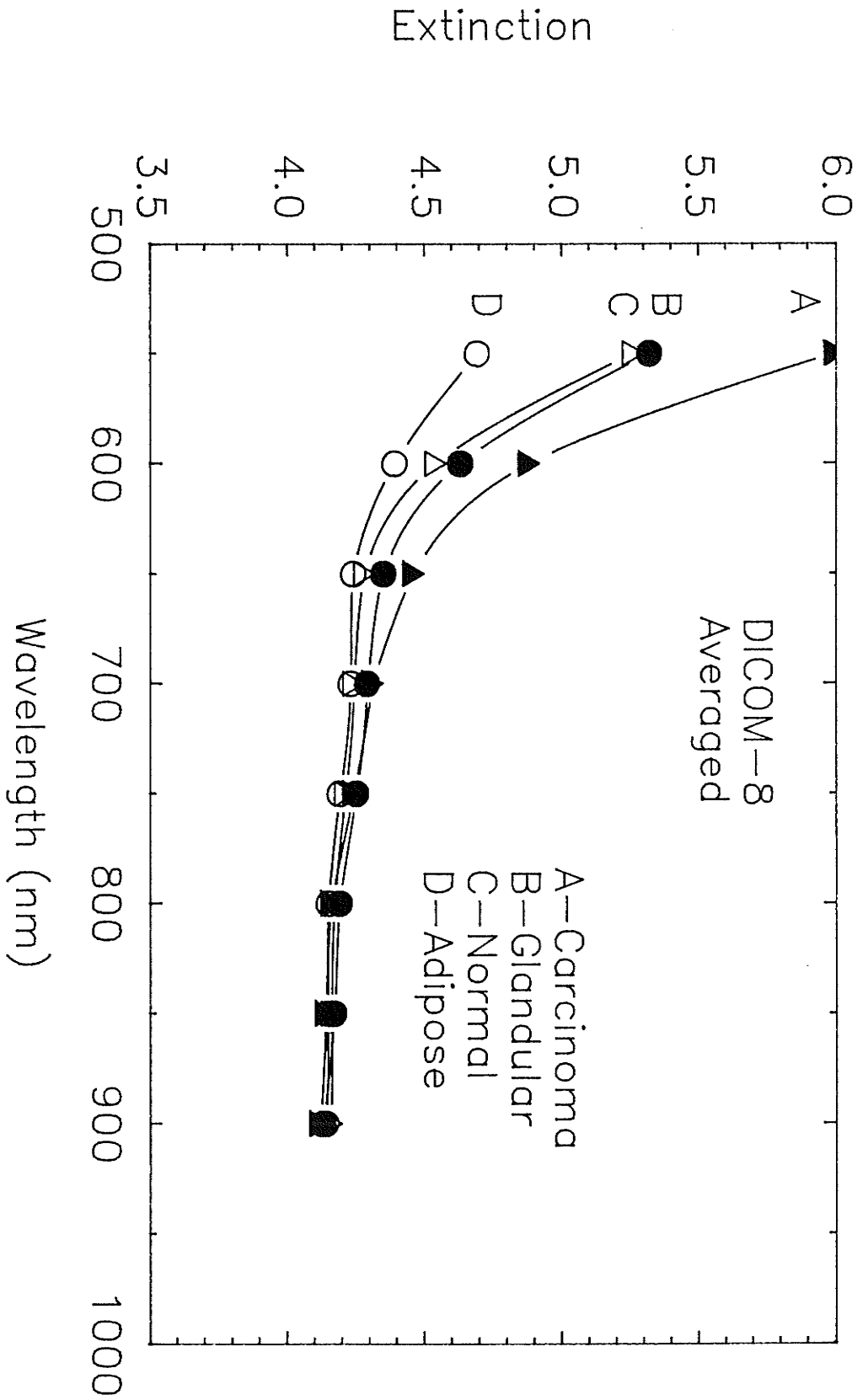


Figure 13.7: Average diffuse spectral extinction curves

per unit volume of tissue will display only a very weak dependence on wavelength over this spectral region, the curves will assume an almost horizontal slope.

The second point which should be noted is the difference in magnitude of the four curves of figure 13.7. Below 700 nm, carcinoma exhibits a higher extinction than normal while glandular tissue removes light more efficiently than adipose. Above 700 nm, meanwhile, the spectral extinction curves are, for all practical purposes, identical. This behavior is attributed to variations in hemoglobin concentration between the three tissue types studied. The vascular structure of a tumor will be composed of two parts, that portion of the host's vasculature not destroyed by the tumor and any new vessels created to accommodate the increased oxygen and nutrient requirements of the rapidly dividing malignant cells. As a result of this new vessel growth, a process referred to as angiogenesis, blood vessel concentration within a tumor will be enhanced over that in normal tissue. Exceptions to this generalization are the central regions of large, rapidly proliferating tumors where the vascular system is unable to keep up with cell growth; as a result of the shortage of oxygen and nutrients, these regions will be necrotic. Glandular tissue, meanwhile, will be characterized by a higher blood content than adipose. Variations in tissue blood (and therefore hemoglobin) concentration will serve to alter the extinction below 700 nm but will have little effect above.

Evidence supporting the claim that differences in the spectral extinction of carcinoma, adipose and glandular tissues are indeed due to variations in hemoglobin concentration is presented in figure 13.8. Curve A is the difference of the averaged normal and carcinoma curves of figure 13.7 while curve B represents the diffuse spectral extinction of hemoglobin as measured in the presence of scatter (intact red blood cells serve as the scatterer). The data for the latter curve was obtained by measuring the spectral extinction of a sample of whole blood (diluted to 7.8×10^6 cells/ml with PBS) and subtracting the value found for 900 nm. This curve gives some indication of the absorption properties of hemoglobin as observed in the presence of scatter. As hemoglobin concentration is increased (through an increase in the number of red blood cells), the short wavelength end of curve B is expected to rise very rapidly and more closely resemble curve A. The shape of the hemoglobin curve coupled with its expected behavior with increasing concentration demonstrate that this blood component could indeed be responsible for the observed difference in spectral extinction of normal and carcinoma breast tissue (extinctions are additive).

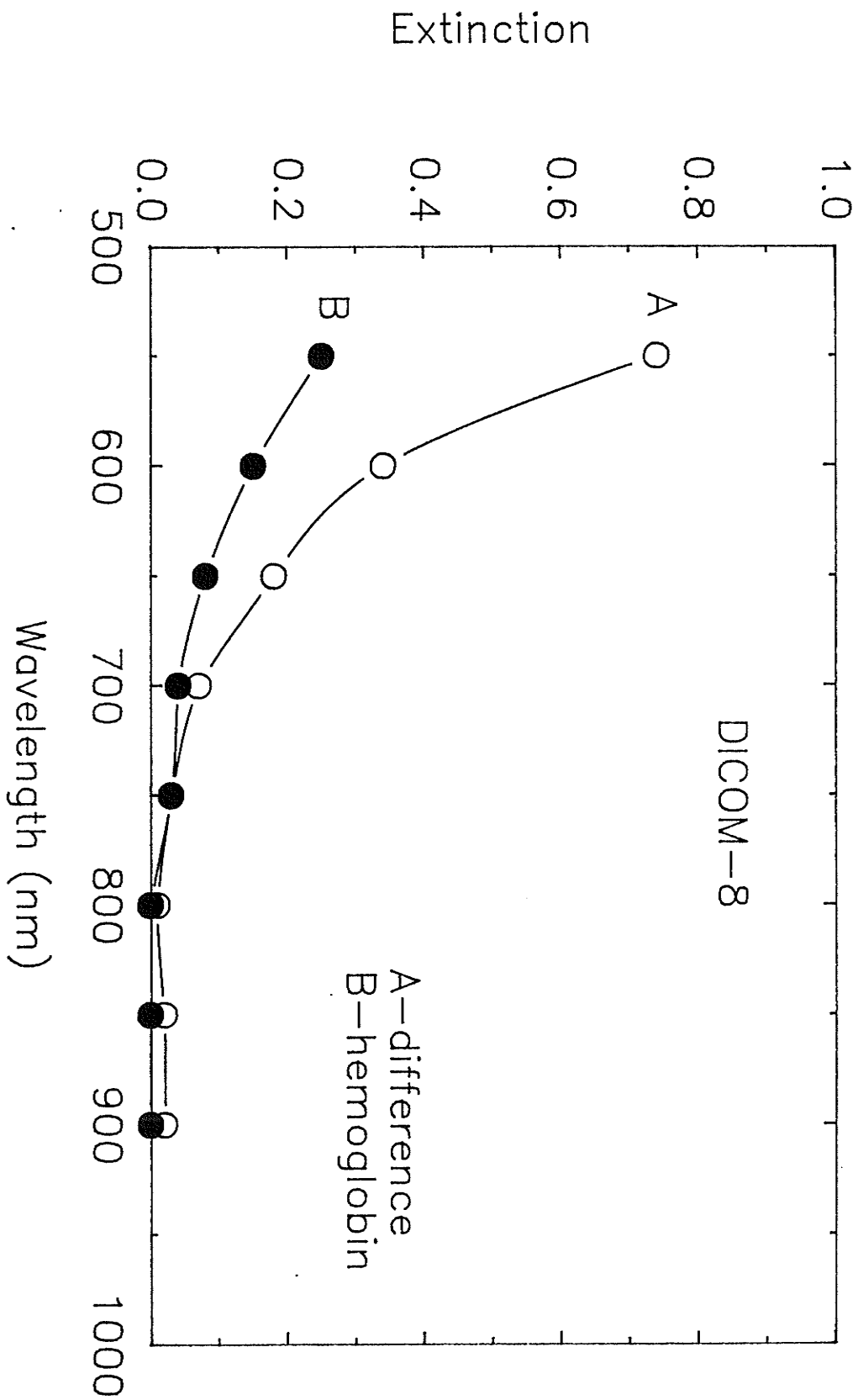


Figure 13.8: Difference in the diffuse spectral extinction curves of carcinoma and normal tissue

The spectral extinction curves of the breast tissue samples examined in this chapter reveal the fact that the ability of light to travel through tissue increases with increasing wavelength (as wavelength increases, extinction drops). This is an important concept to Photodynamic therapy where one would like to maximize light penetration in tissue; the DICOM-8 results suggest that long wavelength light be used. However, a second criterion comes into play when selecting the optimal wavelength, the requirement that the light employed be strongly absorbed by a photosensitizing drug. At present, this condition puts an upper limit of 630 nm on the wavelength used.

With Diaphanography, although maximum light transport is important, normal/tumor tissue contrast must also be considered when selecting a wavelength for transillumination. Contrast will be maximum when the difference in optical properties of the two tissues is greatest and from figure 13.7, it would appear that the highest image contrast will occur when light near the 550 nm absorption peak of hemoglobin is used. However, tissue exhibits very high attenuation in this region so that light transport through the breast will be very inefficient. Although information content will be maximized (as far as the needs of diaphanography are concerned), the signal will be too small to be of use. A compromise must therefore be made. The commercial diaphanography unit in operation at the Manitoba Cancer Foundation (Spectrascan LITE SCAN Model 10), for example, uses light above 700 nm.

Chapter XIV

A BIOLOGICAL TISSUE PHANTOM

Although Diaphanography was first described over 50 years ago, its development into a clinical tool has yet to take place. A number of questions pertaining to its operation must be answered if this situation is to improve. For example, the conditions of examination (ie. wavelength of light used for transillumination, size of the light source, camera viewing angle etc.) yielding the optimum diaphanography image must be determined. Similarly, the limits of the modality, both in terms of maximum tumor depth and minimum tumor size, must be found.

To carry out such studies on samples of excised breast tissue seems impractical. Firstly, there is a very real problem with availability. Tissue samples are difficult to obtain, especially the very large specimens required for breast transillumination studies. Secondly, it is extremely difficult to control experimental conditions when employing real biological tissue. For example, control over such parameters as sample size, shape and homogeneity is almost impossible. Also, the internal placement of lesions within such media, a task which must certainly be performed when examining the tumor detection limits of Diaphanography, will be difficult and very imprecise due to the structured nature of human tissue.

The development of a synthetic material which simulates the optical properties of tissue over the visible and infrared would facilitate these fundamental studies and the above mentioned problems could be alleviated. However, besides possessing optical parameters comparable to biological tissue, a number of other characteristics must be incorporated into the phantom design if it is to be useful. For example, the components of the material should be chosen so as to ensure stability, reproducibility, availability and ease of preparation. Also, construction should be such that one has complete and precise control over its optical properties. Finally, the phantom material should be liquid so that accurate control over the shape and placement of internal lesions is achievable.

A synthetic breast material exhibiting the above characteristics would also find application in the clinical setting, both as a tool for diaphanography operator training

as well as for instrument calibration and quality assurance. At present, technician training involves test examinations of real patients. This makes for a learning environment which is both hurried and tension filled. Relying on patients for training purposes is also inconvenient in that consent must be obtained and a timetable for meetings organized. Finally, the examination of a few select patients cannot be expected to provide one with all the knowledge required to conduct proper diaphanography studies (for example, how does the appearance of a lesion change with increasing depth). Calibration and quality assurance, meanwhile, are currently nonexistent. If diaphanography is to become a useful clinical tool, procedures for both must be developed.

Photodynamic therapy studies would also benefit from the development of a tissue phantom exhibiting the characteristics mentioned above. As with diaphanography, many questions must be answered before this modality can achieve its full clinical potential. At present, the main problem confronting the physicist is that of determining the spatial distribution of light within tissue irradiated by either an internal or external source. To ensure the effectiveness of a particular treatment, one must be able to predict the intensity of light at any point in the treatment volume. At present, this is impossible with treatments being prescribed solely on the basis of the output of the light source. Mathematical models with the ability to theoretically describe the propagation of light through tissue are clearly required. However, the suitability and accuracy of these models must be tested against experimental measurements before they can be used in the clinical setting. In other words, the need exists for the experimental measurement of light distribution in tissue. Unfortunately, to carry out such measurements in real tissue is extremely difficult (the main problem is one of being able to move a detector throughout the solid medium though precise positioning of the probe is also difficult). A liquid phantom material would be ideal for such measurements. Light distribution studies could then be carried out in a medium exhibiting very similar optical properties to tissue but which offered none of the technical difficulties. Secondly, any test of the ability of a theoretical model to describe the propagation of light requires that measurements be carried out under conditions identical to those assumed by that model. Biological tissue, however, does not allow the control over optical parameters required to accomplish this. A well designed synthetic tissue phantom, meanwhile, does. The problem of matching experimental and theoretical environments is especially apparent when one considers that first generation light transport models will tend to be very simple, employing many approximations as to the structure and optical

characteristics of tissue. For example, models will tend to make the following simplifying assumptions: uniform density of interaction centers, infinite tissue size, absence of tissue interfaces etc. Such characteristics cannot be met when utilizing real tissue.

The verification of theoretical models is not the only reason for carrying out experimental measurements of the spatial distribution of light in tissue. These measurements are also required to answer such questions as "How does light source geometry affect tumor irradiation?" or "What is the maximum distance light can be expected to travel in tissue?". Questions of this nature are extremely important to photodynamic therapy and the quest for their answers would be greatly facilitated by the development of a suitable phantom material.

14.1 HISTORY OF TISSUE PHANTOMS

A very limited number of attempts have been made in the past to simulate the optical properties of tissue with a suitable phantom material. One of the earliest was made by Takatani [45]. As a result of the characteristic shape of the spectral extinction curve of most tissue types (almost constant extinction above 600 nm, high absorption below), Takatani concluded that the interaction of light and tissue could be described by two major processes, the virtually wavelength independent scatter (over the entire visible range) by the cellular matrix and the absorption of radiation in the vicinity of 550 nm by hemoglobin. As such, it should be possible to simulate the optical properties of tissue with a two component phantom, one component serving to scatter light, the other being responsible for absorption about 550 nm. Takatani used milk and blood for this purpose and demonstrated that the resulting phantom material possessed the same reflectance as gut tissue in vivo.

The main shortcoming of the Takatani phantom is its use of milk as a scattering material. Milk is homogeneous on the macroscopic scale. In other words, its scattering properties are adequately described by molecular optics. Tissue, meanwhile, is inhomogeneous on the macroscopic scale, it being an irregular arrangement of cells and fibers within a non-living intercellular material. Scatter characteristics should therefore be quite different.

Greenburg and Tribbe [46] employed a mixture of wax, animal fats and dye to construct a phantom material which was shown to possess a diffuse spectral extinction almost identical to that of human breast tissue (removed during a mastectomy) over the range 500 to 700 nm. The authors used

this simulated tissue to study tumor contrast in diaphanography examinations. Opaque and partially transmitting artifacts were embedded in the phantom material to simulate lesions and the resulting model transilluminated with a pulsed organic dye laser operating in a scanning mode. However, the usefulness of simulating breast lesions with opaque objects would seem limited. From the results presented in chapter 13, it would appear that tumor contrast can be attributed to differences in the absorption of light by hemoglobin. The Greenburg and Tribbe phantom fails to account for this mechanism. Also, the suitability of a dye to simulate absorption by hemoglobin is questionable, unless agreement between the optical properties of the dye and those of blood can be demonstrated. Finally, ease of preparation and widespread availability of the component materials do not apply to this phantom design.

Diaphanography contrast was also examined by Drexler et al. [23]. In this study, a breast phantom consisting of a flesh colored balloon filled with whole milk was used. Black, opaque tape of various sizes were suspended in the milk, at different distances from the balloon surface, by thin metal wires. The balloon was then transilluminated with a diaphanography light torch and the maximum depth at which these opaque lesions could be visualized determined as a function of size. Viewing was carried out using a vidicon camera focussed on the balloon surface on the side opposite to the light source. Images were found to be quite similar to those obtained during actual diaphanography breast examinations. From this study, the authors were able to conclude that diaphanography procedures were able to detect opaque objects at depths up to twice their size. However, as with the Takatani phantom there is some question as to the suitability of using whole milk to simulate the scatter properties of tissue. Secondly, as mentioned in the last paragraph, it would seem inappropriate to simulate breast lesions by opaque objects. Finally, the phantom fails to take into account light absorption, a process which has been shown in chapter 13, as well as by other authors, to be extremely important, especially when considering tumor contrast.

A number of authors have reported changes in the optical properties of the tissue of laboratory animals immediately post mortem. The most widely accepted theory attributes this phenomenon to variations in blood content and/or oxygenation upon sacrifice. In an effort to investigate this hypothesis, Wilson et al. [32] developed a tissue phantom based on a 2% agar solution and whole rabbit blood; sodium hydrosulphite was used to control the state of oxygenation of the blood component. Depth of light penetration was then measured as a function of wavelength on a series of phantoms characterized by various states of blood oxygenation and

concentration. Once again, the major shortcoming of this phantom arises as a result of the selection of a macroscopically homogeneous medium to simulate the scatter of tissue. Another major drawback is that agar solidifies to form a gel and this property makes the material inappropriate for light distribution measurements. Although the insertion of detectors is easy, movement of these probes throughout the material results in physical damage to the medium.

Marynissen and Star [43] have adopted the two component approach of Takatani. These authors developed a phantom material from a solution of polyvinyl acetate particles (pure scatter component) and India ink (pure absorption component). This phantom offers the advantage that the scattering component is of particulate form and as such, is macroscopically inhomogeneous. By altering the size of the synthetic particles, one can control the angular dependence of the scatter associated with the individual interaction centers and therefore attain a much closer match to real tissue. The major shortcoming of the Marynissen phantom is its use of India ink to simulate the absorption of blood in tissue. Such a substance has not been shown to be a suitable replacement for hemoglobin.

14.2 DEVELOPMENT OF TEM

In order to facilitate the study of light propagation in tissue, a homogeneous liquid material was developed to simulate the optical properties of tissue over the range 550 to 900 nm. This substance enabled an examination of light transport in a highly controlled and stable environment which displayed many of the optical characteristics of real biological tissue.

The tissue phantom material, or TEM (Tissue Equivalent Medium), is based on the two component approach of Takatani. However, its design avoids many of the shortcomings of other two component models. The materials used in the phantom construction, as well as their concentrations, were chosen so as to yield a substance which exhibited the same diffuse spectral extinction as human glandular breast tissue, as measured in our laboratory. The assumption is made that such a match will yield a substance whose optical properties are very similar to that of real biological tissue in general.

The scatter component of TEM consists of an aqueous solution of powdered coffee creamer and Methocel. When in solution, the creamer (Dickson's Coffee Top), because of its powdered form, constitutes a particulate suspension and

serves to scatter light in a manner similar to the cellular matrix of tissue. Figure 14.1 is a microscope photograph of a typical aqueous solution of creamer particles after staining. The individual granules are ellipsoidal in shape with an average major axis length of $3.5 \mu\text{m}$ and an average minor axis length of $2.3 \mu\text{m}$ (their size is about 1/2 that of an average red blood cell). It is therefore expected that the light scatter characteristics of TEM particles and tissue cells will be similar. The coffee creamer particles were composed of glucose solids, hydrogenated vegetable oils, sodium caseinate, potassium phosphate dibasic, glycerides, sodium aluminum silicate, sodium 2-stearoyl lactylate, lecithin, propyl gallate and citric acid; they do not dissolve in water.

Methocel is a methylcellulose product (Dow Chemical Co.) used to suspend cell colonies grown in culture. When mixed with hot water and then cooled, this flaked material forms an optically transparent, viscous liquid which, in this application, served to do nothing more than support the scattering particles in a rigid arrangement of uniform density. Figure 14.2 illustrates the spectral extinction of a 1.0 cm thick aqueous solution of Methocel as measured by a Spectronic 710 spectrophotometer (measured relative to water). Quite clearly, the contribution to TEM extinction made by this component will be insignificant. The resulting aqueous mixture of creamer and Methocel provides an inhomogeneous particulate solution which, if prepared in the correct concentrations, can be used to simulate the scatter of tissue over the range 500 to 900 nm. Absorption of light over this range will be extremely small (that which does exist may be attributed to the water solvent).

Hemoglobin functions as the absorbing component of TEM. Whole blood, obtained from a patient suffering from no known blood disorders, was lysed by the addition of distilled water. In the lysing process, the individual red blood cells burst, releasing their hemoglobin to the surrounding liquid medium. The direct result is uniform distribution of hemoglobin and, therefore, a liquid substance which is optically homogeneous on the macroscopic scale (the remaining cellular membranes or "ghosts" are transparent and do not constitute an inhomogeneity). The spectral extinction of this hemolyzed solution is shown in figure 14.3 for measurements carried out using a Spectronic 710 spectrophotometer (measurements carried out relative to water). Below 600 nm, this solution exhibits the characteristic absorption peak of hemoglobin. However, scatter is negligible over the entire range 500 to 900 nm and no absorption peaks are evident above 600 nm. The solution is therefore, well suited for simulating the absorption of light by tissue.

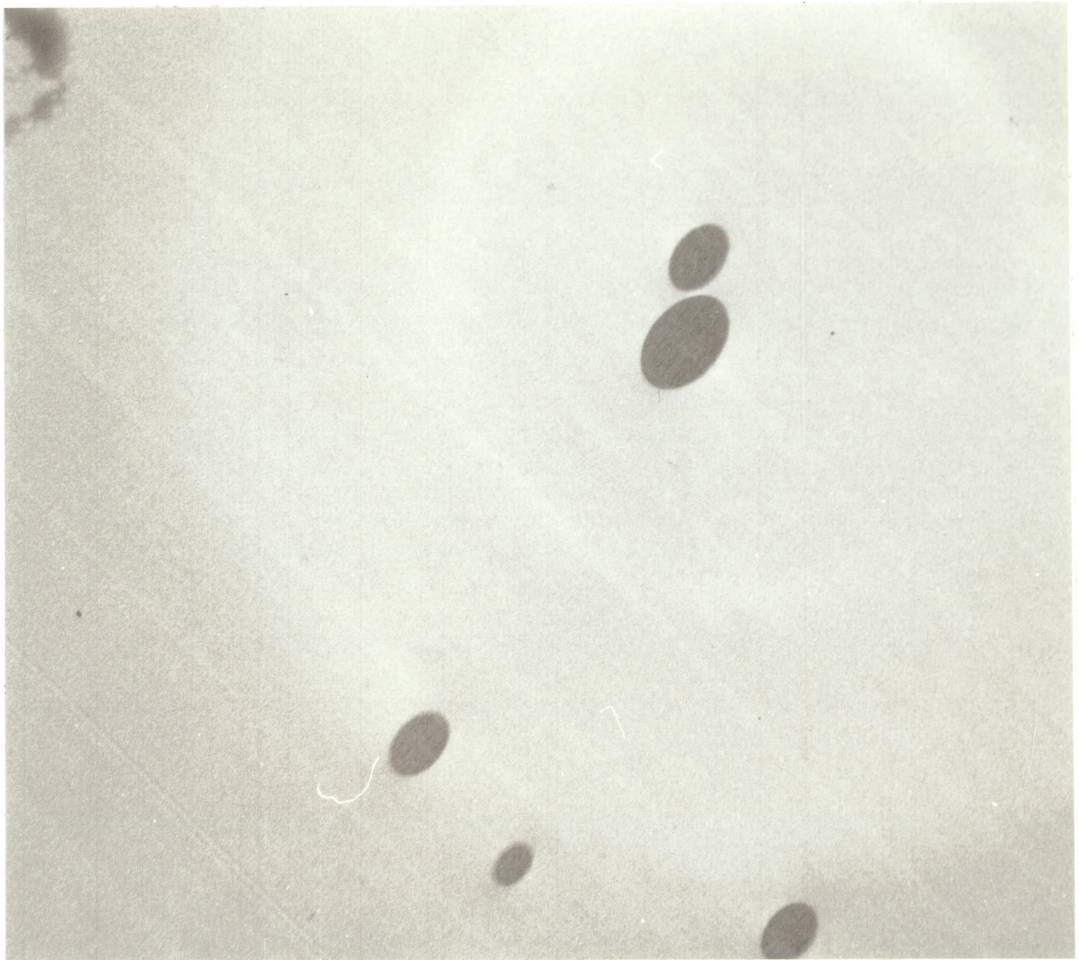


Figure 14.1: Microscope photograph of an aqueous solution of creamer particles (after staining)

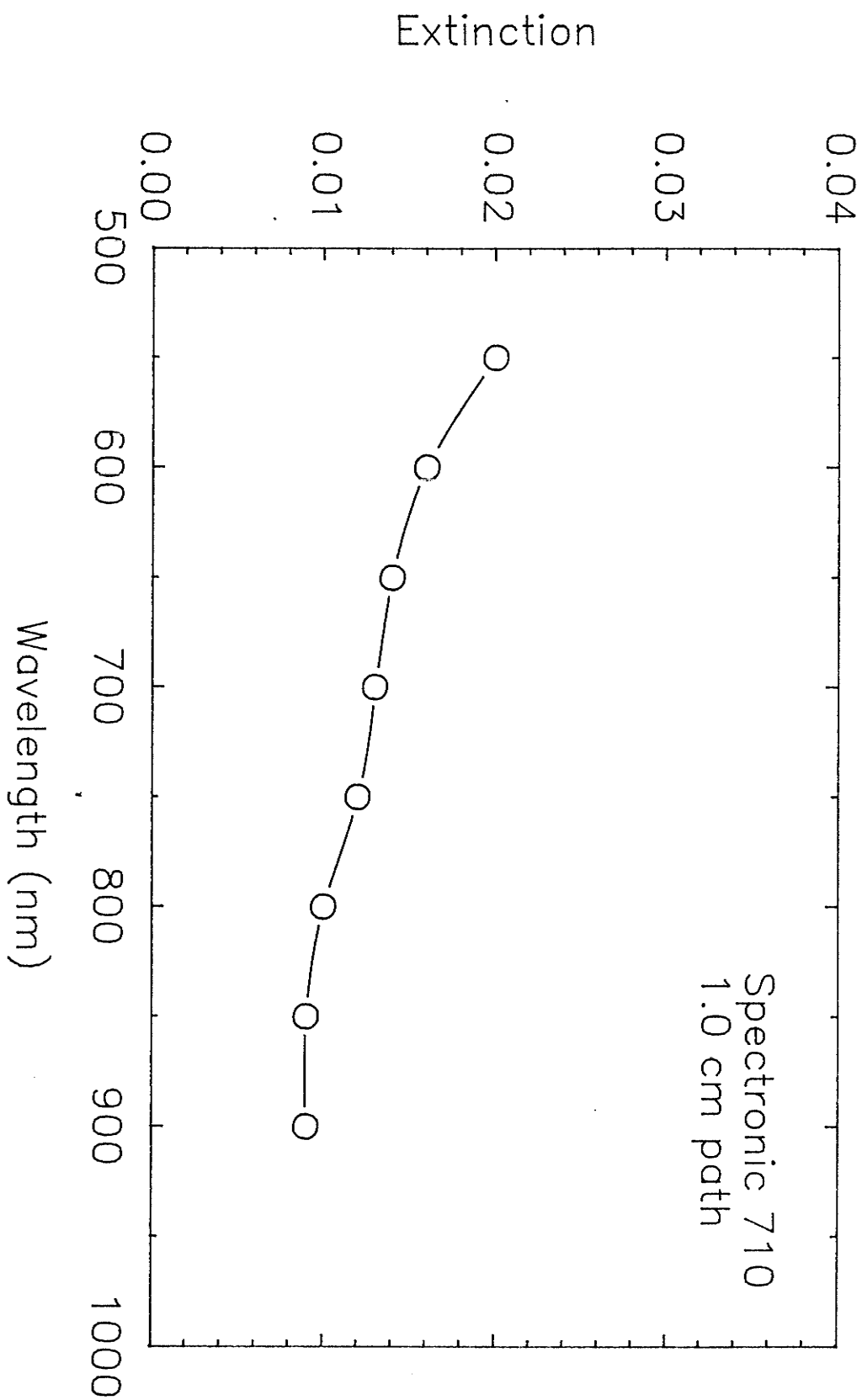


Figure 14.2: Diffuse spectral extinction of an aqueous solution of Methocel

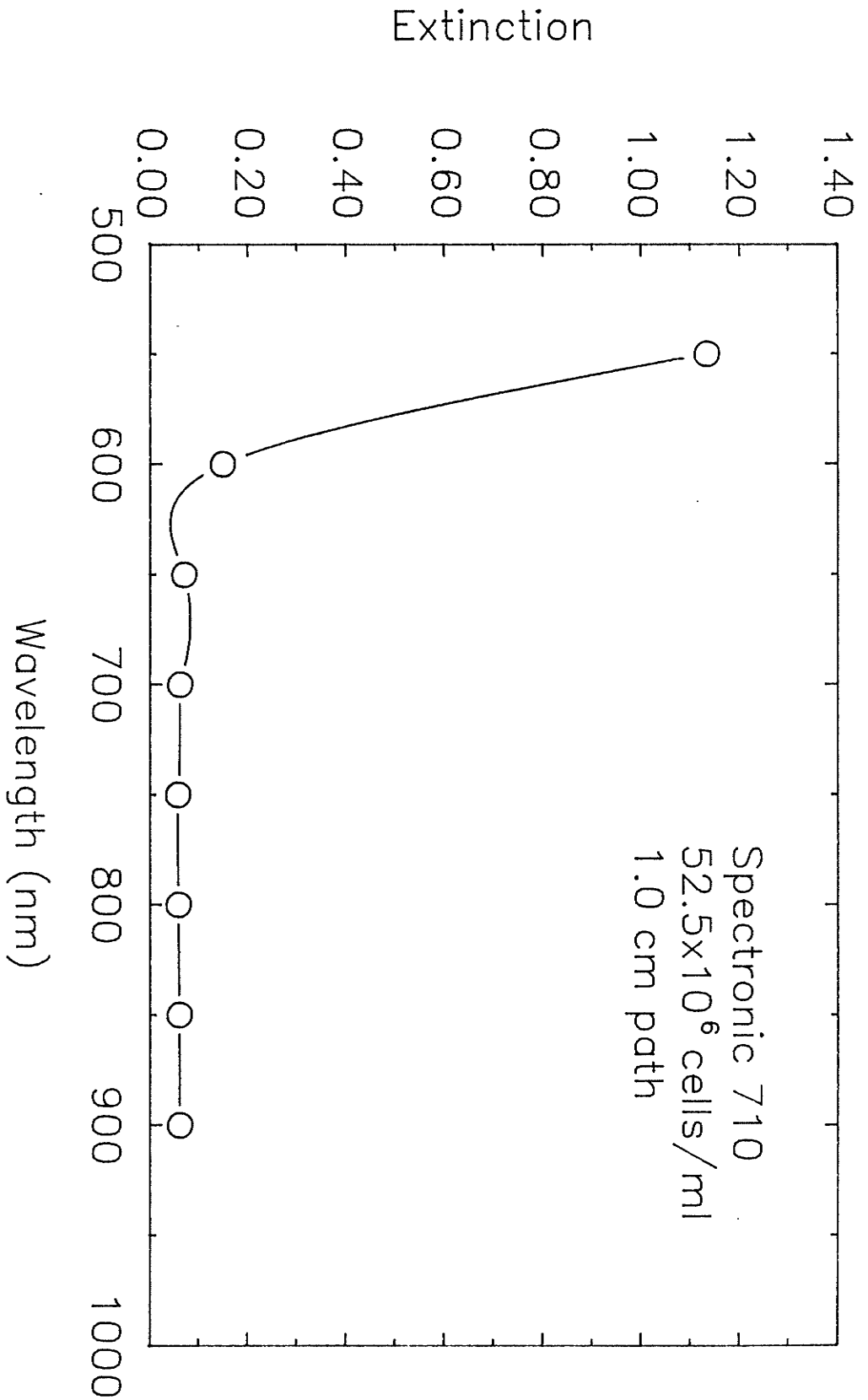


Figure 14.3: Diffuse spectral extinction of hemoglobin

By combining the pure scatter and pure absorbing components described above in the correct proportions, a solution was obtained which exhibited the same diffuse spectral extinction as human glandular breast tissue. Figure 14.4 shows the extinction curves for both as measured by the DICOM-8 system. The particular mixture illustrated in this diagram consists of 0.5% Methocel, 5.0% creamer and 1/800 hemoglobin concentration of normal whole blood. It should be noted that the spectral extinction curve of TEM is not identical to that of real tissue. Agreement could be improved, however, by making slight adjustments to the relative concentrations of the two components. Nevertheless, in view of the variations in the optical properties of breast tissue removed from different patients, this fine tuning was deemed inappropriate and the mixture of figure 14.4 was assumed to exhibit adequate optical equivalence to real breast tissue. A recipe for its preparation is given in Appendix A. The simulation of other tissue types may require different component concentrations.

The most desirable feature of TEM (besides its ability to simulate the optical properties of tissue) is the complete control which one has over its optical properties. By suitably adjusting the relative concentrations of the two components, one can construct media characterized by a very wide range of properties, from very strongly absorbing and weakly scattering, to very weakly absorbing and strongly scattering. Also the very nature of the scatter and absorption components enables one to alter one interaction mode independently of the other. Figure 14.5 demonstrates the effect of adjusting the relative concentrations of the two constituent components. TEM composition, and therefore optical properties, is designated by a two number system A/S where A refers to the concentration of the absorbing component and S to the concentration of the scatter component. A specification of TEM 10/10 refers to the phantom mixture illustrated in figure 14.4, ie to a TEM showing full tissue equivalence. A TEM 5/10 signifies a medium exhibiting the same light scatter properties as glandular breast tissue but with only half the hemoglobin concentration. An A or S of zero indicates that the medium possesses no absorption or no scatter component, respectively.

For a tissue simulating material to be useful, it must exhibit two other characteristics, stability and reproducibility. To demonstrate the former quality, a sample of TEM 10/10 was prepared and its spectral extinction measured on the DICOM-8 system. This sample was then stored at -4.0 degrees celsius for 40 days at which time the sample was brought to room temperature and its spectral extinction remeasured. Figure 14.6 shows both curves, giving some indication of TEM stability. It appears that the optical properties of this phantom material will remain constant

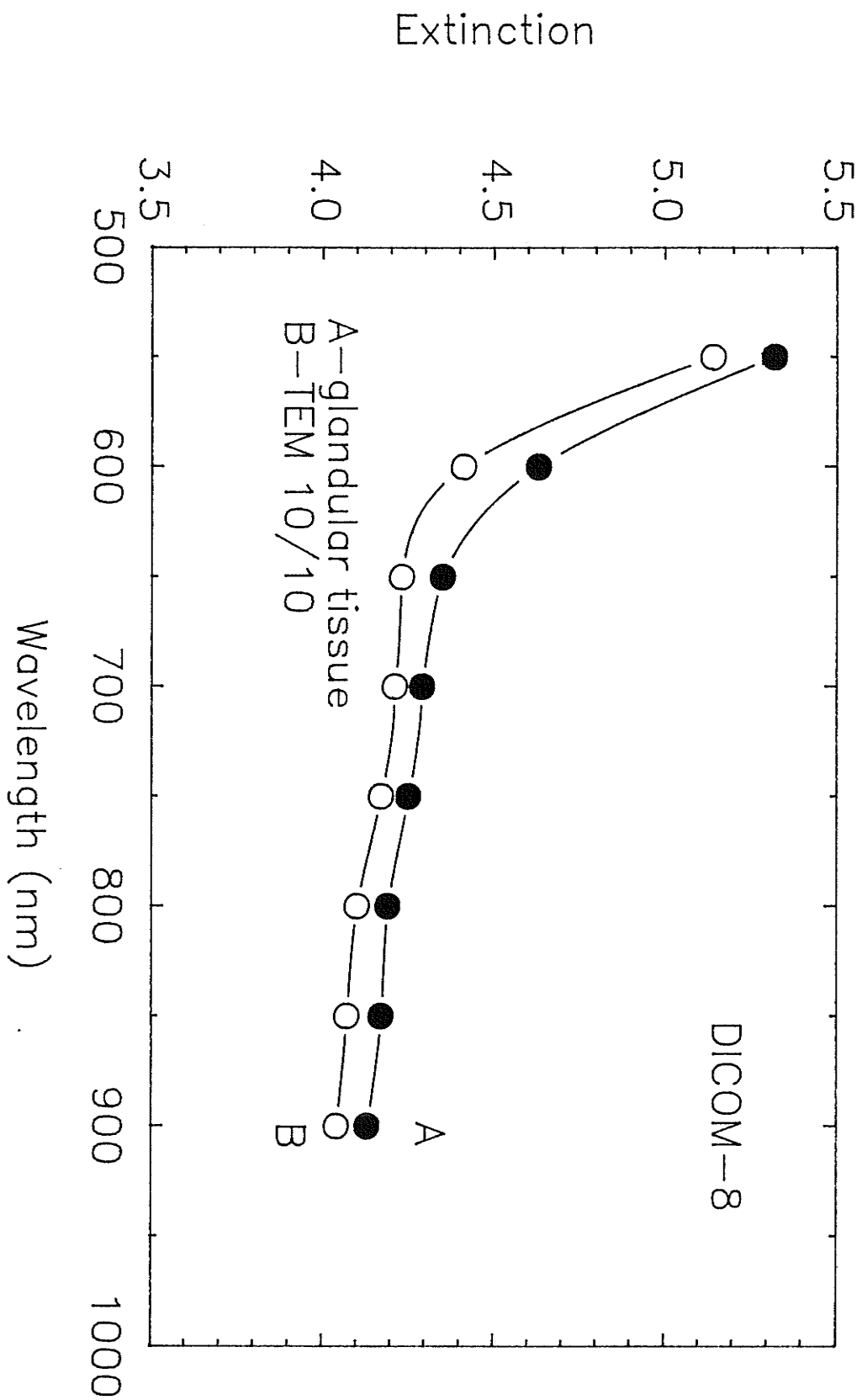


Figure 14.4: Diffuse spectral extinction of glandular breast tissue and TEM 10/10

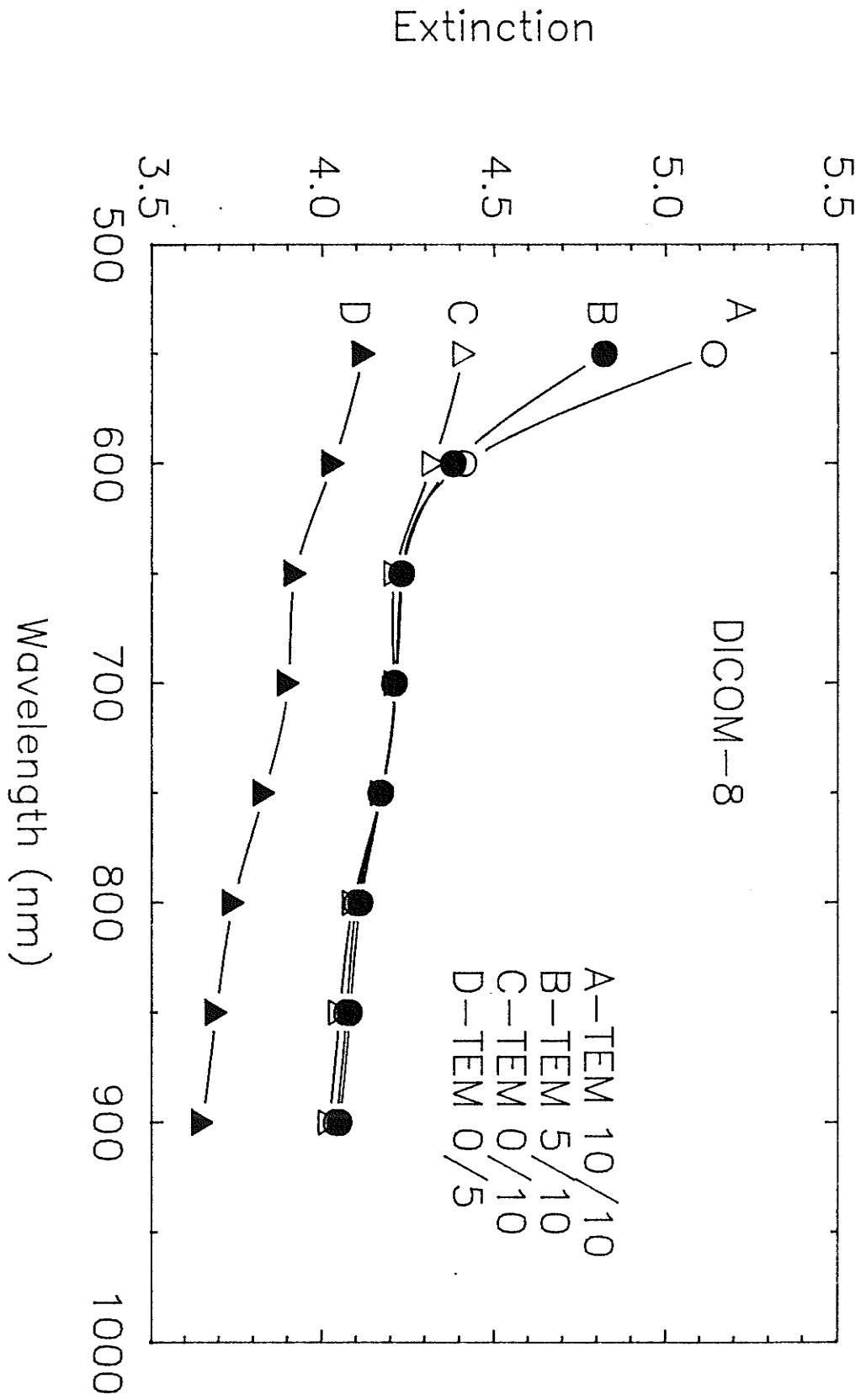


Figure 14.5: Effects of adjusting the relative concentrations of the two constituent components of TEM

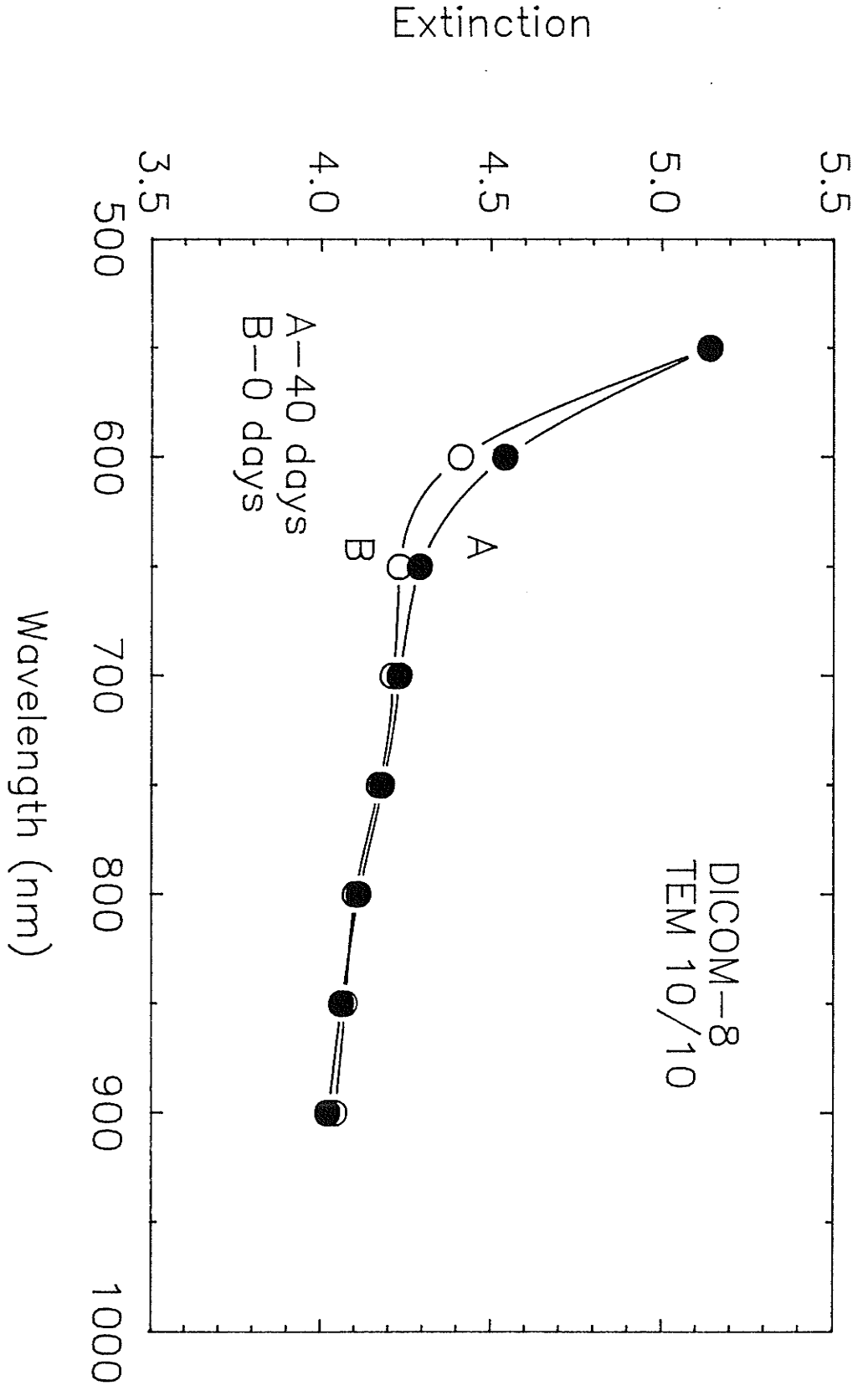


Figure 14.6: TEM stability

DICOM-8
TEM 10/10

over periods of at least 40 days. TEM reproducibility is illustrated in figure 14.7. Two different batches of the phantom material were independently prepared and the spectral extinction of each measured on the DICOM-8 system. It is apparent that the optical properties of TEM are quite reproducible, provided that the proper method of preparation is followed.

14.3 CONCENTRATION OF CREAMER PARTICLES

TEM was developed by determining experimentally the mass of coffee creamer which, when in aqueous suspension, yielded the same spectral diffuse transmittance as human glandular breast tissue. As such, its preparation involves suspending a known mass of creamer rather than a known concentration of particles in a water/Methocel solvent. Nonetheless, by employing a few very reasonable assumptions and approximations, an estimate of the concentration of scatter centers in TEM may be obtained. The procedure is described below.

By monitoring the change in the water level of a half filled graduated cylinder upon submersion of a known mass M of coffee creamer, it is possible to determine the total volume V of particles contained in that sample. Using this technique it was found that an 8.312 g creamer sample will possess a volume of 5.0 cm^3 . Thus, the density of coffee creamer is

$$D = M/V = 8.312/5.0 = 1.662 \text{ g/cm}^3 \quad (14.1)$$

From figure 14.1 it would appear that the creamer scattering particles possess an almost elliptical cross section. It would therefore seem reasonable to approximate their shape by prolate spheroids (such a volume is generated by rotating an ellipse about its major axis). By visually inspecting figure 14.1, a particle was selected as being representative of the average and its major (a) and minor (b) semi-axes measured. Values of 1.75 and $1.15 \text{ } \mu\text{m}$ were obtained, respectively. The volume of the average particle was then calculated as

$$V = (4/3)\pi ab^2 = 9.694 \times 10^{-12} \text{ cm}^3 \quad (14.2)$$

With this information, the mass of an average scatter particle may be estimated.

$$M = DV = 1.611 \times 10^{-11} \text{ g} \quad (14.3)$$

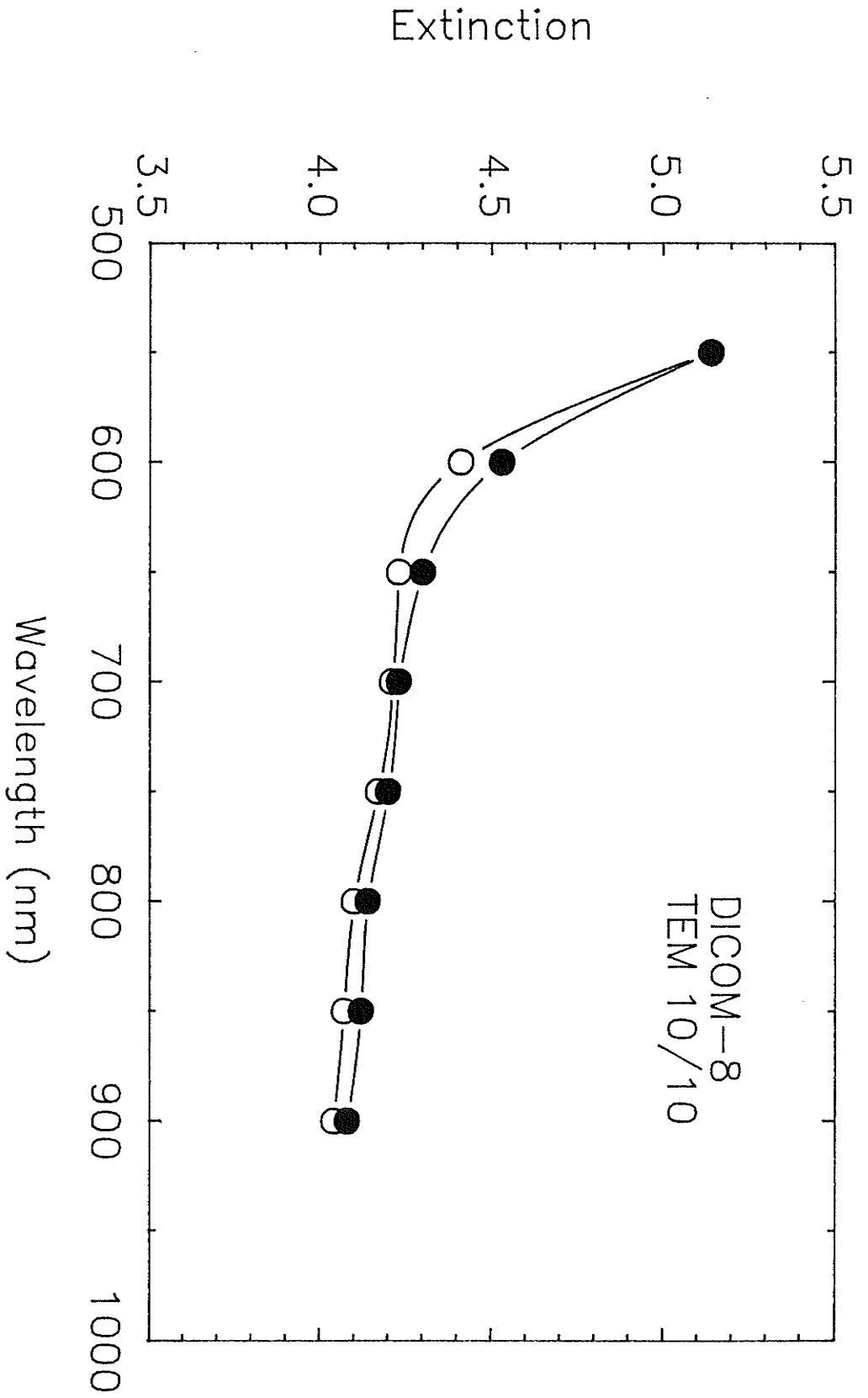


Figure 14.7: TEM reproducibility

TEM 0/10 is produced by suspending 5.0 g of coffee creamer in 50 ml of water and then diluting by a factor of two using a water/Methocel solvent. The number of creamer particles in the typical TEM 0/10 sample is therefore

$$N = 5.0/M = 3.104 \times 10^{11} \quad (14.4)$$

This results in a concentration of scatter centers of

$$C = N/V_1 = 2.928 \times 10^9 / \text{cm}^3 \quad (14.5)$$

where V_1 represents the volume of the water solvent plus the volume occupied by the creamer particles themselves.

Concentration can now be used to determine the average distance of separation of the scatter interaction centers. Assuming the particles to be uniformly dispersed in the solution, the TEM sample may be divided into N volume elements of equal size with each being occupied by one particle positioned at its center. The volume of such an element is given by $1/C = 3.415 \times 10^{-10} \text{ cm}^3$. Assuming each element to be cubic, the average distance between particles is calculated to be

$$X = (1/c)^{1/3} = 6.99 \mu\text{m} \quad (14.6)$$

Van de Hulst has stated that particle suspensions will be characterized by independent scattering if the distance of particle separation is greater than three times particle radius. Using the "worst case" scenario and selecting an average particle radius of $1.75 \mu\text{m}$, it would appear that scatter within TEM may be considered independent ($3 \times 1.75 = 5.25 \mu\text{m}$). Thus, the theoretical results developed for independent scatter systems may be applied to scatter within TEM.

Chapter XV

MULTI-SPECTRAL DIGITAL IMAGING STUDIES

Results presented in chapter 13 suggest that significant differences exist between the diffuse spectral extinction curves, and therefore the optical properties, of normal and diseased breast tissue. Carcinoma, because of a higher hemoglobin concentration, will be characterized by a greater extinction than normal tissue of the same thickness. It is for this reason that tumors will appear as regions of decreased light intensity with respect to normal tissue in diaphanography images. Between 700 and 900 nm, the difference in extinction between these two tissue types is quite small. However, as one moves from 700 nm towards the characteristic absorption peak of blood (550 nm), this difference increases rapidly.

With diaphanography, one is interested in optimizing contrast between the images of normal tissue and carcinoma. As contrast will be directly related to variations in the optical characteristics of the two tissue types, it is desirable to transilluminate the breast with light corresponding to the wavelengths at which these differences are maximum. Using this selection criterion and drawing on the DICOM-8 tissue extinction results, it would appear that diaphanography examinations should be carried out at wavelengths in the vicinity of 550 nm. However, transillumination with short wavelength visible light leads to a very serious technical difficulty, that of low image intensity. Although one can obtain very high image contrast by employing yellow light, the strong attenuation by tissue in this spectral region will result in only a small fraction of the incident light photons being transmitted completely through the breast. As a result, the intensity of the exit surface light pattern will be low and a standard vidicon camera will be unable to acquire a suitable diaphanographic image (low SNR). At higher wavelengths tissue attenuation will be greatly reduced and breast transmittance will increase, but at the expense of contrast.

To examine these ideas further, under conditions more closely resembling those of a breast examination, a bench top diaphanography unit was developed (figure 15.1). The instrument represents a slight modification to the DICOM-8 spectrophotometer. Both the fiber optic cable and fiber optic coupling assembly have been removed from the system so

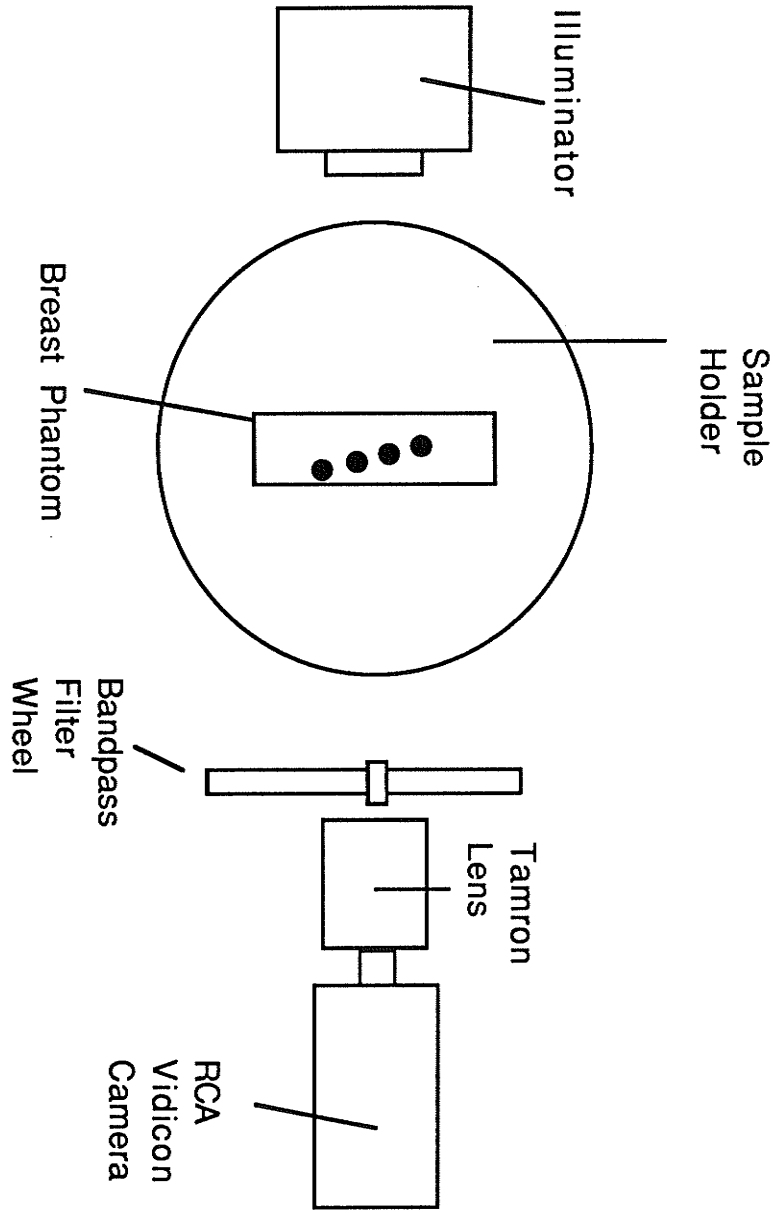


Figure 15.1: Bench top diaphanography unit.

that the lamp output now consists of a large, 35 mm diameter broad beam rather than the thin pencil employed in the spectrophotometer. An opal diffusing screen was attached to the output port of the lamp housing so as to increase uniformity across the beam area. A breast phantom, shown in figure 15.2, is positioned in the sample holder in place of the tissue specimen. The phantom consists of an optically transparent, plastic tissue culture flask (obtained from Falcon) mounted on a support base as shown. The two large parallel faces of the flask serve as entrance and exit surfaces for transillumination. The flask is filled with TEM 10/10 to simulate a 1.8 cm thickness of breast tissue. Four polyethylene tubes (obtained from Intramedic) were positioned vertically inside the flask at distances of 4.0, 8.0, 12.0 and 16.0 mm from the exit surface. Each possessed an inner and outer diameter of 1.19 and 1.70 mm, respectively, while the distance of separation between the front face projection of consecutive tubes was 6.0 mm. These tubes were filled with whole blood to simulate breast carcinoma. Two additional culture flasks, each of thickness 1.5 cm, were filled with TEM 10/10 and positioned between the light source and the phantom so as provide a total tissue-equivalent thickness of 4.8 cm (the four polyethylene tubes remained 4.0, 8.0, 12.0 and 16.0 mm from the exit surface of the phantom material, respectively). The RCA vidicon camera was focussed on the exit surface of the phantom and the video output signal sent to the DICOM-8 computer for digitization and subsequent display. It is of interest to note that the vidicon camera utilized in this system is identical to that of the commercial diaphanography unit marketed by Spectrascan. Melles-Griot bandpass interference filters were used to obtain images at selected wavelengths.

It was suggested in Chapter 13 that normal tissue/tumor contrast in a diaphanography image is the result of differences in hemoglobin concentration between the two tissue types. It would therefore seem reasonable to simulate carcinoma, at least in so far as diaphanography contrast studies are concerned, with whole blood. Such a representation may be considered extreme (hemoglobin concentration in tumors will in fact be much lower) but will yield a model which should incorporate the mechanisms thought to be responsible for the production of the characteristic diaphanography image.

Figure 15.3 is the transilluminated image of the breast phantom for light of 700 nm. Under these conditions, it is difficult to visualize any of the tubes. Although it is conceivable that tube contrast could be improved by transilluminating the phantom with light of a shorter wavelength (ie. 600 nm), attempts to do so failed as a result of the technical difficulty mentioned above. Efforts

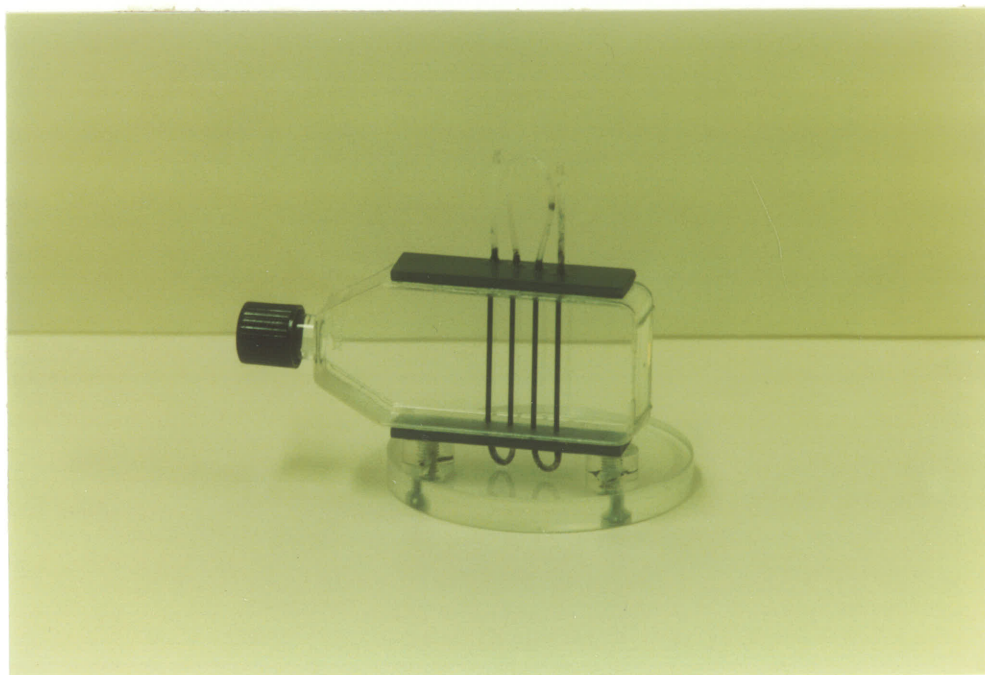


Figure 15.2: Breast Phantom

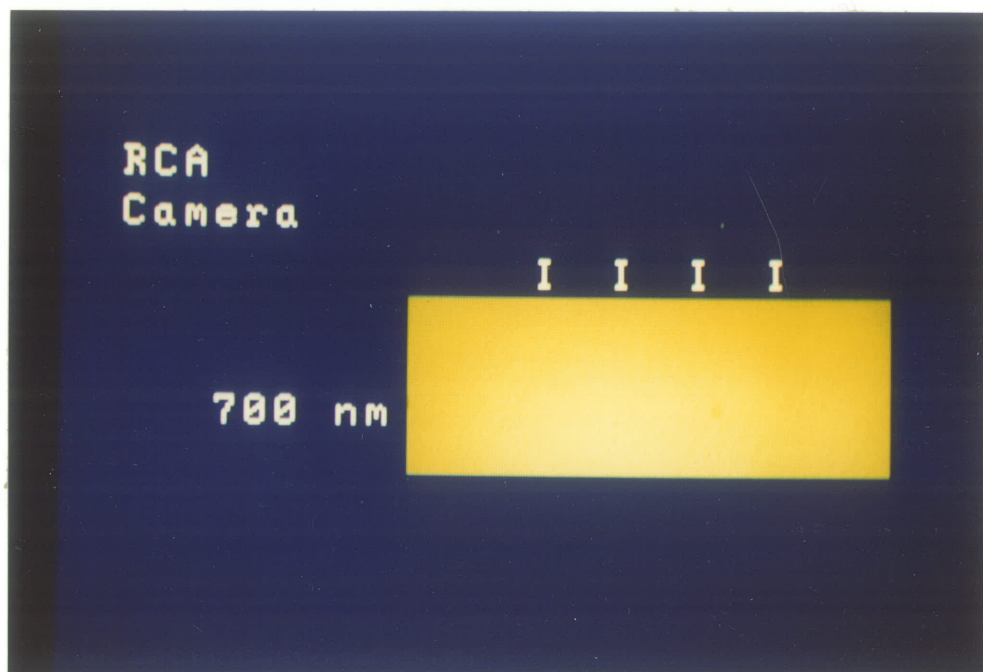


Figure 15.3: Transillumination image acquired at 700 nm using an RCA vidicon camera

to acquire images at longer wavelengths (ie. 850 nm) were also unsuccessful though reduced camera sensitivity rather than inferior light transport was responsible.

In an attempt to overcome these image acquisition problems, the RCA vidicon was replaced with a camera which possessed a much improved response at low light levels. The camera, manufactured by Fairchild, consisted of a CCD array with second generation microchannel image amplifier. Figures 15.4, 15.5 and 15.6 represent images collected at 600, 700 and 850 nm, respectively. Because of the increased sensitivity of the Fairchild camera, the light intensity at the phantom exit face was sufficient for image acquisition at all three wavelengths. To improve the signal to noise ratio, frame averaging techniques were employed (images 15.4, 15.5 and 15.6 represent averages of 256 video frames).

Two important points should be noted. Firstly, lesion contrast is significantly improved at 600 nm compared to 700 nm. Whereas it is virtually impossible to visualize any of the four tubes in the 700 nm image, two can be seen in that obtained with light of 600 nm (the tube closest to the exit face of the phantom being the most visible). This improved contrast can be attributed to the fact that differences in optical properties of the two "tissues" are much greater at the lower wavelength. However, increased tissue attenuation at 600 nm reduces the efficiency with which light is transported through the breast, resulting in a much reduced exit surface intensity and therefore, necessitating the use of a more sensitive camera. One should also keep in mind that light scatter in tissue increases with decreasing wavelength. This suggests that image information carried by light of 600 nm will be lost at a greater rate as it travels through overlying normal breast tissue (that is, tissue overlying the lesion to be imaged) than light of 700 nm. However, the contrast lost as a result of this phenomenon will be insignificant when compared to that gained as a result of the increased variations in optical properties. The second point to be noted is the similarity in lesion contrast between the images collected at 700 and 850 nm. As with 700 nm, transillumination of the phantom with light of 850 nm yielded an image in which no tubes were visible. This similarity in image contrast is due to the fact that differences in the optical properties of normal and carcinoma tissue remain quite constant over this spectral range.

Digitization of a transillumination image allows one the opportunity to employ digital processing techniques to improve image appearance. For example, figure 15.7 is the resultant image obtained by digitally subtracting figures 15.4 and 15.5 (images acquired at 600 and 700 nm, respectively). Such a technique enhances differences between

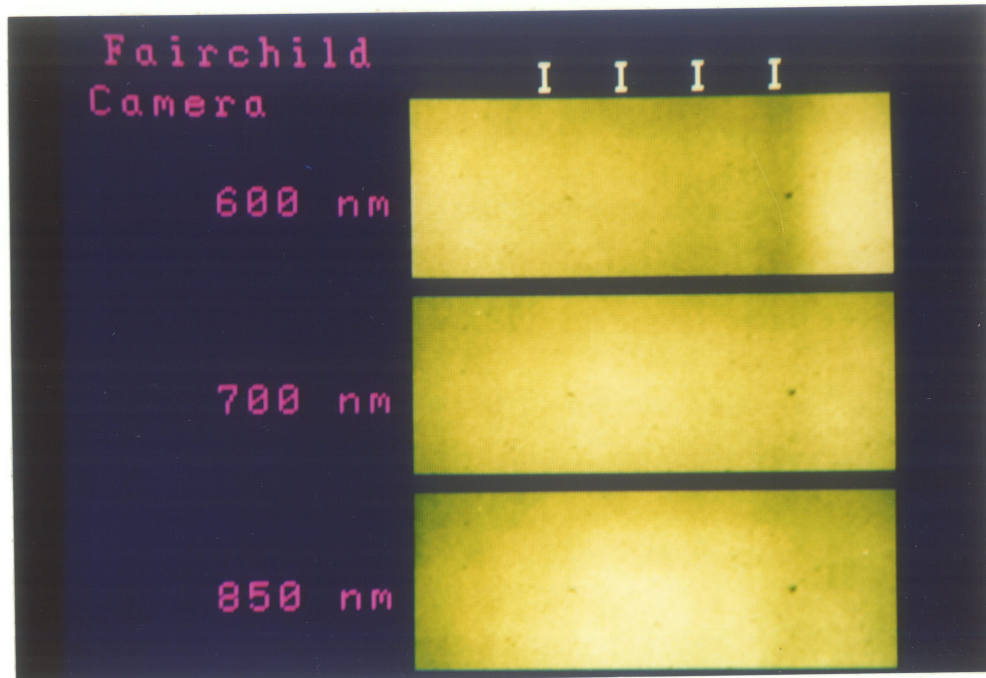


Figure 15.4, 15.5 and 15.6: Transillumination images acquired at 600, 700 and 850 nm using a Fairchild camera

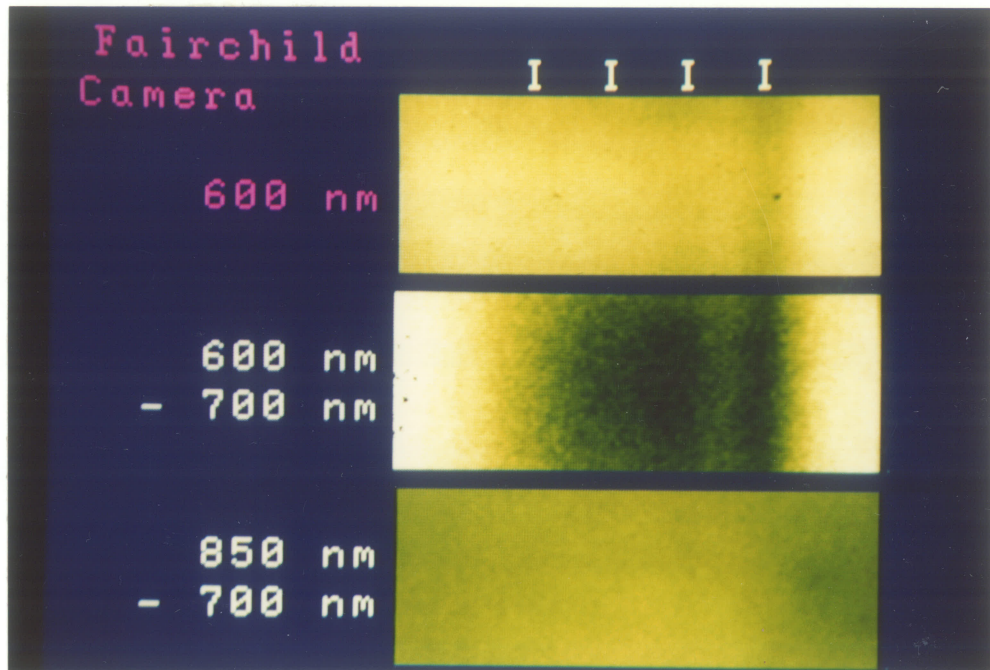


Figure 15.7 and 15.8: Resultant of subtracting the 700 nm image from that acquired at 600 and 850 nm, respectively

the two images and can be seen to improve lesion contrast significantly; three tubes are clearly detectable, while the fourth is just visible. The same procedure was used to generate figure 15.8 although now subtraction involves figures 15.5 and 15.6 (images acquired at 700 and 850 nm, respectively). As the differences between these two images are not as significant, contrast is much poorer than in the previous subtraction.

Tube visualization will also be highly dependent on the way in which the output signal from the camera is displayed on the video monitor ie. on the particular mapping chosen to assign grey levels to the vidicon output voltage. Windowing [49] is a method of display whereby a portion of the total camera signal (ie. a band) is linearly mapped to the full range of 256 grey levels available for display. With this technique, contrast can be increased in a selected region of interest in the image. Information contained in portions of the image falling outside the chosen video band, however, will be lost. A second display technique, referred to as Adaptive Histogram Equalization (AHE) [49], enables one to improve contrast in all regions of the image simultaneously. With the AHE method, the assignment of grey levels to camera signal is automatically adapted in a way that varies smoothly across the image according to local needs for the presentation of contrast. Local mapping is carried out by assigning grey levels in the proportion to the number of pixels in the corresponding range of the output video levels. Figures 15.9 and 15.10 illustrate the improved contrast that can be obtained through windowing and adaptive histogram equalization, respectively; in both instances, processing has been performed on the 600 nm Fairchild image. It is quite clear that digital image processing is powerful tool which can increase the amount of information extracted from a diaphanography image.

The images presented in this chapter demonstrate the improved image contrast that can be attained by utilizing light of 600 nm to transilluminate the breast in diaphanography. Although increased tissue attenuation makes image acquisition more difficult, it appears that this technical problem may be overcome by employing a video camera of increased sensitivity. Finally, it has been shown that significant improvements can be made to diaphanography images through the use of digital image processing techniques.

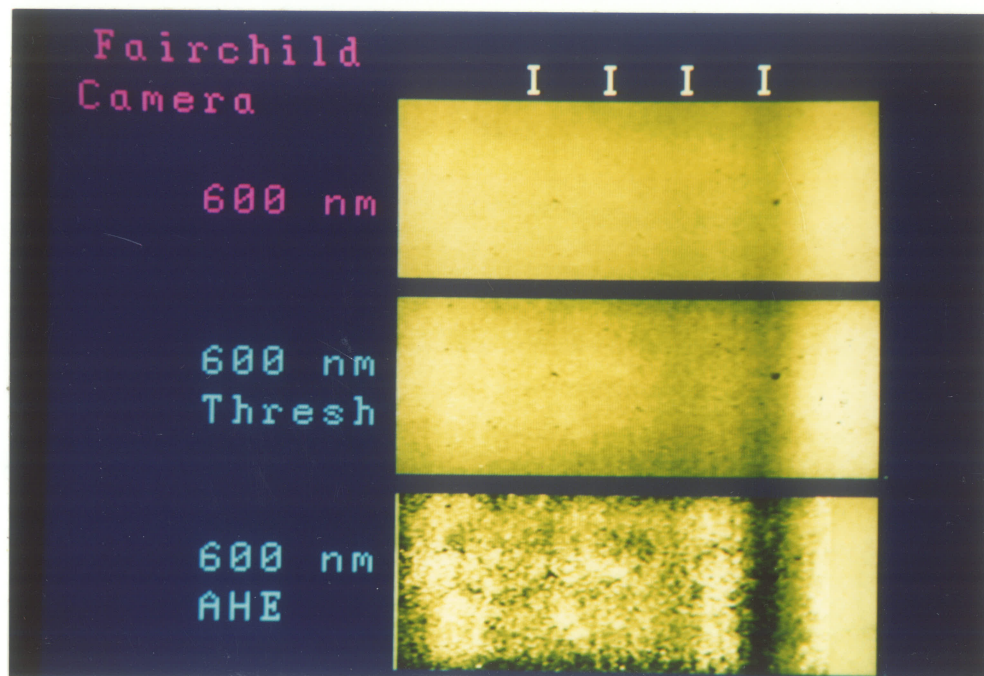


Figure 15.9 and 15.10: 600 nm transillumination image with windowing and adaptive histogram equilization

Chapter XVI

APPLICATION OF THEORETICAL MODELS

Theoretical transport models such as Linear Transport and Diffusion theory are the keys to a better understanding of the propagation of light through biological tissue. Armed with the knowledge they provide, it would be possible to optimize the visible and near infrared light procedures currently in use in medicine. For example, such models could be used to select the optimal wavelength for transillumination in Diaphanography or to predict the spatial distribution of light in PDT treatments. However, before these models can realize such applications, their ability to describe the propagation of light through tissue must be tested.

An investigation into the accuracy of the Linear Transport and Diffusion theories was carried out as part of this thesis, through a comparison of experimental spatial light distributions, measured within a scatter/absorbing medium under highly controlled irradiation geometries, with those obtained theoretically. The medium utilized in these tests was TEM, it being ideally suited for spatial light distribution measurements and allowing one complete control over the optical properties of the medium of propagation. Two irradiation geometries were examined, the internal isotropic point source/infinite medium and internal isotropic planar source/infinite medium, their selection being made on the basis of simplicity and ease of simulation.

To generate spatial light distributions using either the Linear Transport or Diffusion models, two input parameters are required, the mean free path l and the scatter/absorption coefficient c of the medium through which the light is propagating. Both l and c are fundamental parameters in that they depend on the composition and physical structure of the medium (as well as the wavelength of light) but not the irradiation geometry. The procedures used in the measurement of the MFP and scatter/absorption coefficient of TEM are outlined below. Once these parameters have been determined, it is possible to generate the theoretical light distribution associated with any arbitrary irradiation geometry for which the Linear Transport or Diffusion equations have been solved.

16.1 MEAN FREE PATH

The mean free path of a material has previously been defined as the average distance light photons propagating through that medium will travel between successive absorption or scatter interactions. In section 8.1 it was stated that this fundamental property of light transport was equal to the reciprocal of the attenuation cross section per unit volume of the medium. Besides being dependant on the physical properties and structure of the material, MFP will also vary with the wavelength of light.

Two very different approaches may be used to measure the MFP of a material. The indirect method requires that the spatial distribution of light within a test medium be determined for a particular irradiation geometry. Statistical analysis techniques are then used to obtain the "best fit" of a theoretical model describing such a geometry to this data. Such a procedure will generate estimates of the two input parameters (MFP and scatter/absorption coefficient) associated with the mathematical model. However, this procedure suffers from a number of technical limitations. Firstly, results are only as accurate as the theoretical model used in the fitting procedure. The application of models which fall short in their ability to precisely describe the propagation of light through biological tissue will lead to erroneous results. Secondly, this indirect method of determining MFP assumes that the geometry used in generating the experimental distributions can be accurately controlled and simulated by the theoretical model. Such control, however, is often beyond experimental capabilities.

An alternative technique (the direct approach) which may be used to determine the MFP of a material involves measurement of the extinction of very thin samples. If the thickness of the specimen is sufficiently small, light scatter contributing to the sample's attenuation may be considered single and Beer's law applied.

$$E = \sigma(\text{att})d = d/l \quad (16.1)$$

Provided sample thickness is accurately known, MFP may be calculated from sample extinction. In theory, a specimen characterized by single scatter may be produced from any material, regardless of the density of its scatter interaction centers, by making it sufficiently thin. In the case of biological tissue, fulfillment of the single scatter criterion requires sample thickness be less than 100 μm . As tissue is so very inhomogeneous, great care must be taken to ensure that the thin samples used in direct measurements are representative of the tissue type in general and not local fluctuations in composition. This makes for an extremely

difficult task. Wilson et al. [50] have examined the advantages and disadvantages of the direct and indirect methods in some detail.

The MFP of TEM 0/10 was determined using the second approach, through an application of Beer's law to the attenuation of a very thin sample. Transmittance based MFP measurements of TEM do not suffer from the technical difficulties associated with those carried out on biological tissue. Because it is a liquid, TEM thickness may be controlled much more easily. A sample sufficiently thin to ensure single scattering was produced by placing TEM 0/10 between two glass microscope slides (.88 and .99 mm thick, respectively) separated by a 47 μm thick, u-shaped, brass spacer (see figure 16.1). By forcing the glass slides together with tape and alligator clips, a 47 μm thick sample of TEM was formed. Also, because TEM is homogeneous on the macroscopic scale, ensuring that such a specimen be representative of the medium in general and not local fluctuations in composition was no longer a problem.

The 47 μm sample of TEM 0/10 was placed in a Spectronic 710 spectrophotometer and its extinction measured over the range 500 to 950 nm in 50 nm steps. Data was referenced to the extinction of a 47 μm thick water sample placed in an identical microscope slide/spacer assembly. As a result, measured extinction values represent the amount of light removed by the TEM particles only; effects of the sample holder as well as the water solvent in which the particles are suspended were removed. Because absorption by the particle is negligible, extinction will be due almost entirely to the removal of light by scatter. Results are presented in figure 16.2 with each data point representing the average of measurements carried out on three different samples. The mean free path of TEM was then calculated using Beer's law (figure 16.3). One can conclude from this graph that interactions between light and the medium will become less frequent with increasing wavelength. In other words, the removal of light by the TEM particles will decrease as one moves to higher wavelengths. Figure 16.4 shows the mean free path data plotted as a function of the square of the wavelength. The linear relationship implies that the mean free path of TEM 0/10 is proportional to the square of the wavelength of light. This is consistent with Mie theory. Assuming that light scatter by the creamer particles (which are, in the first approximation, spherical) may be characterized by the following conditions:

$$2\pi a/\lambda \gg 1$$

$$(m-1) \ll 1$$

$$2\pi a(m-1)/\lambda \ll 1$$

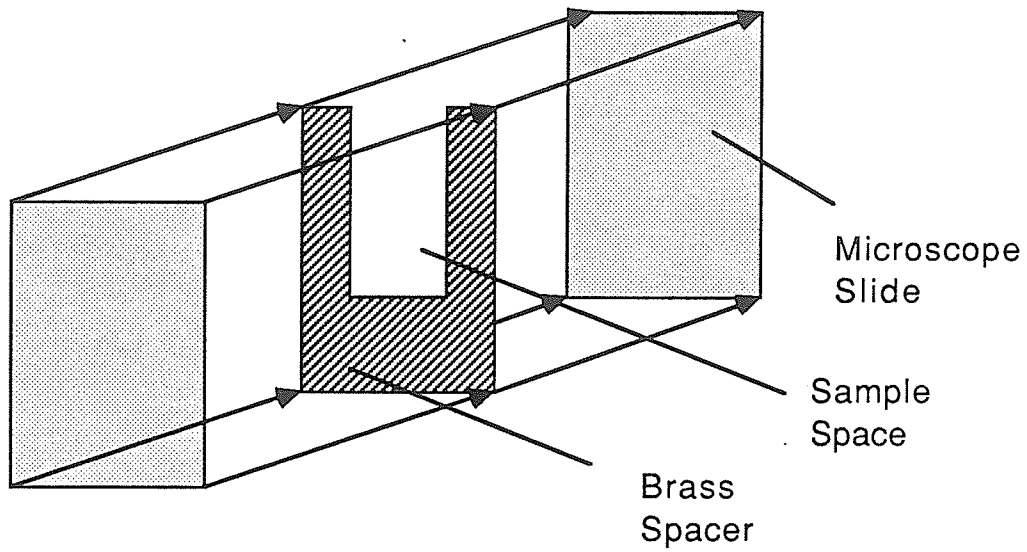


Figure 16.1: Glass microscope slide/brass spacer combination for generating thin TEM samples.

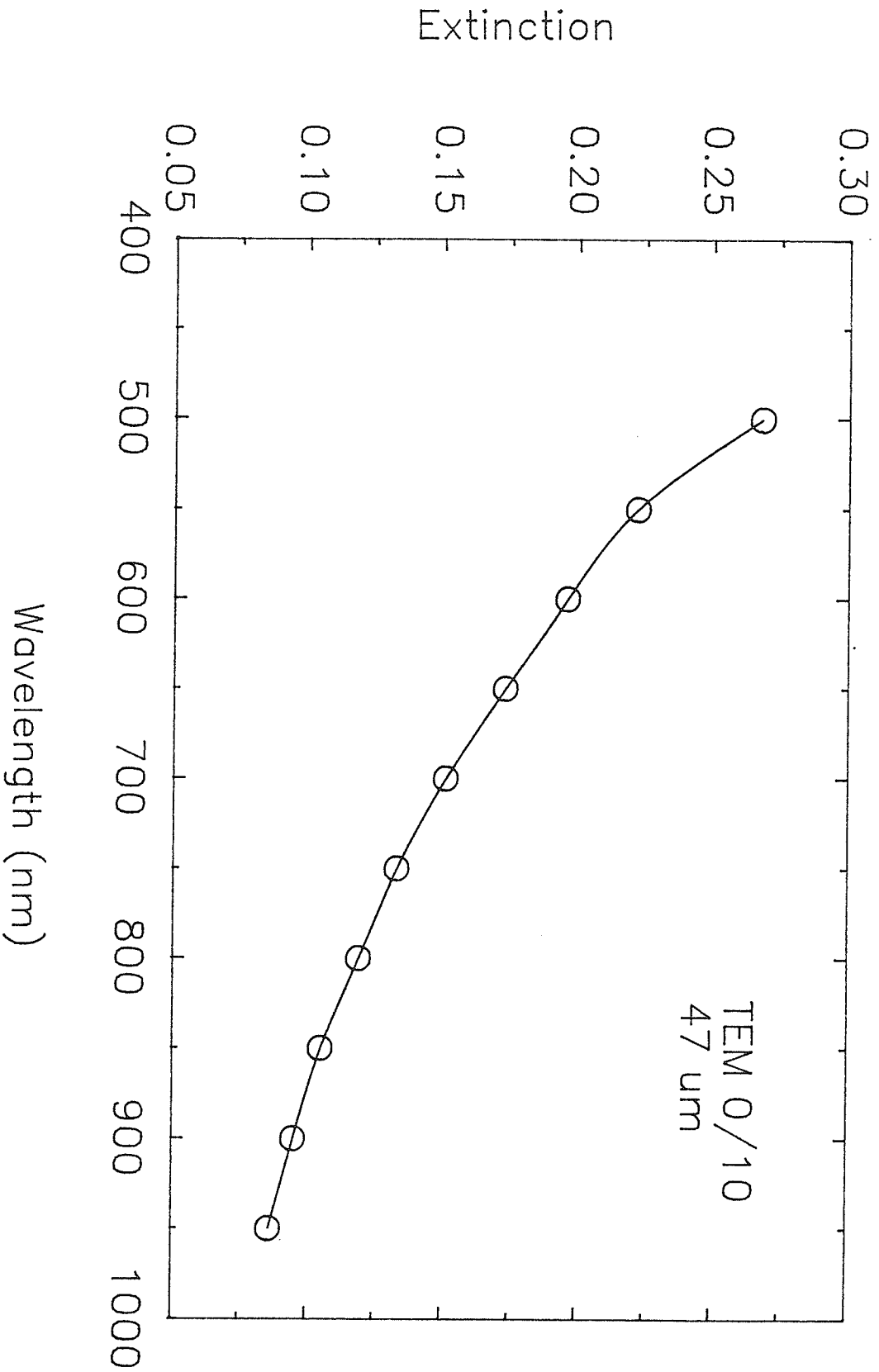


Figure 16.2: Diffuse spectral extinction of a .047 mm sample of TEM 0/10

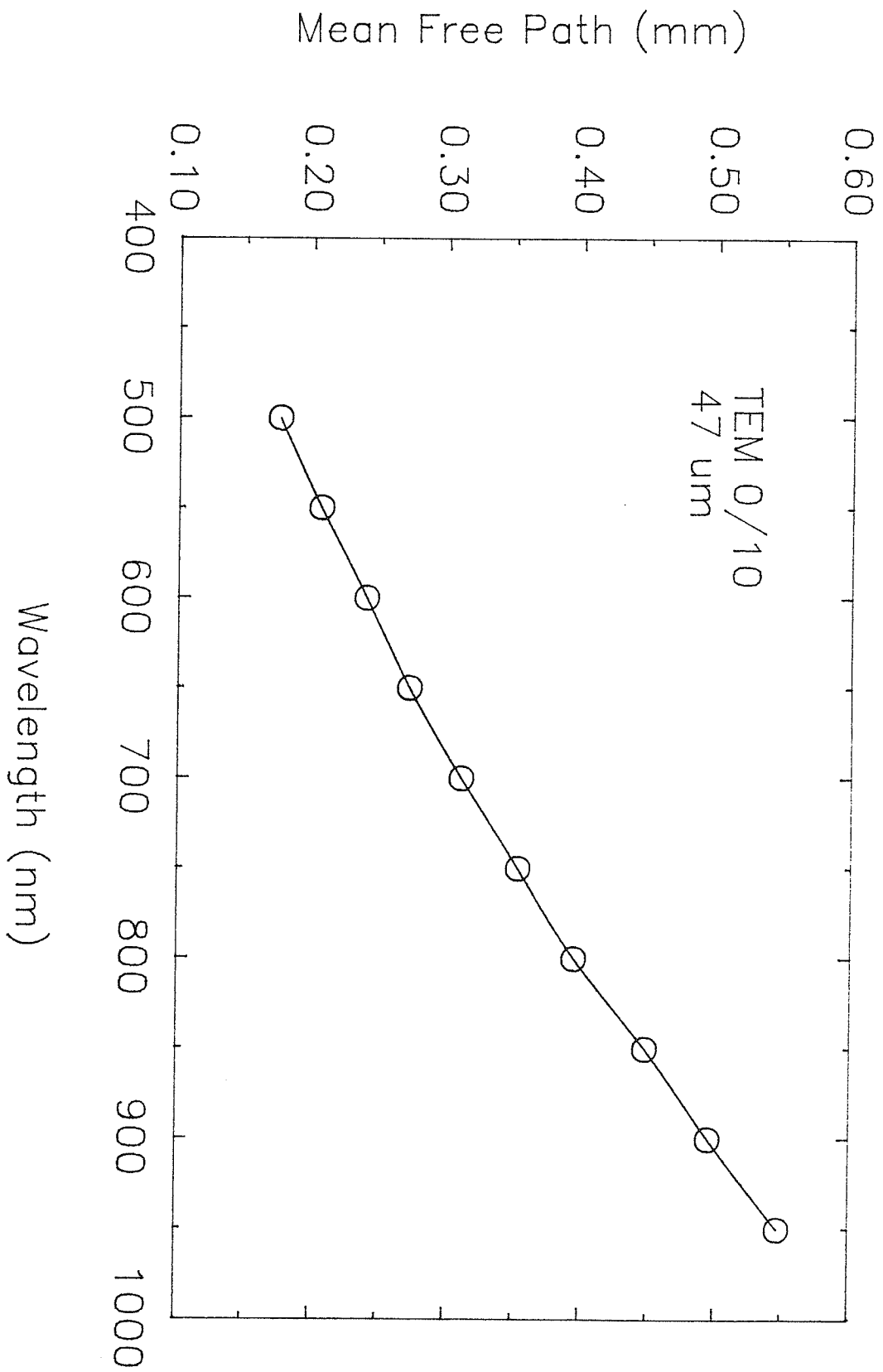


Figure 16.3: Mean free path of TEM 0/10

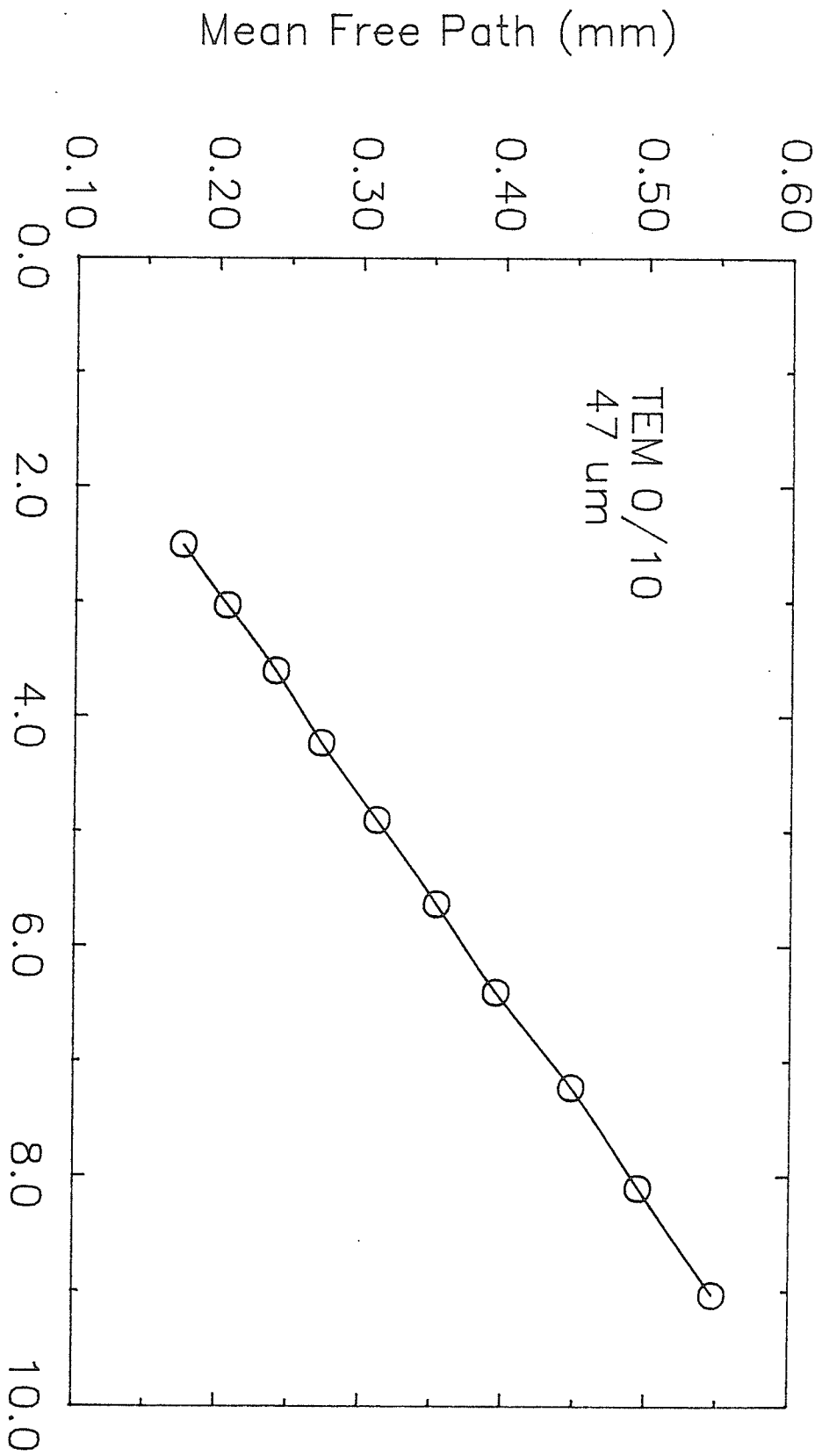


Figure 16.4: Mean free path of TEM 0/10 plotted as a function of the square of the wavelength

this theory predicts (see table 6.1)

$$\sigma(\text{sca}) = 8\pi^3 N a^4 (m-1)^2 / \lambda^2$$

$$l = 1/\sigma(\text{sca}) = \lambda^2 / 8\pi^3 N a^4 (m-1)^2 \quad (16.2)$$

The TEM scattering particles are seen to occupy an overlap region where both the Rayleigh-Gans and Anomalous Diffraction theories provide an accurate description of light scatter. In a very indirect way, these findings tend to justify the application of Linear Transport theory to the modelling of light propagation in TEM and tissue. As already stated, Linear Transport theory will provide an exact description of this transport process provided a beam of light can be treated as a collection of a large number of neutral particles (photons) which pursue their own paths and act independently of one another. This particle model of light will in turn be valid if the wavelength is much smaller than the interaction centers of the medium. The fact that the Anomalous Diffraction theory, a theory whose most important underlying assumption is the particle nature of light, is able to predict the correct relationship between the mean free path of TEM and wavelength (at least its proportionality to λ^2), lends credibility to the use of the "photon" based Linear Transport model.

Determining MFP through the application of Beer's law to thin sample extinction measurements requires that scatter within the specimen be single. Van de Hulst [27] has stated that samples possessing an extinction less than 0.1 will satisfy this requirement. For sample extinctions within the range 0.1 to 0.3, double scattering may exist. Above 0.3, meanwhile, multiple scattering is expected to be significant. As the extinction values obtained in measurements on the 47 μm thick TEM sample lie in the intermediate range, it is necessary to determine whether or not scatter within such a specimen is indeed single. One very simple and conclusive test is to dilute the concentration of scatter centers to 1/2 their initial value. If sample extinction is found to drop by a factor of 2, scatter in the full concentration sample may be considered single. Figure 16.5 illustrates the extinction of a 47 μm thick sample of TEM 0/10 and TEM 0/5 (once again, data represents an average of measurements carried out on three samples). The filled triangle symbols represent the extinction data obtained for the latter sample multiplied by 2. This graph clearly illustrates the proportionality that exists between extinction and concentration and therefore the validity of the single scatter assumption.

Figure 16.6 shows the spectral extinction of various concentrations of TEM (none of which possess the hemoglobin absorbing component). Measurements were carried out on

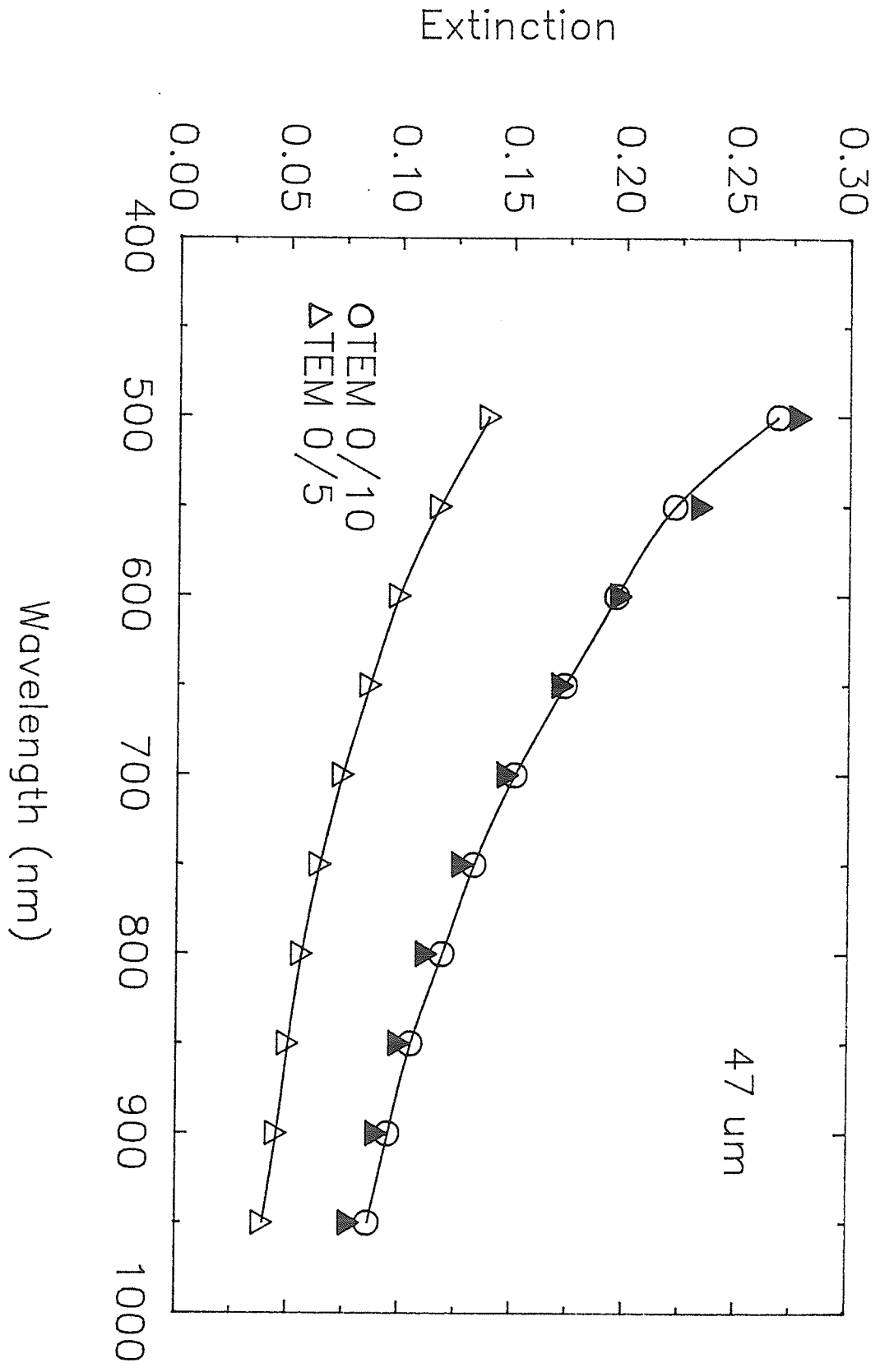


Figure 16.5: Diffuse spectral extinction of a .047 mm thick sample of TEM 0/10 and TEM 0/5

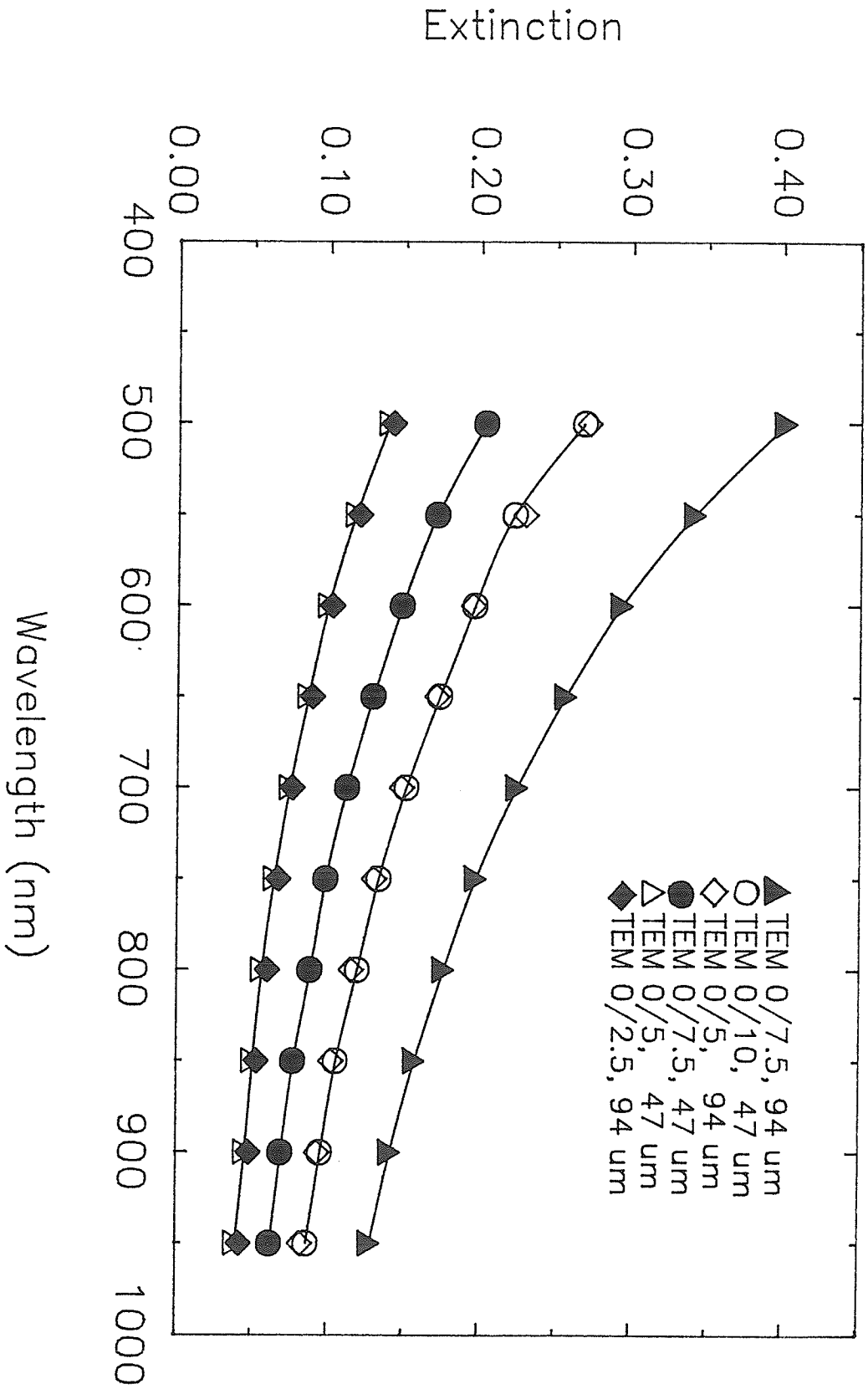


Figure 16.6: Diffuse spectral extinction of various concentrations and thicknesses of TEM

specimens of two thicknesses, 47 and 94 μm . Samples of the latter thickness were produced using two identical brass spacers to separate the glass microscope slides. All data represent the average of measurements carried out on three samples. Extinction is not only seen to be proportional to concentration but also thickness. These conclusions are more obvious in figure 16.7 where extinction has been divided by both sample concentration and thickness (expressed relative to that of the 47 μm TEM 0/10 data). Once again, these results lend proof to the existence of single scatter and justify the use of Beer's law. In addition, however, they also demonstrate some of the other advantages offered by TEM as a medium for studying the propagation of light through biological tissue. Firstly, it becomes evident that rather thick samples of TEM can be transformed into single scattering specimens through a simple dilution. The opportunity therefore exists to carry out MFP measurements (employing Beer's law) on very thick samples. The MFP obtained through such measurements can then be scaled by a simple correction factor to yield an estimate of this fundamental parameter for the full concentration medium. When dealing with actual tissue samples, one is not able to control the concentration of interaction centers and as such is forced to make measurements on very thin specimens which in practice, are very difficult to produce. Such complete and precise control over the concentration of interaction centers is important for another reason. Through the dilution of TEM, one can create media characterized by mean free paths of any magnitude (greater than or equal to that of glandular breast tissue). TEM possessing a large MFP will be extremely useful in experimental studies of light distributions in regions where the Linear Transport and Diffusion theories are expected to differ (ie. in the vicinity of a source or interface separating two media exhibiting different optical properties). With the exception of cases in which the media of propagation are characterized by heavy absorption, these regions are expected to be of the order of tens of MFP's in length. In biological tissue, this would correspond to distances of only a few mm. Meaningful light distribution measurements in such regions, in real tissue would be virtually impossible. TEM, however, offers one the opportunity to simulate regions in which the two transport models disagree on a much larger scale. Through dilution, the size of these regions can be substantially magnified to provide an environment free of the above mentioned technical difficulty but whose optical properties are nonetheless reflective of those of real tissue. Also, the effective size of any detector probe used to sample spatial light density within such an environment will be reduced, thereby decreasing the perturbations its presence will introduce.

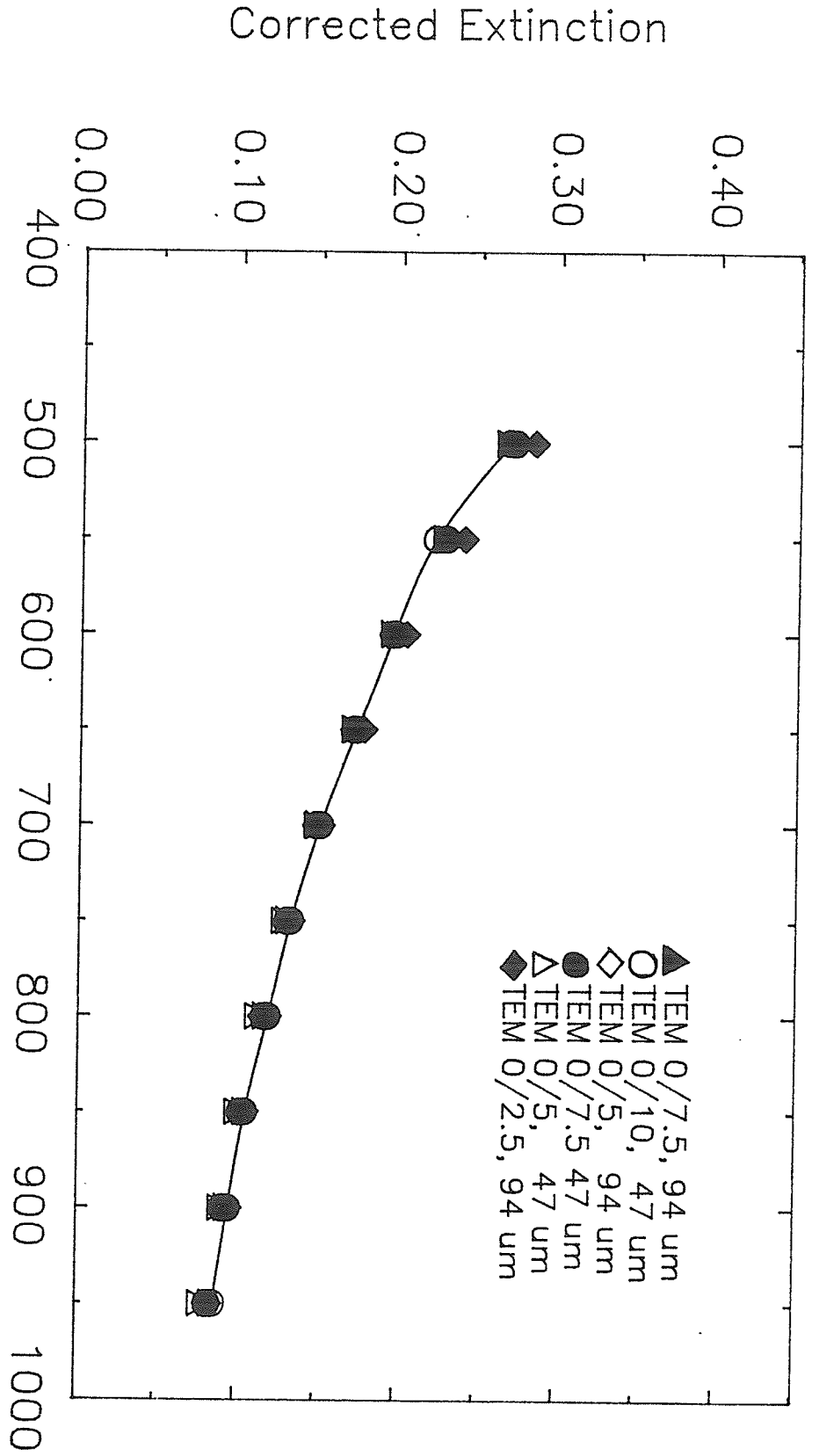


Figure 16.7: Replot of figure 16.6 after dividing diffuse extinction by TEM concentration and thickness

The mean free path of TEM 10/10 will be reduced from that of TEM 0/10 due to the presence of a 1/800 normal blood concentration hemoglobin component. This additional element may be considered a pure absorber of light, its contribution to the overall scatter of TEM being insignificant. As such, the optical properties of the hemoglobin constituent can be completely characterized by an absorption cross section per unit volume. Measurement of this parameter was carried out once again using Beer's law.

An aqueous solution possessing a hemoglobin concentration identical to that of TEM 10/10 was produced by lysing 0.250 ml of whole blood (removed from a patient suffering from no known blood disorders) in 200 ml of distilled water. The hemoglobin sample was then placed in a 10 mm square cuvette and its extinction measured as a function of wavelength with a Spectronic 710 spectrophotometer. Readings were taken relative to a water filled cuvette so as to eliminate the contribution to extinction made by the sample holder and the solvent. As multiple scattering in the 10 mm sample was insignificant, Beer's law was applied and the absorption cross section calculated.

Results are presented in table 16.1. Two very important points should be noted. Firstly, at concentrations found in TEM 10/10 (which is equivalent to glandular tissue), absorption by hemoglobin will be insignificant above 650 nm. Secondly, it is evident that even at 550 nm the absorption cross section per unit volume is extremely small. In fact, at this wavelength it is 500 times smaller than the scatter cross section per unit volume of the particle component of TEM.

The mean free path length of TEM 10/10 will be given by the inverse of the sum of the scatter cross section per unit volume of the particle component (TEM 0/10) and the absorption cross section per unit volume of the hemoglobin component. Because the absorption component per unit volume is so very small, the MFP of TEM 10/10 will be identical to that of TEM 0/10 (see table 16.2).

16.2 SCATTER/ABSORPTION COEFFICIENT

The second input parameter required by the Linear Transport and Diffusion models is the scatter/absorption coefficient of the medium of propagation. Restating its definition

$$c = \sigma(\text{sca}) / (\sigma(\text{sca}) + \sigma(\text{abs})) \quad (16.3)$$

Wavelength (nm)	Absorption Cross Section per Unit Volume (mm^{-1})
550	0.0097
600	0.0026
650	0.0011
700	0.0005
750	0.0004
800	0.0006
850	0.0006
900	0.0006

Table 16.1: Absorption cross section per unit volume of TEM 10/10.

Wavelength (nm)	Mean Free Path (mm)	
	TEM 0/10	TEM 10/10
550	0.206	0.206
600	0.240	0.240
650	0.272	0.272
700	0.311	0.311
750	0.353	0.353
800	0.395	0.395
850	0.448	0.447
900	0.495	0.495

Table 16.2: Mean free path of TEM 0/10 and TEM 10/10.

where $\sigma(\text{sca})$ and $\sigma(\text{abs})$ are the scatter and absorption cross sections per unit volume of the medium, respectively.

TEM 0/10 contains no hemoglobin component. As the absorption of light (over the range 550 to 900 nm) by its components is extremely small, the magnitude of $\sigma(\text{abs})$ of TEM 0/10 is expected to be much less than that of $\sigma(\text{sca})$. Thus, c will take on a value very close to 1.0. More precise values are presented in table 16.3 for $\lambda = 550, 600, 700$ and 850 nm. These estimates were determined from experimental data using a technique described in detail in section 16.3. As predicted, the absorption/scatter coefficient of TEM 0/10 is approximately 1.0 at all wavelengths studied.

The very slight absorption that is detected ($c < 1.0$) is due mainly to water; coffee creamer and Methocel may also absorb light but to a lesser extent. Although small, absorption at these four wavelengths will, nonetheless, exist, its contribution to overall attenuation increasing close to the 970 nm maximum [51]. This trend is indeed illustrated in table 16.3 where C is seen to decrease (denoting a rise in the relative importance of absorption) with increasing wavelength.

The very fact that a TEM 0/10 absorption component does exist and can be detected reveals an inherent shortcoming of the MFP measurements. The values of this fundamental parameter presented in table 16.2 and which will subsequently be used in the theoretical transport models were measured relative to water. Thus, they do not contain the effects of water absorption. The consequences of this inconsistency are discussed in section 17.1.

The scatter/absorption coefficient of TEM 10/10 is listed in table 16.4 for selected wavelengths between 500 and 950 nm. Values were obtained using eq.(16.3). In generating these results, it was assumed that the particle component of TEM was a pure scatterer of light while the hemoglobin component was a pure absorber. From table it is evident that even at wavelengths where absorption by hemoglobin is maximum (550 nm), the scatter/absorption coefficient of TEM will be only slightly less than 1.0. This has important consequences when choosing a suitable transport model to mathematically describe the propagation of light through tissue. For example, it has previously been stated that Diffusion theory will break down in media characterized by c which are much less than 1.0 (ie. relative importance of absorption is high). Under these circumstances, it will be necessary to utilize the far more complex Linear Transport theory. However, the results obtained here suggest that small c values will not be a problem when dealing with biological tissue. Although data have been obtained for glandular tissue only, the extension to other types does not

Wavelength (nm)	Scatter/Absorption Coefficient of TEM 0/10
550	0.9999307
600	0.9999303
700	0.9998779
850	0.9992869

Table 16.3: Scatter/absorption coefficient of TEM 0/10.

Wavelength (nm)	Scatter/Absorption Coefficient of TEM 10/10
550	0.9980044
600	0.9993769
700	0.9998444
850	0.9997315

Table 16.4: Scatter/absorption coefficient of TEM 10/10.

seem unreasonable. This is not to say that all tissues will possess scatter/absorption coefficients close to one. Cheong et al. [?], for example, report a c of .984 for human bladder at 633 nm. However, tissues such as this will be the exception rather than the norm. It therefore appears that one of the conditions responsible for the breakdown of Diffusion theory, that of small c , will not arise when dealing with light propagation in biological tissue. This supports the use of Diffusion theory as a suitable alternative to Linear Transport theory.

16.3 VALIDITY OF THE TRANSPORT MODELS

The ability of Linear Transport and Diffusion theories to accurately describe the propagation of light through TEM was tested by comparing the theoretical light distributions generated by these models with those obtained experimentally. Two different irradiation geometries were chosen for this purpose:

- a) isotropic point source radiating within an infinitely large, homogeneous medium
- b) isotropic, planar source radiating within an infinitely large homogeneous medium

16.3.1 Isotropic Point Source Irradiation

The experimental set-up used to simulate the point source/infinite medium problem is illustrated in figure 16.8. A 20 cm x 20 cm x 20 cm plastic container filled with TEM 0/10 (to a depth of 10 cm) served as an infinitely large, homogeneous scattering medium. Point source irradiation was provided by a 3.2 mm diameter, glass optic fiber bundle inserted into the medium from its underside. The other end of the optic fiber was coupled to the Oriel light source assembly used in the DICOM-8 spectrophotometer. Melles-Griot bandpass interference filters mounted between light source assembly and the input end of the fiber bundle served to isolate discrete wavelength bands. For a more complete description of the optic fiber bundle, light source assembly and bandpass filters, refer to section 12.1. A 1.6 mm diameter optic fiber bundle, identical to the source fiber in all aspects but size, was employed as a detector probe to sample the spatial light density within the infinite medium. This fiber was inserted into the TEM such that it rested directly above and pointed towards the isotropic source. The plastic arm illustrated in figure 16.8

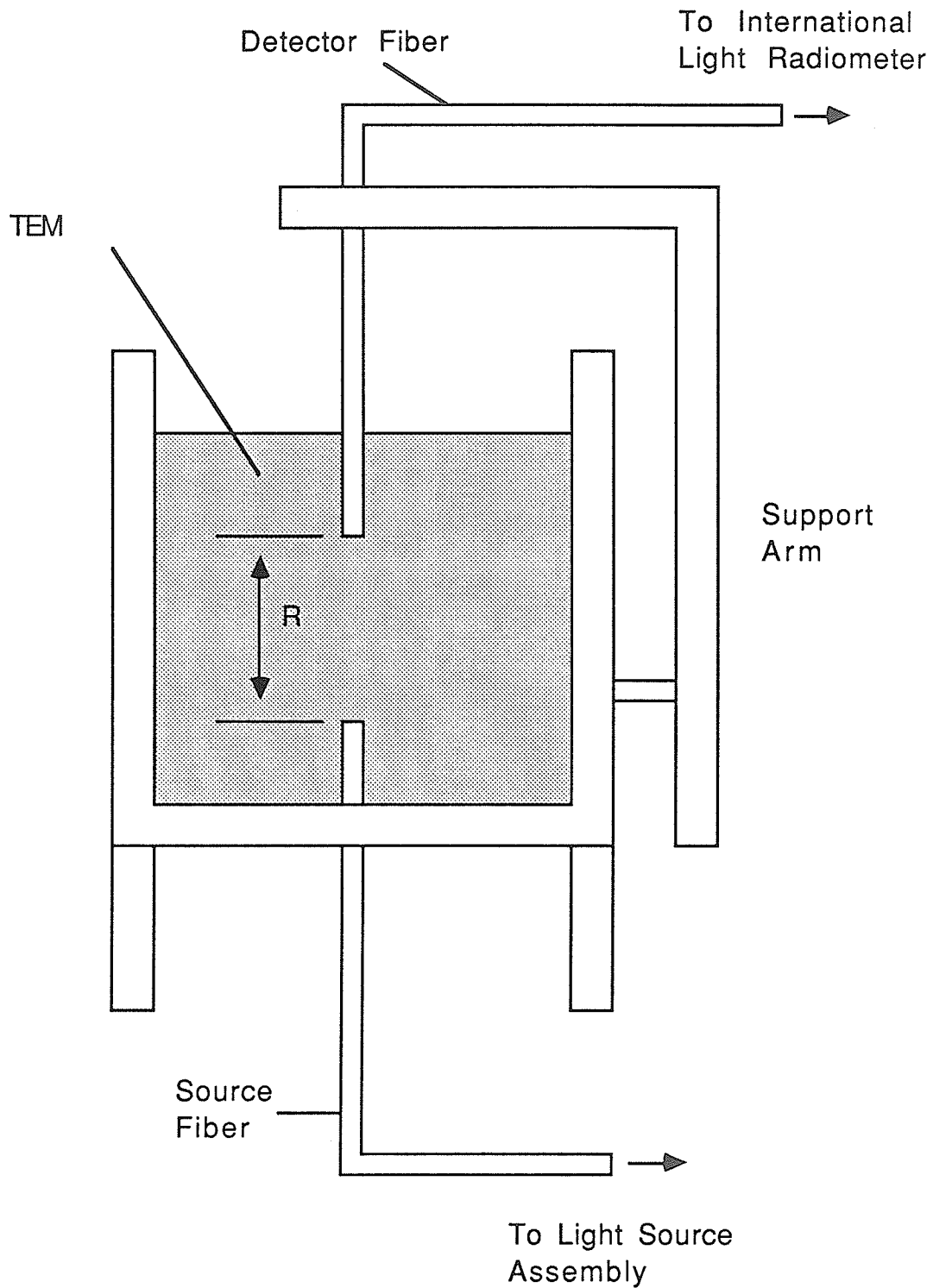


Figure 16.8: Experimental set-up used to simulate the isotropic point source/infinite medium irradiation geometry.

served to align source and probe and to hold the latter in a fixed position. The distance of separation was adjustable, thereby enabling one to sample the density of light at any point along the optical axis of the system. The opposite end of the detector probe was coupled to an International Light radiometer (described in section 12.2).

The very forward directed output of the source fiber bundle was made nearly isotropic by placing a small, semi-spherical shaped, white plastic cap on its tip. This diffuser enabled the fiber bundle to better simulate the isotropic point source required by the theoretical model. The effectiveness of the plastic cap in this capacity is demonstrated in figures 16.9a and 16.9b which show the density of light, as measured by the fiber probe in the absence of TEM (ie. light density in air), at select points along an arc concentric with the point source. The diffusing cap does have its limitations, however, and cannot be expected to yield a perfectly isotropic source. As one increases further the angle made with the optical axis (ie. beyond the 30 degree interval shown in figure 16.9b), light density will begin to fall off rapidly. Nevertheless, because spatial light density for the point source geometry was measured along the optical axis, at large distances from the diffusing cap in a highly scattering medium (see discussion of experimental technique), the effects of this shortcoming on experimental results was negligible. By the time the source output was sampled by the detector, any perturbations caused by a deviation from isotropy would have been removed by multiple scattering.

Light density within the TEM 0/10 was measured as a function of radial distance from the point source along the optical axis of the system (over the range 5 to 30 mm). Distributions were obtained for light of 550, 600, 700 and 850 nm. The results are presented in figures 16.10 through 16.13. The solid lines represent theoretical distributions predicted by Diffusion theory. Because the experimental data was sampled from regions distal to the isotropic source (for light of 550 nm, a distance of 5.0 mm in TEM represents approx. 24 MFP), because absorption was small and because of the absence of interfaces, it is immaterial which theoretical model is used to describe the distribution; Linear Transport and Diffusion theory will yield identical results. This fact is illustrated in figure 16.14 which shows the spatial distribution of light within TEM as a function of MFP, for point source irradiation with light of 550 nm, as predicted by both theories.

The Linear Transport and Diffusion models have two input parameters, the MFP and scatter/absorption coefficient of the medium of propagation. The MFP values presented in table 16.2 were utilized in generating the theoretical

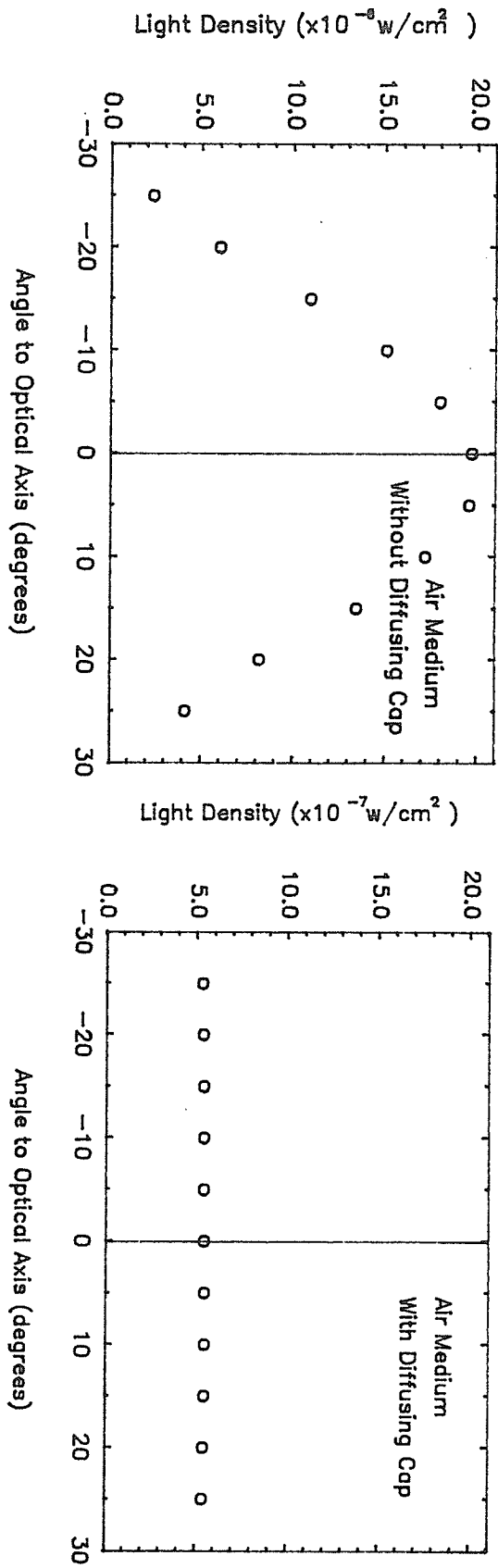


Figure 16.9: Effectiveness of the plastic diffusing cap

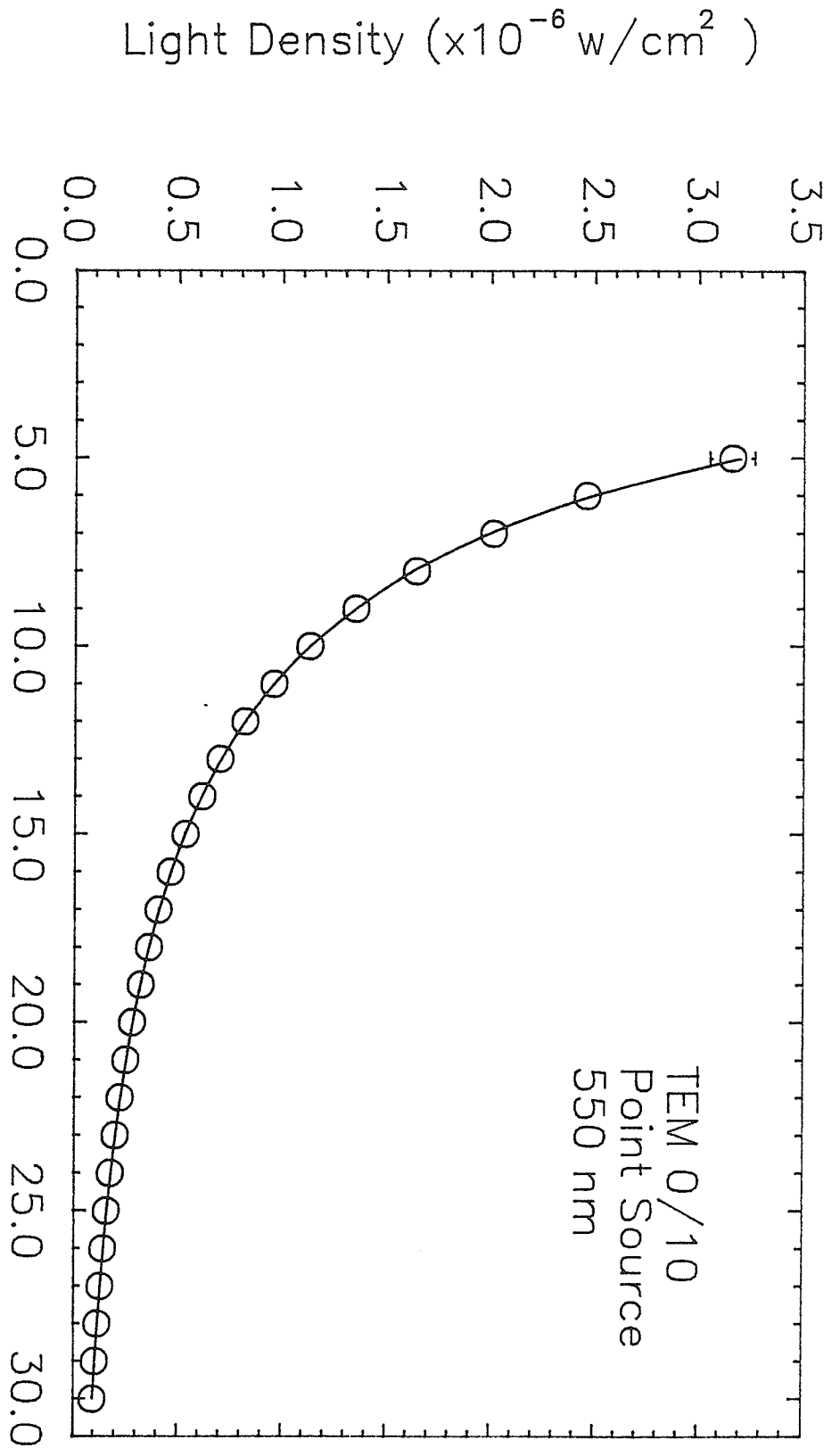


Figure 16.10: Experimental and theoretical light distributions for isotropic point source irradiation of TEM 0/10 at 550 nm

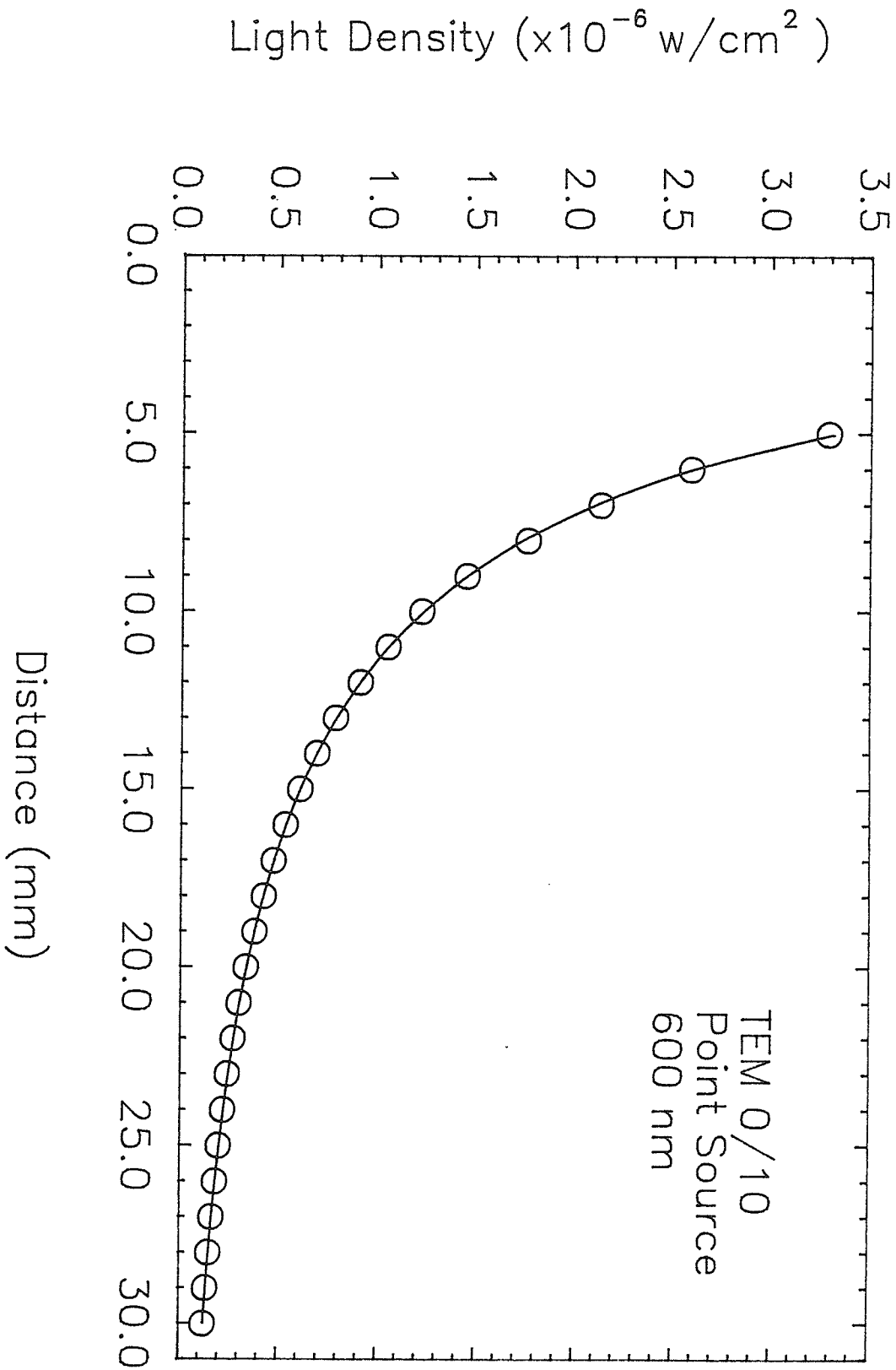


Figure 16.10: Experimental and theoretical light distributions for isotropic point source irradiation of TEM 0/10 at 600 nm

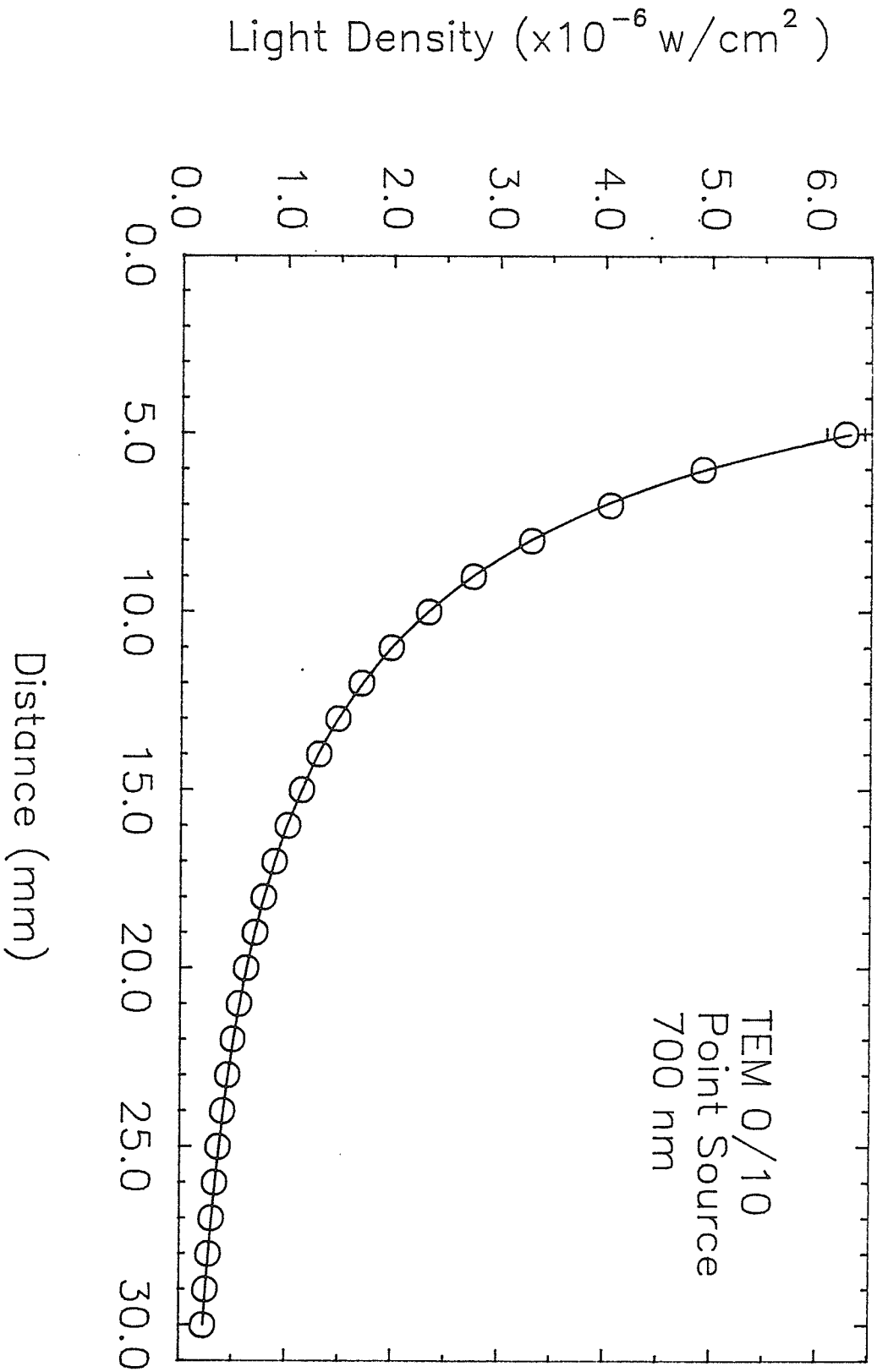


Figure 16.12: Experimental and theoretical light distributions for isotropic point source irradiation of TEM 0/10 at 700 nm

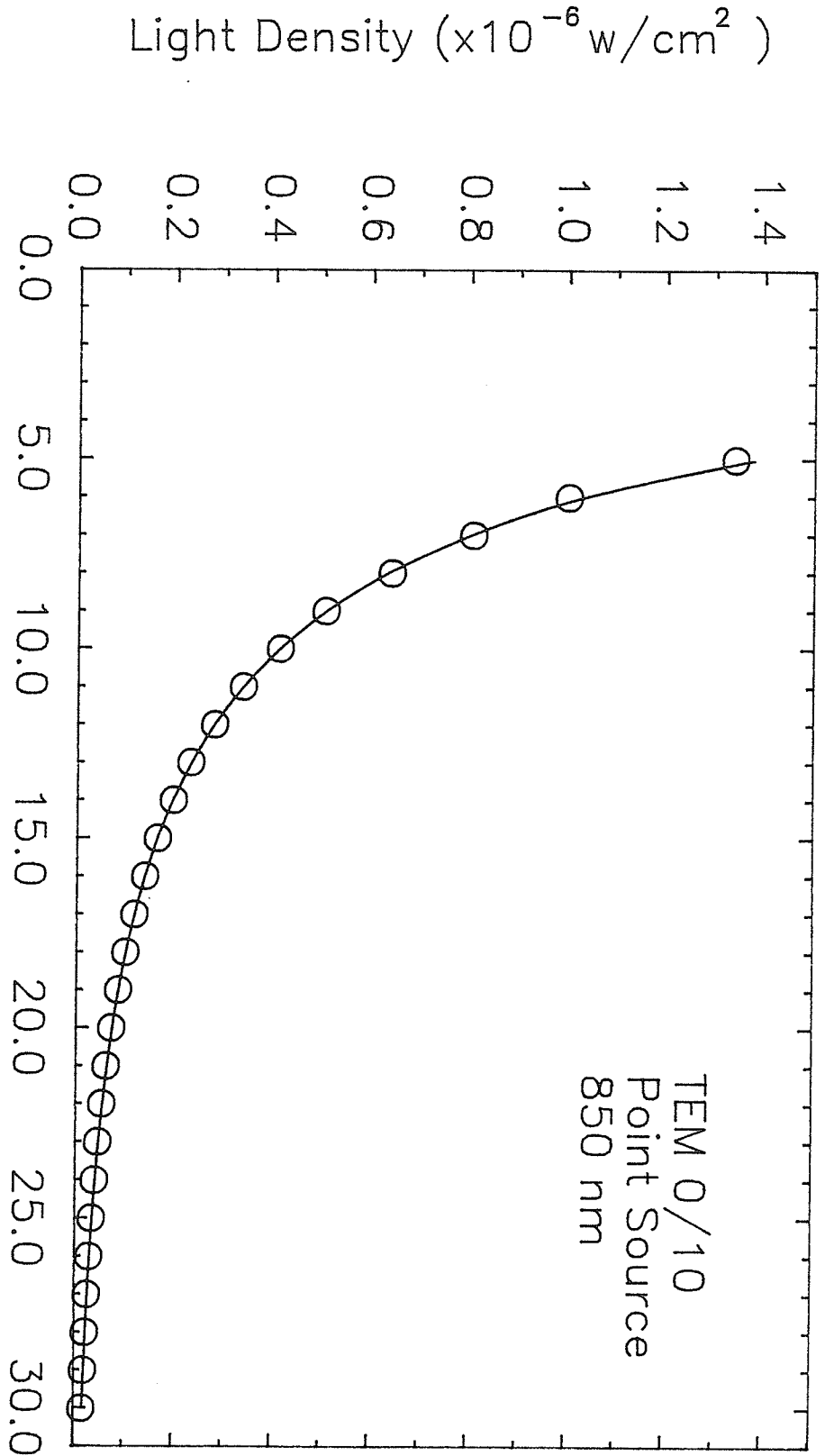


Figure 16.13: Experimental and theoretical light distributions for isotropic point source irradiation of TEM 0/10 at 850 nm

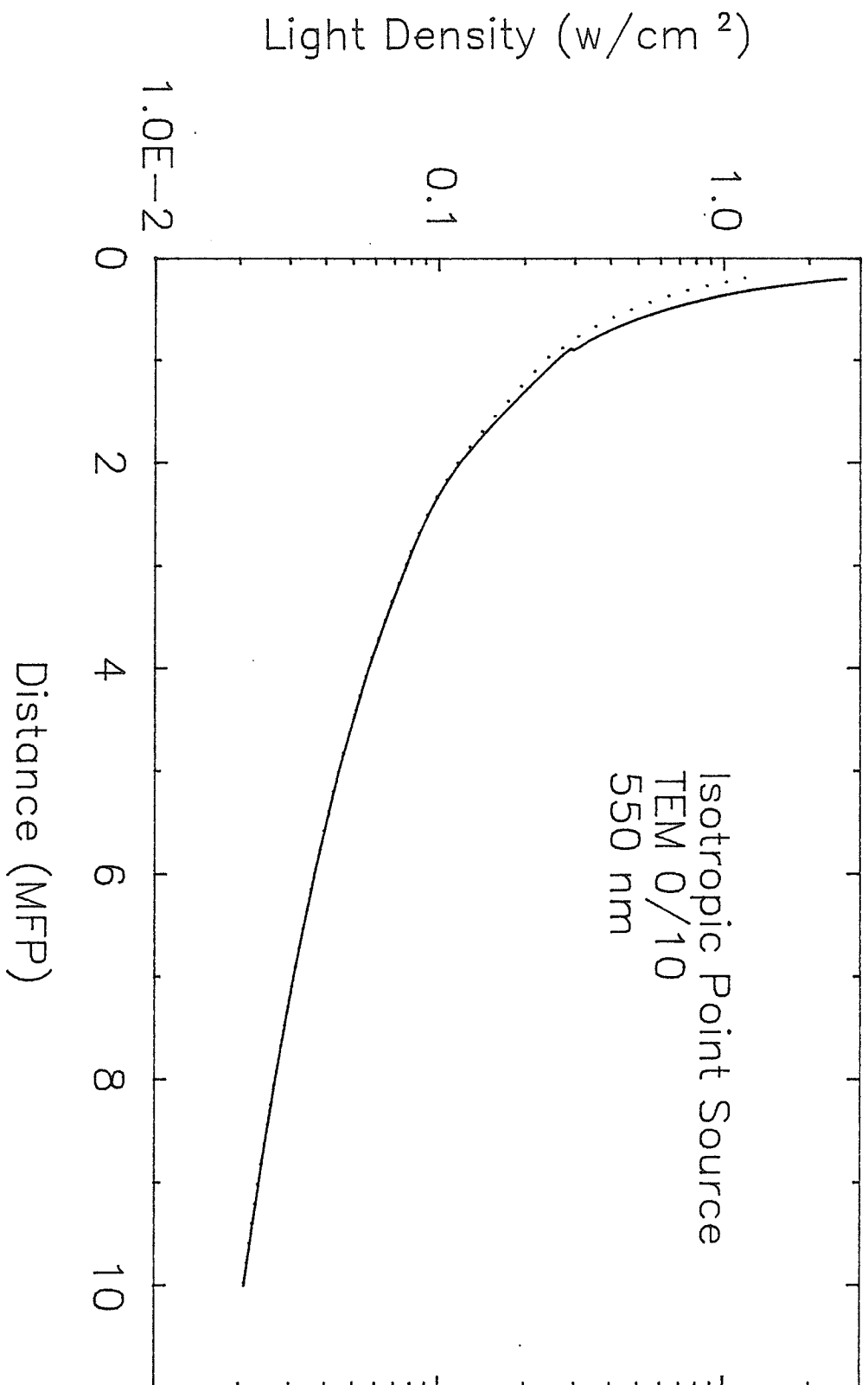


Figure 16.14: Theoretical light distributions generated using Linear Transport and Diffusion theories for point source irradiation

distributions of figures 16.10 through 16.13. The other input parameter, the scatter/absorption coefficient, was obtained using curve fitting techniques. c was treated as a fitting parameter and the SAAM statistical analysis package available on the University of Manitoba Amdahl mainframe computer used to produce the "best fit" of the Diffusion equation to the experimental data. This procedure generated "best fit" estimates of the scatter/absorption coefficient of the TEM (ie. c values which maximize agreement between experimental and theoretical data). Table 16.3 represents the results obtained for the four wavelengths studied. As neither Linear Transport nor Diffusion theory give absolute energy fluence rate, it was necessary to normalize experimental results to those predicted theoretically (or vice versa). This was accomplished by introducing a second fitting parameter, a multiplicative constant, in the theoretical light density expression predicted by Diffusion theory. The "best fit" value of this parameter served as a normalization constant. This approach was used in all experimental/theoretical comparisons.

Agreement between experimental and theoretical light distributions is seen to be quite good. It is evident that both Diffusion theory and Linear Transport theory (which are equivalent under the experimental conditions being examined) provide an accurate description of the spatial distribution of light in regions distal to an isotropic point source radiating within an infinitely large medium possessing no appreciable absorption. Accuracy would appear to be excellent over the entire visible and near infrared spectrum.

To test the ability of Linear Transport and Diffusion theory in describing the propagation of light in the presence of significant absorption (ie. similar to that found in biological tissue), the spatial density measurements were repeated with TEM 10/10. Light density was sampled at 1.0 mm intervals between 5 and 20 mm from the source. The interval of measurement was substantially less than that for measurements in TEM 0/10 due to the reduced light levels. The data obtained for light of 600 nm is plotted in figure 16.15. Included in this graph is the theoretical light distribution (solid line) generated using Diffusion theory; the fact that measurements were made distal to the source and in a medium characterized by an absorption/scatter coefficient nearly equal to 1.0 once again justifies this procedure. The mean free path of TEM 10/10 was taken from table 16.2 while c was treated as a fitting parameter. Linear Transport and Diffusion theories (the two being identical in the region of measurement) are seen to provide a very accurate description of light propagation in a medium characterized by a significant degree of absorption (at least distal to a source of light).

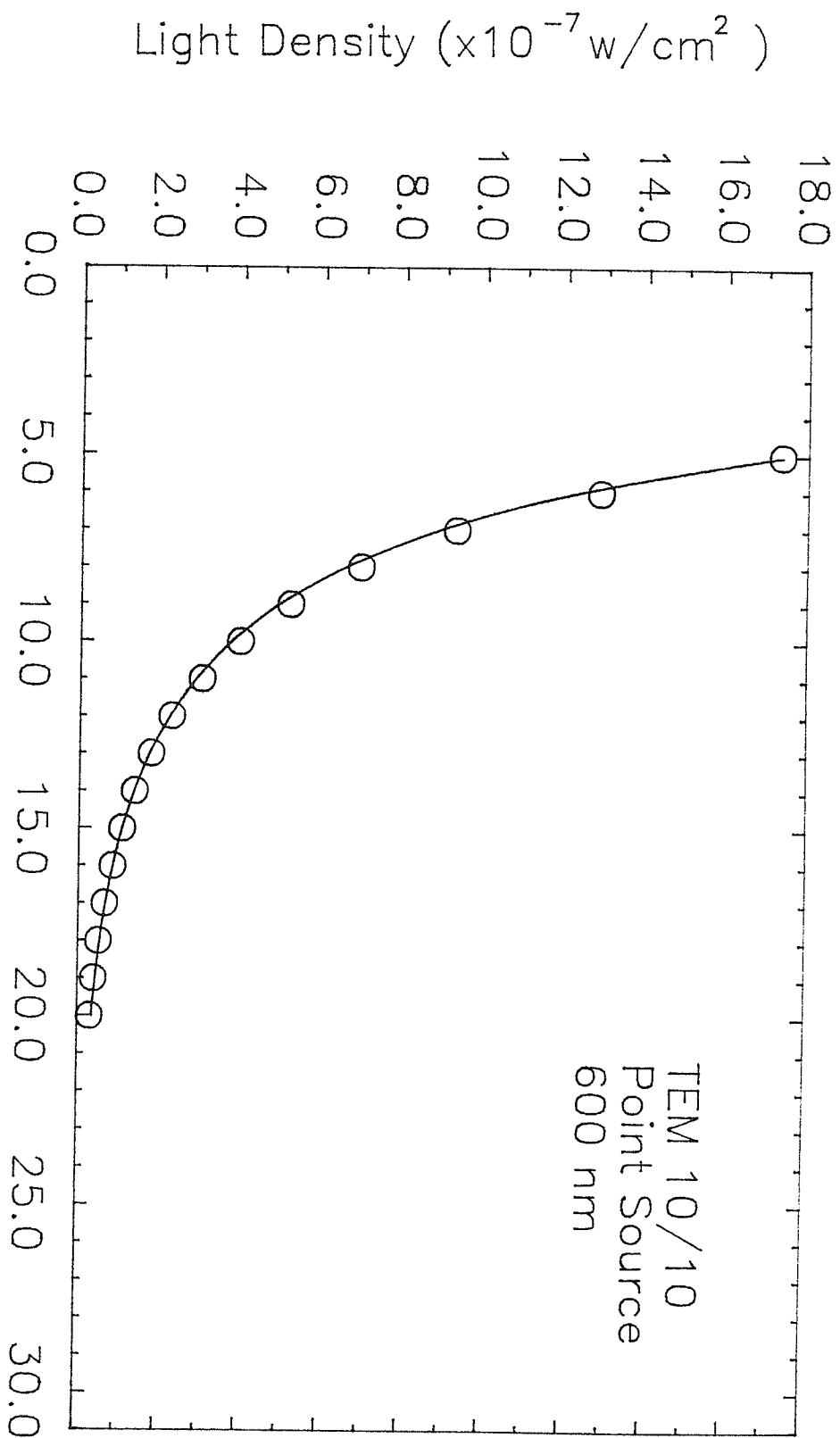


Figure 16.15: Experimental and theoretical light distributions for isotropic point source irradiation of TEM 10/10 at 600 nm

The "best fit" approach used to generate an estimate of c yielded a value of 0.9994529, a result very similar to the value of .9993769 calculated using eq.(16.3) (see table 16.4). The effect of this small difference in scatter/absorption coefficient on the spatial distribution of light predicted by LTT is examined in section 17.1.

16.3.2 Isotropic Planar Source Irradiation

The ability of Diffusion theory and Linear Transport theory to describe the spatial distribution of light within an infinitely large, homogeneous, non-absorbing medium due to a large planar source was examined. Experimental and theoretical results were compared distal to the source (at perpendicular distances greater than 5.0 mm), in the region where Diffusion theory and Linear Transport theory are identical.

The planar source problem was simulated experimentally by placing a large, clear plastic container (18.0 cm x 20.2 cm x 24.5 cm) on top of a high intensity light box (see figure 16.16). The container was then filled with TEM 0/10 to a depth of 10 cm to form an effectively infinite, homogeneous medium. The light box served to illuminate the medium from underneath; the output intensity of the light box was extremely uniform over its surface area. Although such a set-up is not, in the strictest sense, equivalent to a planar source radiating within an infinite medium (since medium exists only above the source), perturbations introduced as a result of this shortcoming are expected to be significant only in the vicinity of the irradiated surface of the TEM space. Thus, as far as the spatial distribution of light within the region of measurement is concerned (> 5.0 mm from the source), the set-up illustrated in figure 16.16 provides a suitable simulation of the desired irradiation geometry. A plastic support arm is used to hold the detector probe (the opposite end of which is coupled to the International Light radiometer) immersed in the TEM medium at a fixed but adjustable perpendicular distance from the planar source. Wavelength selection was with Melles-Griot bandpass interference filters. However, unlike in the point source experiments, selection was made at the detector side of the set-up, the filters being positioned between the output end of the detector probe and the radiometer.

Light density readings were taken at 1.0 mm intervals between 5.0 and 30.0 mm from the source. Figure 16.17 and 16.18 illustrate the results obtained for light of 550 and 700 nm respectively. The solid lines represent the spatial distributions predicted by Diffusion theory (Linear

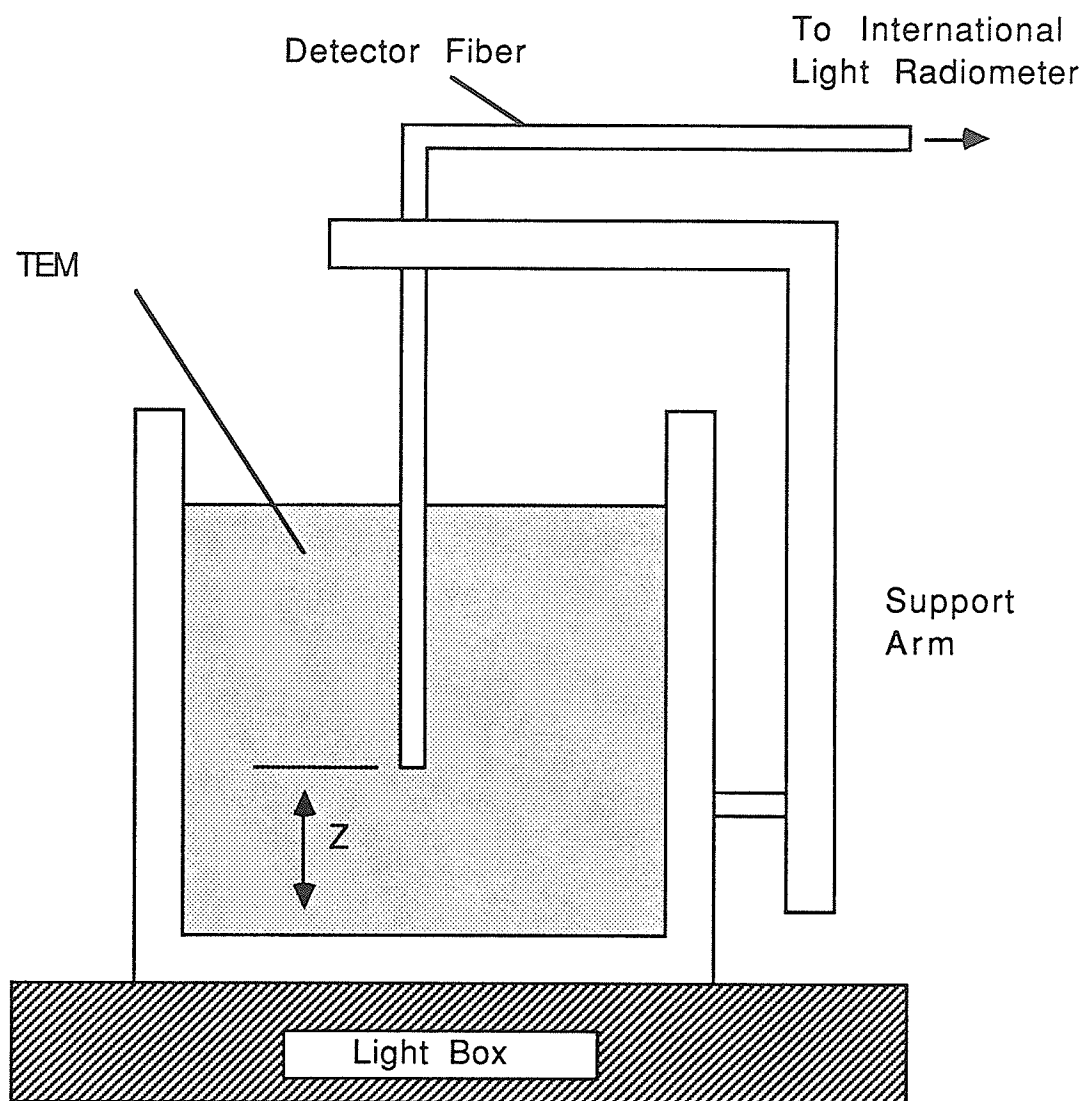


Figure 16.16: Experimental set-up used to simulate the isotropic planar source/infinite medium irradiation geometry.

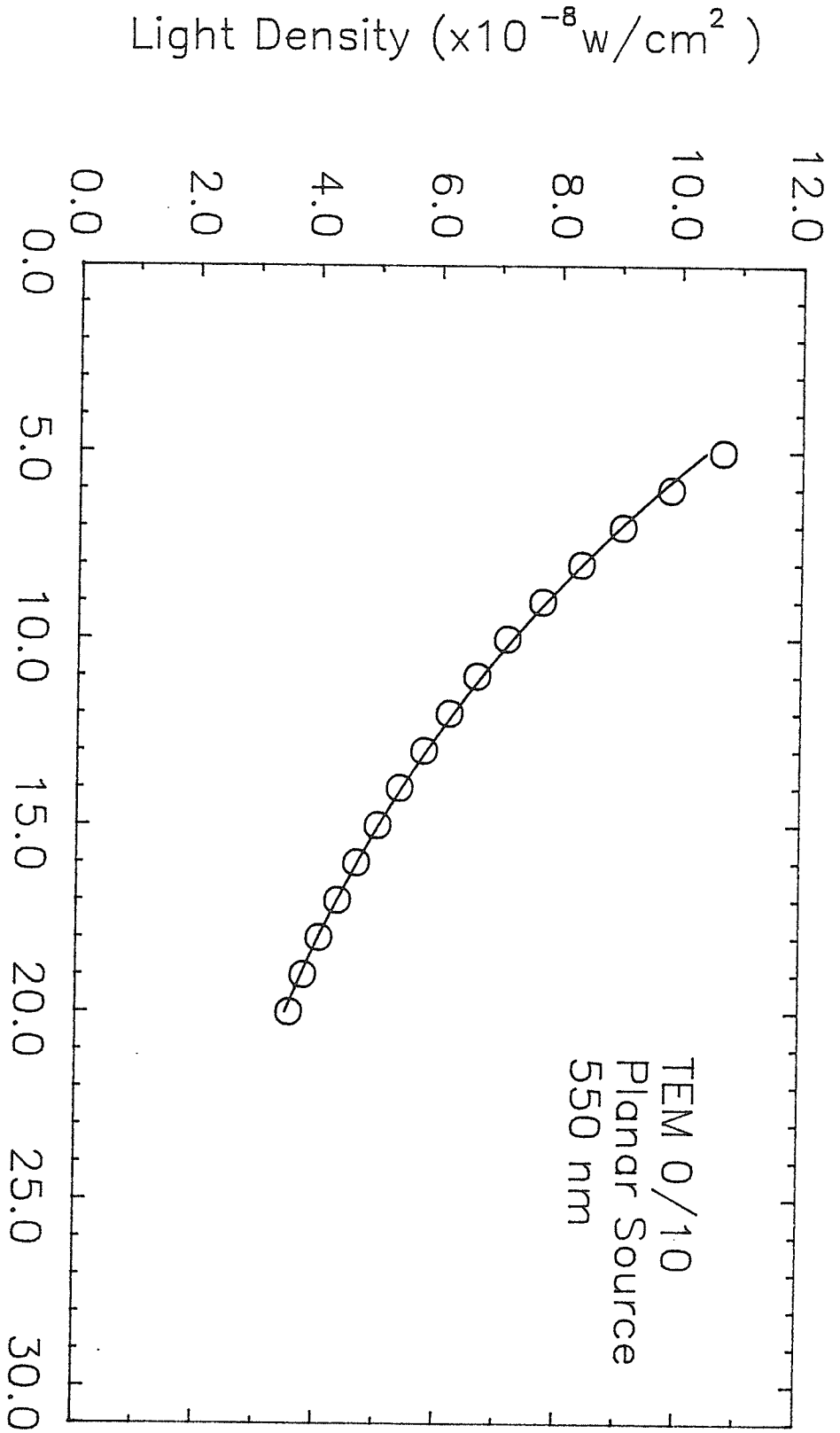


Figure 16.17: Experimental and theoretical light distributions for isotropic planar source irradiation of TEM 0/10 at 550 nm

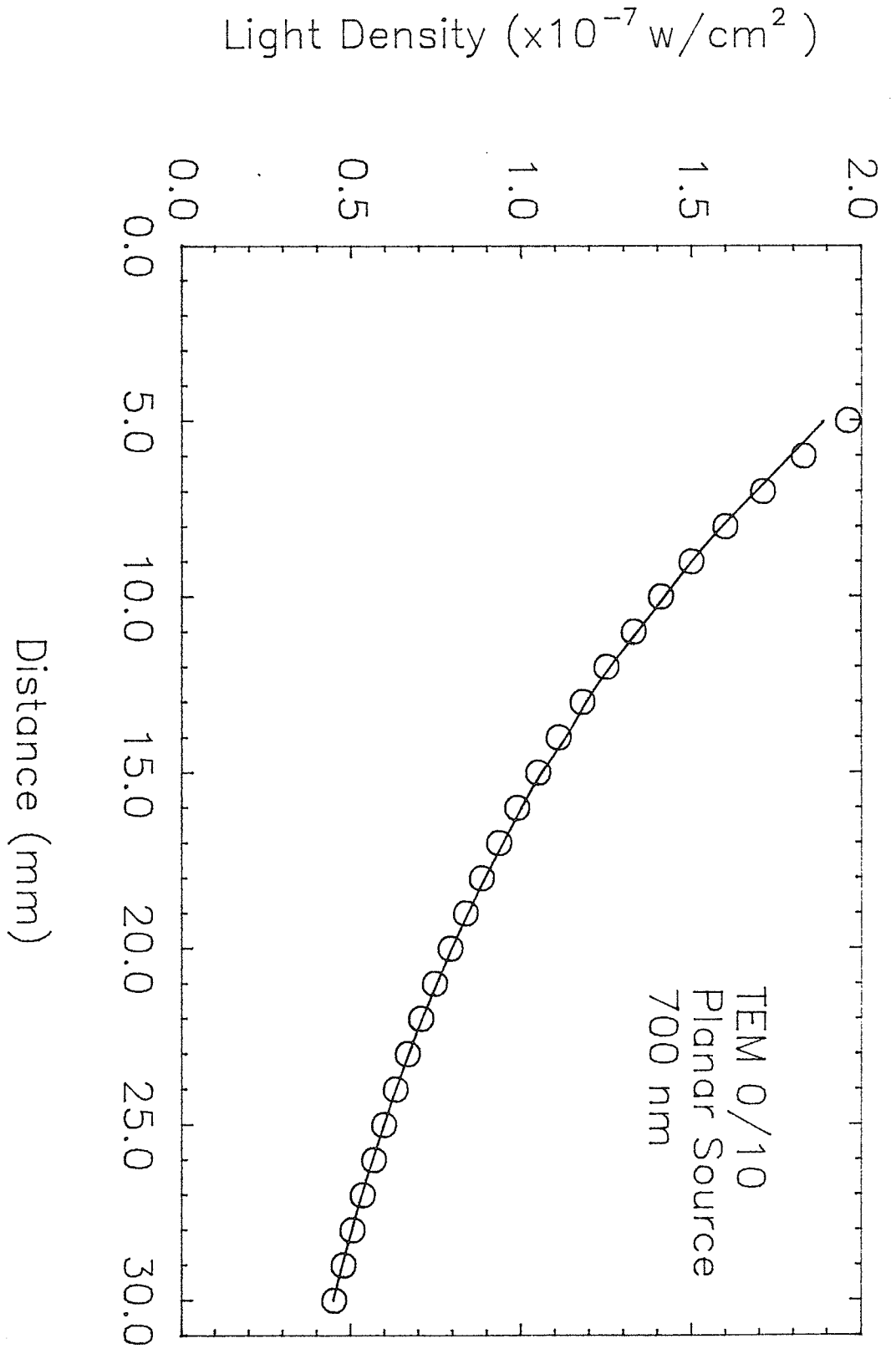


Figure 16.18: Experimental and theoretical light distributions for isotropic planar source irradiation of TEM 0/10 at 700 nm

Transport theory predicts an identical distribution due to the very large distance from the source, the absence of interfaces and the low absorption of TEM). The MFPS presented in table 16.2 were used in the theoretical calculations. Estimates of c for the two wavelengths were obtained using the SAAM statistical analysis package, their magnitude chosen so as to maximize agreement between experimental and theoretical data; such a procedure yielded scatter/absorption coefficients of 0.9999244 and 0.9998920 for 550 and 700 nm, respectively, values very similar to that obtained in the point source experiments. The results presented in figures 16.17 and 16.18 demonstrate the ability of both Diffusion theory and Linear Transport theory to describe the spatial distribution of light distal to a planar source radiating within an infinitely large, homogeneous medium. Although only light of 550 and 700 nm was examined, it is expected that agreement would be just as good at other wavelengths over the visible and near infrared. Differences between experimental and theoretical results, especially near the end of the sampled region, are attributed to the very low light levels recorded in these experiments (these levels being very close to the dark current level of the detector). Light level readings were substantially lower than those taken at the same wavelengths in the point source experiments due to the greatly reduced output power of the planar source.

As in the case of point source irradiation, the ability of Linear Transport and Diffusion theory to describe the spatial distribution of light due to internal, planar source irradiation in a medium characterized by substantial absorption was also examined. In this instance, light density was sampled in 1.0 mm increments between 5 and 20 mm from the planar source. Figure 16.19 illustrates the results obtained for light of 550 nm. Once again, the solid line represents the theoretical distribution as predicted by Diffusion theory (Linear Transport theory will yield identical results). The mean free path used in these calculations was taken from table 16.2 while SAAM was used to generate a value for c which resulted in the best agreement between theoretical and experimental data. This fitting procedure yielded $c=0.9986459$, a result similar to the value of 0.9980044 calculated using eq. (16.3) (see table 16.4). The effect of the small difference in scatter/absorption coefficients generated using the two techniques is examined in section 17.1. It is apparent that both Linear Transport and Diffusion theory can be used to provide an accurate prediction of the spatial distribution of light within a medium showing significant absorption (ie. similar to that in biological tissue) as a result of internal, planar source irradiation.

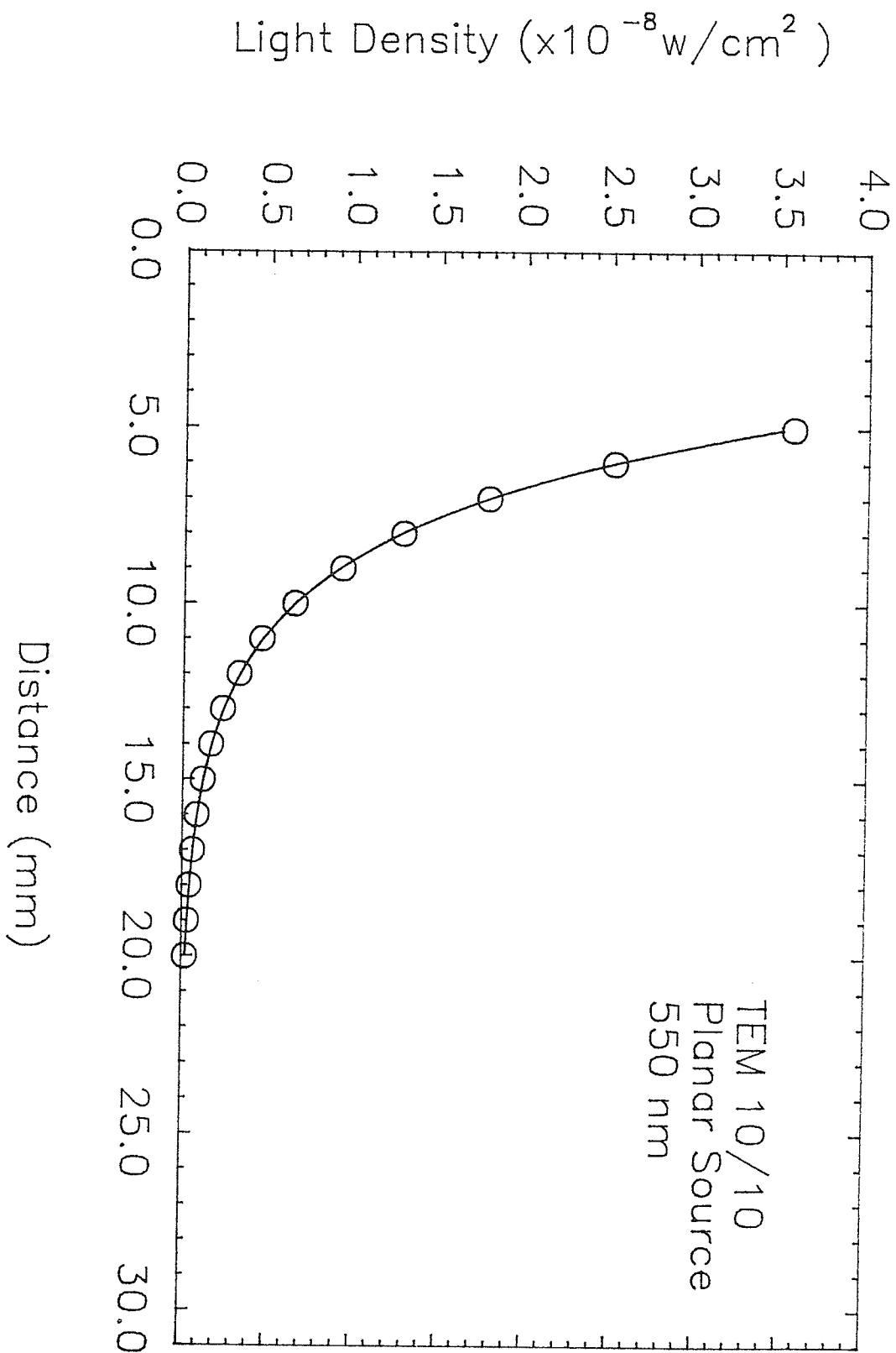


Figure 16.19: Experimental and theoretical light distributions for isotropic planar source irradiation of TEM 10/10 at 550 nm

One should keep in mind that the results presented in this section provide no insight into the suitability of either mathematical model proximal to a source of light or an interface between two regions of different optical properties (ie. in those regions where Linear Transport and Diffusion theories yield different results).

16.4 LIMITATIONS OF RESULTS

In deriving the linear Transport equation, it was assumed that light could be treated as a collection of a large number of photons which act independently of one another and pursue their own path of travel. Evidence justifying the use of this particle model in its derivation, although indirect and limited, has been presented in section 16.1. It would therefore appear that the Linear Transport equation should provide an exact description of light propagation within a scattering/absorbing medium.

However, in solving this integral-differential equation for particular irradiation geometries, a simplifying assumption was introduced, that of isotropic scattering. In other words, the Amplitude function associated with the individual scatter interaction centers of the medium of propagation was assumed to have no angular dependence. This brings into question the ability of the Linear Transport solutions (and therefore the Diffusion solutions) presented in chapter 10 to describe the propagation of light in TEM or tissue, media which may be characterized by anisotropic scatter. The creamer particles of TEM, the component responsible for almost all of the scatter within this synthetic tissue medium, possess sizes which are greater than the wavelength of visible and near infrared light. Scatter by these particles has also been shown to fall in an overlap zone in which both the Rayleigh-Gans and Anomalous Diffraction theories are applicable. These two factors suggest that scatter by the particulate component will be forward directed. Unfortunately, the extent to which its associated Amplitude function deviates from that of an isotropic scatterer is not known. To date, only two studies of the angular distribution of scatter within biological tissue (ie. Amplitude functions of the scatter interaction centers) have been published. Unfortunately, results are conflicting. Wilksch et al. [47] conclude from measurements on pig muscle that scattering in tissue is very forward directed. Conversely, results presented by Marynissen et al. [43] suggest the opposite to be true. Clearly, more research is required in this area.

To examine the consequences of the isotropic scattering assumption on the experimental results presented in this

chapter, consider a large, collimated planar source irradiating in an infinitely large medium characterized by an isotropic Amplitude function. In the Diffusion approximation, spatial light density is given by

$$P(z_0 \rightarrow z) = K \text{ EXP}(-(3(1+c^2w-cw-c))^{1/2} |z-z_0|)$$

where w is the average cosine of the scattering angle and K is a complex function of scatter and absorption cross section but not position [29]. The term $c^2w-cw-c$ is often referred to as an effective scatter/absorption coefficient $c(\text{eff})$. By employing the indirect techniques outlined in section 16.3, an estimate of c for an isotropic medium may be obtained from the "best fit" value of the constant term in the exponential, $(3(1+c^2w-cw-c))^{1/2}$ (provided w is known). Keeping in mind that the factor outside the exponential plays no role in determining c (the theoretical light distribution is normalized to the exponential), a comparison of the above expression with eq. 10.26, its isotropic counterpart, clearly illustrates the shortcoming of applying the latter to measurements made in a forward scattering material: an estimate of the effective scatter/absorption coefficient is obtained rather than the scatter/absorption coefficient itself (c will be slightly smaller than $c(\text{eff})$). As TEM is, in all likelihood, an anisotropic scatterer, c results presented in section 16.3 are expected to reflect this limitation. The magnitude of errors introduced as a result of the isotropic assumption are, however, not known.

In order to test the ability of either Linear Transport or Diffusion theory to describe the propagation of light in TEM, it is necessary to compare theoretical light distributions with those obtained experimentally. Such a comparison requires that the density of light $P(r)$ be measured within TEM samples under highly controlled irradiation geometries. Often referred to as space irradiance, $P(r)$ has the units of photons/cm²-sec. Theoretically, this quantity represents the integral of the angular distribution function $\Psi(r, \Omega)$ over 4π steradians. Experimentally, space irradiance at a point in TEM or tissue is defined as the total power entering a differential sphere concentric with the point, divided by the cross sectional area of that sphere. Due to the finite size and limited collection solid angle of the detector probe used in the experimental measurements, it was not possible to measure true space irradiance for the geometries studied.

The finite size of the detector probe had two consequences. Firstly, it collected light over a rather large area of space rather than at a point. As a result, experimental space irradiance values represent spatial averages. However, errors arising as a result of this shortcoming are significant only in regions where $P(r)$

exhibits substantial change across the face of the detector probe. As all measurements were carried out distal to sources, in regions where Diffusion theory is expected to be valid and spatial changes in $P(r)$ gradual, errors of this nature are expected to be negligible. Secondly, and of greater importance, the finite size of the detector probe will result in a perturbation of the spatial light distributions. Absorption and reflection of light by the probe will alter the true light distribution in the vicinity of the detector, resulting in the measurement of space irradiances which are uncharacteristic of the particular irradiation geometry being studied. To minimize either of these technical shortcomings, the detector probe should be made as small as possible.

The limited solid angle of collection of the probe is the second factor preventing the measurement of true space irradiance. To determine $P(r)$ one must collect all the light entering a differential sphere centered about r . Unfortunately, a flat, cleaved optic fiber can only collect a fraction of this light, that within a small solid angle. As a result, measurements will underestimate space irradiance. To better understand the reasons for this limitation, it is necessary to review the principles by which light is transported down an optic fiber.

Single strands of transparent material such as glass or fused silica can transport light with very low losses by utilizing the phenomenon of total internal reflection. In the simplest configuration, the glass fiber is wrapped with an outer layer of lower index material. For light to be transported down the fiber (by total internal reflection), it must strike this glass-outer layer interface at an angle greater than some critical value a_c (see figure 16.20); light incident upon this surface at angles less than a_c will be lost through the interface. The critical angle is given by

$$\sin(a_c) = n_2/n_1 \quad (16.4)$$

where n_2 and n_1 are the indices of refraction of the cladding and glass fiber, respectively. For a light ray to satisfy this critical angle criterion and therefore be transported down the light guide, it must enter the optic fiber at an angle less than a_c (with respect to the normal - see figure 16.20) where

$$\sin(a_c) = (n_1/n_0) \sin\phi \quad (16.5)$$

Here n_0 is the index of refraction of the medium in which the detector is immersed. From the geometry of figure 16.20, eq. (16.5) may be put into a more useful form:

$$\sin(a_c) = (n_1/n_0) (Y/H)$$

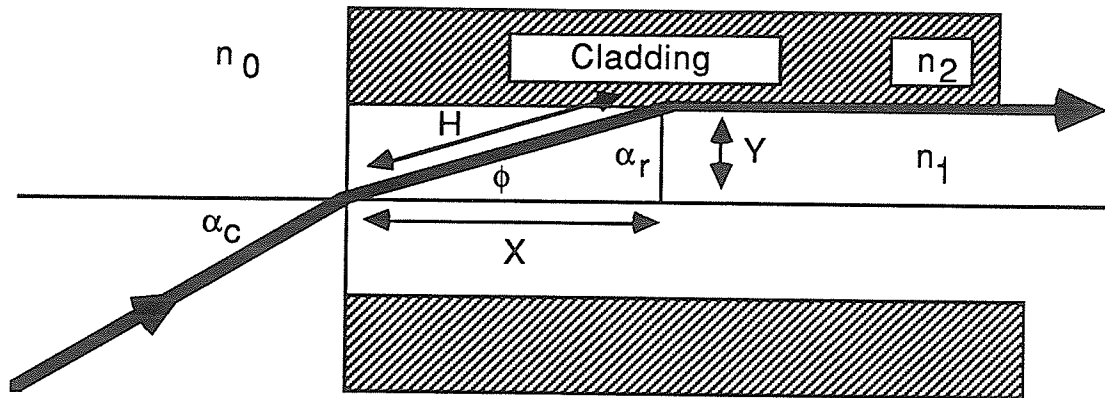


Figure 16.20: Angle of collection of an optic fiber.

$$\begin{aligned}
&= (n_1/n_0) [1-(X^2/H^2)]^{1/2} \\
&= (n_1/n_0) [1-\sin^2(\alpha_r)]^{1/2} \\
&= (n_1/n_0) [1-(n_2/n_1)^2]^{1/2} \\
&= [n_1^2 - n_2^2]^{1/2}/n_0 \\
&= N_A/n_0 \tag{16.6}
\end{aligned}$$

where $N_A = [n_1^2 - n_2^2]^{1/2}$ is referred to as the numerical aperture of the detector probe. Thus, light striking the entrance face of the fiber at an angle less than $\sin^{-1}(N_A/n_0)$ to the normal will be transported down the guide. This, in turn, corresponds to a solid angle of

$$\begin{aligned}
\Omega_c &= 2\pi \{ 1-\cos[\sin^{-1}(N_A/n_0)] \} \\
&\approx \pi(N_A/n_0)^2 \tag{16.7}
\end{aligned}$$

Ω_c is referred to as the solid angle of collection of the detector. Light entering the fiber within this solid angle will be transported, that falling outside will be lost.

The total light collected by a detector probe can be found by integrating the angular distribution function over its entrance face area A and the solid angle of collection Ω_c . The measured spatial irradiance is obtained by dividing this result by the area of the detector face.

$$P_M(r) = \int_{\Omega_c} \int_A \Psi(r, \Omega) da d\Omega / A \tag{16.8}$$

This result may be simplified by assuming the angular distribution function remains constant over the entrance surface of the detector probe. Then,

$$P_M(r) = \int_{\Omega_c} \Psi(r, \Omega) d\Omega \tag{16.9}$$

Quite obviously, $P_M(r)$ will be less than the true spatial irradiance $P(r)$.

In the Diffusion approximation, $\Psi(r, \Omega)$ may be represented by

$$\Psi(r, \Omega) = (1/4\pi) [P(r) + (3/|v|)J(r) \cdot \Omega] \tag{16.10}$$

Substituting this into eq.(16.9),

$$\begin{aligned}
P_M(r) &= \int_{\Omega_c} (1/4\pi) [P(r) + (3/|v|)J(r) \cdot \Omega] d\Omega \\
&\approx (1/4) (N_A/n_0) P(r) \tag{16.11}
\end{aligned}$$

since the second term in the expression is much smaller than the first and is partially cancelled upon carrying out the integration over Ω . To a very good approximation then, measured spatial irradiance will be proportional to true spatial irradiance in regions where Diffusion theory is valid. As the measurements presented in section 16.3 were carried out in regions falling into this category, experimental space irradiance is expected to differ from the true value by a multiplicative constant. This implies that although the measured light density data was incorrect in an absolute sense, it is expected to exhibit relative accuracy.

The detector probe employed in the experimental measurements possessed a numerical aperture of 0.55. Assuming the index of refraction of TEM to be 1.4 (Svaasand [36] uses this value as an approximation to the index of refraction of biological tissue), the constant of proportionality relating measured and true spatial irradiance is calculated to be

$$K = (1/4) (N_A/n_0)^2 = 0.0386 \quad (16.12)$$

In regions where Diffusion theory is expected to break down (ie. in the vicinity of a source or an interface between two materials of different optical properties) eq.(16.11) will not be valid and experimental light density measurements will no longer exhibit the relative accuracy characteristic of those carried out in Diffusion regions. Under these conditions the fraction of the true spatial irradiance recorded by any probe exhibiting a finite solid angle of collection will change as the shape of the angular distribution function changes, which in turn will vary with position in the medium. For example, very close to a source or an interface, the angular distribution function will be expected to be forward directed and a finite angle of collection detector may be able to record a very large fraction of the total light (space irradiance) associated with a particular point in the medium. Conversely, as one moves further from the source and the angular distribution function smooths out to approach that characteristic of a Diffusion region, the fraction of the space irradiance recorded by the probe will be reduced. The direct consequence of this phenomenon will be a measured spatial irradiance which falls off much quicker with distance from a source or interface than is actually the case. In an effort to eliminate this shortcoming in experimental measurements, a number of authors have suggested a special 4π steradians solid angle of collection detector probe be employed. Such a probe consists of a single optic fiber with a small, spherical bulb (made of some strongly diffusing material) attached to its input end. Light photons can enter the bulb from all directions. Once inside, these photons will undergo

a very high degree of scatter and their internal distribution will quickly become isotropic. This distribution is then sampled or recorded by the single optic fiber in the same manner as outlined in the discussion of measurements made in Diffusion regions. In summary, for measurements in non-Diffusion regions, the angular distribution function is first made isotropic and then sampled by the detector probe. Arguments used in the Diffusion region measurements then apply. This approach therefore enables experimental data exhibiting relative accuracy to be collected in regions in which Diffusion theory breaks down.

Chapter XVII

THEORETICAL RESULTS USING LINEAR TRANSPORT THEORY

Once a theoretical model has been shown capable of describing the propagation of light through tissue, it may be utilized to gain a better understanding of this complex phenomenon. The remainder of this chapter will employ Linear Transport and Diffusion theories in this capacity.

17.1 EFFECT OF MEDIUM COMPOSITION AND WAVELENGTH

It has already been stated that the propagation of light through biological tissue will depend on the absorption and scatter properties of that medium. In fact, by quantifying these two processes using the concept of absorption and scatter cross section, the role played by physical structure and composition in determining the spatial distribution of light in a medium may be completely characterized. In Linear Transport and Diffusion theory these two parameters do not appear explicitly. However, recalling the defining equations of the two input parameters required by either theory, c and l , it becomes obvious that knowledge of the scatter and absorption cross sections of a tissue medium are sufficient to completely specify its optical properties at a fundamental level.

$$l = 1/(\sigma(\text{sca}) + \sigma(\text{abs})) \quad (17.1)$$

$$c = \sigma(\text{sca})/(\sigma(\text{sca}) + \sigma(\text{abs})) \quad (17.2)$$

The scatter/absorption coefficient c quantifies the importance of absorption interactions relative to those of scatter as a beam of photons propagates through a medium. The mean free path l , meanwhile, is a measure of the frequency with which both scatter and absorption processes occur. The effect of each on the spatial distribution of light within tissue will now be examined.

The solid line of figure 17.1 illustrates the spatial distribution of light as a function of perpendicular distance from a planar source radiating isotropically within an infinitely large, homogeneous medium. The input parameters required to generate this theoretical distribution were those applicable to TEM 0/10 irradiated

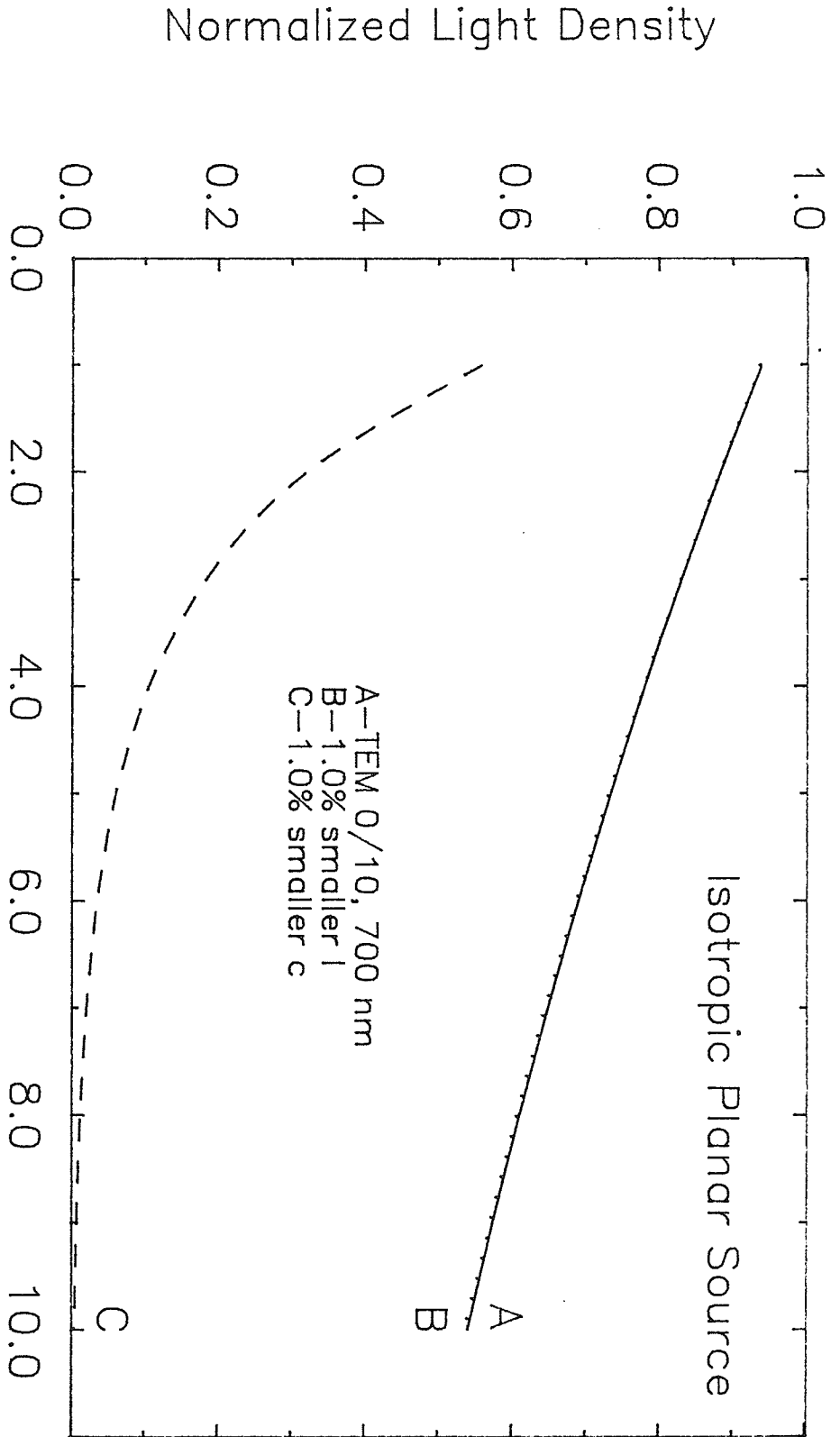


Figure 17.1: Effect of small changes in MFP and scatter/absorption coefficient on spatial light distribution

with light of 700 nm. Also included on this graph are the distributions predicted within media characterized by a scatter/absorption coefficient and mean free path which are 1% larger than those of TEM 0/10 at 700 nm. It is quite clear that such small changes in MFP have little effect on spatial light density. As the absorption cross section per unit volume of tissue is so very small compared to that of scatter, its contribution to MFP will be extremely limited. In fact, even in cases of strong absorption (for example, 550 nm light in TEM 10/10), MFP will vary only slightly from the value it would take on were absorption not present at all. Since small perturbations in MFP will have virtually no effect on the spatial distribution of light within a medium, the absorption cross section per unit volume can, for all practical purposes, be neglected when computing this input parameter. Thus,

$$l = 1/\sigma(\text{sca}) \quad (17.3)$$

Small perturbations in the scatter/absorption coefficient on the other hand will have a significant effect on the spatial distribution of light within a medium (at least when c is close to unity as is the case for tissue). Thus, although its contribution is ever so slight, the absorption cross section per unit volume must be taken into account in any determination of c .

Figure 17.2 illustrates the effects of the variations in the relative importance of absorption on the spatial distribution of light within TEM for isotropic planar irradiation. Shown are the distributions for scatter/absorption coefficients characteristic of light of 550, 600, 700 and 850 nm in TEM 0/10 and 550 and 600 nm in TEM 10/10. Distances have been expressed relative to the appropriate MFP so as to remove the effects of changes in the frequency of interactions as one varies wavelength. Each curve has been normalized to the light density at 0.2 MFP from the source.

In the case of TEM 0/10, absorption is by water. This series of curves clearly demonstrates that the small changes in water absorption at the four wavelengths studied has a very drastic effect on the spatial distribution of light. As a result of the relative importance of absorption being very similar at 550 and 600 nm, the light density curves associated with these two wavelengths will be nearly identical. At a distance of 10 MFPs from the source, light density will have fallen to 86.4% of that at 0.2 MFP in both instances. At 30 MFPs, it will be 64.8%. The decrease in light density with distance from the source is noticeably sharper at 700 nm, it being 82.4% and 56.2% of the 0.2 MFP value at 10 and 30 MFPs, respectively. Water absorption effects are, however, greatest at 850 nm. At this wavelength

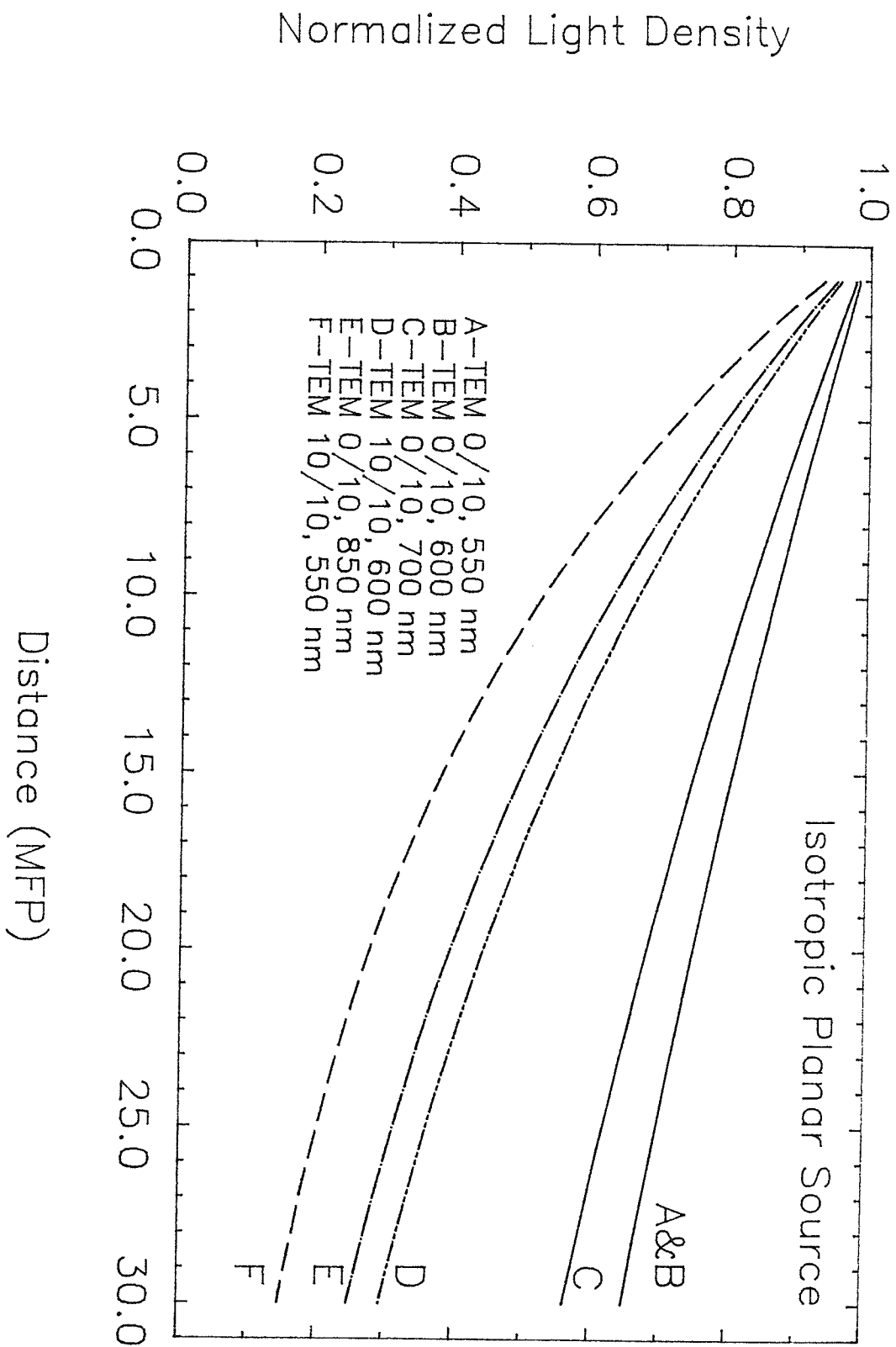


Figure 17.2: Effect of spectral variations in the relative importance of absorption on spatial light distributions (planar source irradiation)

the density of light will fall to 62.6% at 10 MFPs from the source and 24.8% at 30. In summary, despite the fact that the absorption cross section of water is extremely small, the role it plays in determining the spatial distribution of light in TEM and therefore tissue is significant and must be taken into account in any theoretical transport model.

The curves for $c=0.9986459$ and 0.9994529 included in figure 17.2 illustrate the effects of absorption by hemoglobin in TEM at 550 and 600 nm, respectively. In both cases, the reduction in light density due to the presence of this blood component is substantial. For irradiation with light of 550 nm, light density at 10 MFP from the source is reduced to 60.7% of its value in the absence of hemoglobin. At 30 MFPs, it is reduced to 22.7%. The effects of absorption by hemoglobin are much less at 600 nm with light density falling to 76.7 and 45.6% of its value in the absence of this blood component at 10 and 30 MFPs, respectively. Whereas the reduction in light density due to absorption in the absence of hemoglobin was nearly identical at 550 and 600 nm, it is now much greater at the former wavelength. In fact, at 550 nm in the presence of blood the fall off in intensity with distance from the source is substantially greater than that at any of the other wavelengths studied (absorption by hemoglobin at 700 and 850 nm is negligible). The combined effects of absorption by hemoglobin and water at 600 nm is, however, still less than those of water alone at 850 nm.

Identical findings are obtained for isotropic point source irradiation of TEM. Figure 17.3 illustrates the spatial light density as a function of radial distance from the source, expressed relative to MFP, for the same values of c studied in the planar source geometry. In this problem, data is normalized to the light density at 1.0 MFP from the source.

Because the spatial distribution of light within tissue is so greatly affected by small changes in c , it is of interest to examine the consequences of errors incurred in experimentally determining the scatter/absorption coefficient of TEM. For example, different estimates of the scatter/absorption coefficient of TEM 0/10 at 700 nm were obtained by fitting the Diffusion equation to experimental light distributions resulting from both point source and planar source irradiation. With the former irradiation geometry, a c of 0.9998779 was obtained, with the latter a c of 0.9998920. Although these two estimates of the scatter/absorption coefficient are very similar, they will nonetheless yield slightly different theoretical spatial light distributions. Figure 17.4 shows the distributions predicted for these two c values in the case of isotropic planar source irradiation. Light density is once again

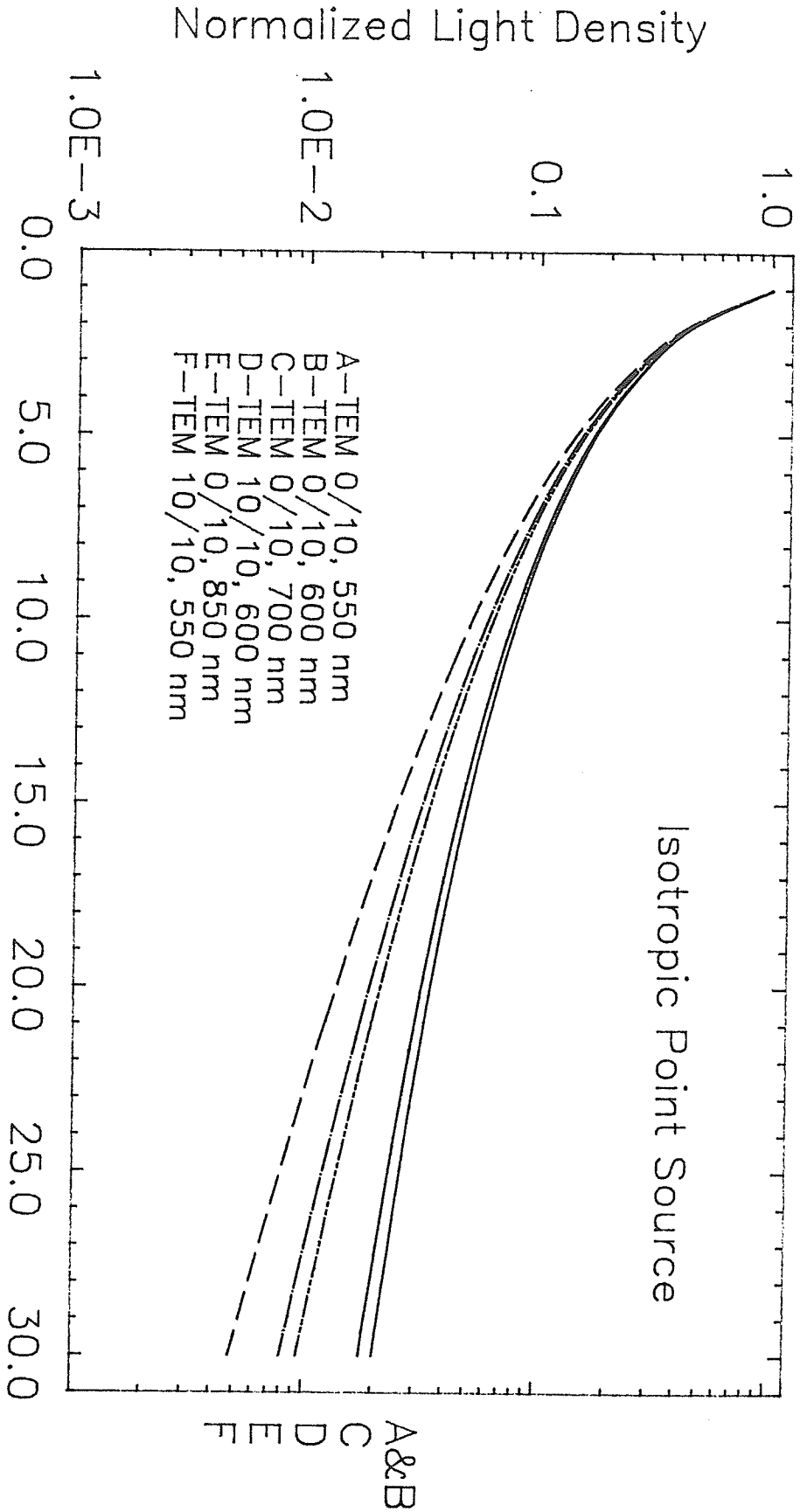


Figure 17.3: Effect of spectral variations in the relative importance of absorption on spatial light distributions (point source irradiation)

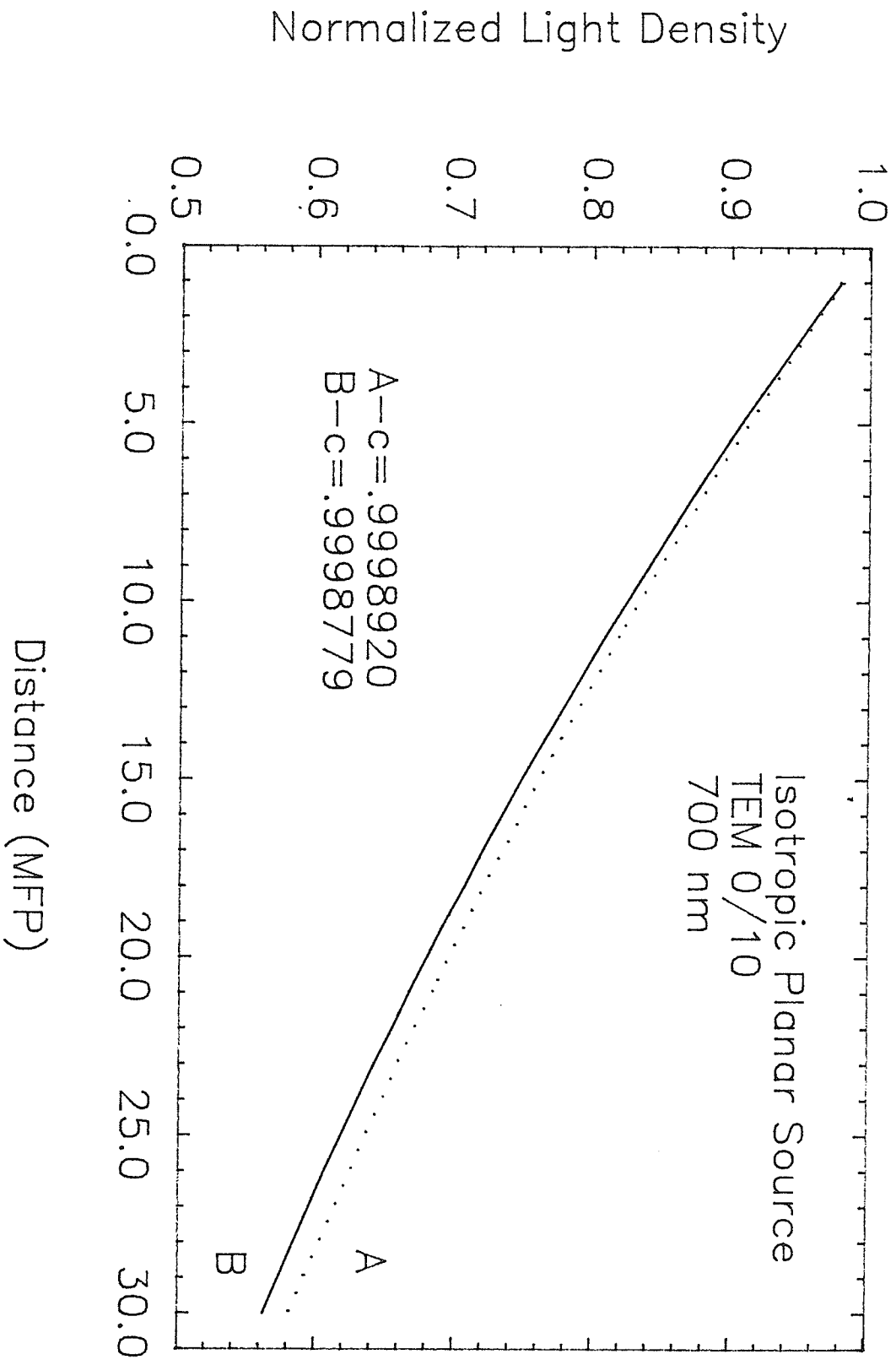


Figure 17.4: Consequences of errors incurred in experimentally determining the scatter/absorption coefficient of TEM 0/10 at 700 nm

normalized to that at 0.2 MFP. At a distance of 10 MFPs from the source, the light density predicted for $c=0.9998779$ is 98.9% of that predicted for $c=0.9998920$. At 30 MFP it has dropped to 96.7%. Two estimates of the scatter/absorption coefficient were also generated for TEM 10/10 at 550 nm, one through a fitting of the Diffusion equation to experimental spatial light density data (planar source irradiation) while the other was calculated using eq.(16.3). Values of 0.9986459 and .9980058 were found, respectively. Variations in the two theoretical planar source distributions generated using these c values are illustrated in figure 17.5.

As previously mentioned, the spatial distribution of light within an irradiated sample of tissue will depend not only on the relative importance of absorption but also on the frequency of interactions within that medium. The combined effect of changes in both of these properties can be examined by plotting light distributions as a function of distance measured in mm rather than relative to MFP. Figure 17.6 shows the results for isotropic planar source irradiation. The values of c and l used to generate these theoretical results are those characteristic of TEM 0/10 for light of 550, 600, 700 and 850 nm and TEM 10/10 for light of 550 and 600 nm. Stated differently, figure 17.6 represents that data of figure 17.2 replotted to take into account differences in the frequency of interactions at the four wavelengths studied. The relative positions of the six curves are severely affected.

In the case of TEM 0/10, the rate at which light density falls off with distance from the source is now much larger at 550 nm than it is at 600 nm. Although the relative importance of absorption is identical at these two wavelengths, the frequency of interactions with the medium is greatly increased at 550 nm. As such the probability of absorption for photons travelling the same distance in the medium will be much higher at the lower wavelength. In spite of the fact that the mean free path and scatter/absorption coefficient change substantially in moving from 600 to 700 nm, the theoretical distributions predicted by the Linear Transport equation for these two wavelengths are very similar. On one hand, the relative importance of absorption is increased at 700 nm from that at 600 nm. On the other hand, however, the frequency of interactions decrease in moving to higher wavelengths. In so far as the ability of light to propagate through TEM is concerned, these two phenomena will have opposite effects, the first serving to make light transport less efficient at 700 nm, the second serving to make it more. In fact, the two effects will nearly cancel and as a result, very little change in the spatial distribution of light will be noted in moving from 600 to 700 nm. As the wavelength of light is further increased to 850 nm, the ability of light to propagate

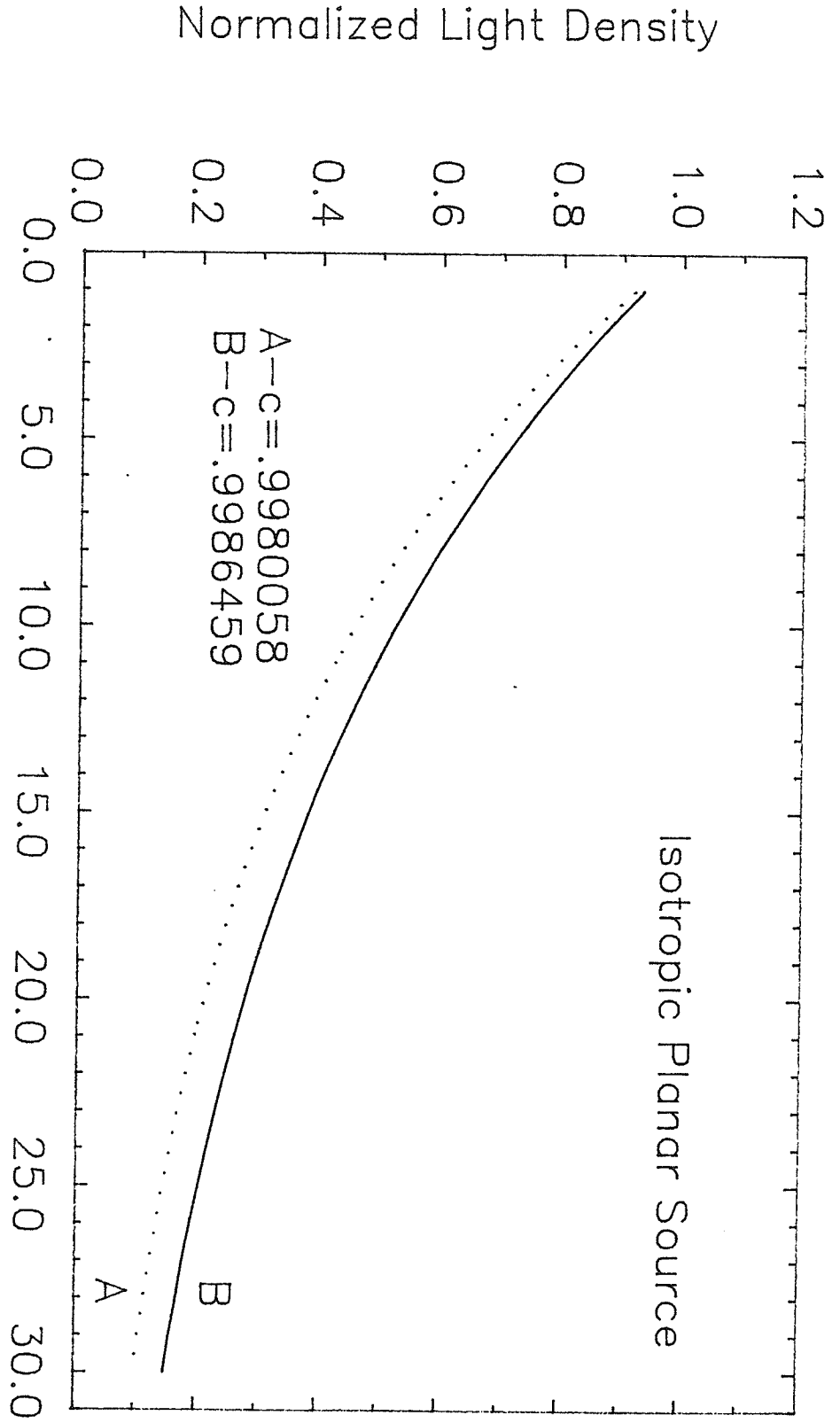


Figure 17.5: Consequences of errors incurred in experimentally determining the scatter/absorption coefficient of TEM 10/10 at 550 nm

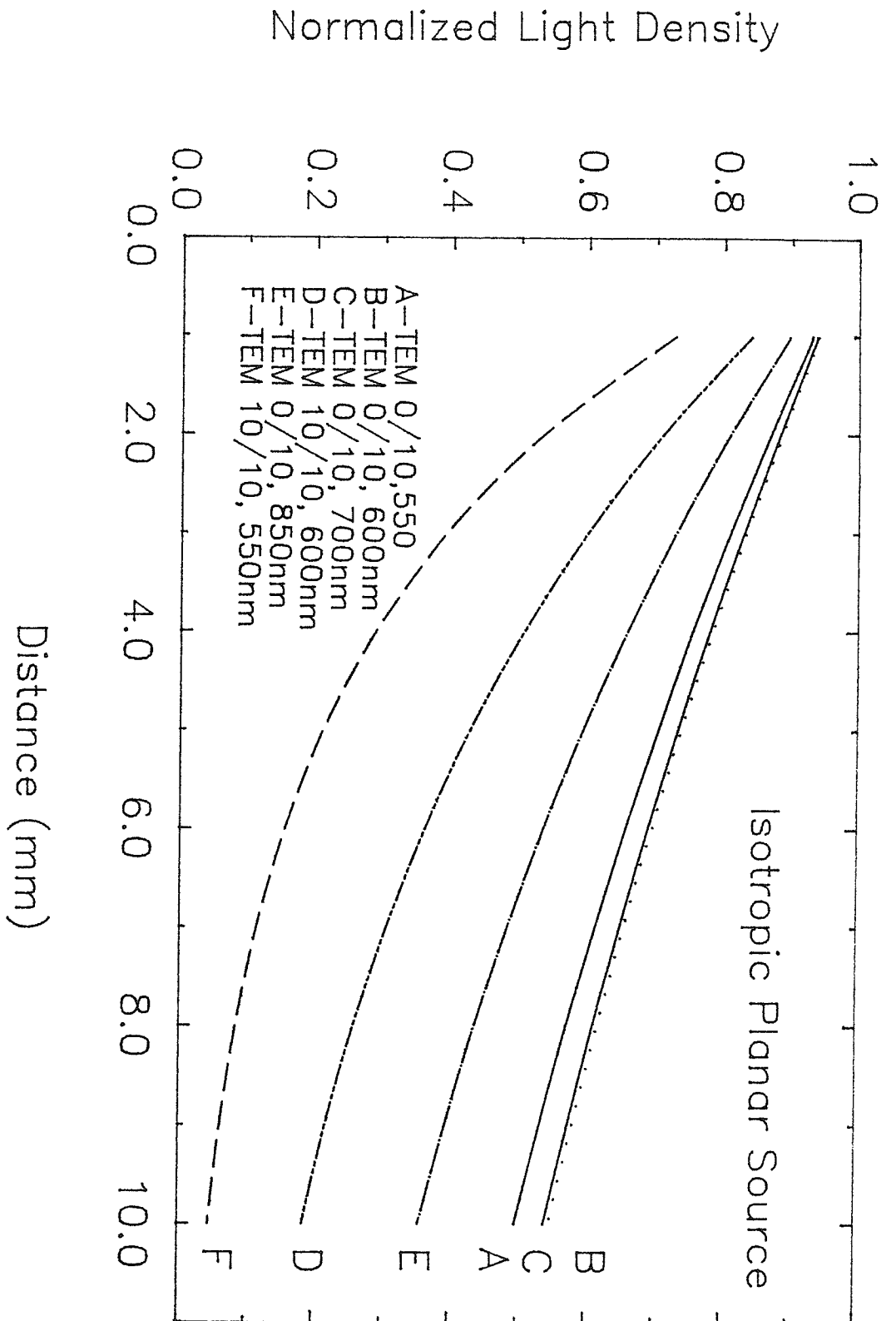


Figure 17.6: Effect of spectral variations in MFP and scatter/absorption coefficient on spatial light distribution (planar source irradiation)

through tissue is once again diminished. Although the frequency of interactions with TEM are much lower at this wavelength, the improvement in light transport resulting from this phenomenon will be greatly overshadowed by the effects of the increased relative importance of absorption.

When the absorption of hemoglobin is taken into account, the rate at which light density falls off with distance from the source is greatly reduced at 550 and 600 nm. The spatial distributions for light of 700 and 850 nm, however, remain unaltered. The presence of hemoglobin does nothing to alter the frequency with which interactions with the medium take place. However, it will increase the relative importance of absorption at 550 and 600 nm, this in turn reducing the ability of light at these wavelengths to propagate through tissue. Light density is now seen to fall off much more rapidly with distance at 550 and 600 nm than at 850 nm.

The ability of light to propagate through tissue-like media characterized by an absence of hemoglobin (for example TEM 0/10) was found to be greatest at 600 and 700 nm. The transport of 850 nm light was much less efficient due to the increased relative importance of absorption. The ability of light of 550 nm to propagate through tissue was also found to be reduced although at this wavelength the increased frequency of interactions was responsible. When the effects of absorption by hemoglobin are taken into account, the efficiency with which light propagates through tissue is substantially reduced at 550 and 600 nm; the optical properties of tissue at 700 and 850, however, are not affected.

17.2 EFFECT OF PLANAR SOURCE COLLIMATION

The Linear Transport equation may also be utilized to examine the effects of source collimation on the spatial distribution of light within an irradiated tissue sample. Figure 17.7 illustrates the theoretical distributions within an infinitely large, homogeneous medium for both isotropic and collimated planar irradiation. Data was generated using the programs IPLSIM and CPLSIM, respectively. A scatter/absorption coefficient of 0.9999303 was chosen for this comparison (ie. that applicable to light of 600 nm in TEM 0/10) so as to simulate conditions of absorption which are generally considered weak.

In the vicinity of the source, dissimilarities (both in terms of shape and magnitude) between the two distributions are attributed to differences in the direction of travel of the individual photons making up the light beams in this region. As the distance from the source is increased

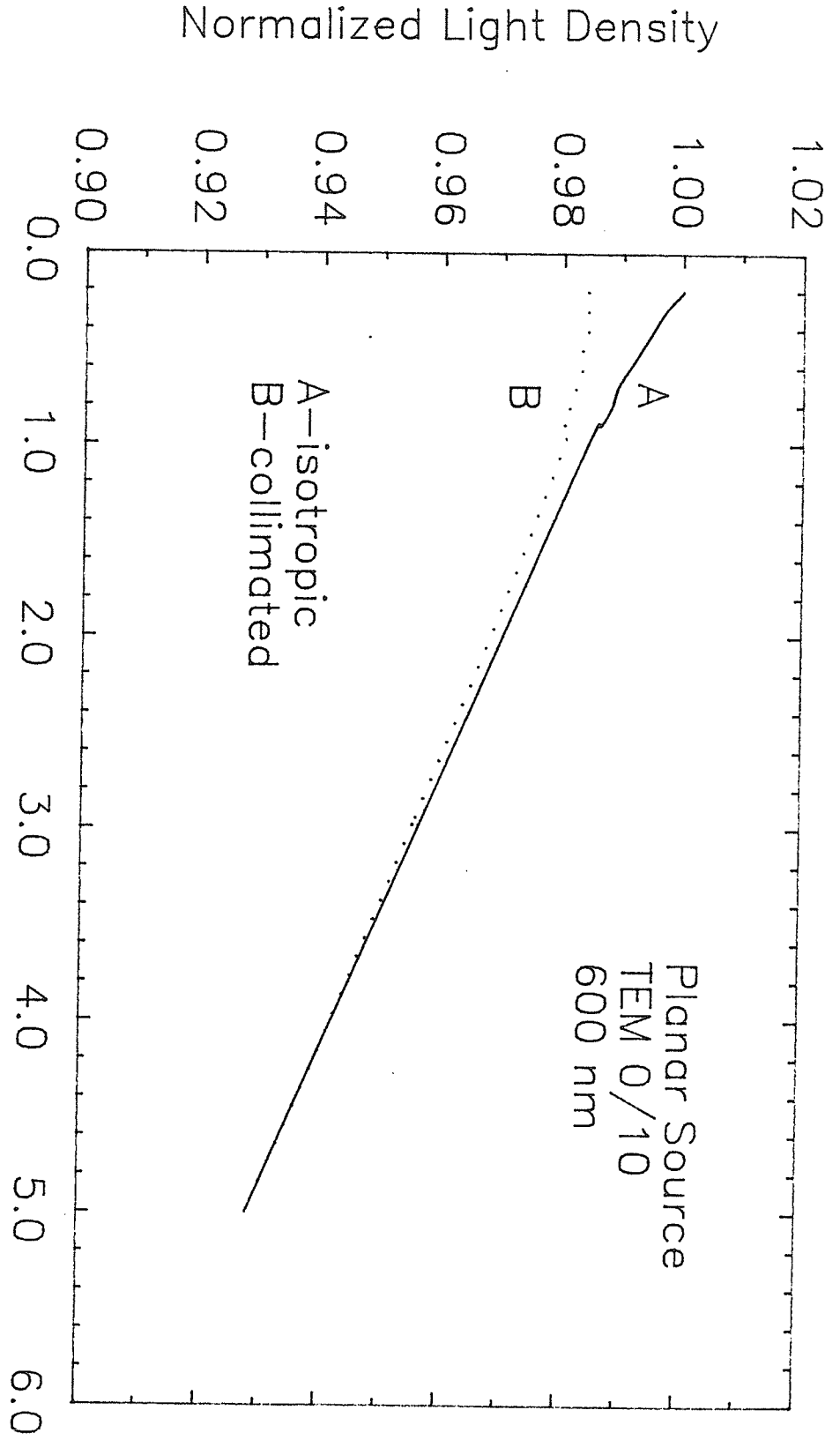


Figure 17.7: Effect of source collimation on the spatial distribution of light within media characterized by weak absorption

however, directional differences will decrease. As the initially collimated beam undergoes more and more scatter interactions, the directions of its constituent photons will become scrambled. Eventually, a distance will be reached where the photon directions may be considered completely random (ie. identical to that of the isotropic source beam). From this point on, the shape of the two beams will be identical. The magnitude of the light intensity at any point in this distal region will however, be slightly greater for collimated irradiation due to fact that more photons leave the source in the forward direction. The curve for isotropic irradiation in figure 17.7 has been normalized to its collimated counterpart at a point far removed from the source so as to correct for this difference.

The region over which dissimilarities exist between the two distributions is seen to be rather small. At a distance of 0.5 MFP from the source, the light density predicted for collimated irradiation is only 99.0% of that for the isotropic geometry. With light of 600 nm, this would correspond to .120 mm in TEM 0/10. For field points at a distance of 0.2 MFP, the collimated light density is 98.4% of the isotropic.

In figure 17.8 the same comparison is made for a medium considered to be a strong absorber of light. A scatter/absorption coefficient of 0.9986459 (ie. that applicable to light of 550 nm in TEM 10/10) was used to generate suitable distributions. The spatial distributions are once again found to be identical at larger distances from the source (after normalization). Under these conditions, the light density predicted for the collimated planar source will climb to 99.0% of that for isotropic irradiation at a distance of 1.7 MFP. This corresponds to a distance of .350 mm in TEM 10/10 for light of 550 nm. At 0.2 MFP from the source, the collimated source light density will be 93.1% of that predicted for the isotropic source.

The theoretical results presented in this section suggest that the degree of collimation of a planar source will have little effect on the spatial distribution of light within tissue. At large distances from the source, the distributions generated with collimated and isotropic irradiation geometries are expected to differ only by a small constant factor (not apparent in the results presented due to curve normalization). In other words, the light distributions will possess the same shape but be of slightly different magnitudes. In the vicinity of the source both the shape and magnitude of the distributions will be dissimilar. However, the extent of this region will be very limited, of the order of 0.5 mm. Differences are expected to be greatest in tissue characterized by strong absorption.

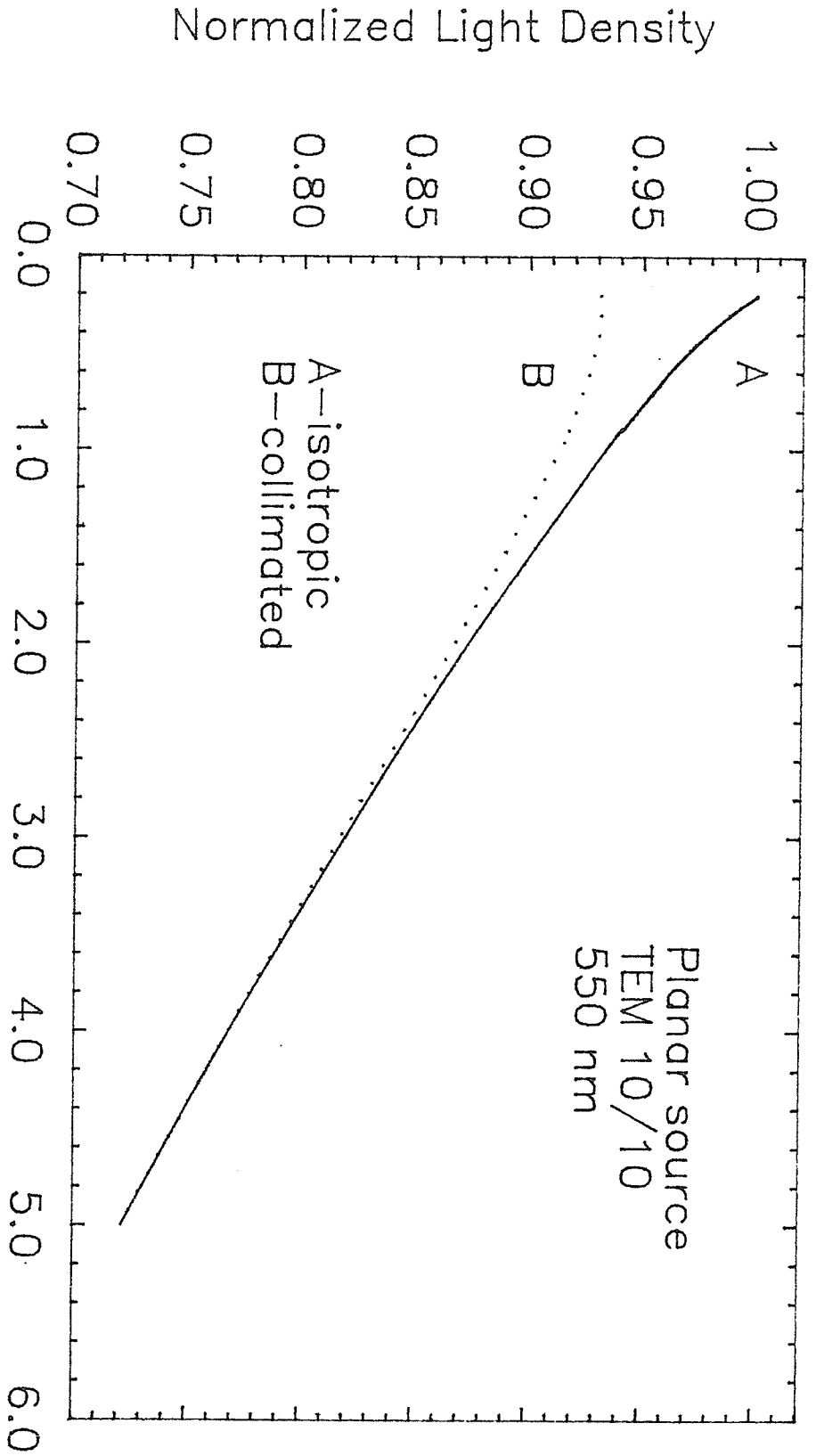


Figure 17.8: Effect of source collimation on the spatial distribution of light within media characterized by strong absorption

17.3 EFFECTS OF A TISSUE-AIR INTERFACE

Consider the Albedo geometry described in section 10.4. The problem is one of finding the spatial distribution of light within a semi-infinite tissue sample (the other half of space is assumed to be vacuum) due to irradiation by a large collimated beam of light normally incident upon its surface. Although its location in the vacuum will have no effect on the spatial distribution within the tissue half space, it will be of use to position the planar source responsible for the irradiation at the interface. The Albedo problem will then differ from the collimated planar source/infinite medium geometry only in that the region behind the source will not be occupied by tissue. A comparison of the spatial distributions associated with these two geometries will then demonstrate the effects an air interface will have on tissue light density. The spatial distributions for these two geometries were generated using the programs CPLSIM and ALBEDO. Results are shown in figure 17.9 for $c=0.9999303$ (ie. that applicable to light of 600 nm in TEM 0/10), chosen so as to simulate conditions in which absorption is considered weak. Data has been normalized to the light density predicted for the Albedo problem at 0.2 MFP from the source.

The presence of the air interface is seen to perturb the spatial distribution of light from that predicted for the CPLSIM problem. With the Albedo geometry, light density is seen to be maximum a finite distance from the source (or interface). For CPLSIM irradiation, on the other hand, this maximum is located at 0 MFP. Differences between the two distributions are seen to be greatest at the source. As distance is increased and the Albedo curve climbs to a peak, disagreement between the two models will lessen. In regions distal to the source, the effects of the interface will be negligible and the two models will yield identical results.

Dissimilarities in the distributions of figure 17.9 exist as a result of differences in scatter. In the CPLSIM problem, light scattered by the medium lying in front of and behind the source will contribute to the irradiation of a field point at 0 MPF. With Albedo irradiation, however, there will be no such contribution from the medium lying behind the source. As vacuum cannot scatter light, photons entering the space behind the source will have no opportunity to re-enter the tissue. Light density is therefore reduced. As one moves further from the Albedo interface, however, the scatter contribution from the medium lying behind the field point will increase. Initially, the number of photons gained as a result of this enhanced scatter will outweigh the number lost due to increased attenuation associated with larger interlying tissue thicknesses. Light density will therefore rise. However, the

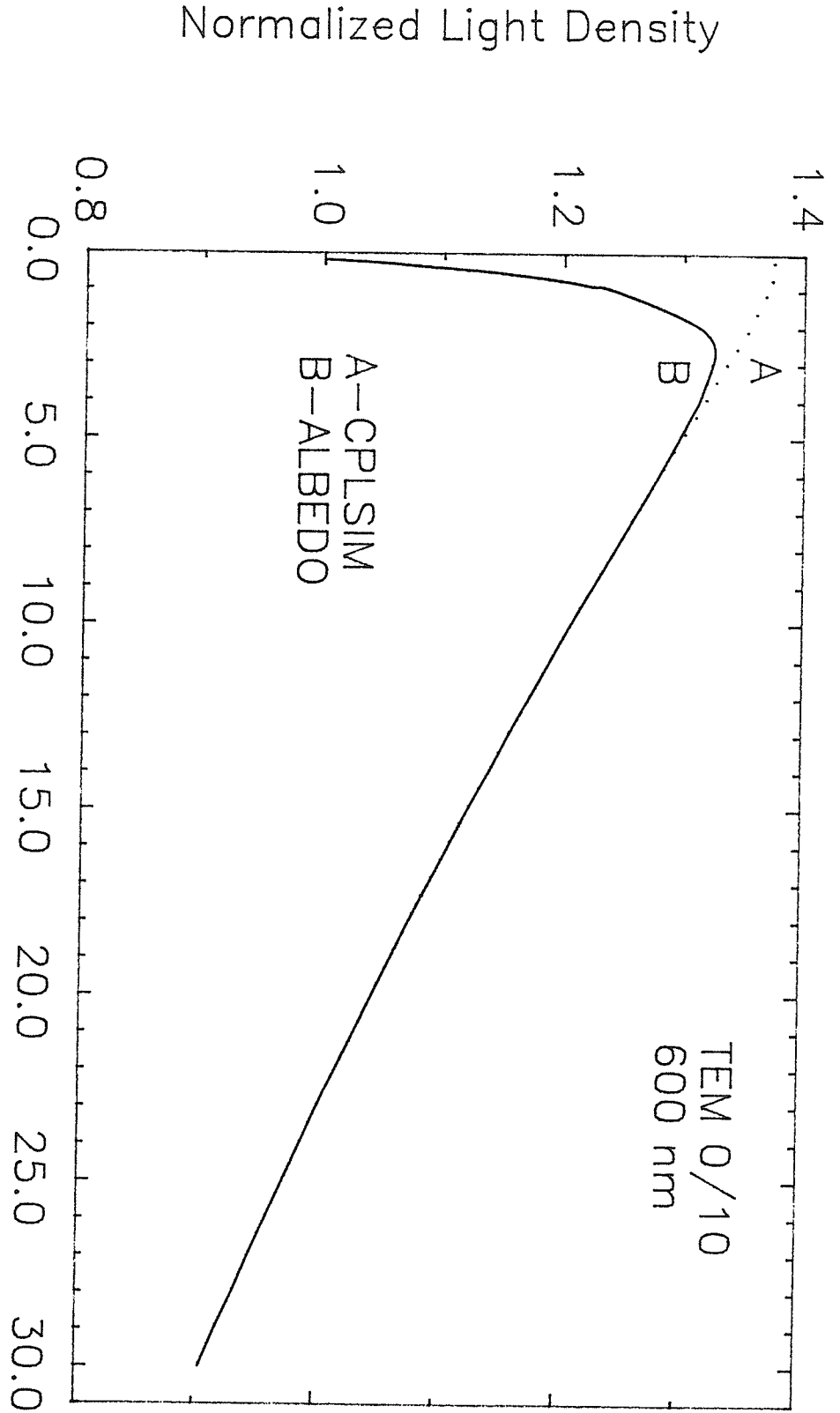


Figure 17.9: Effect of tissue-air interface on the spatial distribution of light within media characterized by weak absorption

thickness of medium lying behind a field point which is able to contribute scatter is finite. Once this thickness has been attained, further increases will do nothing to augment the scattered light density at that field point. Hence, a location will eventually be reached where movement to greater tissue depths will result only in a loss of photons and light density will begin to drop. In this region, scatter in the Albedo problem will be identical to that in the CPLSIM geometry and the two distributions will assume indistinguishable shapes. It should be pointed out, however, that the magnitude of the two curves will differ, that describing the Albedo irradiation geometry being somewhat lower than the CPLSIM curve due to the loss of photons to the vacuum. The Albedo curve of figure 17.9 has been normalized to its CPLSIM counterpart at a point far removed from the interface so as to remove this effect.

The results of figure 17.9 suggest that perturbations in the spatial light distribution will extend to depths of 3.0 MFP from the air interface (at this distance, the light density predicted by ALBEDO is 99.0% of that predicted by CPLSIM). This would correspond to a distance of .720 mm in TEM 0/10 for irradiation with light of 600 nm. Very near the source (0.2 MFP), the Albedo density is 72.7% that for CPLSIM irradiation.

A similar comparison may be carried out for a situation in which absorption would be considered strong. Results are shown in figure 17.10. In this instance, curves were generated assuming a scatter/absorption coefficient of 0.9986459 (ie. that applicable to light of 550 nm in TEM 10/10). Once again, the ALBEDO data has been normalized so that the two distributions will agree at large distances from the interface. The range of the perturbation is seen to be very similar to that found for weak absorption. In fact, the light density predicted for the albedo geometry will be 99.0% of that for the CPLSIM problem at a distance of 3.0 MFP from the source. This corresponds to .618 mm in TEM 10/10 for light of 550 nm. At 0.2 MFP from the source, the light density predicted for the Albedo problem will be 74.6% of that estimated for the CPLSIM geometry; disagreement between the two models is therefore slightly less when absorption is strong.

It is also of interest to examine the effect of the scatter/absorption coefficient on air interface perturbations. Figure 17.11 illustrates the spatial distribution of light generated by the program ALBEDO for 6 c values typical of those which would be encountered in biological tissue studies. In particular, distributions have been predicted for coefficients representative of TEM 0/10 for light of 550, 600, 700 and 850 nm and TEM 10/10 for light of 550 and 600 nm. From this figure it is apparent that the light density peak will shift ever so slightly

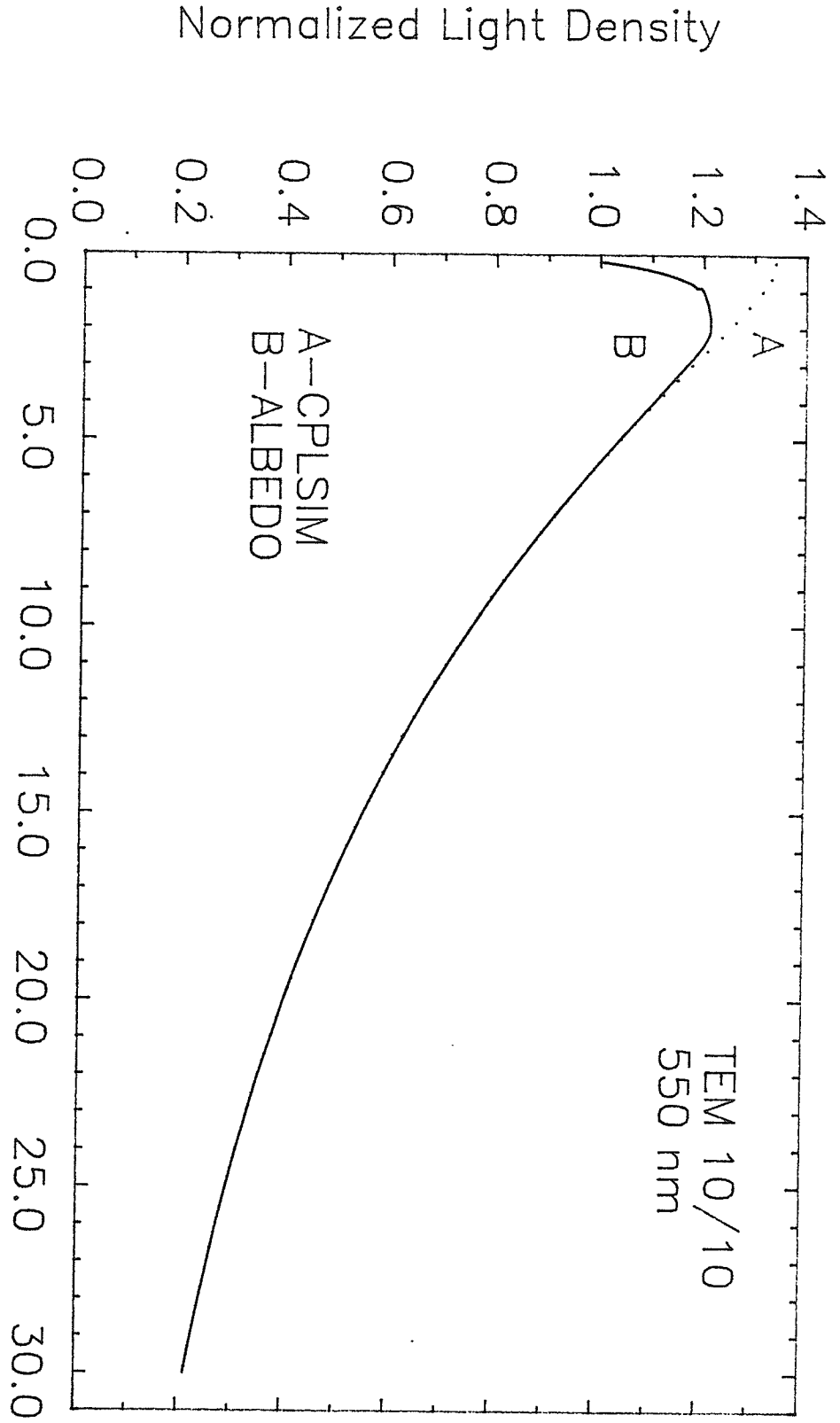


Figure 17.10: Effect of tissue-air interface on the spatial distribution of light within media characterized by strong absorption

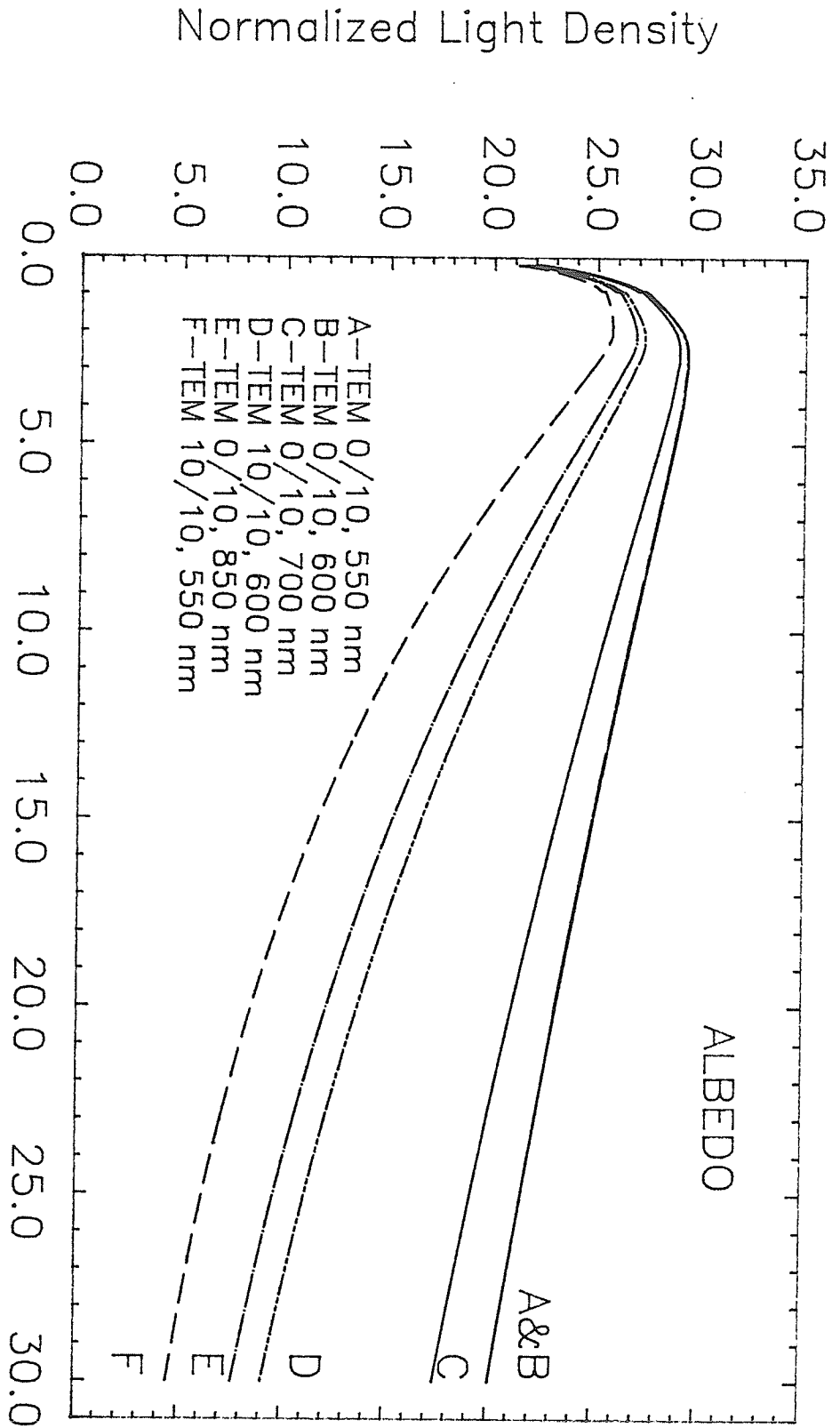


Figure 17.11: Effect of scatter/absorption coefficient on tissue-air interface perturbations

closer to the source as the relative importance of absorption increases. In situations characterized by weak absorption (TEM 0/10 at 600 nm), the peak will be located 2.8 MFP from the source. When absorption is strong (TEM 10/10 at 550 nm) the maximum will be found at a distance of 1.6 MFP. The magnitude of the peak is also seen to be dependant on the relative importance of absorption interactions within the medium, it being 132.3% of the 0.2 MFP light density for $c=0.9999303$ and 121.3% for $c=0.9986459$. In addition, the entrance light density in the case of heavy absorption (that at 0.2 MFP from the source) will be 95.5% of that for weak absorption.

17.4 THE ERRORS OF DIFFUSION THEORY

It has previously been pointed out that Diffusion Theory will yield inaccurate predictions of the spatial light density within tissue whenever the associated angular distribution function $\Psi(z,\Omega)$ becomes too large in one preferred direction. The three possible conditions under which such a distribution function will exist are as follows:

- 1) in media characterized by strong absorption relative to scatter
- 2) in the vicinity of a light source
- 3) in the vicinity of an interface between two media of different optical properties

Under all other conditions, Diffusion theory will provide an accurate description of the propagation of light within tissue (assuming the irradiation geometry and input parameters are precisely known). In this section, the magnitude of the errors incurred by employing Diffusion theory to describe spatial light distributions will be examined in all three of the above "problem areas". Estimates of the errors involved will be obtained by comparing the Diffusion distributions to those obtained using the Linear Transport equation, a theoretical model which will provide an exact description of light propagation under any circumstances.

The first condition under which Diffusion theory is expected to break down is that of heavy absorption. Stated more precisely, Diffusion theory will yield inaccurate light density predictions in media characterized by a scatter/absorption coefficient which is much less than unity (ie. in media where the relative importance of absorption as compared to scatter is significant). However, from the

measurements of c for TEM presented in section 16.2, it is apparent that this condition will not be encountered in the study of light propagation through biological tissue. Even in situations in which the absorption of light is considered heavy, c will deviate only very slightly from 1.0 (for example the transport of 550 nm light through TEM 10/10 is associated with a scatter/absorption coefficient of 0.9986459). It should be pointed out, however, that TEM was developed to simulate the optical properties of normal breast tissue. As such, to say that its absorption characteristics are representative of tissues in general is incorrect. For example, kidney or liver may possess absorption cross sections per unit volume which are indeed larger than that of TEM 10/10 at 550 nm. Nonetheless, differences in $\sigma(\text{abs})$ are not expected to be so large that c will deviate markedly from 1.0. Even under the extreme conditions with which one is confronted in Photodynamic therapy - light propagation through biological tissue which has been chemically sensitized to increase its absorption of visible light - c is expected to remain close to unity. Results presented by Powers et al. [35] serve as evidence supporting this claim. Through measurements on rats, these authors have shown the transport of 630 nm light through photosensitized brain to be very similar to that of 488 nm light through normal brain.

The second area in which the Diffusion model is expected to break down is in the vicinity of a source of light. Figure 17.12 illustrates the spatial distribution of light generated by an isotropic point source radiating within an infinitely large homogeneous medium as predicted by both the Diffusion and Linear Transport equations. Results are for a scatter/absorption coefficient of 0.9999303 (ie. that applicable to TEM 0/10 for light of 600 nm) chosen so as to simulate conditions in which absorption is considered weak. Data points have been normalized to the light density predicted by Linear Transport theory at a distance of 0.2 MFP. As expected, the two theories yield identical results in regions distal from the source and disagree in regions proximal (in the vicinity of the source Diffusion theory will underestimate light density). However, the region over which dissimilarities between the two theories exist will be very small. In fact, at a distance of 2.2 MFP from the source, the light density predicted by Diffusion theory will be 99.0% of that predicted by the Linear Transport equation. This would correspond to a distance of .528 mm in TEM 0/10 at 600 nm. Diffusion theory light density will be 44.2 and 91.4% of the exact value at 0.2 and 1.0 MFP, respectively.

Results typical of those expected in transport problems involving what is considered strong absorption are shown in figure 17.13. In this instance, distributions were generated assuming a scatter/absorption coefficient of 0.9986459 (ie.

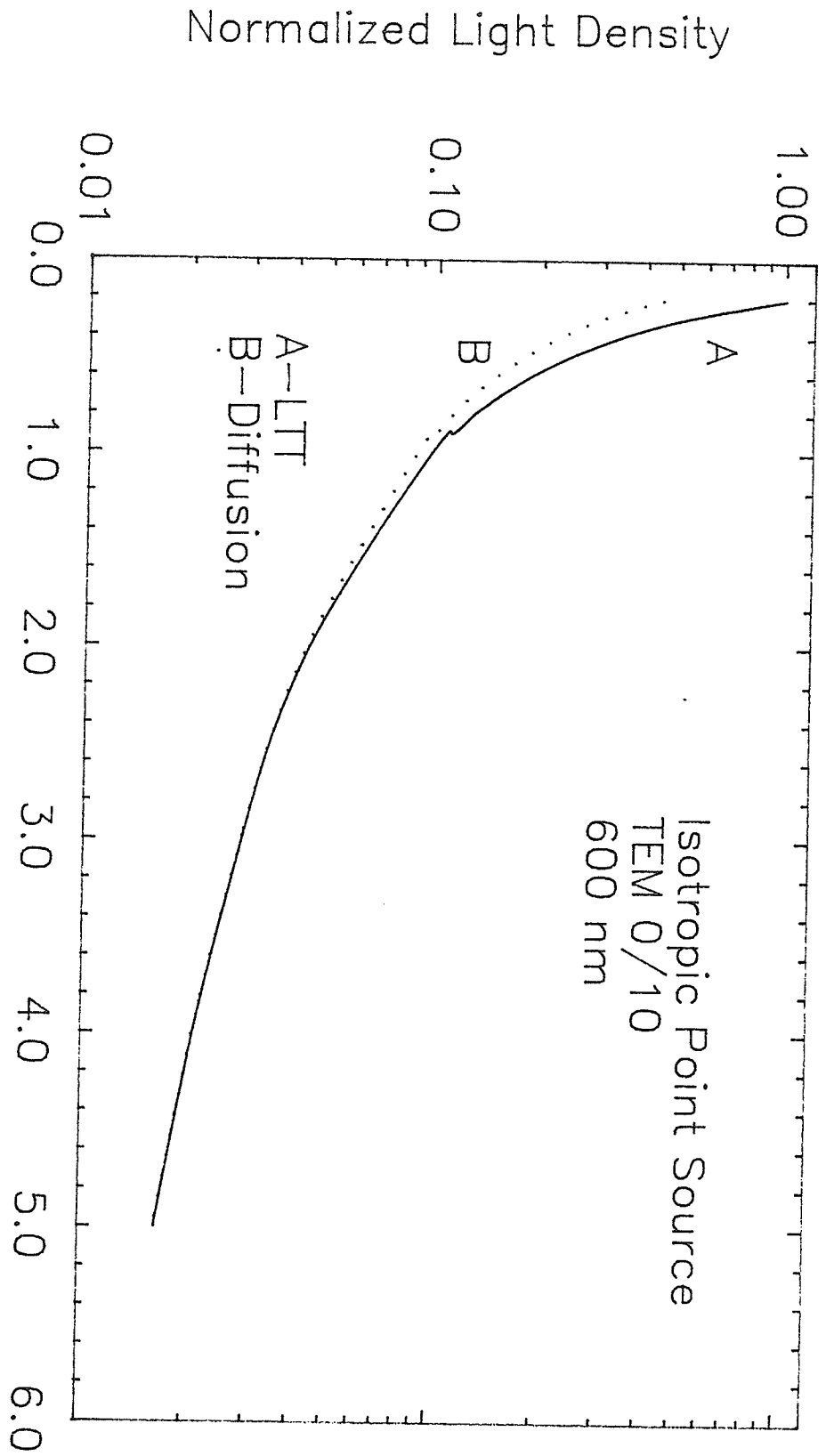


Figure 17.12: Dissimilarities between Linear Transport and Diffusion theory in the vicinity of an isotropic point source (weak absorption)

Normalized Light Density

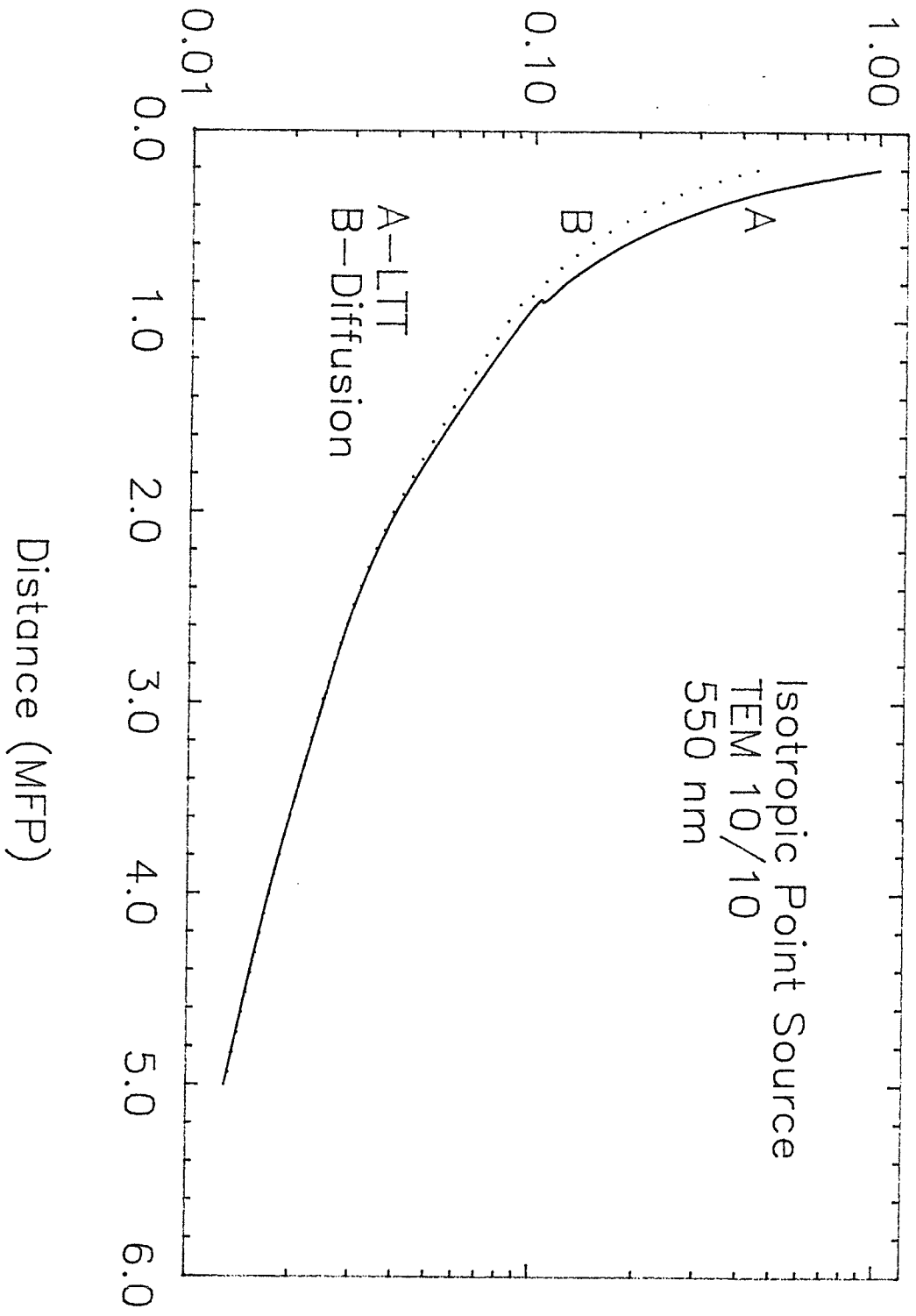


Figure 17.13: Dissimilarities between Linear Transport and Diffusion theory in the vicinity of an isotropic point source (strong absorption)

that applicable to TEM 10/10 at 550 nm). The region over which the two curves differ is very similar to that found in the case of weak absorption. The Diffusion estimate will be 99.0% of the Linear Transport prediction at a distance of 2.2 MFP from the source. For irradiation with light of 550 nm, this would correspond to .453 mm in TEM 10/10. The light density predicted by the 1st order approximation theory for distances of 0.2 and 1.0 MFP is 44.0 and 91.1% of its true value, respectively.

Results for isotropic planar source irradiation are illustrated in figure 17.14 ($c=0.9986459$). Once again, Diffusion and Linear Transport theory are seen to agree in regions distal to the source. However, the region in which the Diffusion approximation is seen to break down is now greatly reduced. In fact, at a distance of 0.2 MFP, the Diffusion model yields a light density which is only 98.0% of that predicted by Linear Transport theory.

The above findings indicate that Diffusion theory will indeed yield inaccurate results in the vicinity of a source of light. However, the spatial extent of these regions will be very limited. For transport problems in which tissue irradiation is with point source geometry, Diffusion theory is expected to be accurate within 3.0 MFP of the source. This distance is almost independent of the relative importance of absorption. When planar sources are employed, errors incurred using Diffusion theory will be almost negligible at distances of 0.2 MFP.

The third and final area in which Diffusion theory is expected to deviate from the exact Linear Transport model is in the vicinity of an interface. Figure 17.15 shows the spatial distribution of light predicted by the two theories near an air interface (ie. albedo geometry). Once again, a scatter/absorption coefficient of 0.9999303 is used (ie. that applicable to TEM 0/10 at 600 nm) so as to simulate conditions of weak absorption. Data is normalized to the light density predicted by Linear Transport theory for a distance of 0.2 MFP from the interface.

As expected, the Diffusion approximation provides an accurate estimate of spatial light density in regions distal to the interface. However, at small distances the first order approximation model will yield a distribution which differs markedly in shape and magnitude from that of Linear Transport theory. Whereas the exact theory predicts tissue light density to assume a maximum at some finite distance from the interface, Diffusion theory generates a distribution in which the peak light level resides at the interface. In this respect, the Diffusion solution is very similar to that predicted by Linear Transport theory for a collimated planar source radiating within an infinitely

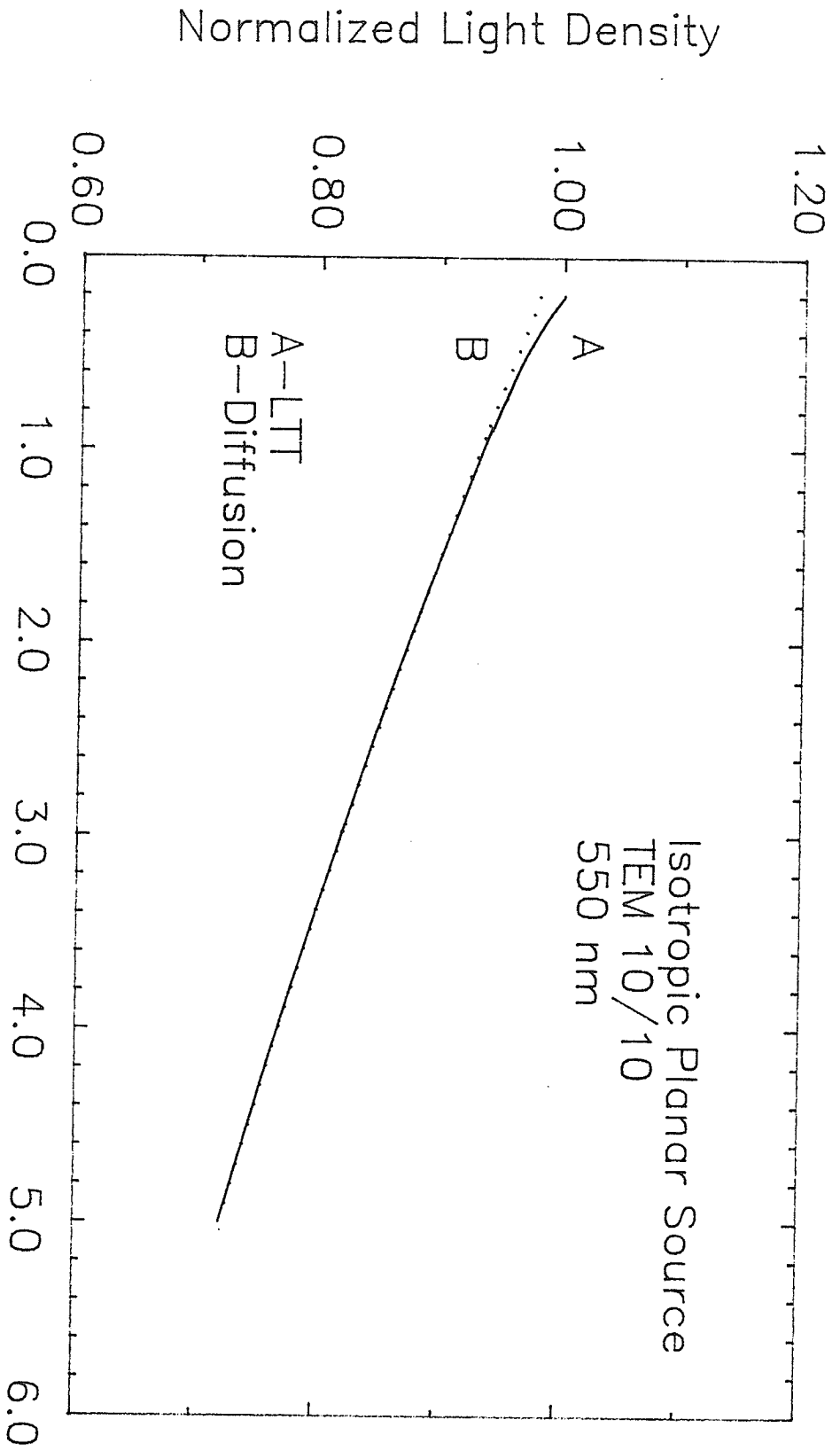


Figure 17.14: Dissimilarities between Linear Transport and Diffusion theory in the vicinity of an isotropic planar source (strong absorption)

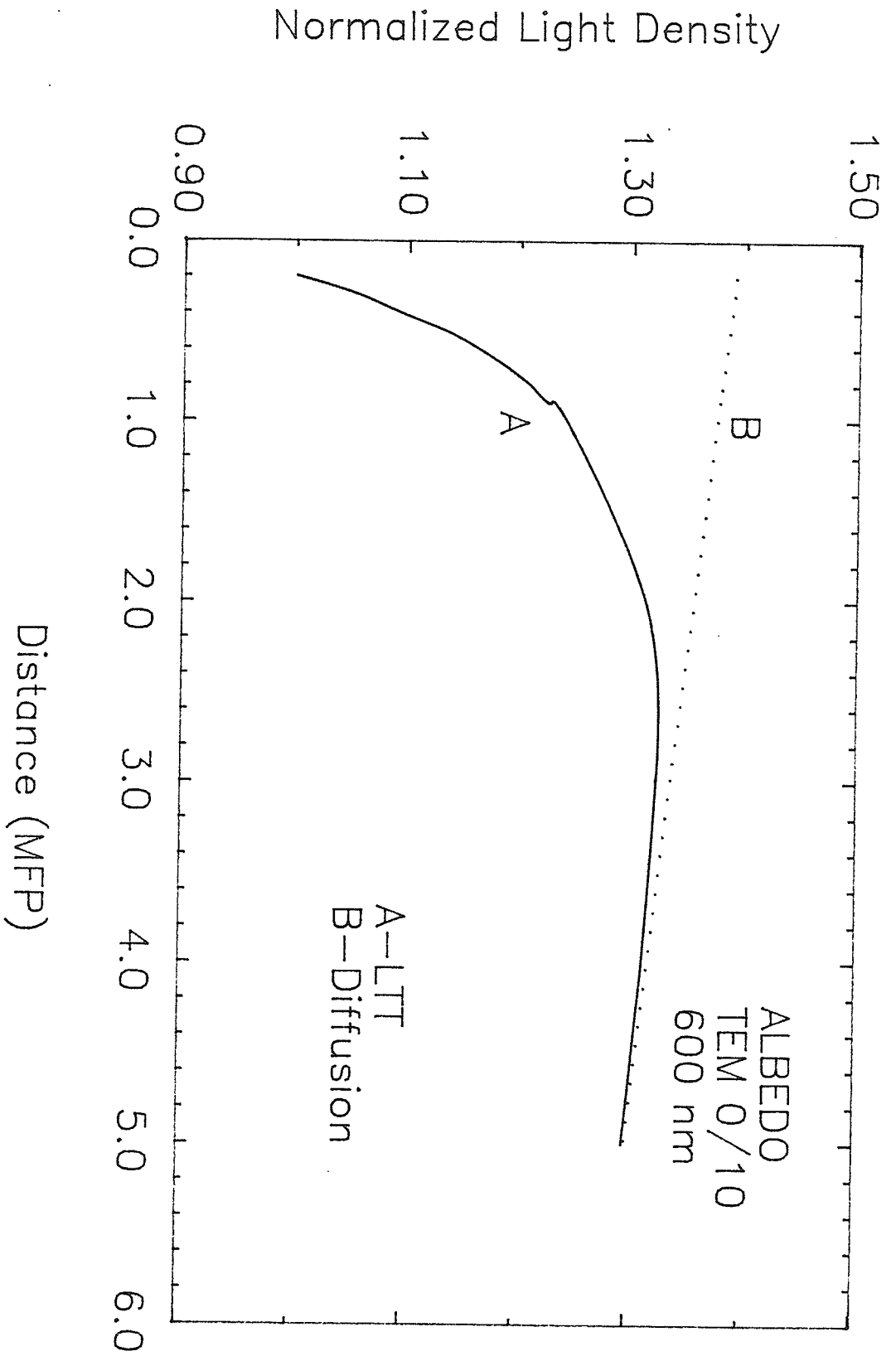


Figure 17.5: Dissimilarities between Linear Transport and Diffusion theory in the vicinity of a tissue-air interface (weak absorption)

large medium. In so far as the magnitude of the distribution is concerned, Diffusion theory will overestimate light density within this "breakdown region". At a distance of 0.2 MFP, the predicted light level will be 139.1% of its true value. This deviation from the Linear Transport solution will diminish with distance from the interface with the Diffusion curve falling to 101.0% of the exact model at a distance of 3.0 MFP. For irradiation with light of 600 nm, this would correspond to .720 mm in TEM 0/10.

Results typical of those found under conditions in which absorption is strong are shown in figure 17.16. Curves were generated assuming a c of 0.9986459 (ie. that applicable to TEM 10/10 for light of 550 nm). Findings are similar, although now the region over which the two models disagree is noticeably larger (the Diffusion distribution will fall to 101.0% of that predicted by Linear Transport theory at a distance of 3.3 MFP; this corresponds to a distance of .680 mm in TEM 10/10 at 550 nm). The magnitude of the dissimilarities encountered in this "breakdown region" are also seen to be greater than in the case of weak absorption. At 0.2 MFP, Diffusion theory predicts a light density which is 141.1% of the Linear Transport estimate.

The above comparison of Linear Transport and Diffusion theory demonstrates that substantial dissimilarities will exist in the spatial light distributions predicted by each for regions proximal to an air interface. Under conditions normally encountered in light transport studies, this region of disagreement is expected to be of the order of 4 MFP in length, although its size will show a slight dependance on c (the length of the "breakdown region" will increase as the relative importance of absorption increases). One should keep in mind however, that these results reflect a very extreme situation. At interfaces between two tissues of different optical properties, disagreement between Linear Transport and Diffusion theory will be much less. Also, interface results presented in this section were generated using a collimated incident beam. As the distribution of light near a source depends upon the angular distribution of the emitted radiation, different results are expected for an isotropic incident beam. The effect of incident radiation collimation, however, is expected to be slight (see Linear Transport/Diffusion theory comparisons in the vicinity of a source).

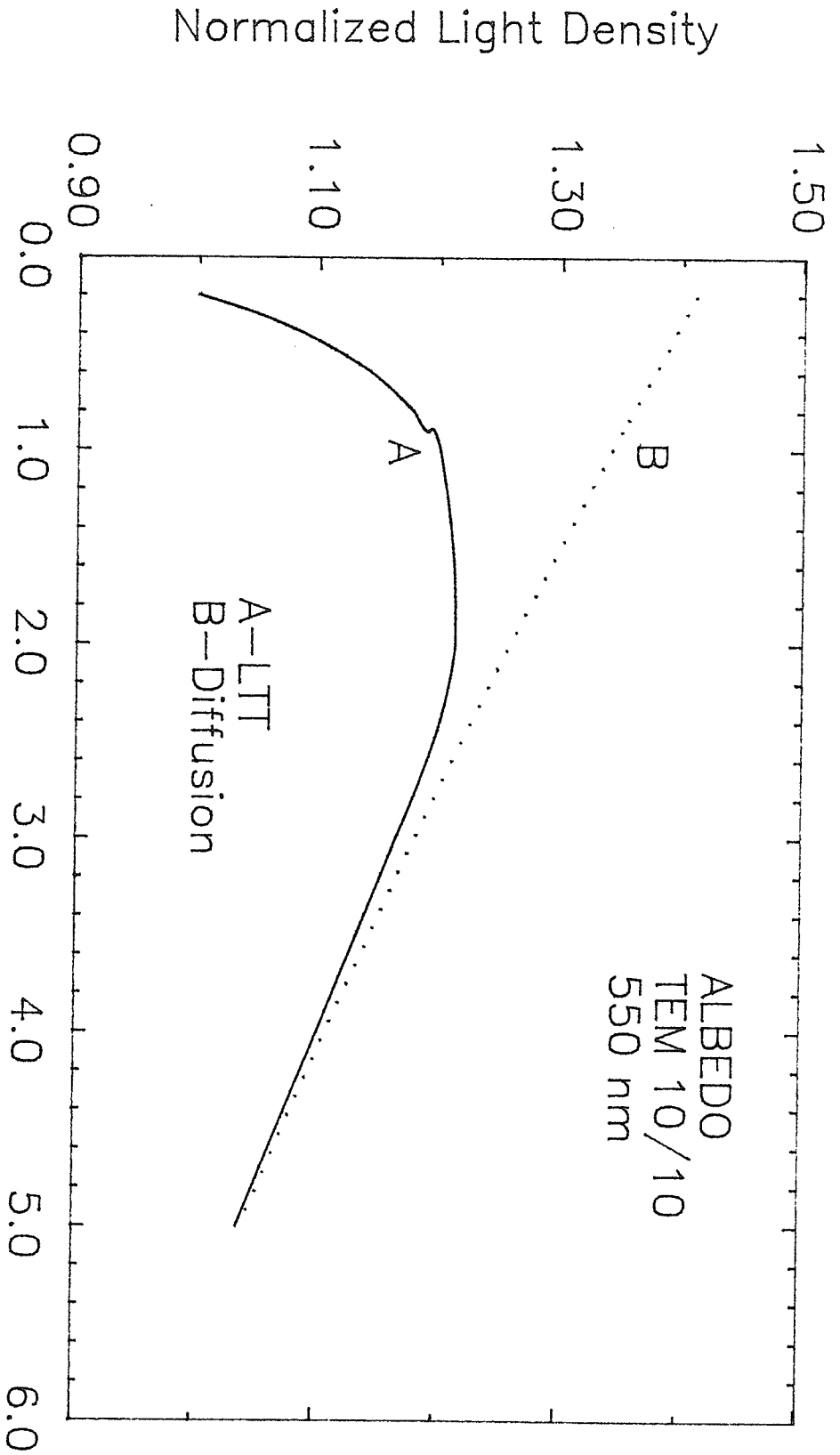


Figure 17.16: Dissimilarities between Linear Transport and Diffusion theory in the vicinity of a tissue-air interface (strong absorption)

Chapter XVIII

SUMMARY

A spectrophotometer-type instrument, referred to as the DICOM-8, was developed to quantify the optical properties of biological tissue through the measurement of diffuse spectral extinction. The main components of the system were a 100 w quartz tungsten halogen source and a vidicon camera detector. Tissue samples were inserted into cylindrical glass tubes (8.5 mm dia.), positioned between source and detector and transilluminated. The vidicon camera was focussed on the exit surface of the irradiated sample and its output signal fed to an image processing computer for digitization and subsequent display on a 512x512x8 bit video refresh plane. As the magnitude of the camera output signal will be dependant on the brightness of the object being viewed, the digitized images contained information pertaining to tissue extinction. A calibration program was developed to convert image brightness (ie. grey level) to sample extinction. Melles-Griot bandpass interference filters mounted in front of the camera lens enabled measurements to be carried out at select wavelengths between 550 and 900 nm.

Three independent tests were conducted to check the accuracy of the system. In the first, the diffuse spectral extinction of a dilute, aqueous red blood cell suspension was measured using both the DICOM-8 and a commercial spectrophotometer, the Bausch and Lomb Spectronic 710. The curves were found to possess identical shapes but slightly different magnitudes with the DICOM-8 predicting a higher extinction at all wavelengths. This discrepancy was attributed to differences in the solid angle of collection between the two instruments. The second test consisted of measuring the extinction of Trypan Blue at 650 nm with both the DICOM-8 and spectronic 710. As Trypan Blue may be considered a pure absorber of light at 650 nm, variations in solid angle of collection will be of no consequence and the two instruments should yield identical results. This was indeed found to be the case. In the final test, Melles-Griot neutral density filters were treated as samples and measured for extinction using the DICOM-8 system. Results were found to be very similar to those obtained using an International Light radiometer.

The DICOM-8 system was ideally suited for measuring the diffuse spectral extinction of biological tissue. The very intense output of the 100 w source combined with the low light level response of the vidicon camera enabled measurements to be carried out on thick samples (ie. high extinctions). In addition, the architecture of the instrument (specifically the use of sample rotation during transillumination) was such that repeat measurements on the same sample could be conducted quickly and with relative ease. These two attributes made it possible to generate extinction curves which were representative of a tissue sample in general rather than local fluctuations in composition.

Once its accuracy had been verified, the DICOM-8 system was used to measure the diffuse spectral extinction of both normal and diseased human breast tissue. Twenty-nine tissue samples were measured in all, 18 normal and 11 carcinoma; 8 of the normal specimens were further divided into groupings of adipose and glandular. The need for using averages to quantify the optical properties of a tissue sample (ie. automatic sample rotation) was demonstrated by measuring spectral extinction for three different light paths through the same sample of glandular tissue; the spread between these curves was substantial. All subsequent curves were generated using automatic sample rotation (averaging 100 individual measurements).

Substantial differences were found to exist between the diffuse spectral extinction curves of similar tissues removed from different patients. Variations were greatest at short wavelengths. Although the significance of these findings to the clinical application of light transport models is not known, the need for further research in this area is clear. As it will be impractical to measure the optical properties of tissue on a patient to patient basis, one set of optical parameters (mean free path and scatter/absorption coefficient) must be assigned to each tissue type and applied universally. In view of the above mentioned variations between individuals, such an approach will introduce a certain amount of uncertainty in predicted spatial light distributions. Before transport models can attain clinical application, these errors must be quantified. Such an analysis, however, requires that a large data base of light transport parameters be obtained through experimental measurement on a sizable population. As uncertainties are expected to be larger at the lower end of the visible spectrum, the usefulness of theoretical light models at short wavelengths maybe somewhat limited.

Patient averaged curves were generated for each of the tissue classifications studied, normal, glandular, adipose and carcinoma. The four curves were found to exhibit a

common shape, characterized by a continuous decrease in extinction with increasing wavelength. Below 700 nm, in the region where absorption by hemoglobin plays a major role in the light attenuation phenomenon, slopes were steep. In the near infrared, meanwhile, scatter processes dominate and the spectral extinction curves showed very little wavelength dependence. In contrast to the similarities found in shape, the magnitude of the tissue plots differed markedly with carcinoma possessing a higher extinction than normal and glandular tissue removing light more efficiently than adipose; variations were seen to diminish with increasing wavelength and were virtually nonexistent above 700 nm. This behavior was attributed to differences in the hemoglobin concentration of the three tissues studied. This blood component served to enhance light attenuation at wavelengths within the visible spectrum but had no effect in the infrared. Carcinoma, as a result of its increased hemoglobin concentration exhibited a greater extinction than normal tissue at short wavelengths. Similar arguments hold for the glandular/adipose tissue comparison.

The results obtained from the breast tissue study may be used to select an optimal wavelength of light for Photodynamic therapy and Diaphanography. With the former modality, it is desirable to maximize the efficiency of light transport through tissue. As such, long wavelength light would appear most suitable (provided a suitable photosensitizing drug can be developed for use with long wavelength light) although the advantages gained by moving beyond 700 nm are minimal. In the case of Diaphanography, both light transport efficiency and normal tissue/carcinoma contrast must be considered. Short wavelength light in the vicinity of the 550 nm hemoglobin absorption peak will yield the greatest contrast. However, the efficiency with which light of this wavelength is transported through the breast is extremely low, making image acquisition impossible. When transillumination is carried out at higher wavelengths, transport efficiency is improved but at the expense of contrast. Quite clearly, a compromise is required.

The DICOM-8 spectral extinction curves served as a basis for the development of TEM, a two component model which simulated the optical properties of biological tissue over the range 550 to 900 nm. The materials used in the construction of this homogeneous liquid (as well as their relative concentrations) were chosen so as to yield a substance exhibiting the same diffuse spectral extinction as glandular breast tissue.

One component of TEM consisted of an aqueous solution of powdered coffee creamer and Methocel. The particulate nature of the creamer, when in suspension, served to scatter light in a manner similar to biological tissue. The Methocel, on

the other hand, was optically transparent and functioned only to prevent settling. The individual scatter particles of this component were ellipsoidal in shape and possessed, on average, major and minor axes lengths of 3.5 and 2.3 μm , respectively (ie. approx. 1/2 the size of a typical red blood cell). Absorption by the scatter component was small over the entire 550 to 900 nm range. Hemoglobin, the other component of TEM, served to simulate the absorption of light in biological tissue. Its contribution to scatter was negligible.

A mixture of 0.5% Methocel, 5.0% creamer and a 1/800 hemoglobin concentration of normal whole blood was found to provide adequate optical equivalence to glandular breast tissue (ie. similar diffuse spectral extinction as measured by the DICOM-8). However, by adjusting the relative concentrations of the TEM components, media exhibiting a wide range of optical properties could be generated. In order to differentiate between these mixtures, TEM media were associated with a number pair A/S where A and S represented the relative concentrations of the absorption and scatter components, respectively. A value of 10 signified equivalence to glandular tissue. For example, a TEM mixture with the designation 5/10 exhibited similar scatter properties to breast tissue but only half the hemoglobin absorption.

The average distance between scatter particles in a TEM 10/10 mixture was calculated to be 6.99 μm . As this is greater than three times the average particle radius, scatter in TEM 10/10 was considered independent.

Measurements of diffuse spectral extinction were also conducted to demonstrate the stability and reproducibility of TEM 10/10, two very important characteristics of any tissue model.

TEM 10/10 was then utilized to construct a breast phantom for bench top diaphanography studies. Three tissue culture flasks, placed in contact with one another and filled with TEM 10/10, provided a 4.8 cm thickness of tissue equivalent material. Four blood filled polyethylene tubes (of inner dia. 1.19 mm and outer dia. 1.70 mm) positioned vertically at varying depths from the surface of the phantom simulated carcinoma tissue. Although extreme (hemoglobin concentration in tumors will be substantially less than in whole blood), this model is expected to incorporate those mechanisms thought to be responsible for image formation in Diaphanography.

The breast phantom was placed between a 100 w broad beam light source and RCA vidicon camera and transilluminated. Images of the exit face of the model were acquired at select

wavelengths (600, 700 and 850 nm) using Melles-Griot bandpass interference filters (mounted in front of the camera) and sent to an image processing computer for digitization and subsequent display. It is of interest to note that the video camera employed was identical to that used in the commercial Diaphanography unit marketed by Spectrascan.

The technical difficulties associated with using short wavelength light for transillumination was clearly evident in this study. As a result of the very poor efficiency of transport, image acquisition at 600 nm was unsuccessful. Failure was also encountered at 850 nm although in this case, inferior camera sensitivity (as compared to that at 700 nm) rather than reduced light transport efficiency was responsible.

Technical difficulties were overcome by replacing the RCA vidicon with a Fairchild CCD camera (with light amplifier). The improved low light level response of this detector made possible the acquisition of images at all three wavelengths. The Fairchild camera images clearly illustrated the improved contrast available at 600 nm as compared to 700 nm. In the former image, two tubes were visible while in the latter, none could be detected. Contrast at 850 nm was similar to that at 700 nm.

Results obtained from the bench top study suggest that normal tissue/tumor contrast can be significantly improved by transilluminating the breast with short wavelength light (ie. 600 nm). In addition, it would appear that the technical difficulties associated with reduced transport efficiency may be overcome by employing a video camera with an improved low light level response (such as a Fairchild CCD camera with light amplifier). Image degradation as a result of the enhanced scatter at lower wavelengths would seem to be insignificant.

Finally, the bench top study provided an opportunity to demonstrate the improvements in tumor visualization that can be attained by employing digital processing techniques to Diaphanography images. Dual wavelength image subtraction, windowing and adaptive histogram equalization were examined. Image contrast was improved to the extent that the fourth tube could just be detected.

TEM was also used to examine the ability of mathematical transport models to describe the propagation of light through biological tissue. In this application, TEM 0/10 and TEM 10/10 functioned as test media in which light distributions resulting from highly controlled irradiation geometries could be experimentally measured and compared with those obtained theoretically. Two mathematical models

were examined, Linear transport theory and Diffusion theory. The former provides an exact description of light propagation within a scattering/absorbing medium while the latter gives only a first order approximation. Comparisons with experimental data were carried out in regions far removed from light sources or interfaces. As the two transport models will yield identical results in these regions, the comparison studies could not be used to demonstrate the superiority of Linear Transport theory.

Application of either transport model required that the mean free path l and scatter/absorption coefficient c of the medium of propagation be determined. Extinction measurements carried out on a $47 \mu\text{m}$ thick sample were used to calculate the mean free path of TEM 0/10. Values ranging from 0.206 mm at 550 nm to 0.495 mm at 900 nm were obtained. Mean free path was found to be directly proportional to the square of the wavelength indicating that the individual light scattering particles of this synthetic breast material occupy an overlap region where both the Rayleigh-Gans and Anomalous Diffraction theories provide an accurate description of their attenuation properties. Estimates of the scatter/absorption coefficients of TEM, meanwhile, were assigned using the criterion that agreement between theoretical and experimental data be maximized.

Calculation of the mean free path of TEM 10/10 required that both the scatter cross section per unit volume of its scatter component (ie. MFP of TEM 0/10) and the absorption cross section per unit volume of its hemoglobin component be determined. Quantification of the latter parameter was through a straightforward application of Beer's law to extinction measurements carried out on a 10 mm thick hemoglobin solution of the same concentration as found in TEM 10/10. Values ranging from 0.0097 mm^{-1} at 550 nm to 0.0006 mm^{-1} at 900 nm were obtained. Although absorption plays a very large role in light transport through TEM 10/10, the cross section per unit volume describing this process was found to be extremely small (compared to that for scatter) and subsequent MFP calculations yielded results which were, for all practical purposes, identical to those obtained for TEM 0/10. Estimates of the scatter/absorption coefficient of TEM 10/10 were generated using the same approach employed for TEM 0/10.

A comparison of theoretical and experimental spatial light distributions were carried out for two irradiation geometries, an isotropic point source and an isotropic planar source radiating within an infinitely large, homogeneous medium. The point source geometry was simulated by inserting the output end of an optic fiber bundle/light source assembly into a large container of TEM from its underside. The highly forward directed output of the fiber

was made isotropic by attaching a small plastic diffusing cap to its end. A second optic bundle, coupled to an International Light radiometer, served as a probe for sampling light density as a function of radial distance from the source. Experimental distributions were obtained for light of 550, 600, 700 and 850 nm in TEM 0/10 (between 5 and 30 mm from the source) and 600 nm in TEM 10/10 (between 5 and 20 mm from the source). In all cases, Diffusion theory was able to predict spatial light distribution with a very high level of accuracy. Results were not generated using the Linear Transport model due to its equivalence to Diffusion theory over the region studied. Estimates of the scatter/absorption coefficients of TEM 0/10 and TEM 10/10, obtained by requiring that agreement between experimental and theoretical data be maximized, were as follows: 0.9999307, 0.9999303, 0.9998779 and 0.9992869 for TEM 0/10 at 550, 600, 700 and 850 nm, respectively; 0.9994529 for TEM 10/10 at 600 nm.

Isotropic planar source geometry was simulated by uniformly irradiating the underside of a large container of TEM with light from a high intensity output view box. As with the previous geometry, light density was sampled as a function of distance from the source using an optic fiber bundle coupled to an International Light radiometer. Experimental distributions were obtained for light of 550 and 700 nm in TEM 0/10 (between 5 and 30 mm from the source) and 550 nm in TEM 10/10 (between 5 and 20 mm from the source). The corresponding theoretical distributions, generated using the Diffusion model, showed excellent agreement. Scatter/absorption coefficients generated through comparisons with experimental data were very similar to those found in the point source study, lending some credibility to results. Values of 0.9999244, 0.9998920 and 0.9986459 were obtained for TEM 0/10 at 550 nm, TEM 0/10 at 700 nm and TEM 10/10 at 550 nm, respectively.

The scatter/absorption coefficient of TEM 10/10 was also determined using a more direct approach, through calculations involving the absorption cross section per unit volume of its hemoglobin component and the mean free path of its scatter component. Values of 0.9980044 and 0.9993769 were obtained for light of 550 and 600 nm, respectively. Results were similar to those found using the less direct comparison of experimental and theoretical distributions.

Besides providing some indication of the ability of Linear Transport and Diffusion models to describe the propagation of light through tissue, the experimental-theoretical distribution comparisons served as a method for quantifying the scatter/absorption coefficient. For TEM 10/10, c was found to range from 0.9986459 at 550 nm to 0.9997315 at 850 nm. These results suggest that even at

wavelengths where absorption is generally considered to be strong (ie. 550 nm), tissue will be characterized by a scatter/absorption coefficient which differs only slightly from unity. As such, it would appear that one of the conditions responsible for the breakdown of Diffusion theory, that of small c , will not be encountered when dealing with the propagation of light through this biological medium.

Once their ability to describe light transport through TEM had been demonstrated, Linear Transport and Diffusion theory were utilized to gain a better understanding of this complex phenomenon.

The Linear Transport model was used to examine the effects of small changes in MFP and scatter/absorption coefficient on spatial light density. Theoretical distributions were generated for three sets of input parameters, one being typical of TEM 0/10 at 700 nm, the other two representing 1% increases in MFP and scatter/absorption coefficient, respectively. Planar source irradiation was assumed. Results suggest that small changes in l will have little effect on spatial light density. As such, the absorption cross section per unit volume may be neglected in calculations of this parameter, the slight perturbations in MFP it leads to having no effect on the predicted light distributions. In contrast, small changes in c have a very drastic effect on theoretical light density patterns (at least when c is close to unity as in the case of biological tissue). The absorption cross section per unit volume must, therefore, be incorporated in calculations of this input parameter.

Linear transport theory was also used to compare spatial distributions arising in TEM 0/10 for planar source irradiation with light of 550, 600, 700 and 850 nm. Light density was first plotted as a function of MFP so that the effects of spectral changes in the scatter/absorption coefficient could be examined independent of variations in the frequency of interactions. In TEM 0/10, absorption (the presence of which is indicated by a c less than unity) was by water. Although generally considered weak, absorption by this solvent was shown to have a very drastic effect on the distribution of light within TEM. Spectral variations in its relative importance were responsible for the substantial differences in light transport efficiency observed at the four wavelengths studied. The rate at which light density decreased with increasing distance from the source was found to be greatest at long wavelengths. Distributions obtained for light of 550 and 600 nm were very similar.

Theoretical distributions for TEM 10/10 at 550 and 600 nm were plotted on the same graph to illustrate the effects of

absorption by hemoglobin. The presence of this blood component greatly reduced light transport efficiency, its effects being much greater at the shorter wavelength. Whereas the spatial distributions for light of 550 and 600 nm were almost identical in its absence, differences were now substantial.

Spatial variations in the frequency of interactions were taken into account by replotting the TEM 0/10 and TEM 10/10 spatial light distributions as a function of distance from the source as measured in mm. The ordering of the curves was greatly altered. In TEM 0/10, light transport efficiency was found to be greatest at 600 and 700 nm. Although characterized by significantly different MFPs and scatter/absorption coefficients, the theoretical distributions generated for these two wavelengths were almost identical (in moving to the higher wavelength, gains incurred in transport efficiency due to increased MFP were cancelled by losses resulting from a reduced scatter/absorption coefficient). At higher wavelengths (850 nm), increased absorption by water reduced the efficiency with which light propagated through TEM 0/10. A reduction was also observed at lower wavelengths (550 nm) although in this case, an increase in the frequency of interactions was responsible. Light transport was least efficient in TEM 10/10, the curves associated with light of 550 and 600 nm falling off much quicker with distance from the source than those predicted in the absence of the hemoglobin component.

The effects of planar source collimation were examined using the theoretical light distributions arising within TEM for both collimated and isotropic irradiation. Curves were generated using the Linear Transport model. Differences were shown to exist only in the vicinity of the source. Under conditions of weak absorption (simulated using input parameters for TEM 0/10 at 600 nm), the distributions were found to be virtually identical at distances greater than 0.5 MFPs from the source. This corresponds to 0.120 mm in TEM 0/10 at 600 nm. For media generally considered to be strong absorbers of light (ie. TEM 10/10 at 550 nm), dissimilarities were observed up to 1.7 MFP from the source, a distance of 0.350 mm in TEM 10/10 at 550 nm.

Perturbations in spatial light density in the vicinity of an air interface were quantified by comparing theoretical distributions generated for Albedo and collimated planar source/infinite medium geometries. Large differences were observed in the vicinity of the interface. In particular, the distribution predicted for the Albedo geometry assumed a maximum light density a finite distance from the interface while that for the infinite medium decreased monotonically with source separation. Dissimilarities were attributed to differences in the volume of the medium contributing scatter

at a particular field point. In regions distal to the interface, distributions were identical. Air interface perturbations were found to extend to depths of 3.0 MFP in both weakly and strongly absorbing media (ie. TEM 0/10 at 600 nm and TEM 10/10 at 550 nm) with Albedo light density being approximately 75% of that predicted for the infinite medium geometry at the tissue boundary. Theoretical Albedo distributions were generated for TEM 0/10 at 550, 600, 700 and 850 nm and TEM 10/10 at 550 and 600 nm. Peak height (relative to interface light density) and depth were both found to decrease with decreasing scatter/absorption coefficient. For TEM 0/10 and 600 nm light, peak density was 132.3% larger than that at the boundary; in TEM 10/10 at 550 nm, peak height was reduced to 121.3%. Peak depth, meanwhile, shifted from 2.8 to 1.6 MFP.

Errors incurred when using Diffusion theory to describe the propagation of light through tissue were quantified by comparing distributions obtained using this model with those of the exact Linear Transport theory, both in the vicinity of a source and close to an interface.

For comparisons proximal to a source of light, distributions were generated assuming isotropic point source/infinite medium geometry. In media characterized by weak absorption (ie. TEM 0/10 at 600 nm), dissimilarities in the two theories were found to exist up to distances of 2.2 MFP from the source. This corresponds to 0.528 mm in TEM 0/10. In regions closer to the source, Diffusion theory underestimated light density; at a distance of 0.2 MFP, the density predicted by the Diffusion model was 44.2% of the Linear Transport result. In media generally considered to be strong absorbers of light (ie. TEM 10/10 at 550 nm) similar results (both in terms of the magnitude of the dissimilarities and the distance over which they extend) were obtained. Linear Transport and Diffusion distributions generated for isotropic planar source/infinite medium geometries were, for all practical purposes, identical for distances greater than 0.2 MFP.

Comparisons were also carried out in the vicinity of an air interface using distributions generated with an Albedo irradiation geometry. For media characterized by weak absorption (ie. TEM 0/10 at 600 nm), dissimilarities were found to exist up to distances of 3.0 MFP from the interface (0.720 mm in TEM 0/10 at 600 nm). In regions closer, distributions differed markedly in both shape and magnitude with the Diffusion model overestimating light density (at 0.2 MFP from the source, it gave a value which was 139.1% of the true density). Whereas Linear Transport theory predicted the maximum density to occur at a finite distance from the interface, the Diffusion distribution was monotonically decreasing. For media exhibiting strong absorption (ie. TEM

10/10 at 550 nm), the region over which Diffusion theory broke down was slightly increased (to 3.3 MFP). The magnitude of the dissimilarities was also larger, with the first order approximation model predicting a light density at 0.2 MFP which was 141.1% of the Linear Transport value.

Chapter XIX

REFERENCES

1. J. Pooler and D. Valenzeno, "The Role of Singlet Oxygen in Photooxidation of Excitable Cell Membranes", *Photochem. Photobiol.* 30, pp. 581-584 (1979)
2. B. Wilson and M. Patterson, "The Physics of Photodynamic Therapy", *Phys. Med. Biol.* 31:4, pp. 327-360 (1986)
3. O. Raab, "Uber Die Wirkung Fluoreszirenden Stoffe Auf Infusoria", *Z. Biol.* 39, p. 524 (1900)
4. R. Lipson and E. Baldes, *Arch. Dermatol.* 82, pp. 508-516 (1960)
5. T. Dougherty, "Photodynamic Therapy", *Clinics in Chest Medicine* 6:2, pp. 219-236 (1985)
6. M. Arnfield, S. Gonzalez, P. Lea, J. Tulip and M. McPhee, "Clinical Irradiator Fiber Tip for Photodynamic Therapy", *Las. Surg. Med.* 6, pp. 150-154 (1986)
7. M. McPhee, C. Thorndyke, G. Thomas, J. Tulip, D. Chapman and W. Lakey, *Las. Surg. Med.* 4, pp. 93-98 (1984)
8. H. Hasazumi, N. Miyoshi, T. Misaki, "A Trial Manufacture of a Motor Driven Laser Light Scattering Optic for Whole Bladder Wall Irradiation", in *Porphyrin Localization and Treatment of Tumors* (Alan R. Liss Inc., New York, 1984), pp. 249-256
9. D. Jocham, G. Staehler, C. Chaussy, E. Unsold, C. Hammer, U. Lohrs and W. Gorisch, "Integral Dye-Laser Irradiation of Photosensitized Bladder Tumors with the Aid of a Light Scattering Medium", in *Porphyrin Localization and Treatment of Tumors* (Alan R. Liss Inc., New York, 1984), pp. 249-256
10. A. Profio, L. Wudl and J. Sarnaik, "Dosimetry Methods in Photodynamic Therapy", pp. 35-41
11. C. Gros, Y. Quenville and Y. Hummel, "Diaphanologie Mammaire", *J. Radiol. Electrol.* 53, pp. 297-306 (1972)
12. M. Cutler, "Transillumination as an Aid in the Diagnosis

- of Breast Lesions", Surg. Gynecol. Obstet. 48, pp. 721-
(1929)
13. C. Gros and R. Sigrist, "La Radiographie Et La
Transillumination De La Mamelle", Strasbourg Med., pp.
451-455 (1951)
 14. C. Jones and S. Newbery, "Visualization of Superficial
Vasculature using a Vidicon Camera with Silicon Target",
Brit. J. Radiol. 50, p. 209 (1977)
 15. R. Morton and S. Miller, "Infrared Transillumination
using Photography and Television", J. Audiovisual Media
in Medicine 4, p. 86 (1981)
 16. R. Bartrum and H. Crow, "Transillumination Light Scanning
to Diagnose Breast Cancer: a Feasibility Study", Amer. J.
Rad. 142, p. 409 (1984)
 17. D. McIntosh, "Breast Light Scanning: a Real-Time Breast
Imaging Modality", J. Can. Ass. Rad. 34, p.288 (1983)
 18. H. Schipper and R. Brown, "Electronic Diaphanography as
an Adjunct to the Early Diagnosis of Breast Cancer:
Concept, Pilot Study and Blended Clinical Trial",
presented at the 13th Int. Cancer Congress, Seattle 1982
(unpublished)
 19. G. Geslien, J. Fisher and C. Delaney, "Transillumination
in Breast Cancer Detection: Screening Failures and
Potential", Amer. J. Rad. 144, p. 619 (1985)
 20. B. Ohlsson, J. Gundersen and D. Nilsson, "Diaphanography:
a Method for Evaluation of the Female Breast", World J.
Surg. 4, pp. 701-707 (1984)
 21. D. Watmough, "Diaphanography: Mechanism Responsible for
the Images", Acta Radiol. Oncol. 21, pp. 11-15 (1982)
 22. E. Carlsen, "Transillumination Light Scanning", Diagnostic
Imaging 4, p. 28 (1982)
 23. B. Drexler, J. Davis and G. Schofield, "Diaphanography in
the Diagnosis of Breast Cancer", Radiol. 157, pp. 41-44
(1985)
 24. J. Longworth, "On Light, Colors and the Origins of
Spectroscopy", in The Science of Photomedicine (Plenum
Press, New York, 1982), pp. 21-68
 25. A. Giese, "Basic Photobiology and Open Problems", in Lasers
in Photomedicine and Photobiology (Springer-Verlag, Berlin,
1980), pp. 27-39

26. R. Anderson and J. Parrish, "Optical Properties of Human Skin", in *The Science of Photomedicine* (Plenum Press, New York, 1982), pp. 147-194
27. H. van de Hulst, *Light Scattering by Small Particles* (Dover, New York, 1981), pp. 11-39, 63-134 and 172-191
28. K. Case and P. Zweifel, *Linear Transport Theory* (Addison-Wesley, Reading Mass., 1967), pp. 3-24, 58-76, 94-99, 110-133 and 194-203
29. S. Ertefai and A. Profio, "Spectral Transmittance and Contrast in Breast Diaphanography", *Med. Phys.* 12:4, pp. 393-400 (1985)
30. F. Bolin, L. Preuss and B. Cain, "A Comparison of Spectral Transmittance for Several Mammalian Tissues: Effects at PRT Frequencies" (unpublished)
31. S. Wan, J. Parrish, R. Anderson and M. Madden, "Transmittance of Nonionizing Radiation in Human Tissues", *Photochem. Photobiol.* 34, pp. 679-681 (1981)
32. B. Wilson, W. Jeeves and D. Lowe, "In Vivo and Post Mortem Measurements of the Attenuation Spectra of Light in Mammalian Tissues", *Photochem. Photobiol.* 42:2, pp. 153-162 (1985)
33. L. Preuss, F. Bolin and B. Cain, "A Comment on Spectral Transmittance in Mammalian Skeletal Muscle", *Photochem. Photobiol.* 37:1, pp. 113-116 (1983)
34. L. Svaasand, "Optimalization of the Depth of Selective Response of Neoplastic Tissues", pp. 27-34
35. S. Powers and J. Brown, "Light Dosimetry in Brain Tissue: an In Vivo Model Applicable to Photodynamic Therapy", *Las. Surg. Med.* 6, pp. 318-322 (1986)
36. L. Svaasand and R. Ellingsen, "Optical Properties of Human Brain", *Photochem. Photobiol.* 38:3, pp. 293-299 (1983)
37. L. Preuss, F. Bolin and B. Cain, "Tissue as a Medium for Laser Light Transport - Implications for Photodynamic Therapy", *SPIE - Lasers in Medicine and Surgery* 357, pp. 77-84 (1982)
38. L. Svaasand and R. Ellingsen, "Optical Penetration in Human Intracranial Tumors", *Photochem. Photobiol.* 41:1, pp. 73-76 (1985)
39. A. McKenzie, "Can Diffusion be Assumed in Correcting for Oblique Incidence in Laser Photodynamic Therapy", *Phys. Med. Biol.* 31:3, pp. 285-290 (1986)

40. B. Wilson, P. Muller and J. Yanch, "Instrumentation and Light Dosimetry for Intra-Operative Photodynamic Therapy (PDT) of Malignant Brain Tumors", *Phys. Med. Biol.* 31:2, pp. 125-133 (1986)
41. B. Wilson and G. Adam, "A Monte Carlo Model for the Absorption and Flux Distributions of Light in Tissue", *Med. Phys.* 10:6, pp. 824-830 (1983)
42. A. Profio and D. Doiron, "Dosimetry Considerations in Phototherapy", *Med. Phys.* 8:2, pp. 190-196 (1981)
43. J. Marynissen and W. Star, in *Porphyrin Localization and Treatment of Tumors* (Alan R. Liss Inc., New York, 1984), pp. 133-148
44. K. Shibata, A. Benson and M Calvin, "The Absorption Spectra of Suspensions of Living Micro-Organisms", *Biochimica et Biophysica Acta* 15, pp. 461-470 (1954)
45. S. Takatani, Ph.D. Thesis, Case Western Reserve University, (1978)
46. D. Greenburg and M. Tribbe, "Tissue Diagnosis by Laser Transillumination and Diaphanographic Methods", in *The Biomedical Laser* (Springer-Verlag, New York, 1981), pp. 283-291
47. P. Wilksch, F. Jacha and A. Blake, in *Porphyrin Localization and Treatment of Tumors* (Alan R. Liss Inc., New York, 1984), pp.149-161
48. A. Profio and D. Doiron, "Transport of Light in Tissue in Photodynamic Therapy", *Photochem. Photobiol.* 46, pp. 591-599 (1987)
49. S. Pizer, J. Zimmerman and E. Staab, "Adaptive Grey Level Assignment in CT Scan Display", *J. Comput Assist Tomogr.* 8(2), pp. 300-305 (1984)
50. B. Wilson, M. Patterson and S. Flock, " Indirect Versus Direct Techniques for the Measurement of the Optical Properties of Tissues", *Photochem. Photobiol.* 46, pp. 601-608 (1987)
51. R. Pearse and A. Gaydon, *The Identification of Molecular Spectra* (Chapman and Hall Ltd., London, 1950), p. 39

Appendix A - Preparation of TEM 10/10

Ingredients: 5.0 g powdered coffee creamer
phosphate buffered saline (PBS)
sample of normal whole blood
Methocel (methylcellulose product manufactured
by the Dow Chemical Co.)

Preparation:

- 1) 1% Methocel in PBS
 - a) bring 50 ml of PBS to boil
 - b) add 1.0 g Methocel powder while stirring
 - c) remove mixture from heat and add 50 ml cold PBS
 - d) mix gently and store overnight at 4 degrees to clear
- 2) 10% Creamer in PBS
 - a) heat 50 ml PBS to 80 degrees celsius in water bath
 - b) add 5.0 g coffee creamer powder and stir well
 - c) remove mixture from bath to cool at room temperature - stir frequently
- 3) 2.5% Hemoglobin Solution
 - a) add 0.5 ml freshly drawn whole blood to 10 ml distilled water to hemolyze
 - b) add 9.5 ml PBS
- 4) TEM 10/10
 - a) combine 45 ml of 1% Methocel in PBS, 5 ml of 2.5% hemoglobin solution and 50 ml of 10% creamer in PBS
 - b) mix by gentle inversion
 - c) the resulting TEM 10/10 mixture consists of 0.5% Methocel, 5.0% creamer and 1/800 hemoglobin concentration of whole blood